Investigation of The Efficacy of Some Hydroxypyridinone Iron Chelators

Lu, Zidong

Awarding institution:
King's College London

Investigation of The Efficacy of Some Hydroxypyridinone Iron Chelators

THESIS

Submitted for the degree of

DOCTOR OF PHILOSOPHY

in the

KING'S COLLEGE LONDON

by

ZIDONG LU

Institute of Pharmaceutical Science
Faculty of Life Sciences & Medicine
150 Stamford Street
London SE1 9NH

May 2016

Acknowledgements

Firstly, I would love to thank my parents for their continued support throughout my study.

Many thanks to my supervisors, Prof Robert Hider and Prof Peter Hylands for their advice and guidance, especially for Prof Hider's generous assistance in the writing of this thesis.

I am indebted to all the members of the Hider's group and also in labs in corridor C and D, 5th floor, Franklin-Wilkins Building, both past and present. However, several individuals merit a special mention:

- Dr Sukhi Bansal, for his generous help with using the mass spectrometry, for his constructive advice on analytical science.
- Dr Norman Smith, for his generous help with using the mass spectrometry and the sharing of his expertise on HILIC chromatography
- Prof Yuan Yuan Xie and Jun Pei Li, for synthesising the HPO compounds and their encouragement to my research
- Prof Yong Min Ma, Dr Xiao Le Kong and Dr Vincenzo Abbate, for their valuable advices throughout my research
- Dr Manasi Nandi and her research members, for conducting the animal surgical procedures for the *in vivo* efficacy model
- Ranko Gacesa, for the sharing of his expertise on chemical structure software use and for helping me with the thesis formatting

Finally, I would love to express my gratitude to Zu dong Liu and Prof Yong Ping Yu (Zhe Jiang University, China), for the collaboration of the CN128 preclinical studies and financial support.

This has been such a wonderful journey since I started my PhD research programme in July 2012. During this journey, the beauty of research science has revealed itself in remarkable ways. I am intrigued with the experience of exploring the charm of science, which is a circle of pursuing novel questions, solving the problems, appreciating the discoveries and asking new questions. The attraction of science is such that it never ends with a full stop but continues on and on, and while we are exploring science, we develop a better understanding about ourselves.

Declaration

This thesis submitted for the degree of Ph.D. entitled “Investigation of The Efficacy of Some Hydroxypyridinone Iron Chelators” is based upon work conducted by the author in the Institute of Pharmaceutical Science, King’s college London between July 2012 and May 2016. All of the work described herein is original unless otherwise acknowledged in the text or by references. None of the work has been submitted for another degree in this or any other university.

ZIDONG LU

July, 2016

List of Publications

- Y.Xie*, **Z.Lu***(contributed equally), X.Kong, T.Zhou, S.Bansal and R.Hider, Systematic comparison of the mono-, dimethyl, and trimethyl 3-hydroxy-4(1H)- pyridones attempted optimisation of the orally active iron chelator, deferiprone. *Eur. J. Med. Chem*. **2016**, 115:132-40.

- J.Li*, **Z.Lu***(contributed equally), X. Kong, Y. Ma, X.Zhang, S.Bansal,V. Abbate and R.Hider, Design and synthesis of novel pegylated iron chelators with decreased metabolic rate. *Future Med. Chem.* **2015**, 7(18): 2439-2449.

- Pangjit, K., R. Banjerdpongchai, C. Phisalaphong, S. Fucharoen, Y. Xie, **Z. Lu**, R.Hider and S. Srichairatanakool, Characterisation of a novel oral iron chelator: 1-(N-Acetyl-6-Aminohexyl)-3-Hydroxy-2-Methylpyridin-4-one. *J. Pharm. Pharmacol.* **2015**, 67(5): 703-713

Abstract

Patients who suffer from secondary iron overload, such as β-thalassemia, are heavily iron overloaded due to their dependence on frequent blood transfusions. Iron chelation therapy has been required for the treatment of the iron overload when the body iron homeostasis has been disrupted. CP20/deferiprone, which belongs to the 3-Hydroxypyridin-4-one (3-HPO) family, has been used as a clinically useful iron chelator by virtue of its oral activity and good iron mobilisation potency. However, it has been associated with some side effects due to the large dose administered, which is related to the extensive Phase II glucuronic acid conjugation at one of the essential iron chelation sites (3-hydroxyl group) in the liver. So novel iron chelators with reduced glucuronide conjugates at the 3-hydroxyl group are sought.

The research questions approached in the thesis are to investigate the *in vitro* hepatic drug metabolism and *in vivo* iron mobilisation efficacy of 2nd generation 3-hydroxypyridin-4-one chelators. The specific aim is to screen their *in vitro* liver metabolic clearance profiles using liver microsomes and to select the candidate compounds with potential potency in iron chelation for further *in vivo* iron mobilisation efficacy study using a Fe^{59}-Ferritin loaded rat model.

A rapid, but sensitive and selective bio-analytical method for screening and quantification of the hepatic *in vitro* metabolic clearance of novel 3-hydroxypyridin-4-ones has been developed. This new approach is suitable for screening a series of 3-HPOs with high-throughput. A series of 3-HPO derivatives including two stereoisomers of chiral compounds, deferiprone analogues and pegylated 3-HPOs have been screened using the developed method and have represented different structure related metabolic profiles, which are of great relevance to investigate the structure activity relationships. One of the chiral enantiomers**,** CN128, was demonstrated to be much less susceptible towards the glucuronidation conjugation enzyme in the *in vitro* microsomal model (the percentage of glucuronidation is only 20% less compared to that of CP20/deferiprone). Another HPO, the acetamido-alkyl analogue of deferiprone, CM1, was found to be extensively conjugated by glucuronic acid (the percentage of glucuronidation is roughly 70% less compared to that of CP20/deferiprone). However, CM1 possesses a higher LogP

value compared with CP20/ deferiprone, consequently, it was predicted to remove intracellular iron more efficiently from iron overloaded sites. These two compounds were selected for the *in vivo* iron mobilisation efficacy study in a Fe^{59}-Ferritin loaded rat model. CN128 displayed significantly higher iron mobilisation from the rat liver at lower doses when compared with therapeutic doses of CP20/deferiprone. CM1, although more effective than CP20/ deferiprone, was much less effective than CN128.

Contents

Table of Contents

List of Figures

List of Tables

List of Schemes

Abbreviations

ACN Acetonitrile

ACS Acute Chest Syndrome

B.W. Body Weight

BEH Ethylene Bridged Hybrid

BMP Bone Morphogenetic Protein

CYP Cytochrome P450

Dcytb Duodenal cytochrome-b

DFO Desferrioxamine

DFP Deferiprone

DFS Deferasirox

DMT Divalent Metal Transporter

ER Endoplasmic Reticulum

ERFE Erythroferrone

ESI Electrospray Ionisation

FPN Ferroportin

GDF15 Growth Differentiation Factor

GPI Glycosylphosphatidylinositol

HCP1 Haem Carrier Protein 1

HH Hereditary Haemochromatosis

HILIC Hydrophilic Interaction Liquid Chromatography

HLMs Human Liver Microsomes

HPO Hydroxypyridinone

ICH International Conference on Harmonisation

IDA Iron Deficiency Anaemia

IREs Iron Response Elements

IRP Iron Response Protein

IS Internal Standard

LC Liquid Chromatoraphy

LLOQ Lower Limit of Quantification

LPI Labile Plasma Iron

MAX Mix-Mode Anion-exchange

MCX Mixed-Mode Cation Exchange

MP Mobile Phase

MPS Mononuclear Phagocytic System

MRM Multiple Reaction Monitoring

MS Mass Spectrometry/ Spectrometer

NaCMC Sodium Carboxymethyl Cellulose

NADPH Nicotinamide Adenine Dinucleotide Phosphate

NTBI Non Transferrin Bound Iron

PAD Photodiode Array Detector

PBS Phosphate Buffered Saline

PFOA Pentadecafluorooctanoic Acid

PLRP Polymer Reversed Phase

QC Quality Control

QCL Quality Control Low

QLH Quality Control High

QLM Quality Control Medium

QqQ Triple-Quadrupole

RBCs Red Blood Cells

RE Reticulo-Endothelial

RLMs Rat Liver Microsomes

RP Reversed Phase

SCD Sickle Cell disease

SD Sprague-Dawley

SF Serum Ferritin

SPE Solid Phase Extraction

SRA Structure Related Activity

STf Serum Transferrin

TfR Transferrin Receptor

UDPGA Uridine 5'-DiphosPhoGlucuronic Acid

UGT Uridine Diphosphate Glucuronosyl Transferases

ULOQ Upper Limit Of Quantification

UPLC Ultra Performance Liquid Chromatography

UTRs Untranslated Regions

UV Ultra Violet

WAX Weak Anion-eXchange

WCX Weak Cation-eXchange

S.I.D Semel In Die (once a day)

B.I.D. Bis In Die (twice a day)

CHAPTER ONE

General Introduction

Chapter 1 General introduction

1.1 The biological role of iron

Iron is an essential metal for any life form. It participates in a wide variety of biological reactions in a range of iron-containing metallo-proteins. These proteins can be divided into three groups: (1) Haem proteins: oxygen carriers, such as haemoglobin, myoglobin; oxygen activators, such as cytochromes P450, peroxidases and catalases; electron transfer proteins, such as cytochromes a, b and c; (2) Iron sulfur proteins, such as dehydratases (4Fe-4S cluster containing) and (3) Non-haem, non-iron-sulfur, iron dependent proteins, such as ribonucleotide reductase and ferritin (Finkelstein, 2009).

1.2 Cellular iron uptake, storage and export

The way in which cells import iron from the external environment and export it for functional use or store it in temporary storage depots is regulated by a variety of proteins, as illustrated by Figure 1.1 (Hentze et al., 2004).

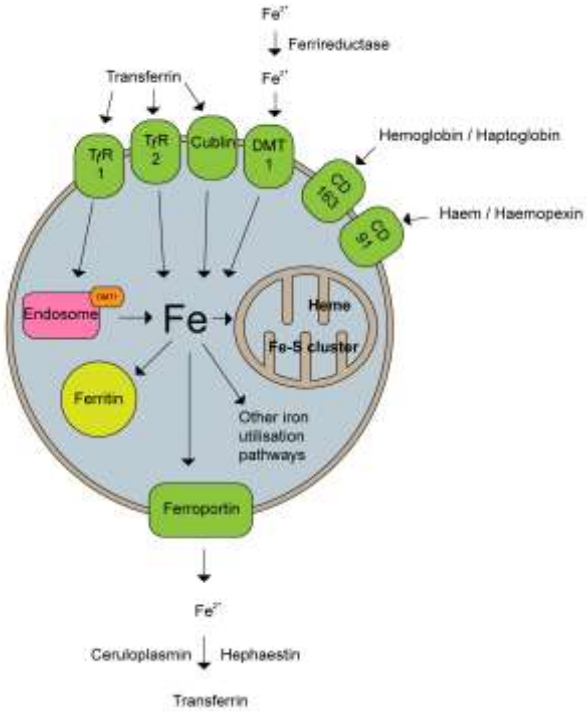

Figure 1.1 Cellular iron metabolism
modified from Hentze, Muckenthaler et al. (2004)
TfR: Transferrin Receptor; DMT1: Divalent Metal Transporter

1.2.1 Celluar iron uptake

1.2.1.1 Transferrin (Tf) bound iron

Under normal circumstances, iron circulating in the plasma is tightly bound to serum transferrin (Tf), in which manner iron is nonreactive (Mizutani et al., 2012). Tf is a glycoprotein of molecular weight around 80kD. It possesses two iron binding sites, with each binding site consisting of two tyrosines, one histidine, one aspartate and a synergistically bound carbonate anion, being able to bind iron(III) tightly with an affinity of 10^{-20} M^{-1} (Mizutani et al., 2012). Tf, synthesised in the liver is secreted into the circulation. The level of Tf circulating in the blood is typically 35 μM, with 25% to 35% of the iron binding sites occupied. Tf plays a vital role in iron transportation, in brief, Tf bound iron is delivered from the absoption site (the gastrointestinal tract) and haem degradation (the reticuloendothelial system) to sites of utilisation (for erythropoiesis, and incorporation into iron containing proteins) and storage (in ferritin) (Mizutani et al., 2012). Iron uptake from transferrin is mediated by transferrin receptors (TfR), which are TfR1 expressed on many cell types and TfR2 limited to hepatocytes and erythrocytes (Cheng et al., 2004) (Figure 1.1). The uptake of iron bound Tf via TfR1 follows the receptor mediated endocytosis pathway. The complex of iron(III) bound Tf and TfR1 localises to clathrin-coated pit and is endocytosed. The release of iron (Fe^{3+}) from transferrin-TfR1 complex within the endosome requires a pH dependent conformational change, which is provided by the ATP dependant proton pump in the endosome (Cheng et al., 2004). The released Fe^{3+} is reduced to Fe^{2+} by a ferrireductase on the endosomal membrane and is transported to the cytosol by the divalent metal transporter (DMT-1) (Fleming et al., 1998). Alternatively, Steap3 has been identified as the endosomal ferrireductase required for efficient Tf dependent iron uptake in erythroid cells (Ohgami et al., 2006). Apo-Tf and TfR1 are recycled back to cell membrane, in readiness for another cycle of iron binding, transport and release. It has been estimated that Tf molecules experience more than 200 cycles during their life span (Cheng et al., 2004). Transferrin receptor 2 (TfR2) also mediates transferrin bound iron with the iron binding affinity significantly lower than that of TfR1 (Figure 1.1). TfR2 contributes to the susceptibility of the liver to iron loading in hereditary haemochromatosis. A truncation mutation in TfR2 is associated with a rare form of hereditary haemochromatosis, an iron overload disorder characterised by excessive dietary iron absorption and iron deposition in liver and other parenchymal tissues

(Camaschella et al., 2000). There are three subtypes of transferrin receptors. TfR1 has iron response elements in its mRNA and, as a consequence, is down regulated in conditions of iron overload. In contrast, TfR2 does not have iron response elements (IREs) and is not reciprocally regulated in response to the level of plasma iron (Rouault, 2006). The iron supply for kidney is also provided by Tf bound iron but through megalin-dependent, cubilin-mediated endocytosis by a third type of TfR located in epithelial kidney cells (Kozyraki et al., 2001) (Figure 1.1).

1.2.1.2 Non-transferrin bound iron (NTBI)

Under normal circumstance, the Tf iron saturation is 25% to 35%. However, in pathological iron overload patients, the Tf iron binding sites are often fully saturated, leading to the appearance of circulating “free” iron, namely non transferrin bound iron (NTBI) (Hider, 2002). NTBI is characterised by an iron pool whose chemical nature is not well established. Studies on the nature of NTBI have suggested that it consists of heterogeneous forms of iron, which may or may not be accessible for chelation. The proportion of the iron isoforms varies depending on the source and degree of iron overload, involving both non-protein and protein forms (Brissot et al., 2012). Studies have provided evidence that citrate with a probable involvement of acetate and plasma albumin are the possible NTBI ligands (Hider, 2002). A component of NTBI is susceptible to iron chelation and is redox active, which is termed labile plasma iron (LPI). Due to these attributes, LPI play an essential role in causing pathogenesis of iron toxicity. There are indications that LPI is rapidly cleared from plasma by the liver (Cabantchik et al., 2005). The NTBI is taken up by cardiac and endocrine tissues by membrane bound carrier molecules. It has been reported that the transportation of NTBI into hepatocytes occurs via DMT-1 (Shindo et al., 2006) (Figure 1.1). The Zrt–Irt-like protein 14 (ZIP14) (SLC39A14) is a zinc transporter and mediates hepatocellular NTBI uptake (Liuzzi et al., 2006). The uptake of NTBI by cardiac myocytes has been reported to be facilitated by L-type voltage-dependent calcium channels (Oudit et al., 2003).

1.2.1.3 Dietary Iron

The uptake of dietary iron is through the intestinal mucosal cell at the upper part of the gastrointestinal tract, duodenum (Aisen et al., 1999). Dietary iron, not bound to transferrin, is

composed of highly bioavailable haem iron and relatively bio-unavailable non-haem iron (Carpenter and Mahoney, 1992). Non-haem iron Fe^{3+} is reduced to Fe^{2+} by a brush-border membrane reductase, Dcytb (Duodenal cytochrome-b) (McKie et al., 2001) and transported across the apical enterocyte membrane into the cell through a proton coupled process via DMT-1 (Fleming et al., 1997). Haem iron uptake is via a separate pathway by the transport erythrocytes protein haem carrier protein 1 (HCP1), once absorbed, haem is degraded by haem oxidase to form Fe(II) (Shayeghi et al., 2005).

1.2.1.4 Haptoglobin and haemopexin iron transporters

Iron may also be absorbed in the protein bound forms, such as haemoglobin. Intravascular haemolysis, associated with senescent erythrocyte degradation by tissue macrophages in normal individuals and enhanced under pathological conditions such as haemolytic anaemias, thalassaemias etc., lead to the release of haemoglobin into plasma (Garby and Noyes, 1959). Haemoglobin turnover releases “free” iron, which is redox-active and can be a source of free radical formation (Ascenzi et al., 2005). Haptoglobin, an acute phase protein produced by the liver circulates in high concentrations (0.45–3 mg/mL) in plasma and forms a complex with haemoglobin (Wada et al., 1970). The haptoglobin-haemoglobin complex can be cleared in the reticulo-endothelial (RE) system by receptor-mediated endocytosis. The uptake of this complex is via the internalisation by a scavenger receptor CD163 in tissue macrophages (Kristiansen et al., 2001) (Figure 1.1). Destruction of the haptoglobin-haemoglobin complex thereby minimises haemoglobin toxicity and also contributes to iron recycling (Kristiansen et al., 2001).

Haem arising from the degradation of haemoglobin, myoglobin, and of enzymes with haem prosthetic groups could be delivered in plasma (Ascenzi et al., 2005). Haemopexin, a serum protein, sequesters free haem as a backup mechanism for haptoglobin and delivers the haem to target cells via specific receptors. The haem-haemopexin complex is internalised by CD91 receptor-mediated endocytosis, and the haem is then released and degraded intracellularly in the hepatic parenchymal cells, while haemopexin is recycled back into the circulation (Figure 1.1). In this way, haem clearance by the haemopexin pathway prevents extracellular damage by free haem, and conserves iron by recycling the haem iron (Smith and Morgan, 1981).

1.2.1.5 Serum ferritin bound iron

Iron may also be taken up by cells in the plasma ferritin bound form. It has been reported that almost all of radio-iron labeled ferritin injected into rats is taken up by the liver in *in vivo* studies (Unger and Hershko, 1974). *In vitro* studies have demonstrated that rat hepatocytes take up ferritin by receptor-mediated endocytosis and the ferritin protein is destroyed by lysosomal degradation. The associated iron is re-used for hepatocyte ferritin synthesis (Osterloh and Aisen, 1989).

1.2.2 Cellular iron storage

Once iron enters the cell via different transport mechanisms, the portion that is not needed for immediate use is stored in ferritin, located predominantly in the liver, spleen and bone marrow, where 25% of total body iron (800-1000 mg) is stored (Laulhere et al., 1989). Ferritin is an oligomeric protein composed of an apoprotein shell of 24 subunits, forming a hollow protein shell, capable of storing up to 4500 iron atoms. Ferritin sequesters the metal in the water-soluble, nontoxic, bioavailable ferric oxyhydroxide form and stores iron as the mineral ferrihydrite core. The 24 subunits are heteropolymers of light (L) and heavy (H) chain subunits. The ratio of H to L subunits varies depending on tissue type and physiologic status. H and L subunits cooperate in the iron mineral core formation. Ferritin has ferroxidase property, converting Fe^{2+} to Fe^{3+} as iron is internalised and packed into the mineral core. This ferroxidase activity is an inherent feature of the H subunit, which is characterised by a diiron, ferroxidase centre, while L subunits enhance oxidation activity by the increasing the binding affinity of ferric iron at the nucleation sites of the iron core. Iron is also stored in haemosiderin, which is derived from the intralysosomal aggregation and degradation of ferritin. The storage of iron, whether in the form of ferritin or haemosiderin, can be mobilised for cellular utilisation, and released by lysosomal degradation (Munro and Linder, 1978).

1.2.3 Intracellular iron distribution

1.2.3.1 Labile iron pool

Extracellular iron and intracellular iron released from endogenous haem breakdown and ferritin degradation enter a transit iron pool, which is a redox-active, labile iron pool (LIP) and can be scavenged by iron chelators. This pool was first defined by Jacobs (Jacobs, 1976) (Figure 1.2). The nature of LIP has been proposed to be iron(II) bound to a single molecule of glutathione and the concentration of this pool falls into a range of 0.5-2 μM. (Hider and Kong, 2013). The level of LIP should be under tight control as non-coordinated free iron can generate oxygen derived free radicals and render tissue damage (Halliwell and Gutteridge, 1984).

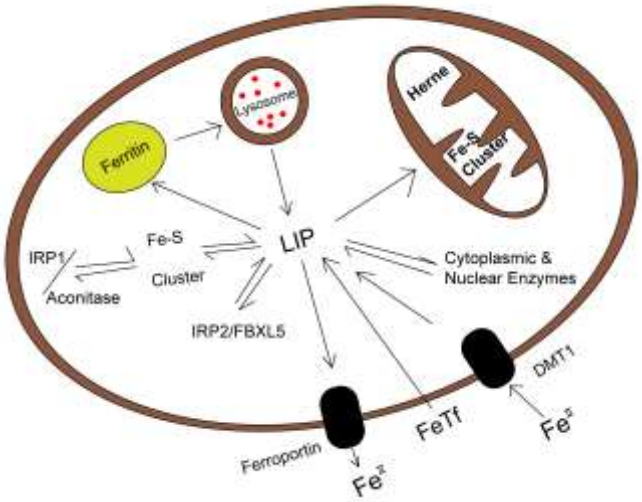

Figure 1.2 Labile iron pool and cellular iron homeostasis
modified from Hider and Kong (2013)
DMT1 divalent metal transporter-1; IRP iron responsive protein,. FBXL5 F-box and leucine-rich repeat protein 5

1.2.3.2 Intracellular Iron distribution

LIP is routed to for haem and iron sulfur cluster biosynthesis in mitochondria and for iron incorporation into metalloenzymes and ferritin (Ajioka et al., 2006, Lill and Muhlenhoff, 2006). The iron uptake by mitochondria is dependent on the membrane potential and facilitated by the transport proteins mitoferrin-1 and mitoferrin-2 (Paradkar et al., 2009). The yeast homologue of human frataxin, plays a role as an iron chaperone, delivering iron to both the iron sulfur cluster and haem biosynthetic pathways. Frataxin gene deletion causes the neurodegenerative disorder Friedreich ataxia (Huynen et al., 2001). Erythrocyte precursor cells and hepatocytes are the two major sites of haem biosynthesis, where haemoglobin and heam-containing

enzymes (e.g. cytochrome P450) are synthesised respectively. Iron-sulfur clusters play multiple functional roles in electron transport, in catalysis of metabolic reactions and as sensors of mitochondrial iron status (Heinemann et al., 2008).

1.2.4 Cellular Iron Export

The expression of SLC40A1 gene has lead to the identification of an iron exporter ferroportin. It plays an essential role in iron export of cells requiring mechanisms to release iron in a controlled fashion for different functional use. Ferroportin is specific for iron(II) and is the only iron exporter protein identified to date. It is located on the basolateral side of duodenal enterocytes and in the cytoplasmic membranes of both macrophages and hepatocytes (McKie et al., 2000, Donovan et al., 2000, Abboud and Haile, 2000). Ferroportin functions in concert with different ferroxidases, such as hephaestin (Vulpe et al., 1999), ceruloplasmin (Harris et al., 1999) and glycosylphosphatidylinositol (GPI)-anchored form of ceruloplasmin, to export (Jeong and David, 2003) iron from duodenal enterocytes, reticuloendothelial macrophages, hepatocytes and cells of CNS respectively.

1.3 Regulation of Iron homeostasis

1.3.1 Cellular iron homeostasis

Cellular iron uptake, storage, utilisation and export pathways described above must be regulated in a coordinated fashion. Regulation of iron homeostasis is achieved at the level of mRNA translation (protein synthesis). The IRE-IRP system constitutes a regulatory mechanism for regulating cellular iron homeostasis (Rouault, 2006). Single Iron regulatory elements (IREs) are located at the 5'-untranslated regions (UTRs) of ferritin (Leibold and Munro, 1988) and multiple IREs are located at the 3'-UTRs of transferrin receptor mRNA respectively (Owen and Kühn, 1987). The iron regulatory proteins IRP1 and IRP2, which are iron regulated cytosolic RNA binding proteins, bind to the IREs and form IRE/IRP complexes (Rouault, 2006). IRPs binding to the single IREs located in the 5'-UTR of ferritin mRNA inhibits mRNA translation, whereas binding to the IREs present in the 3'-UTR of transferrin receptor mRNA prevents nuclease degradation. This ensures that iron uptake is stimulated in iron deplete cells. In

contrast, when iron storage is expanded, the IRPs no longer bind to the IREs, ferritin mRNA is translated while transferrin receptor mRNA undergoes endonuclease cleavage. In this case, unnecessary iron uptake is suppressed, which avoids potential iron toxicity by up-regulation of the storage protein (Wallander et al., 2006). IRP1 and IRP2 both act as iron sensors, essentially by existing in two different conformations, regulating either the translation or turnover of the iron dependent protein mRNA. The cellular labile iron pool regulates binding of IRP1 and IRP2 to IREs through distinct mechanisms. When iron levels are high, IRP1 assembles a [4Fe-4S] cluster, which transforms the protein into a functional cytoplasmic aconitase, inhibiting IRE binding activity. When cellular iron stores are low, IRP1 was targeted as apoprotein and bound to IRE. In contrast, IRP2 does not contain an [4Fe-4S] cluster. It accumulates in iron-deficiency and is rapidly degraded by proteasome when iron levels are elevated. The protein FBXL5, which targets IRP2 to the proteasome, is also degraded upon iron depletion (Vashisht et al., 2009) (Figure 1.2).

1.3.2 System iron homeostasis

1.3.2.1 Body iron distribution

Around 1 to 2 mg of dietary iron is absorbed by duodenal enterocytes per day. Roughly 1 to 2 mg of iron is lost from the body per day by means of sloughed mucosal cells, desquamation and menstruation. Adult men normally have 35 to 45 mg of iron per kilogram of body weight. More than two thirds of the body's iron content is distributed to the bone marrow, incorporated into haemoglobin in contributing to haemoglobin synthesis. Uptake of erythroid iron is facilitated via the receptor-mediated endocytosis of diferric transferrin bound to transferrin receptors. Each erythrocyte contains a billion atoms of iron; hence, at normal rates of turnover, $2x10^{20}$ atoms of iron are incorporated into haemoglobin per day. Most of the remaining body iron is deposited in hepatocytes and reticuloendothelial macrophages, which serves as iron storage depots. The liver extracts dietary nutrients by the "first pass effect" and can readily take up an amount of circulating iron, which is not bound to transferrin and store iron in ferritin. Reticuloendothelial macrophages recycle iron by ingesting senescent red blood cells, catabolising haemoglobin to scavenge iron, and loading the iron onto transferrin for reuse. Minor amounts of iron are distributed to other tissues: 3.5% is distributed to myoglobin; 0.5% is incorporated into iron

containing enzymes (cytochromes, dioxygenases, ribonucleotide reductase, lipoxygenases etc.); only 0.1% is bound to transferrin at any one time (Andrews, 1999).

The circulating iron bound to plasma transferrin, although less than 0.1% of total body iron, represents a kinetically active iron pool, due to the rapid turnover of plasma transferrin. The plasma Tf iron pool turns over more than 20 times per day, iron being recycled for the requirement of erythrocyte production (Gkouvatsos et al., 2012).

1.3.2.2 Regulation of body iron status

As there is no efficient pathway for iron excretion in the human, iron balance requires mechanisms for regulating iron entry into and mobilisation from stores. Hepcidin is a small, cysteine-rich peptide, which regulates iron export from cells by interacting with an iron efflux protein located on cell surface, ferroportin (Section 1.2.4) and inactivates its cellular iron export function by the internalisation and degradation of this iron efflux protein. Thus, under high hepcidin levels, ferroportin located in the duodenal epithelial cells and macrophages will be internalised and as a result, such cells are unable to efflux iron into plasma resulting in low transferrin saturation. In contrast, decreased expression of hepcidin leads to increased cell surface ferroportin, iron absorption is enhanced and high iron fluxes enter the serum (Nemeth et al., 2004). Hepcidin plays a vital role in regulation of iron homeostasis. Dysregulation of hepcidin expression results in iron disorders. Overexpression of hepcidin results in the anemia of chronic disease, while depression of hepcidin synthesis leads to hereditary hemochromatosis (De Domenico et al., 2007)

Plasma hepcidin levels are regulated by different stimuli, including plasma iron, erythropoietic signals, cytokines, and hypoxia. Hepcidin expression regulation occurs at the level of transcription. Hepcidin antimicrobial peptide (*HAMP*), which is the gene that encodes hepcidin, plays an essential role in the regulation of hepcidin expression. The synthesis of hepcidin is regulated by signaling through the bone morphogenetic protein/Smad (BMP/Smad) pathway. BMPs bind to cell surface *HJV* positions and activates BMP receptors on the cell membrane, leading to the generation of phosphorylated RSmads, which dimerize with Smad4. The RSmad/Smad4 heterodimer translocates into the nucleus and activates transcription of the

HAMP gene and thereby controls hepcidin synthesis (Casanovas et al., 2009). Inflammatory cytokines, predominately IL-6, also stimulate the transcription of *HAMP* in hepatocytes by activation of Stat3, binding a regulatory element in the *HAMP* (Verga Falzacappa et al., 2007). The regulation of hepcidin expression is also modulated by increased erythropoietic activities. A candidate erythroid factor, Growth Differentiation Factor 15 (GDF15), was identified, which suppresses hepcidin synthesis. It also serves as an oxygen-regulated transcript responding to hypoxia, indicating that hypoxia stimulates suppression of hepcidin expression (Lakhal et al., 2009). A recently discovered hormone, erythroferrone (ERFE), has also been found to mediate the suppression of hepcidin during stress erythropoiesis (such as after hemorrhage) (Kautz et al., 2014).

1.4 Disorders of Iron overload

The accumulation of excessive iron in various tissues causes tissue damage, and ultimately, organ failure, which results from iron-generated production of highly reactive free radicals (Beutler, 2007). The iron balance in man is predominantly determined by iron absorption, because the human body does not have a physiological mechanism to excrete iron (McCance and Widdowson, 1937). Inappropriately high duodenal iron absorption in hereditary haemochromatosis (HH) and transfusional, parenteral or dietary iron overload (secondary iron overload) leads to disorders of systemic iron overload (Andrews, 1999).

1.4.1 Assessment of body iron burden

The assessment of body iron balance is essential, because it facilitates the diagnosis of disorders of iron overload and monitors the iron balance during chelation therapy. The body iron burden can be measured by various means. The most common and inexpensive indicator to estimate the body iron store is the serum ferritin concentrations. However, the level of serum ferritin concentrations can be complicated by various other pathological conditions, such as acute infection, chronic inflammation, hepatic damages, and may give inaccurate estimates of total body iron (Cavill, 1999). Percentage transferrin saturation with a normal range of 20~30% and ~100% for iron overloaded patients can also be used as a combined indicator with the serum ferritin level (Wish, 2006). Liver biopsy was used as a gold standard for monitoring body

iron balance in the past, as the liver is the dominant iron storage organ and its iron concentration correlates tightly with the total iron balance. Unfortunately, liver biopsy is invasive, expensive and can be unreliable due to the heterogeneity of iron loading in the liver (Crisponi et al., 2000). At the present time, Magnetic Resonance Imaging (MRI) has emerged as the noninvasive technique of choice for the estimation of liver iron content, due to its sensitivity, reproducibility (Wood, 2007). The closely related MRI T2* technique is especially useful for monitoring cardiac iron overload (Anderson et al., 2001).

1.4.2 Primary iron overload

1.4.2.1 Hereditary haemochromatosis (HH)

HH is a group of genetically distinctive disorders of iron overload. They are hereditary, usually transmitted as autosomal recessive. The common clinic-pathology is the inappropriately low level of hepatic hepcidin secretion, which renders excessive level of the iron export protein ferroportin (FPN1). This unrestricted activity of FPN1 leads to iron transfer to circulation from the duodenum and the macrophages, increasing transferrin saturation (from 30% to fully saturation) and serum ferritin levels. The progressive accumulation of iron in parenchymal cells can result in severe consequences, such as diabetes, arthritis and cirrhosis of the liver. HH is composed of five major types of different genetic disorders (Pietrangelo, 2006). HFE haemochromatosis (Type 1 haemochromatosis) is the most widely prevalent form of HH. The gene mutated in HH encodes a 348 residue type I transmembrane glycoprotein, HFE. Most HH patients are homozygous for the C282 Y mutation (Feder et al., 1996). HFE is partitioned between TfR1 and TfR2. High serum iron concentration renders the formation of the HFE/TfR2 complex, which signals hepcidin up-regulation, leading to a reduction in both intestinal iron absorption and macrophage iron release. While low serum iron concentration favours the HFE/TfR1 complex. Upon the mutation of either HFE or TfR2, dysregulation of iron homeostasis occurs (Schmidt et al., 2008).

1.4.2.2 Treatment of Primary Iron overload

Therapeutic phlebotomy is so far the most effective treatment for haemochromatosis, in which one unit (400–500 ml) of blood (containing approximately 200-250mg of iron) is removed weekly until serum ferritin drops below 30 µg/l and transferrin saturation is less than 30%. Phlebotomy is maintained with the typical removal of 2-4 units per year for the rest of the patient's life. Once organ impairment develops, Phlebotomy should be replaced by other iron removal strategies (e.g.chelatIion therapy) (Pietrangelo, 2006).

1.4.3 Secondary iron overload

Secondary iron overload occurs in haematoglogical diseases (thalassaemia, sickle cell anaemia etc.), which are treated with repeated blood transfusion. As there is no mechanism for iron excretion, repeated transfusion results in iron overload. Multiple blood transfusions also produce erythroid factors, Growth Differentiation Factor 15 (GDF15), leading to down-regulation of hepcidin, which initiates hepatic iron overload (Section 1.3.2.2). In chronic haemolytic disorders, excess gastrointestinal absorption of iron is observed prior to transfusion as a consequence of ineffective erythropoiesis. In contrast to HH, iron deposition in secondary iron overload patients primarily affects cells of the mononuclear phagocytic system (MPS), with parenchymal iron loading occurring at larger stages of the disease (Kushner et al., 2001). In severely iron-loaded patients, the capacity for transferrin to bind iron is exceeded, and non-transferrin bound iron (NTBI) is found in serum, which is highly toxic and causes tissue iron loading. NTBI occurs in 80% of patients with thalassemia major (Brissot et al., 2012). NTBI is avidly taken up by several tissues, such as liver, heart and endocrine, which support the role of NTBI as an important source of parenchymal organ iron deposition. In contrast to transferrin iron uptake which is down regulated by the IRE/IRP system, in a fashion that a depression of transferrin receptor expression responds to an elevated iron store, NTBI uptake is not regulated by this system and iron loading from NTBI is apparently rapid and unregulated (Baker et al., 1998). One component of NTBI, the so-called labile plasma iron (LPI), found when transferrin saturation exceed 75%, is iron chelatable, capable of redox cycling and may represent a marker of toxicity, due to its potential for generating reactive oxygen radicals *in vivo*. The direct capture of LPI has been suggested as a way to avoid the dangerous accumulation of cellular iron and to

prevent the resultant adverse consequences (Cabantchik et al., 2005).

1.4.3.1 Sickle cell anemia

Sickle-cell disease (SCD) refers to a group of genetic haemoglobin disorders that are associated with mutations in the HBB gene. A single base pair in the β-globin gene is mutated from adenine to thymine generating a corresponding substitution in the sixth position of the β-subunit from glutamic acid to valine. Under conditions of low oxygen tension, the abnormal deoxyhaemoglobin polymerizes and eventually leads to a sickle-shaped red blood cell (Luzzatto and Goodfellow, 1989). SCD is characterised by chronic haemolytic anaemia and vaso-occlusive events. These events result in acute complications including stroke, acute chest syndrome (ACS) and heart failure etc. (Hagar and Vichinsky, 2008). These serious complications related to SCD can be prevented by appropriate regular blood transfusions. However, regular transfusion leads to iron overload, which should be treated by chelation therapy (Lucania et al., 2011).

1.4.3.2 β-Thalassemia

Thalassemia is a hereditary anemia resulting from haemoglobin production defects. It is predominantly classified into α-thalassemia and β-thalassemia, of which β-thalassemia is associated with more significant morbidity and mortality. β-thalassemia is clinically heterogeneous and can be categorised into (1) β-thalassemia trait (minor); (2) β-thalassemia major; and (3) β-thalassemia intermedia. The pathophysiology of the β-thalassemia is well outlined. The mutations at the β-globin gene result in an absence or a reduction of the β-globin chain production, which lead to an excess of α-globin chain. The unbound α-globin chains precipitate in the erythroid precursor cells and cause accelerated apoptosis. The accelerated apoptosis is the major reason of ineffective erythropoiesis and hemolysis, which consequently cause anemia accompanied with bone marrow expansion and extramedullary haematopoiesis in the liver, spleen, and other sites (Schrier, 2002). The life-saving, routine treatment of β-thalassemia major (associated with the total absence of β-subunits) is by blood transfusion thereby maintaining haemoglobin at normal level. This can markedly suppress ineffective erythropoiesis and bone marrow expansion (Rund and Rachmilewitz, 2005).

1.4.3.3 Treatment of secondary iron overload

Although phlebotomy therapy is applied in patients with thalassaemia intermedia associated with ineffective erythropoiesis, iron chelation therapy is the predominant treatment for secondary iron overload patients: (i) thalassaemia major patients; (ii) thalassaemia intemediate patients who are nontransfusion dependent but become iron loaded because of increased iron absorption but are too anaemic to undergo phlebotomy; and (iii) regularly transfused patients with sickle cell anaemia and myelodysplasia, aplastic anaemia (Beutler et al., 2003).

Iron chelators are used to alleviate body iron burden in order to prevent damage parenchymal organs, such as liver, endocrine and, in particular, heart (Hider et al., 1996).

1.5 Iron chelators

High-spin iron(III) is a spherically symmetrical tripositive cation with a radius 0.65 Å, which is classified as a hard Lewis acid by virtue of its high charge density. It forms most stable bonds with 'hard' ligands with oxygen as the donor atoms (Zhou et al., 2012). Based on this understanding, efforts to design iron chelators with a high iron scavenging efficacy from overloaded sites have been undertaken over the past four decades. Three iron chelators are presently in clinical use.

1.5.1 Desferrioxamine

Desferrioxamine B (DFO, Desferal®) is the first clinical effective iron-chelating agent developed by Ciba-Geigy in 1960s and has been extensively used for treatment of iron overload for the past four decades (Bernhardt, 2007). DFO is derived from a microbial siderophore of *Streptomyces pilosus*. DFO is a hexadentate ligand, of which three bidentate hydroxamate moieties are deprotonated and are coordinated with a single ferric iron and form a 1:1 ratio complex in a distorted octahedral $Fe^{III}O_6$ fashion (Figure 1.3). DFO has exceptionally high affinity (pFe^{3+} 26.6) and selectivity to iron(III) (Zhou et al., 2012). This highly hydrophilic molecule ($logD_{7.4}$ = -2) can enter the liver via facilitated transport and interacts with both hepatocelluar and reticuloendothelial iron stores to promote both biliary and urinary iron excretion (Hershko, 1978). Ferrioxamine, the DFO-iron complex $[Fe^{III}(DFO)]^+$, is a charged

compound (1+) with low lipophilicity at pH 7.4 and is kinetically inert and unlikely to redistribute iron to other cells (Zhou et al., 2012). However, oral inactivity (molecular weight 560), rapid plasma metabolism (plasma half-life of 5-10 min) and fast renal clearance prevent it from being an ideal therapeutic agent. In order to alleviate the elevated body iron burden, DFO must be given by continuous subcutaneous or intravenous infusion for 8-12h per day, 5-7 days per week at a standard dose of 40 mg/kg/day. Consequently, patient compliance with this cumbersome and expensive regimen is often poor (Porter et al., 1989a). Moreover, side effects have been associated with intensive therapy in young patients with relatively low body iron stores, such as neurotoxicity and abnormalities of cartilage formation (Porter et al., 1989b).

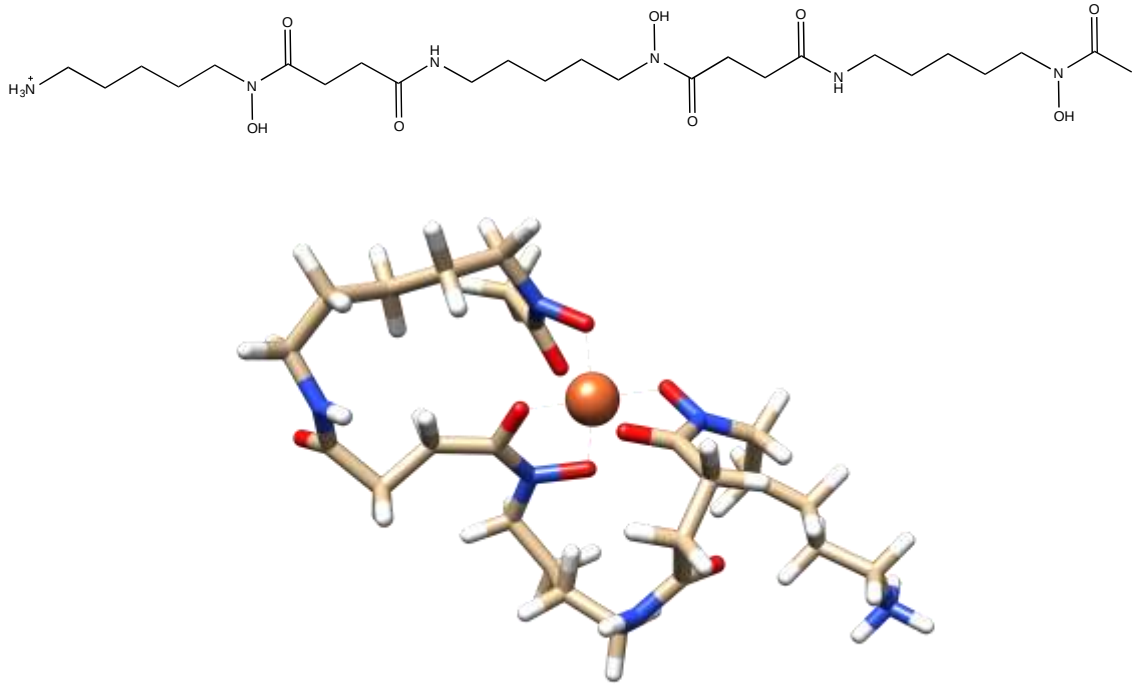

Figure 1.3 Desferrioxamine and energy minimised structure of Fe(III) DFO complex
(Obtained from Avogadro 1.1.1 (Hanwell et al., 2012) and visualised by UCSF Chimera 1.10.1 (Pettersen et al., 2004)) (Dhungana et al., 2001)

1.5.2 Deferasirox

Deferasirox (DFS, Exjade®, ICL670) is the lead compound of triazole ligands and was developed by Novartis and approved by the FDA in 2005 as the first and only iron chelator administered orally in the USA and also used worldwide. Deferasirox possessing a pFe^{3+} value of 22.5, acts as a tridentate ligand forming a 2:1 iron complex with one triazolyl nitrogen and two phenolate oxygens both deprotonated upon coordination (Figure 1.4). Potentiometric titrations of the ligands demonstrated that the ligand is a monoanion at physiological pH 7.4, with the p*K*a of the two phenol groups lying within the range 8.7 to 11 and the pKa of the carboxylic acid group as 3.7. Speciation plots suggested that trianionic complex $[Fe^{III}(DFS)_2]^{3-}$ is formed exclusively and was redox inactive under physiological conditions (Bernhardt, 2007). DFS has good oral activity (molecular weight 373) and permeates membranes easily by virtue of its high hydrophobicity ($logD_{7.4}$ = 1.0) (Zhou et al., 2012). It promotes iron excretion four to five times more effectively than DFO in hypertransfused rate model. Furthermore, the pattern of iron excretion produced by DFS is quite distinct from that of DFO. Whereas with DFO a substantial proportion of iron derived from RE cells is excreted in the urine, with DFS all iron excretion is limited to the bile regardless of whether it is derived from RE or hepatocellular stores (Hershko et al., 2001). By virtue of a high proportion of both the free ligand and the iron complex binding to albumin (greater than 98%), the ligand possesses low toxicity despite its strong lipophilic character (Weiss et al., 2006). DFS is administered orally in single daily dose owing to its long plasma life (~12 h). It has been demonstrated to be efficient at removing liver iron from regularly transfused patients (Cappellini et al., 2010) but is apparently less effective at removing cardiac iron (Wood et al., 2010). Kidney toxicity is the prevalent side effect of this chelator (Rafat et al., 2009).

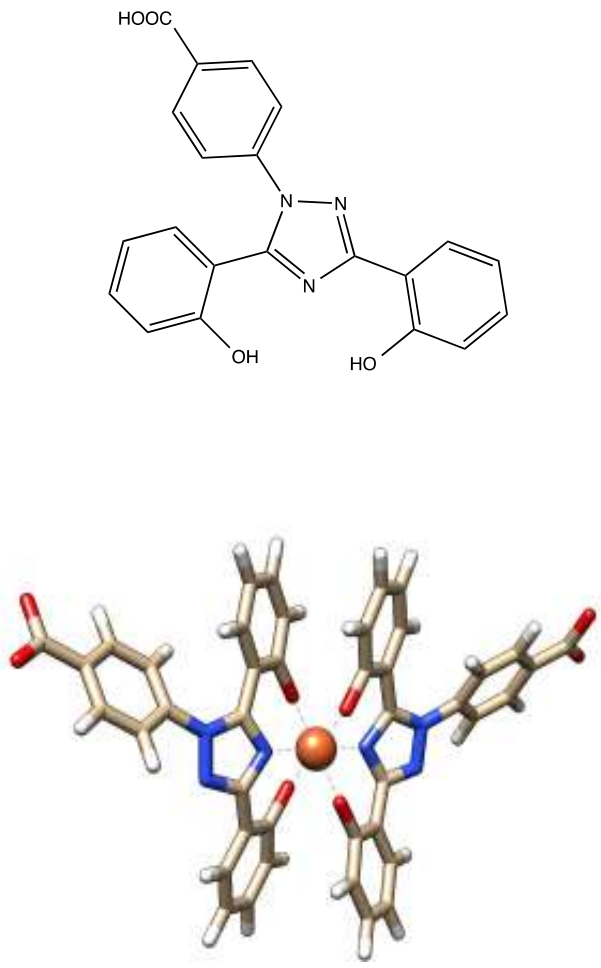

Figure 1.4 Deferasirox and energy minimised structure of Fe(III) DFS complex
(Obtained from Avogadro 1.1.1 (Hanwell et al., 2012) and visualised by UCSF Chimera 1.10.1 (Pettersen et al., 2004)) (Bernhardt, 2007)

1.5.3 CP20/deferiprone

CP20/deferiprone (DFP), the 1, 2-dimethyl derivative of 3-hydroxypyridin-4-one family, was designed by Hider et al (1982), and demonstrated to be active in man in 1987 (Kontoghiorghes et al., 1987) was granted for receiving full marketing authorisation by European Medicines Agency in 2002 and was approved by the FDA in 2011 (Figure 1.5). It is marketed by Apotex Inc. Toronto, Canada as Ferriprox™ (Zhou et al., 2012). The 3-hydroxypyridin-4-one family emerged as the first potentially orally active iron chelator for iron overload chelation therapy. HPO compounds possess two *pKa* values, corresponding to the *pKa* values of 4-carbonyl group (~3.6) and 3-hydroxyl group (~9.9), hence, the ligands are monoprotic acid under physiological pH 7.4 (Liu and Hider, 2002). DFP is a small molecule (M.W. 139), which facilitates its good oral absorption by the gastrointestinal tract. CP20/deferiprone possesses a pFe^{3+} value of 20.5 and forms an 1:3 iron complex $[Fe^{III}(DFP)_3]$ in a bidentate fashion (Figure 1.5). It is a quite hydrophilic compound with the distribution coefficient ($logD_{7.4}$ = -0.77). It is able to penetrate cells and coordinate with iron, forming a neutral complex, which can also permeate cell membranes. Thus, iron can be readily removed from iron-loaded cells including those of cardiac tissue. The complex is largely excreted by the urinary route (Glickstein et al., 2006). However, CP20/deferiprone rapidly loses its chelating efficacy by undergoing extensive Phase II glucuronidation reaction at the 3-hydroxyl group in the liver (Scheme 1.1). Therefore, the dose required to achieve body iron homeostasis is relatively large, which is administered at 75 mg/kg/day fractionated in three doses. Consequently, some side effects are associated with the use of CP20/deferiprone, the most significant being agranulocytosis and neutropenia (Hoffbrand et al., 2003).

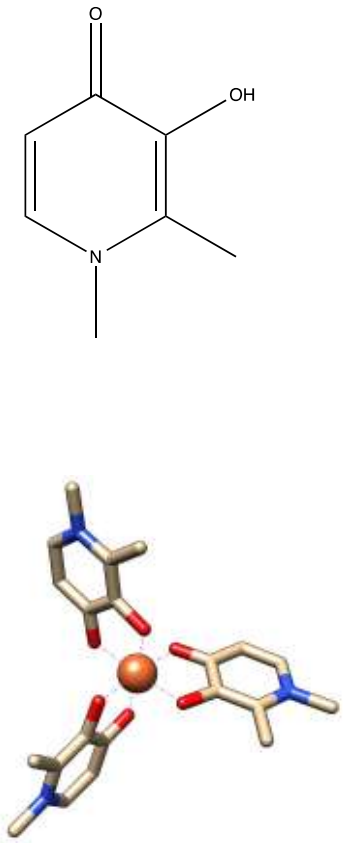

Figure 1.5 CP20/deferiprone and energy minimised structure of Fe(III) DFP complex
(Obtained from Avogadro 1.1.1 (Hanwell et al., 2012) and visualised by UCSF Chimera 1.10.1 (Pettersen et al., 2004))
(Zhou et al., 2012)

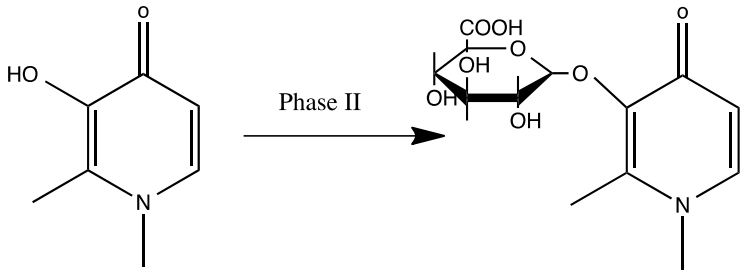

Scheme 1.1 Phase II glucuronidation of CP20/deferiprone (CP20)

1.5.4 Chelator Pharmacokinetics

Desferrioxamine is not orally active and cleared by the kidney very rapidly with a half-life of 20 min. In contrast, CP20/deferiprone is rapidly absorbed from the gastrointestinal tract (Porter, 2001). The peak plasma concentration value is typically achieved between 40 and 80 min. Due to the extensive glucuronidation of CP20/deferiprone, the concentration of the non-chelating metabolite is higher than that of CP20/deferiprone 60min after the oral administration (Al-Refaie et al., 1995). Deferasirox is also orally active. The maximum plasma concentration is reached after 4 h and the drug remains in the blood stream for much longer periods of time experiencing a slow renal clearance, which is a direct result of its tight binding to albumin. In many patients, there are appreciable levels of the chelator present after 24 h (Chirnomas et al., 2009).

1.5.5 Combined therapy with Desferrioxamine(DFO) and CP20/deferiprone(DFP)

The plasma half-life is short for both DFO and DFP, 5-10min and 3-4 hrs respectively (Summers et al., 1979). The treatment regime cannot provide 24-hour chelation coverage which is probably necessary to achieve negative iron balance (Cabantchik et al., 2005). Hence, the combination of DFO and DFP has been investigated to treat iron overload and promote urinary iron excretion (Giardina and Grady, 2001). Due to the small molecular weight and ability to penetrate cells, DFP scavenges intracellular iron efficiently and the formed iron complex can also permeate cell membranes and enter the extracellular environment. However, by virtue of the bidentate nature of CP20/deferiprone, it is highly concentration dependent in chelating Fe(III) and at relatively low concentrations (<5 μM) the iron CP20/deferiprone complex will dissociate and redistribute iron. In the case of sequential use of DFO and DFP, the DFP iron complex will readily donate iron to the kinetically more inert extracellular DFO sink and DFP promotes plasma NTBI clearance in the presence of DFO (Devanur et al., 2008). It has shown that treatment of thalassaemic patients with this combination regime reduces myocardial iron overload (Piga et al., 2003).

1.5.6 Second generation hydroxypyridinones.

In order to further improve chelation efficacy and to avoid agranulocytosis, considerable effort has been devoted to the design of novel hydroxypyridinones with enhanced affinity to iron(III) (Zbinden, 1997, Hider R. C., 1998).

Under biological conditions, the comparison of iron affinity of clinical iron chelators is evaluated by the pFe^{3+} value. pFe^{3+} is defined as the negative logarithm of the concentration of the free iron(III) in solution. Typically pFe^{3+} values are calculated for total [ligand] = 10^{-5} M, total [iron] = 10^{-6} M at pH 7.4 (Raymond and Carrano, 1979). In general, the pFe^{3+} value of an ideal iron chelator is above 20. However, if the pFe^{3+} value is too high, the chelator will be toxic because it might scavenge iron from essential metallo-enzymes.

A number of iron chelators with high pFe^{3+} have been introduced. Novartis has promoted a range of bidentate hydroxypyridinone ligands, which possess an aromatic substituent at the 2-position. The lead compound CGP65015 (Figure 1.6) was found to be orally active (Lowther et al., 1999) and highly effective at scavenging iron from both the iron loaded rat and marmoset (Zbinden, 1997). CGP65015 promoted iron excretion in amounts of about 2500-µg iron/kg body weight at a dose of 150 µmol/kg in iron overloaded marmosets, which is equivalent to the amount promoted by Deferasirox at the same dose (Figure 1.7 a). When comparing the iron chelation efficacy with hydroxypyridinones, CGP65015 was 4 times more potent than the most effective 1st generation HPO chelator used in this study, CP102 (Figure 1.7 b). (Sergejew et al., 2000).

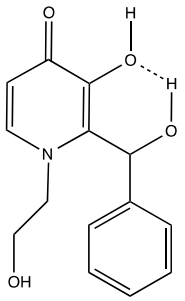

CGP65015

Figure 1.6 High iron(III) affinity hydroxypyridinone, CGP65015

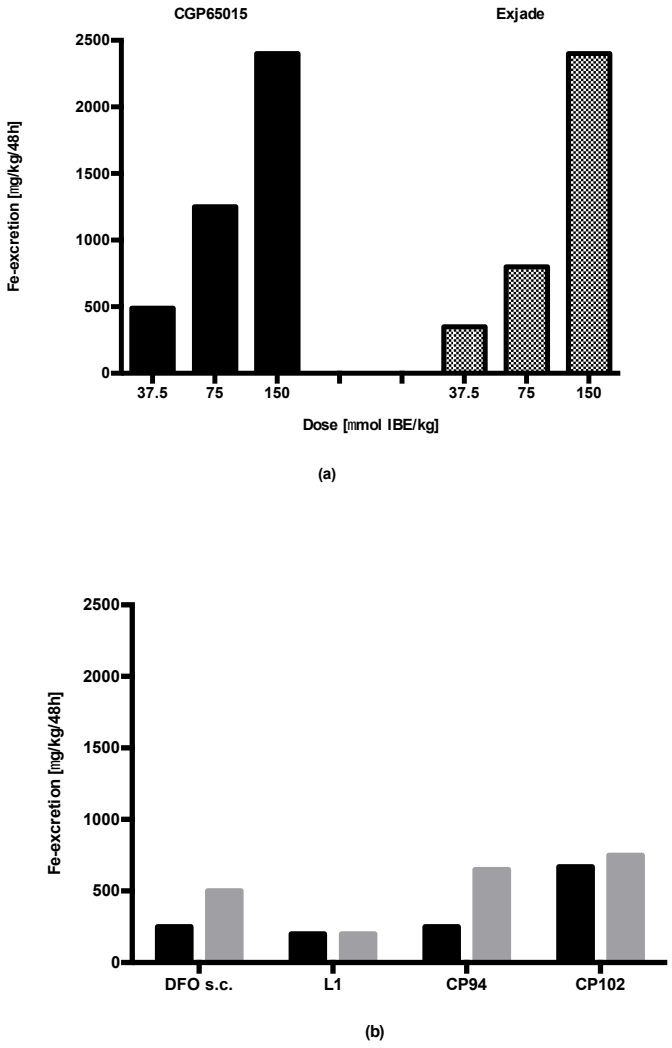

Figure 1.7 (a) Dose-dependant total iron excretion in iron-overloaded marmosets induced by CGP65015 and Exjade. (b) Comparison of total iron excretion in iron-overloaded marmosets (black columns) and *Cebus* monkeys (white columns).
All iron chelators indicated were applied at 150 µmol/kg. (Sergejew et al., 2000)

In a similar way, Hider and coworkers demonstrated that the introduction of either a 1'-hydroxyalkyl group (Figure 1.8 a) or an amido function (Figure 1.8 b) at the 2-position of 3-hydroxypyridin-4-ones increases the affinity for iron(III) in the pH range 5–8 (Liu et al., 1999b, Piyamongkol et al., 2010). This effect results from stabilising the ionised species, due to the combined effect of intramolecular hydrogen bonding between the 2-substitutent with the adjacent 3-hydroxyl function and electron withdrawal from the pyridinone ring. Although the overall iron(III) stability constant is reduced so are the pKa values of the chelating function thereby reducing competition from proton, these overall changes lead to an increase in the respective pFe^{3+} values. These novel high pFe^{3+} HPOs were found to be promising in their ability to remove iron under *in vivo* conditions. Further dose-response studies imply that chelators with high pFe^{3+} values scavenge iron more effectively at lower doses when compared with simple dialkyl substituted hydroxypyridinones. A small number of related compounds were selected for preclinical investigation. However, none of these compounds had significantly improved therapeutic ratios when compared with CP20/deferiprone and so have not been further pursued (Liu and Hider, 2002).

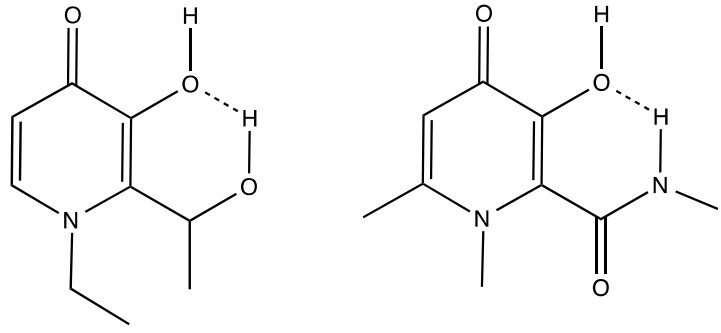

CP365 **(a)** **CP502** **(b)**

Figure 1.8 High iron(III) affinity hydroxypyridinones (a) CP365 (b) CP502

Over the past fifteen years, lysosomotrophic HPOs (Ma et al., 2015), HPO prodrugs (Rai et al., 1999) have also been thoroughly investigated. However, none of these compounds demonstrated superior efficacy/ toxicity ratios to that of CP20/deferiprone.

In this study, a range of novel HPOs has been investigated. Although pegylated HPOs and long chain acetamido HPOs (CM1) have been considered, our main effort was directed to enantiomeric pairs. Obviously, chiral compounds share essentially the same physicochemical properties, such as partition coefficient, water solubility, pKa values, iron(III) affinity constants and pFe^{3+} values. However, due to the three dimensional structures of chiral centers, the absorption (A), distribution (D), metabolism (M) and excretion (E) can be in principle different. For absorption, the movement of HPOs into cells is predominantly by simple diffusion and thus largely dependent on the physical properties of HPOs (i.e. enantiomers will have similar properties). For distribution, the binding to plasma proteins (largely albumin) can be stereoselective, although differential albumin binding of enantiomeric pairs is minimal. In contrast, for metabolism, due to the enantioselectivity of the metabolising enzymes, metabolic profiles of enantiomers can be quite different (Lu, 2007). Glomerular filtration, tubular secretion and reabsorption of chiral drugs also demonstrate stereoselectivity, leading to different drug excretion profiles, although here is no evidence for HPO receptor mediated reabsorption by the kidney (Patel and Hutt, 2004). Thus, HPO chirality can serve as a good strategy to modify HPO structures in order to influence metabolism and in this way identify the optimal efficacy/toxicity ratio for a given structure. In consequence, ten pairs of enantiomers have been investigated, many of the pairs demonstrated diverse efficacy in iron mobilisation in the *in vivo* rat model (Brown, 2012) (Figure 1.9). A dominant drawback of CP20/deferiprone is the extensive glucuronidation conjugation at one of the essential iron(III) binding sites, 3-hydroxyl moiety, which results in loss of the iron chelation ability. By selecting an enantiomer with a low rate of metabolism, it was considered likely that we could improve the overall efficacy. Hence, although the difference in the iron chelation efficacy of chiral pairs might be attributed to different ADME characters and a comprehensive investigation on their ADME profiles is required, their metabolic profiles in liver appear to make a dominant contribution to the overall efficacy.

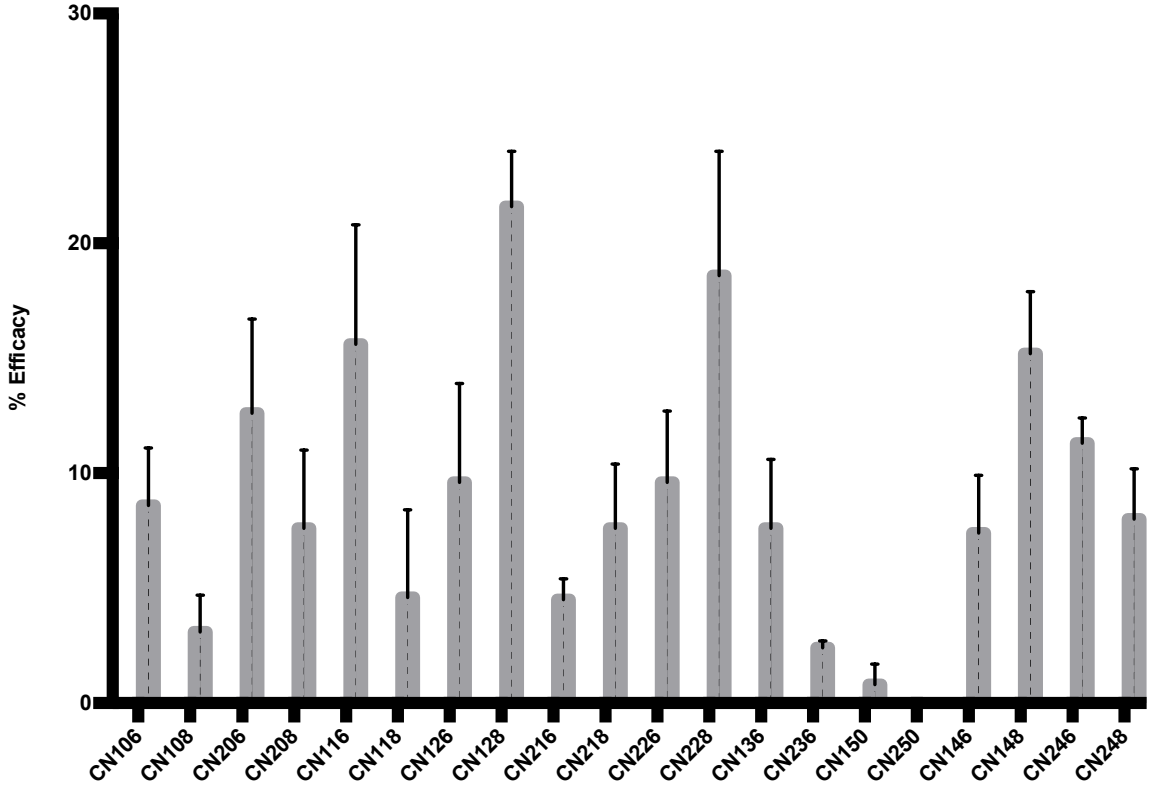

Figure 1.9 Efficacy of iron mobilisation of chiral HPO pairs in *in vivo* rat model (Brown, 2012)

1.6 Metabolism of 3-hydroxypyridinones

Drug metabolism by the host organism is one of the crucial determinants of the pharmacokinetic profile of a drug. High metabolic lability usually results in poor bioavailability and high clearance. In consequence, optimisation of the metabolic liability of the new chemical entities is one of the significant steps during the drug discovery process (Kumar and Surapaneni, 2001).

As demonstrated above, CP20 undergoes extensive Phase II conjugation at the 3-hydroxyl group, which is crucial for iron scavenging, and forms the 3-O-glucuronide conjugate. One of the properties required for an ideal iron-chelating agent is a slow rate of any metabolic route leading to inactive chelators. In order to achieve a maximum therapeutic effect, the metabolic rate of the chelator to inactive components should be low. This is particularly important if the majority of iron scavenging occurs in hepatocelluar iron pool (Porter et al., 1989a).
Thus structural modifications of the CP20 structure have been made in an attempt to optimise the efficacy of this molecule class.

Drug metabolism reactions are broadly divided into two categories: Phase I and Phase II reactions (Coleman, 2010). Phase I reactions are functionalisation reactions which introduce a polar functional group onto the molecule. Examples of the Phase I reactions are hydrolysis of ester or amide groups to their respective acid and alcohol/amines, hydroxylation of aromatic and aliphatic carbons, heteroatom dealkylation (secondary/tertiary amines, ethers, thioethers), heteroatom oxidation (N-, S- oxidation) and reduction. In some incidences, Phase I metabolites are excreted as such or undergo further Phase II metabolism prior to elimination. The most important enzymes involved in Phase I metabolism are the cytochrome P450 (CYP) superfamily of enzymes, flavin-containing monooxygenases, esterases, and amidases (Pearson and Wienkers, 2009). Phase II reactions are usually conjugation reactions, which introduce a polar functional group onto either the parent molecule or its Phase I metabolite. The resulting Phase II metabolites, termed conjugates, are usually more polar than the parent molecule and in consequence are more readily eliminated from the host. The most prevalent Phase II metabolic pathways include glucuronidation, sulfation, methylation, acetylation and glutathione conjugation. UDP-Glucuronosyltransferases (UGT)-mediated glucuronidation is a predominant

pathway of Phase II metabolism. Endogenous substrates of UGT include bilirubin, thyroxin and steroid hormones. Several xenobiotics metabolised by UGT include morphine, aspirin, azidothymidine, ibuprofen, and acetaminophen. β-Glucuronidase, an enzyme produced by gut microflora can hydrolyse glucuronide conjugates excreted into the gut via bile to the parent drug. The parent drug can then be reabsorbed. The UGT group of enzymes is classified into two families based on amino sequence homology. The major subfamilies involved in drug metabolism are UGT1A1 (bilirubin, estradiol, EE, and buprenorphine), UGT1A4 (planar phenols such as imipramine, doxipen, amitriptyline, and chlorpromazine), UGT1A6 (planar phenols such as naphthol and p-nitrophenol), UGT1A9 (bulky phenols such as propofol, propranalol, and labetolol), and UGT2B7 (NSAIDs, naproxen and ibuprofen, and valproic acid, clofibric acid, benzodiazepines, morphine) (Sies and Packer, 2005).

Microsomes isolated from different organs and species have been widely used for the study of xenobiotic metabolism including potential drug materials. Hepatic and extrahepatic cells contain a multitude of xenobiotic- and endobiotic- metabolising enzymes that are usually localised to intracellular specific organelles. The two major categories of metabolising enzymes, namely cytochrome P450 (CYPs) (Phase I) and UDP-glucuronosyltransferases (UGTs) (Phase II), are predominantly localised within the endoplasmic reticulum (ER). Thus, microsomes (vesicles of endoplasmic reticulum) isolated from multiple organs and species are the most popular subcellular fraction for *in vitro* metabolism studies. The advantages of an *in vitro* model using microsomes include the ease of preparation, commercial availability, flexibility of incubation conditions (cofactors, buffer, pH and temperature for optimal catalysis), simple storage protocols and the concomitant decrease in the use of animals in drug discovery and development (Pearson and Wienkers, 2009)

1.7 Efficacy studies of 3-hydroxypyridinones

Preclinical efficacy study of iron chelators is essential as it provides preliminary data on the efficiency of the compound to scavenge iron and the subsequent routes of iron excretion. Combined with information on physicochemical properties and metabolic profiles, a comprehensive profile of an iron chelator can be evaluated. *In vivo* animal models are essential

in order to establish the disposition and distribution of the chelator, including absorption from the gastrointestinal tract. A few models have been developed to investigate the efficacy of iron chelators.

In several studies, hypertransfused rat or mice models have been used for screening the biological evaluation of potentially useful iron chelators in both small and large-scales. However, procedures of iron overloading by hypertransfusion are technically demanding and time-consuming (Graziano et al., 1974, Grady et al., 1978, Pitt et al., 1979). Hence, iron dextran has been introduced for iron loading in the fashion that iron is initially extracted by the reticuloendothelial system and then is equilibrated and redistributed to parenchymal tissues, which has been used in a mouse model to evaluate a range of N-substituted 3-hydroxypyrid-4-one chelators (Gyparaki et al., 1987). However, rapid depletion of iron stores occurred after cessation of iron dextran supplement, in consequence, using ferrocene-loaded rats has demonstrated a more stable iron loading model and a histological similarity in the iron-overloaded liver to that of primary haemochromatosis (Ward et al., 1991). Although the iron-overloaded animal models appear ideal and simulate the iron overloading pathological conditions in man, the iron loading process is time consuming and not always reproducible in providing the equivalent iron mobilisation abilities of iron chelators (Liu et al., 1999c). A rapid assay for evaluation of iron-chelators in non-iron-overloaded rats has been developed by Pippard and co-workers using ^{59}Fe-ferritin to label hepatic parenchymal cells (Pippard et al., 1981). It has been demonstrated that using a radio-labelled iron probe in the animal model can greatly simplify the monitoring of iron excretion by circumventing many of the drawbacks associated with faecal contamination and intraluminal chelation observed with cold iron measurements. A further advantage is that specific iron pools can be targeted with different forms of radio-labelled iron, allowing a more precise investigation of differences in sources and routes of excretion of chelatable iron in the presence of various chelators. Thus, it has been demonstrated that ^{59}Fe-labelled ferritin and haemoglobin–haptoglobin complexes are predominantly taken up by hepatocytes in rats, whereas ^{59}Fe-labelled heat-damaged red blood cells can be used to selectively label reticuloendothelial cells (Hershko et al., 1973, Hershko, 1978). Since the liver is the major iron storage organ under iron-overloaded conditions, ^{59}Fe-

labelled ferritin appeared to be the ideal radio-iron model (Pippard et al., 1981). Two hours after radio-iron labeling, a challenge with test chelator was administered at a time when radio-iron released by lysosomal degradation of the exogenous ferritin was maximally available. In details, the time window of ^{59}Fe is accessible for chelation was when in transit within the hepatocyte, but that it became relatively unavailable subsequent to incorporation in endogenous ferritin, which was shown to occur between the second and sixth hour after ^{59}Fe-ferritin injection. With the chelators tested, almost all the ^{59}Fe was excreted via the bile. In this study, it was concluded that animals with normal iron stores could be used for a rapid bioassay of iron chelators (Pippard et al., 1981). Subsequently, this *in vivo* model was elaborated by Liu et al (1999c) in screening of some 3-hydroxypyridin-4-ones for the development of an orally active iron chelator. The impact of several key parameters in this model has been systematically investigated. Different time periods after the injection of ^{59}Fe-ferritin and the distribution of injected ^{59}Fe were monitored. It was demonstrated that the efficient ^{59}Fe-ferritin labelling in the liver was conducted after 60 min (Figure 1.10) (Liu et al., 1999c). The time intervals between administration of ^{59}Fe-ferritin and chelator were also investigated in order to provide maximal accessibility of the ^{59}Fe label to the administered chelators. The results revealed a separation of 1 hr between ferritin and chelator injections gave higher gut content and faeces counts resulted from biliary excretion, which compensate to a corresponding decrease in liver ^{59}Fe levels (Liu et al., 1999c). This is also in concert with a plasma half-life of 0.5–1.5 hr previous pharmacokinetic studies with orally administered HPOs in the rat (Choudhury R., 1995). The bile iron excretion assay using the bile duct cannulation model in normal rats confirmed that the peak of iron excretion varied with different chelators. Therefore, collections of excreted iron were ideally made over a 24-hr period (Liu et al., 1999c). In summary, the labelled iron pool was challenged by oral administered iron chelators 1 hr after the injection of ^{59}Fe-ferritin (Figure 1.11). 24 hr after injection of ^{59}Fe-ferritin, rats were sacrificed.

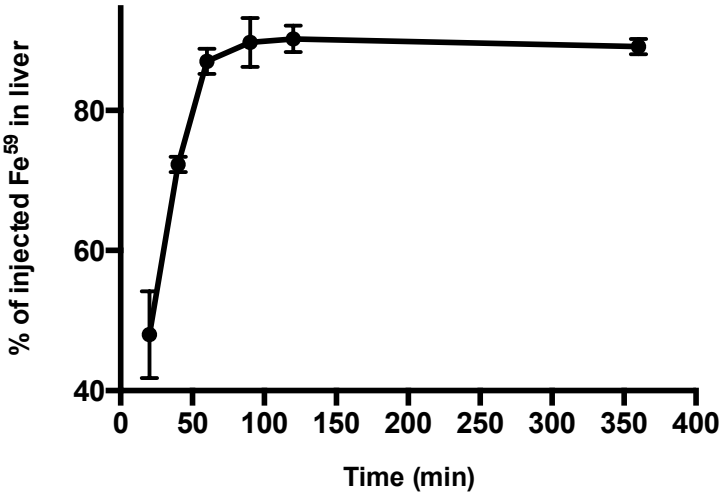

(a)

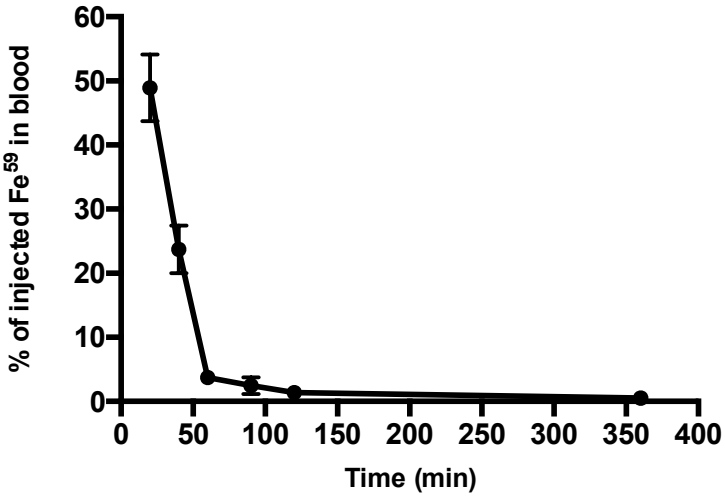

(b)

Figure 1.10 The distribution of injected ^{59}Fe-ferritin with time
(a) Percentage of injected ^{59}Fe in liver; (b) Percentage of injected ^{59}Fe in blood. Modified from Liu (1999c).

Liver, gastrointestinal tract contents, urine and faeces were collected separately for gamma counting (Scheme 1.2). The Iron mobilisation (%) was used to evaluate the efficiency of ^{59}Fe scavenged from the hepatocytes by iron chelators, which is termed as the percentage of ^{59}Fe activity in the gut and faeces compared with the sum of ^{59}Fe activity in gut, faeces and liver. Efficacy (%) is the Iron mobilisation (%) of drug group minus the Iron mobilisation (%) of control

group (animals administered with water). Total recovery (%) was used to assess the efficiency of ^{59}Fe labeling, which is termed as the percentage of ^{59}Fe activity in the gut, faeces and liver compared with the total ^{59}Fe activity administered by tail vein injection. The reliability and reproducibility of this above method has been verified with various ligands. The total recovery of ^{59}Fe fell in the range of 76%~ 87% and the mean values together with the standard deviation (SD) indicate that the errors associated with this assay were acceptable for comparative purposes (Liu et al., 1999c).

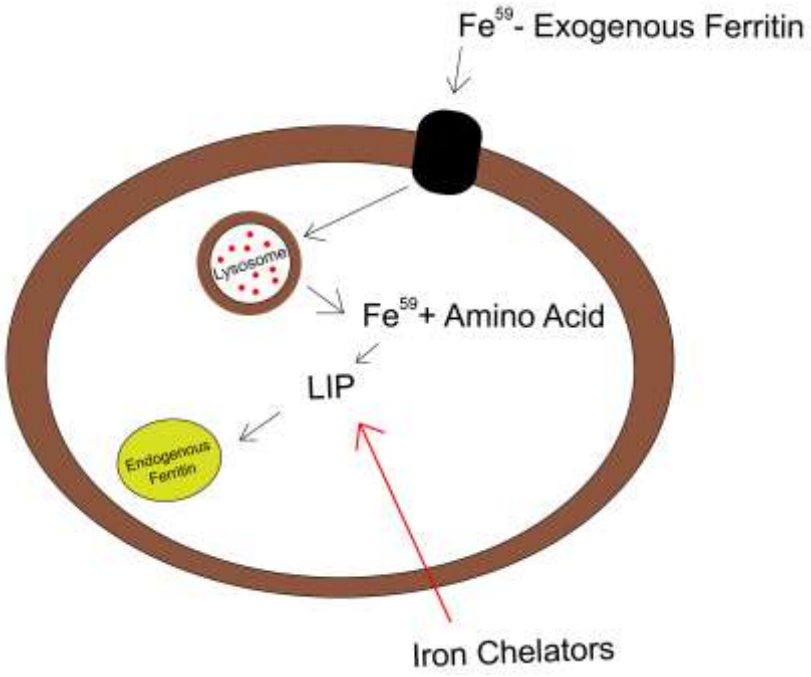

Figure 1.11 Hepatocellular iron pool labelled by ^{59}Fe-ferritin and scavenged by iron chelators

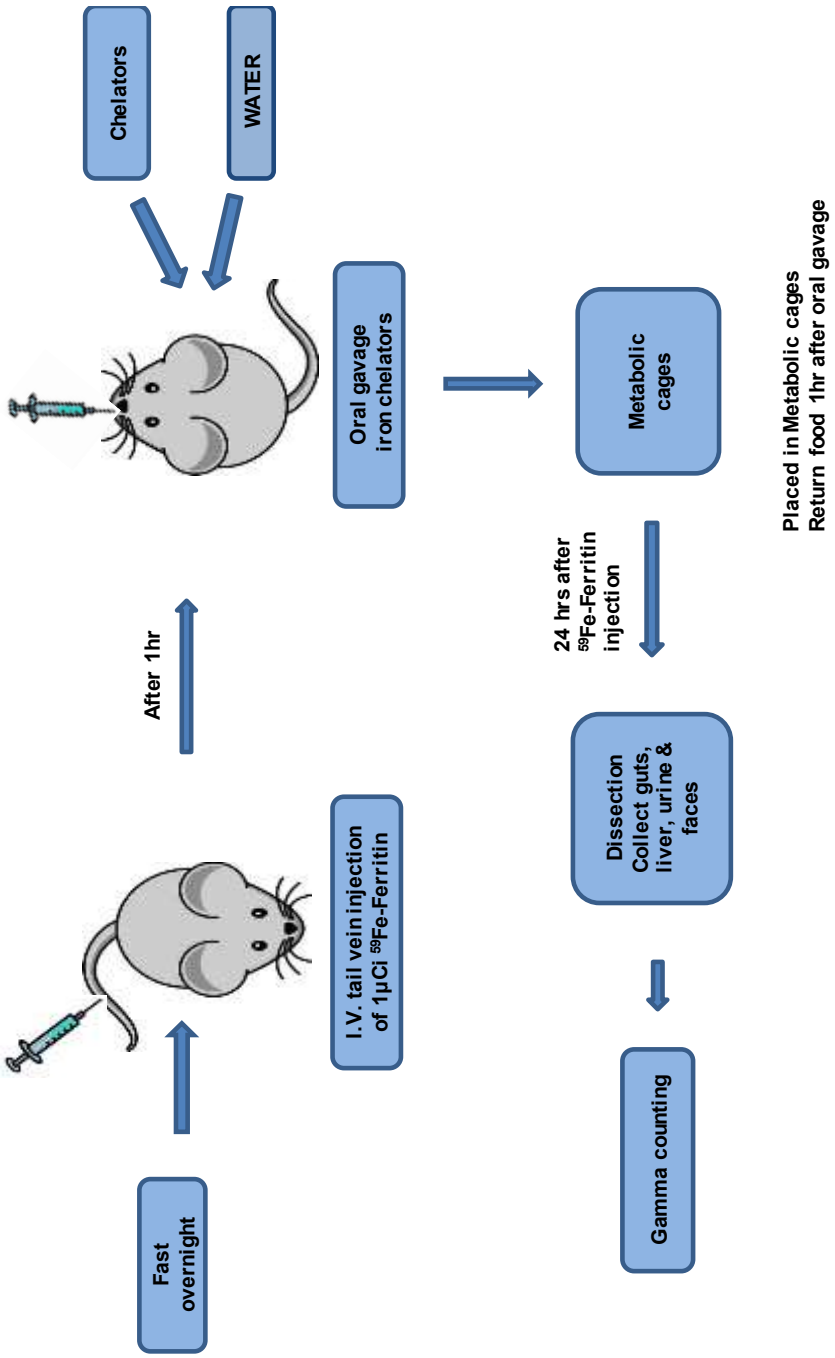

Scheme 1.2 Hepatic iron chelation efficacy study mode

1.8 Aim of project

Clearly there is still a requirement for improved orally active chelators. Therefore, we have undertaken several novel approaches of iron chelator design all based on the hydroxypyridinone ring. A range of candidate compounds have been synthesised consisting of chiral pairs (Figure 1.12, CN106 and CN108), a ω-acetamido-6-alkyl substituted CP20 analogue (Figure 1.12, CM1), a group of closely related CP20 analogues (Figure 1.12, CP679, CP616 and CP617) and pegylated HPOs (Figure 1.12, K31, C31, K5 and K6). All these compounds were predicted to possess similar pFe^{3+} values to that of CP20/deferiprone. Their hepatic metabolic profiles were investigated in order to select compounds with the lowest hepatic metabolic clearance. On the basis of this comparison, selected compounds were subjected for iron mobilisation efficacy studies. The overall aim of the project is to identify a second-generation hydroxypyridinone to replace CP20/deferiprone. For this to be a reality, the compound should remove iron from the liver more efficiently than CP20/deferiprone, possess a lower susceptibility towards metabolism and lack the side effects of agranulocytosis and neutropenia. The above work forms the basis of this Ph.D. thesis.

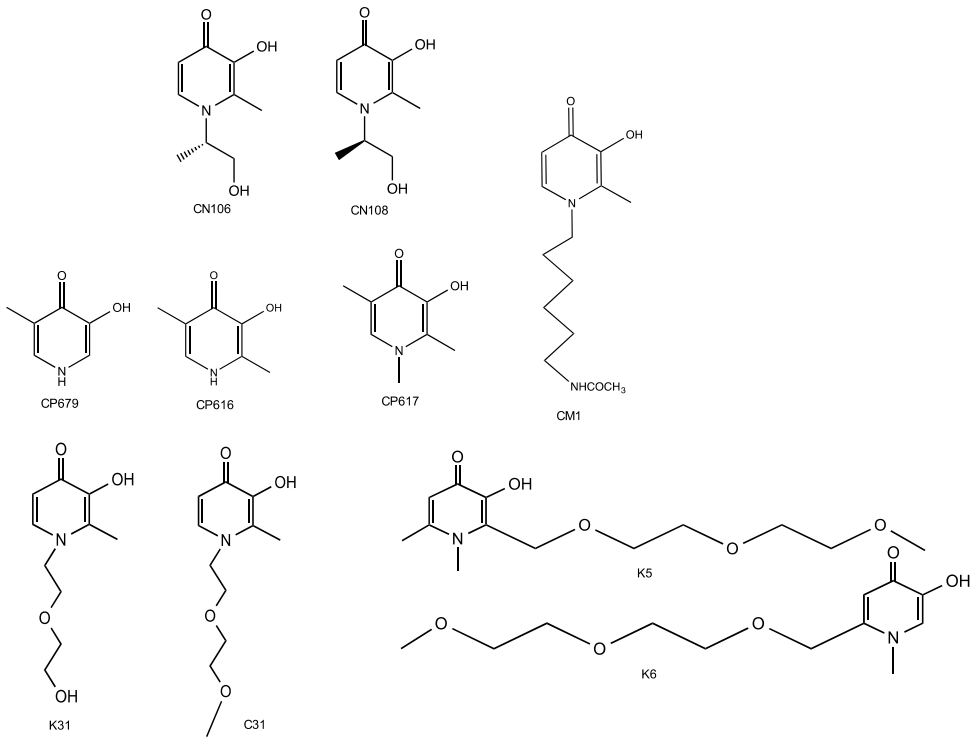

Figure 1.12 Chemical structures of HPOs investigated

CHAPTER TWO

Development of *in vitro* bio-analytical method for hepatic metabolism study of hydroxypyridinones

Chapter 2 Development of *in vitro* bio-analytical method for hepatic metabolism study of hydroxypyridinones

2.1 Introduction

2.1.1 Development of the *in vitro* microsomal incubation model

As liver is the major metabolising organ and the hepatic metabolic profiles of iron chelators are particularly important as the majority of iron scavenging occurs in hepatocellular iron pool, liver microsomes isolated from multiple species, containing concentrated Phase I and Phase II (UGT-mediated) enzymes are useful subcellular fractions for use in *in vitro* metabolism studies of 3-hydroxypyridinones. In the isolation process of liver microsomes, the cofactors that either mediate the oxidation (e.g. nicotinamide adenine dinucleotide phosphate, NADPH) or the conjugation (e.g. UDP-glucuronic acid, UDPGA) pathways are lost (Lee and Zhu, 2011). Supplementing the microsomal incubations with these cofactors can be used to identify the different metabolic pathways and to determine their relative contributions to the hydroxypyridinone metabolism. Microsomal incubation conditions can be adjusted to achieve the optimum rate of metabolising enzyme catalysis.

2.1.1.1 Disruption of UDP-glucuronosyltransferases (UGT) latency

Glucuronidation is accomplished by a set of enzymes known as UDP (Uridine Diphosphate) glucuronosyl transferases, or UGTs. The UGT protein can be conceptually divided into amino- and carboxyl-terminal domains. The C-terminal binds the cofactor UDPGA and the N-terminal binds the substrate. The active site of UGT is positioned on the lumenal surface of the microsomes (Figure 2.1) (Coleman, 2010). Intact microsomes are mainly composed of endoplasmic reticulum (ER) membranes, which are “right side out” closed vesicles and hence display enzyme latency. Permeation of microsomal membrane is a rate-limiting step for the transport of substrates, cofactors and products. Hence, the full glucuronidation potential of the microsomes is not exposed unless the microsomal membranes are disrupted by chemical or physical methods. Sonication, cycles of freezing and thawing, pore-forming agents and detergents can all be used to enhance the microsomal UGT activity (Meech and Mackenzie, 1997). We have investigated the ability of a detergent and a pore-forming peptide to disrupt the

membrane barrier and achieve the optimal enzymatic activity for the glucruonidation of hydroxypyridinones.

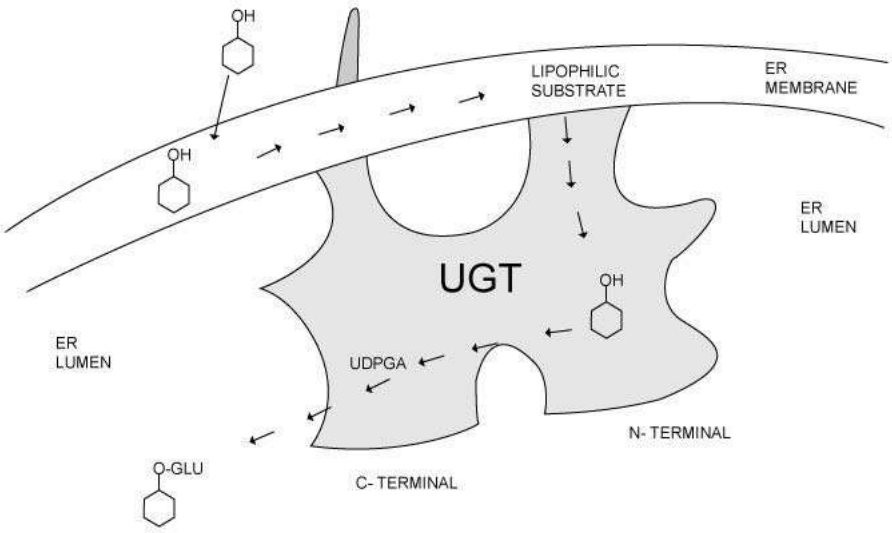

Figure 2.1 Glucuronosyl transferases (UGTs) in endoplasmic reticulum (ER) membranes
Modified from (Coleman, 2010)

2.1.1.2 Endogenous β-glucuronidase

The enzyme-catalysed hydrolysis of the newly formed glucuronide by the endogenous β-glucuronidase might also affect the measured UGT activity in microsomal incubations. Human endogenous β-glucuronidase has been found in all tissues and body fluids, with the highest activity in liver and one third of the β-glucuronidase found in liver cells localised in the endoplasmic reticulum (Oleson and Court, 2008). The endogenous β-glucuronidase activity in human liver microsomes has been demonstrated to cause 10-20% degradation of both estradiol-3-glucuronide and estradiol-17-glucuronide (Oleson and Court, 2008). Thus, glucuronidation studies using microsomes can be complicated by the presence of endogenous β-glucuronidases, leading to underestimation of glucuronide formation rates. Oleson and Court (2008) have also examined the effect of a most frequently used β-glucuronidase inhibitor, D-

saccharic acid 1, 4-lactone (saccharolactone), on eight different UGT activities using pooled human liver microsomes (pHLMs) and recombinant UGTs (rUGTs) and found that saccharolactone at concentrations ranging from 1 to 20mM did not increase any of the glucuronidation activities assessed that could be considered consistent with β-glucuronidase inhibition. However they still suggested that if saccharolactione is to be used, concentrations should be titrated to achieve activity enhancement. Consequently, saccharolactone was included in preliminary HPO microsomal incubation mixtures used in this study and concentrations were titrated in order to investigate the impact of the endogenous β-glucuronidase on the glucuronidation.

2.1.2 LC method development

2.1.2.1 Reversed Phase separation mode

The 3-hydroxypyridin-4-one iron chelators display poor chromatographic behavior on conventional bonded silica phase, generating non-symmetrical and multiple peaks. This is due to the interaction of the compounds with saturable free silanol groups and residual metal impurities on the bounded silica phase (Epemolu et al., 1994). Therefore, non-silica-based columns with high carbon loading, such as Ultracarb, polymer PLRP and Hypercarb PGC columns were adopted. The aqueous mobile phase was adjusted to pH 3.0 and 2 mM of EDTA included (Epemolu et al., 1990). However, this system proved to be unsatisfactory when applied to more hydrophilic HPOs and their metabolites, their retention times being short and not well resolved from the interfering matrix. These problems were largely overcome by using the polymer PLRP column with the aqueous mobile phase containing the ion-pair reagent 1-heptanesulfonic acid and pH adjusted to 2.0 (Liu et al., 1999a). The same polymer PLRP column was adopted for the studies reported in this chapter.

2.1.2.2 HILIC separation mode

Hydrophilic interaction LC (HILIC) phase has been increasingly applied to separate the highly polar components in biological samples (Dejaegher et al., 2008). HILIC is characterised by the use of a hydrophilic stationary phase and an aqueous-polar organic solvent mobile phase with

high organic component (e.g. 90/10 v/v ACN/H_2O). The more polar aqueous fraction of the mobile phase will preferentially adsorb on the polar HILIC stationary phase creating a semi-stagnant, water-rich stationary phase and a water-depleted mobile phase. Polar analytes can then partition into the aqueous-enriched phase (Buszewski and Noga, 2012). Hydrophilic analytes are retained on the HILIC phase by hydrophilic partitioning between the mobile phase and the water-enriched aqueous layer, with subsequent interactions with the stationary phase functional groups, e.g. dipole–dipole, ion exchange and hydrogen bonding (Goucher et al., 2010) (Figure 2.2). The retention time increases with increased polarity of the analytes and with decreased mobile phase polarity (Dejaegher et al., 2008). Drug metabolism typically produces more hydrophilic metabolites, which facilitate drug elimination. This is often a challenge for traditional reversed-phase liquid chromatography separation. Because hydrophilic interaction liquid chromatography (HILIC) is capable of retaining polar compounds and is compatible with mass spectrometry (MS), HILIC has been used as a complementary separation technique to RPLC for the analysis of polar drugs and their metabolites (Li et al., 2015b).

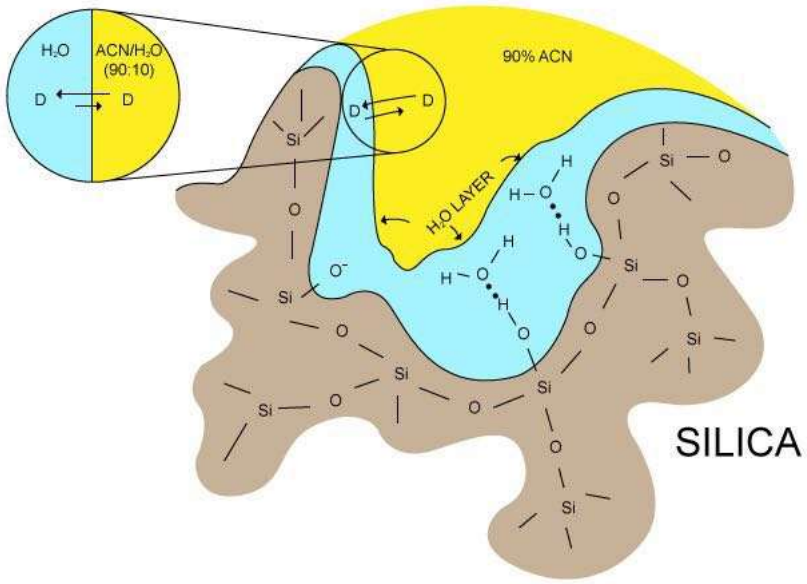

Figure 2.2 HILIC retention mechanism on a silica column
The analyte D partitions into the H_2O layer on the silica surface of the packing and further interacts with the stationary phase functional groups by dipole–dipole, ion exchange or hydrogen bonding. Modified from (Waters, 2015)

Consequently in this study, several different HILIC columns were investigated for their ability to resolve HPO compounds. HPO compounds possess two *pKa* values, corresponding to the *pKa* values of 4-carbonyl group (~3.6) and 3-hydroxyl group (~9.9) (Liu and Hider, 2002). Therefore, in extreme acidic and basic environments, they can be protonated or deprotonated, thereby possessing ionic properties. Two Waters Acquity® UPLC columns were investigated, which are the BEH and BEH Amide columns. Both columns are sub-2 μm columns, which offer advantages of increased separation speed with superior resolution and high sensitivity (Swartz, 2005). The modification of the silica stationary phase by Ethylene Bridged Hybrid (BEH) particle introduced by Waters improves the column stability under the ultra-performance LC (UPLC) high-pressure conditions over a wide pH range (1–12), in comparison to conventional RP columns. This is because nearly one-third of the surface silanol groups are masked by the ethylene-bridged groups embedded within the silica matrix (Jian et al., 2010). Another HILIC phase, zwitterrionic SP (ZIC HILIC), has also been examined for chromatographing HPOs. ZIC HILIC phase carries sulfoalkylbetaine zwitterionic functional groups attached to porous silica, which the oppositely charged sulfonic acid and quaternary ammonium groups present in a ratio of 1:1, providing a net charge of zero and promoting weak ion exchange interactions (Buszewski and Noga, 2012). The bonded phase is highly polar, strongly adsorbing water, which facilitates the formation of an aqueous layer. Both neutral and charged compounds can be retained on ZIC HILIC phase primarily by hydrophilic partitioning and electrostatic interaction (Jian et al., 2010).

2.2 Materials

Microsomes

Male Sprague-Dawley (SD) rat liver microsomes (M00001), *in Vitro*CYP™ H-class 25 donor male-pooled human liver microsomes (MX008065) were purchased from Celsis *in vitro* technologies (Neuss, Germany). Microsomal protein concentrations were 23.7mg/mL and 20.3mg/mL, respectively. Microsomes were aliquoted and stored at -80 °C. Frozen microsomes were thawed prior to use by placing the vial under cold running water. Once thawed, the vials of microsomes were kept in a wet ice bath.

Hydroxypyridinones

CP20 (1,2-dimethyl-3-hydroxypyridin-4-one) was purchased from Sigma Aldwich. CP94 (1,2-diethyl-3-hydroxypyridin-4-one, hydrochloride form), CP102 (1-(2'-hydroxyethyl)-2-ethyl-3-hydroxypyridin-4-one, hydrochloride form), CP95 (1-propyl-2-ethyl-3-hydroxypyridin-4-one, hydrochloride form), were synthesised in King's College London. CP20, CP94 and CP102 each have quite different metabolic profiles, which have been extensively investigated (Singh et al., 1992, Singh et al., 1996). CP95 was adopted as the internal standard it is a hydroxypyridinone analogue, which has the similar but readily distinguishable signal response compared with the analytes of interest

Other biological and chemical materials

Reduced β-nicotinamide adenine dinucleotide 2'-phosphate tetrasodium salt hydrate (NADPH), uridine 5'-diphosphoglucuronic acid trisodium salt (UDPGA), triton X-100, alamethicin (from *Trichoderma viride*), D-saccharic acid 1,4-lactone monohydrate, β-glucuronidase type H-3 (from *Helix pomatia*), tris(hydroxymethyl) aminomethane were purchased from Sigma Aldrich (Dorset, UK). All solvents and reagents were purchased from Fisher Scientific Ltd (Loughborough,Leicestershire,UK).

2.3 Methods

2.3.1 Microsomal incubation

Phase I + II (glucuronidation) metabolism reactions were investigated in male SD rats liver microsomes and *in Vitro*CYP^{TM} H-class 25 donor male-pooled human liver microsomes for CP20, CP94 and CP102 respectively.

2.3.1.1 Stock solution preparation

NADPH stock solution (10mM), UDPGA stock solution (10mM), $MgCl_2$ stock solution (50mM), phosphate buffer (1mM, pH 7.4) and D-saccharic acid 1,4-lactone (100mM) were prepared in Milli-Q water. CP20 stock solution (200mM) was prepared in 50% methanol, then further diluted to 2mM in Milli-Q water. CP94, CP102 and CP95 stock solutions (20mM) were prepared in in

Milli-Q water and further diluted to 2mM in Milli-Q water.

2.3.1.2 Phase I + II (glucuronidation) microsomal incubation

To investigate phase I metabolism, the following was spiked into an enpendorf tube: 25μL of cold liver microsomes (giving a final concentration of 1 mg/mL protein), 50μL of $MgCl_2$ stock solution (10mM), 50μL of phosphate buffer (1mM, pH 7.4), 50μL of CP20, CP94 or CP102 stock solution (2mM) and 25μL of Milli-Q water. The combined components were then pre-incubated at 37 °C for 10 min, after which 100μL of NADPH stock solution (10mM) and 100μL of UDPGA stock solution (10mM) were added to initiate metabolic reactions. The mixture was then incubated at 37 °C in a thermostat incubator for 24h with gentle shaking to prevent protein sedimentation. The reactions were terminated by spiking in 50μL of 10% trichloroacetic acid to remove protein, followed by spiking of 50μL of CP95 (2mM) as the internal standard. Samples were mixed evenly by the vortex mixer and followed by centrifuge at 14,000 rpm in a Spectrafuge™ 16M microcentrifuge (Labnet International Inc., NJ, USA) for 10min. Blank samples were prepared by substituting cofactors (NADPH and UDPGA) with water. The supernatants were collected for the further analysis. Moreover, in order to disrupt the latency of UGT activity and inhibit the endogenous β-glucuronidase, detergent or pore-forming peptide and D-saccharic acid 1,4-lactone were added to the microsomes before initiating the reactions and their concentrations were optimised as below.

Addition of the detergent to overcome UGT latency

TritionX-100 was added into 25μL of cold liver microsomes and incubated on ice for 10min before adding into the reaction mixture. The detergent/microsomal protein ratios were adjusted from 0.1, 0.2, 0.3, 0.5 to 1mg/mg**.** The optimal detergent activation of liver microsomal UGTs was determined as the detergent/microsomal protein ratio, which could induce the maximal glucuronidation conversion of the parent drug.

Addition of the pore-forming peptide to overcome UGT latency

The pore-forming peptide, alamethicin, was incubated with 25μL of cold liver microsomes, with an alamethicin/microsomal protein ratio of 5, 10, 25, 50, 100μg/mg on ice for 10min before

adding into the reaction mixture. The optimal alamethicin activation of liver microsomal UGTs was determined as the alamethicin/microsomal protein ratio, which could induce the maximal glucuronidation conversion of the parent drug.

Addition of D-saccharic acid 1,4-lactone as an endogenous β-glucuronidase inhibitor

D-saccharic acid 1,4-lactone was included in the reaction mixture in order to investigate whether it effectively inhibits the effect of endogenous β-glucuronidase on the glucronidation rate. The stock solution of D-saccharic acid 1,4-lactone (100mM) prepared in 1 mM phosphate buffer was adjusted to pH 7.4 with potassium hydroxide, and diluted into the reaction mixture before adding in the liver microsomes. The final concentrations of D-saccharic acid 1,4-lactone were adjusted to 1, 2, 5, 10 and 20mM. The effect of endogenous β-glucuronidase inhibition was confirmed by whether an increase of glucuronidation conversion of parent compound was observed compared with the D-saccharic acid 1,4-lactone excluded control sample.

Addition of divalent metal ion (Mg^{2+})

Physiological concentrations of magnesium chloride (5mM) was also added in the microsomal incubation mixture (Zakim et al., 1973). Divalent metal ions modify UGTs by direct binding to the enzyme to increase their catalytic activities. It has been reported that addition of Mg^{2+} to the alamethicin treated microsomal incubation enhanced the UGTs activity (Fisher et al., 2000).

Blank samples were prepared by substituting cofactors (NADPH and UDPGA) with water. Phase I + II microsomal incubates for each HPO compound were prepared in triplicate.

2.3.2 Development of HPLC conditions using reversed phase (RP) mode

2.3.2.1 Instrumentation

A polymer reversed phase (PLRP) column (250mm×4.6mm, 5μm) (Polymer Laboratories Ltd, Shropshire, UK) was used on a Hewlett-Packard HPLC 1100 (Agilent Technologies Ltd., Shropshire, UK) equipped with UV-Vis detector.

2.3.2.2 HPLC conditions

Supernatants (20μL) of Phase I + II microsomal incubation samples for CP20, CP94 and CP102 were injected onto the polymer PLRP column. The mobile phases consisted of 1-heptane sulfonic acid (5mM, pH 2) and acetonitrile. The flow rate was 1.0 ml/min with the following gradient system with 2% to 40% of CH_3CN in 20 min and a post-run was followed for 5 min at 2% of CH_3CN.

2.3.2.3 Confirmation of glucuronidation

Glucuronidation was confirmed by the deconjugation by β-glucuronidase from *Helix pomatia*. Before terminating the reaction, samples were removed from the incubator at 24h. 5000 units of β-glucuonidase were added. Samples were returned to the incubator for another 16h before the addition of trichloroacetic acid and the internal standard. After 16hr incubation, samples were vortexed and followed by centrifugation at 14,000rpm in a Spectrafuge™ 16M microcentrifuge (Labnet International Inc., NJ, USA) for 10min. The supernatants from the protein pellet were subjected to HPLC analysis. The deconjugation of glucuronidation was confirmed by an increase of the parent drug signal.

2.3.2.4 Percentages of hydroxypyridinone metabolic conversion

CP20, CP94 and CP102 sample solutions at concentrations of 25μM, 50μM, 100μM, 200μM, 400μM, 800μM were used to construct calibration curves, CP95 added as the internal standard (IS) and the concentration of CP95 was constant in each calibration standard, namely 300 μM. Calibrations were conducted for each HPO compound (Peak area ratio of HPO/IS vs Concentration). The unknown concentrations of the HPO parent drug in the microsomal incubates were calculated from the corresponding calibration curve. Percentages of Phase I + II reactions were determined by Equation 2.1

$$\%\ Parent\ compound\ disappearance = \left\{1 - \left[\frac{Parent\ compound\ concentration\ (Cofactors\ included)}{Parent\ compound\ concentration\ (Cofactors\ excluded)}\right]\right\} \times 100$$

(Equation 2.1)

2.3.3 Development of UPLC conditions using HILIC mode

2.3.3.1 Instrumentation

HILIC phase columns

Acquity UPLC BEH column, 130Å, 1.7 µm, 2.1 mm X 50 mm, Waters, Elstree, UK

Acquity UPLC BEH Amide column, 130Å, 1.7 µm, 2.1 mm X 100 mm, Waters, Elstree, UK

SeQuant ZIC-HILIC, 100Å, 1.0 x 150 mm; 3.5 um, Merck Millipore, Feltham UK

UPLC-MS

A Thermo Finnigan MAX LCQ™ 3D ion trap mass spectrometer (San Jose, CA) interfaced to ESI was coupled to a Jasco X-LC™ system (JASCO UK Ltd, Essex, UK), which was composed of two semi-micro pumps (pump A and pump B, 3085 PU), a dynamic mixer, a degasser and an auto-sampler. A Thermo Finnigan LCQ™ Deca XP 3D ion trap mass spectrometer (San Jose, CA) interfaced to ESI was coupled to a Waters® Acquity UPLC system (Waters Corp., Milford, MA, USA), equipped with a binary solvent delivery system, an Acquity® auto-sampler.

MS conditions

The LCQ™ 3D ion trap MS was operated in positive ESI mode. Data was acquired in MS full scan mode with a mass range of 50 - 300. ESI ion source parameters were as follows, a sheath gas (N_2) and an auxiliary gas (N_2) flow rates were 99.56 L/min and 19.23 L/min respectively. The capillary and source voltage were set at 11.42 V and 4.55 kV, respectively. The capillary temperature was 199.70 °C.

2.3.3.2 Sample preparation

A stock solution of 5mg/mL for each HPO, CP20, CP94 and CP102 in 95/5 v/v ACN/H_2O was prepared separately. 10µL of each HPO stock solution was spiked into 970µL 95/5 v/v ACN/H_2O in an eppendorf tube tube and mixed evenly on a vortex mixture for 1 min to produce a clear solution of 50 µg/mL. 100 µL of the 50µg/mL solution was spiked into 900µL 95/5 v/v ACN/H_2O solvent in an eppendorf tube and mixed evenly on a vortex mixture for 1 min to produce a clear solution of 5 µg/mL in 95/5 v/v ACN/H_2O solvent.

2.3.3.3 Investigation of HPOs on HILIC phase

Mobile phase preparation

Acidic mobile phases (pH 3) consisted (A) 95/5 v/v ACN/H_2O + 0.125% HCOOH + 10mM $HCOONH_4$ and (B) 5/95 v/v ACN/H_2O + 0.125% HCOOH + 10mM $HCOONH_4$

Neutral mobile phases (pH 7) consisted of (A) 95/5 v/v ACN/H_2O + 10mM CH_3COONH_4 and (B) 5/95 v/v ACN/H_2O + 10mM CH3$COONH_4$.

Basic mobile phases (pH 9) consisted of (A) 95/5 v/v ACN/H_2O + 0.04% NH_4OH + 10mM CH_3COONH_4 and (B) 5/95 v/v ACN/H_2O + 0.04% NH_4OH + 10mM CH_3COONH_4

Basic mobile phases (pH 8) consisted of (A) 95/5 v/v ACN/H_2O + 0.04% NH_4OH + 10mM CH_3COONH_4 and (B) 5/95 v/v ACN/H_2O + 0.04% NH_4OH + 10mM CH_3COONH_4, acidified with CH_3COOH to pH 8

The measurement of pH of the mobile phases was undertaken in the aqueous media before mixing with organic phase.

Chromatography

50µg/mL of HPOs (CP20, CP94 and CP102) solutions were introduced by a loop injection into the ESI source at acidic (pH 3), neutral (pH 7), basic (pH 9) conditions in both ESI positive and negative ionisation modes. The ESI ion source parameters were optimised automatically to give the greatest signal strength of the ionised compounds.

10µL of CP20, CP94 and CP102 solutions (5µg/mL) were injected onto an Acquity UPLC BEH HILIC column and an Acquity UPLC BEH Amide column eluted with acidic (pH 3), neutral (pH 7) mobile phases; onto a SeQuant ZIC-HILIC column eluted with acidic mobile phases (pH 3). The above injections were performed using a Jasco X-LC™/LCQ™ ion trap MS system. The same samples and columns were also run under basic conditions using the Waters® Acquity UPLC/ LCQ™ Deca XP Ion Trap MS system. Two BEH columns were run with basic mobile phases at pH 9, while ZIC-HILIC column at pH 8. The elution was 0.1% to 99.9% mobile phase B at a flow rate of 0.45mL/min for a running time of 10min.

2.3.4 Statistical analysis

Results are expressed as the Mean ± S.D.. Bar graphs was plotted using "GraphPad Prism 5.0" software and statistical analysis was performed using "Two-Way ANOVA" by "GraphPad Prism 5.0" software. Chromatographs were plotted using "Origin 8" software.

2.4 Results and Discussion

2.4.1 Hydroxypyridinones adopted to test various bio-analytical systems

Three HPOs, CP20/deferiprone, CP94 and CP102, were used as the control groups during the development of an *in vitro* bio-analytical method for hepatic metabolism study of 3-hydroxypyridinones, due to their metabolic profiles being well established under *in vivo* conditions in both rat and human.

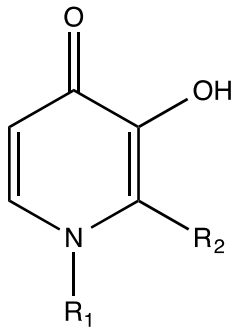

HPOs	R_1	R_2	Molecular Weight	$LogD_{7.4}$
CP20	CH_3	CH_3	139	0.17
CP94	CH_2CH_3	CH_2CH_3	167	1.78
CP102	CH_2CH_2OH	CH_2CH_3	183	0.22

Log $D_{7.4}$ values cited from (Liu et al., 1999a)

CP20/deferiprone is both extensively conjugated at the 3-hydroxyl group in rat and human. The predominant metabolites in urine were 3-O-glucuronides, which accounted for > 44% in rats and > 85% in man of the dose administered respectively (Singh et al., 1992). The dominant metabolite of CP94 in rat was the 2-(1'-hydroxyethyl) derivative, which accounted for about 40% of administered dose recovered in urine (Singh et al., 1992, Lu et al., 2000). In contrast, in human, 3-O-glucuronidation accounted for the majority of the biotransformation and more than 90% of the dose administered was recovered in urine (Porter et al., 1994). CP102 was reported not to be metabolised to any considerable extent in rat with the unchanged CP102 as the dominant form and minor glucuronide found in urine (Singh et al., 1996, Lu et al., 1998). Consequently, the validity of the various methods were assessed by comparing the observed metabolic conversions of these three HPOs using the different bio-analytical methods with the previously reported *in vivo* hepatic metabolic conversion results.

2.4.2 Development of HPO chromatography using Reversed Phase mode

The addition of an ion-paring reagent, 1-heptanesulfonic acid, into the acidified mobile phase led to prolonged retention times of both the hydrophilic parent compounds and more hydrophilic metabolites. This chromatographic system also led to sharp, symmetrical peaks (Figure 2.3, 2.4 and 2.5). The percentage of parent CP20 depletion can be calculated by comparing the concentration of CP20 in the microsomal incubation sample (NADPH+UDPGA included, Figure 2.3) and of CP20 in the blank (NADPH+UDPGA excluded, Figure 2.4). The concentrations of CP20 in both preparations were extrapolated from the calibration curve of CP20 Concentration vs Peak Area Ratio (CP20/CP95), which were 148μM, 198μM, respectively. Recovery of the parent HPO was observed when the microsomal incubation mixture (NADPH+UDPGA included) was treated with β-glucuronidase from *Helix pomatia,* when the CP20 level in the β-glucuronidase treated sample (NADPH+UDPGA included, Figure 2.5) rose to188μM, thereby confirming that the parent HPO was conjugated via glucuronidation (Figure 2.5). The percentages of parent HPOs depletion for CP94 and CP102 were determined in the same fashion (Appendix I).

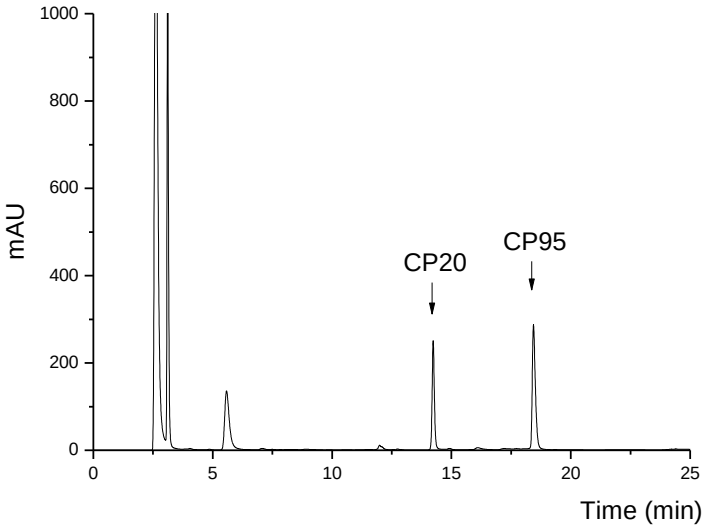

Figure 2.3 Chromatography of CP20 rat liver microsomal incubates
(NADPH+UDPGA included, alamethicin/microsomal protein ratio: 25 μg/mg).

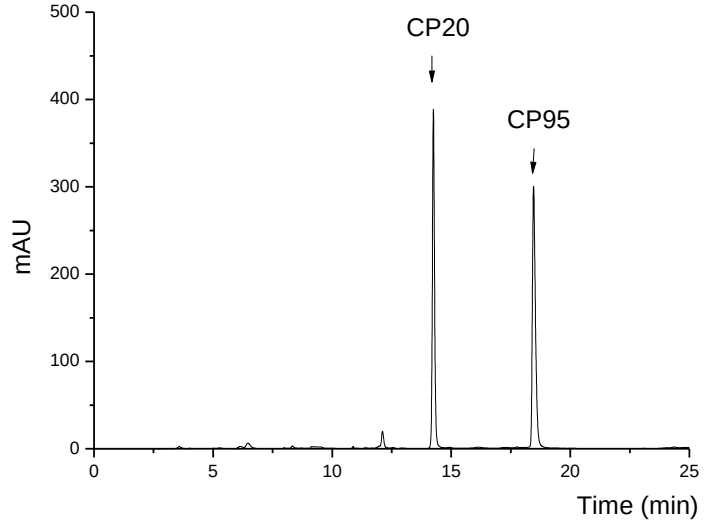

Figure 2.4 Chromatography of blank rat liver microsomal incubates
(NADPH+UDPGA excluded, alamethicin/microsomal protein ratio: 25 μg/mg).

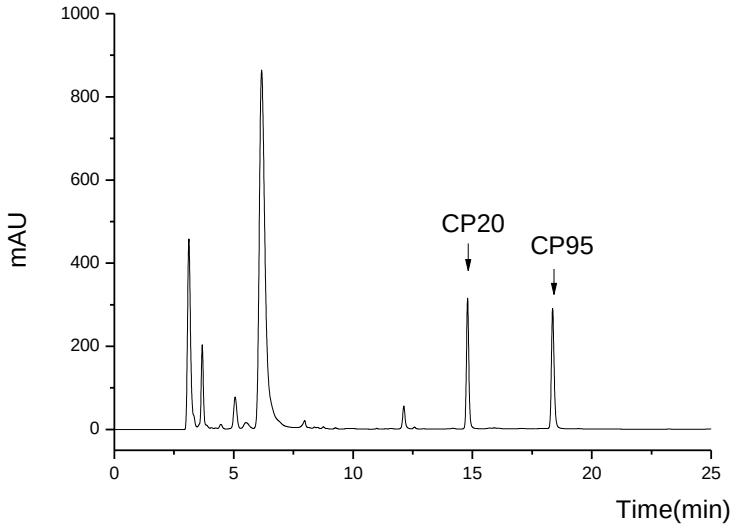

Figure 2.5 Chromatography of CP20 rat liver microsomal incubates deconjugated by β-glucuronidase
(NADPH+UDPGA included, alamethicin/microsomal protein ratio: 25 μg/mg).

2.4.3 Development of Phase I+II microsomal incubation conditions

Due to the latency of UGTs and possible effects of endogenous β-glucuronidase, incubation conditions for glucuronidation by microsomes usually include an agent to disrupt the membrane barrier, a divalent metal ion, and the selection of an optimal pH to obtain maximal glucuronidation activity (Jia and Liu, 2007).

2.4.3.1 Addition of detergent to overcome UGT latency

Detergents solubilise UGTs, which are loacated on the lumenal surface of microsomes (Sies and Packer, 2005). This permits access of the hydrophilic cofactor UGPDA, which is normally synthesised in the cytosol, to the active site of UGTs (Section 2.1.1.1, Figure 2.1). There are various types of detergents that can be used to minimise UGT latency, such as the non-ionic detergents: triton, digitonin; the ionic detergents: cholate, deoxycholate; the zwitterionic detergents: CHAPS (Sies and Packer, 2005). TritonX-100 is commonly added as a detergent in order to fully remove UGT latency (Lett et al., 1992) and was adopted in this study. Experimental conditions for achieving optimal UGT activation for each HPO substrate incubated with both rat and human liver microsomes can be determined by titrating microsomes with

increasing concentrations of TritonX-100 (0.1 to 1 mg per mg of microsomal proteins) on ice for ten minutes before adding into the reaction mixture. The detergent/microsomal protein ratios inducing the maximal UGT activity for each HPO in both rat and human liver microsomes were determined (Appendix II). However, the optimal detergent/microsomal protein ratio varied for each HPO substrate. For instance, at the detergent/microsomal protein ratio of 0.2, UGT activity increased to a maximum for CP20 in the rat microsomes. When the detergent/microsomal protein ratio was further increased from 0.3 to 1, the activity of UGTs was reduced (Figure 2.6). At higher detergent/microsomal protein ratios, the progressive disruption of the microsomal membrane organisation probably leads to inactivation of the enzyme (Lett et al., 1992). Consequently, the detergent/microsomal protein ratio of 0.2 was applied in CP20 rat microsomal Phase I+II incubates to activate the UGTs.

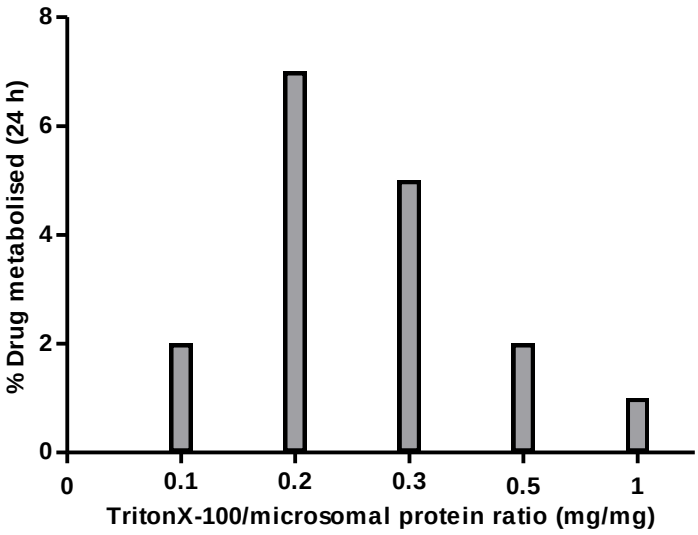

Figure 2.6 Percentage of CP20 metabolism by Phase I+II pathway in rat liver microsomal incubations titrated with Triton X-100

However, the extent of glucuronidation conversion of HPOs in the detergent-activated microsomal incubates did not reflect their *in vivo* metabolic profiles (outlined in Section 2.4.1). CP94 was found to be more resistant to glucuronidation compared with CP20 in the *in vivo* rat models. However, CP94 experienced a higher extent of glucuronidation, when compared with CP20, in the TritonX-100 activated rat liver microsomal incubation (Figure 2.7, Table 2.1). CP102, which was not metabolised via conjugation reactions to any considerable extent in *in vivo* rat models, was found to be extensively conjugated in TritonX-100 activated rat and human liver microsomal incubations ((Figure 2.7, Table 2.1). There are a few possibilities, which might contribute to these contradictory results. The detergent not only solubilises the microsomal membrane in order to permit the free access of UDPGA to the enzyme active site, but also disrupts the integrity of the microsomal membrane, which may affect the activity of the UGTs either by altering the microsomal vesicle structure or by solubilising an appreciable amount of microsomal proteins (Fulceri et al., 1994). It has also been reported that detergent can render the UGT enzyme intrinsically more active (Trapnell et al., 1998).

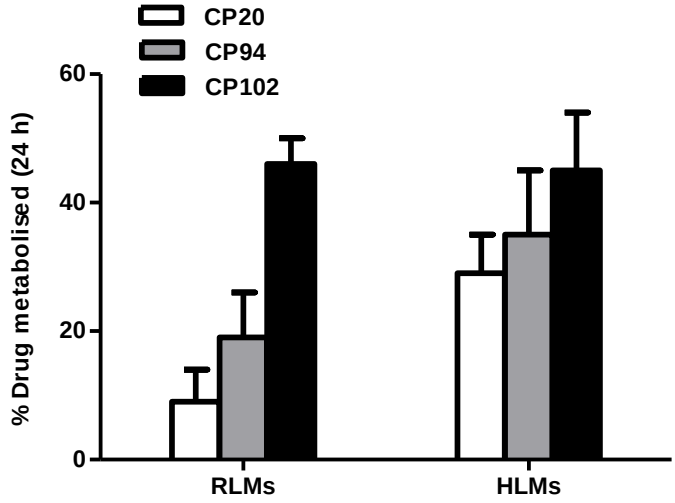

Figure 2.7 Percentage of CP20, CP94 and CP102 metabolism by Phase I+II pathway in rat and human liver microsomal incubates
(Triton X-100/microsomal protein ratios varied depending on the substrate and microsomal source)

A disadvantage of this approach is that establishment of conditions for optimal activation will vary for each detergent, substrate and microsomal source used and therefore it requires the determination of such conditions each time one of these parameters changes (Sies and Packer, 2005). Consequently, in order to avoid possible non-physiological effects on the native catalytic activity of the UGT enzymes and the labor-intensive microsomal incubation procedures, a substrate and enzyme source-independent, non-detergent agent is required to disrupt microsomal UGT latency.

Table 2.1 Percentage of CP20, CP94 and CP102 metabolism by Phase I+II pathway in the rat and human liver microsomal incubates
(Triton X-100/microsomal protein ratios varied depending on the substrate and microsomal source)

HPOs	% Drug metabolised (24 h) (Mean ± SD, n=3)	Triton X-100/microsomal protein ratios
CP20/deferiprone RLMs[1]	9 ± 5	0.2
CP20/deferiprone HLMs[2]	29 ± 6	0.2
CP94 RLMs[1]	19 ± 7	0.1
CP94 HLMs[2]	35 ± 10	0.2
CP102 RLMs[1]	46 ± 4	0.3
CP102 HLMs[2]	45 ± 9	0.2

[1]RLMs Rat Liver microsomes; [2]HLMs Human Liver microsomes

2.4.3.2 Addition of alamethicin to overcome UGT latency

The antibiotic fungal peptide, alamethicin, is known to insert into membranes and form well defined pores, facilitating entry of substrate and UDPGA into, and the diffusion of conjugate and UDP out of the lumen of the microsomes. In addition, alamethicin enhances UGT activity in a substrate-independent fashion, without affecting the intrinsic enzyme catalytic activity. Thus, in principle, it is a more effective activator of UGTs as compared with conventional detergents

(Fisher et al., 2000). Alamethicin was used in HPO microsomal incubations. Alamethicin/microsomal protein ratios of 5, 10, 25, 50, 100μg/mg were investigated. The maximal UGT activity, illustrated as the most extensive glucuronidation of CP20 incubated in rat liver microsomes was observed at an alamethicin/microsomal protein ratio of 25μg/mg (Figure 2.8).

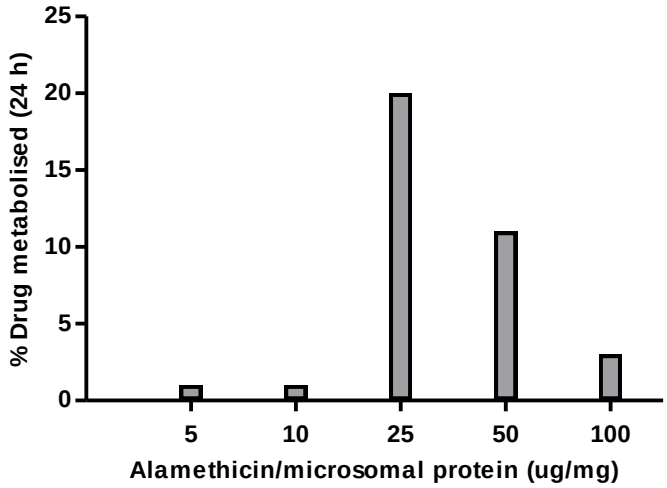

Figure 2.8 Percentage of CP20 metabolism by Phase I+II pathway in rat liver microsomal incubates titrated with alamethicin

Similar alamethicin titration studies were performed for each HPO substrate incubated in both rat and human liver microsomes (Appendix III). The optimal alamethicin/microsomal protein ratios was found to be 25μg/mg for all three HPOs in two microsomal sources, which further implied that alamethicin removed the microsomal UGTs latency regardless of substrates and enzyme sources. Consequently, all HPO microsomal mixtures were all incubated in the presence of 25μg alamethicin per mg microsomal protein. The depletion of parent HPOs by glucuronidation is illustrated in Figure 2.9 and Table 2.2. CP20 experienced relatively extensive glucuronidation in both rat and human microsomes. CP94 was conservatively glucuronidated in rat, but appreciable metabolism was observed in human microsomes. Very low levels of glucuronidation of CP102 occurred in rat and human microsomes. These results are

comparable with the *in vivo* metabolic profiles of these HPO compounds reported previously (Section 2.4.1).

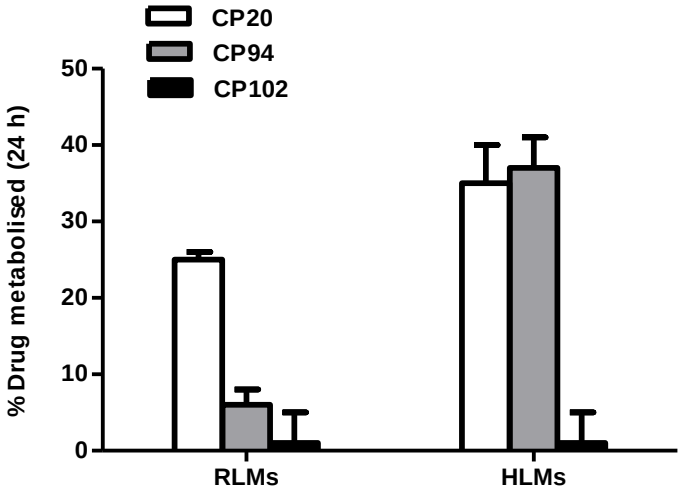

Figure 2.9 Percentage of CP20, CP94 and CP102 metabolism by Phase I+II pathway in rat and human liver microsomal incubates
(alamethicin/microsomal protein ratio: 25 µg/mg)

Table 2.2 Percentage of CP20, CP94 and CP102 metabolism by Phase I+II pathway in rat and human liver microsomal incubates
(alamethicin/microsomal protein ratio: 25 µg/mg)

HPOs	% Drug metabolised (24 h) (Mean ± SD, n=3)
CP20/deferiprone RLMs[1]	25 ± 1
CP20/deferiprone HLMs[2]	35 ± 5
CP94 RLMs[1]	6 ± 2
CP94 HLMs[2]	37 ± 4
CP102 RLMs[1]	1 ± 4
CP102 HLMs[2]	1 ± 4

[1]RLMs Rat Liver microsomes; [2]HLMs Human Liver microsomes

2.4.3.3 Addition of saccharolactone as an endogenous β-glucuronidase inhibitor

A range of saccharolactone (D-saccharic acid 1, 4-lactone) concentrations was titrated to HPOs rat and human liver microsomal incubates in order to observe the degree of inhibition of endogenous β-glucuronidase (Appendix IV). A saccharolactone concentration-dependent increase in glucuronidation activity was expected. However, percentage glucuronidation of parent HPOs in human liver microsomes showed no increase when saccharolactone was included (p>0.05) (Figure 2.10). Oleson and Court (2008) have investigated the effect of different enzyme sources and estradiol glucuronide substrates on the amount of glucuronide degraded by endogenous β-glucuronidase in relation to glucuronide formation. The degradation as a percentage of glucuronide formed for different estradiol glucuronides fell in a range of 9 to 19%, which indicated that although human liver microsomes exhibit β-glucuronidase activity, different types of glucuronides might differ in susceptibility to hydrolysis by β-glucuronidase. Since the addition of saccharolactone did not shown any enhancement of glucuronidation formation, implied that HPO glucuronides were not labile to endogenous β-glucuronidase hydrolysis under the adopted incubation conditions.

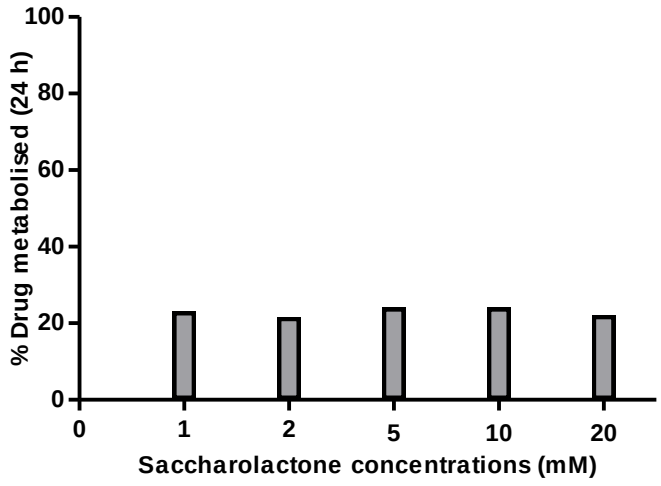

Figure 2.10 Percentage of CP20 metabolism by Phase I+II pathway in rat liver microsomal incubates titrated with saccharolactone

2.4.4 Development of HPO chromatography using HILIC mode

Since the introduction of the electrospray ionisation (ESI), which is a relatively gentle ionisation technique, suitable for labile conjugation metabolites, LC-MS has become a preferred metabolite detection tool owing to its superior specificity, sensitivity and efficiency. Therefore, in order to further confirm the Phase I+II results of HPOs using the HPLC-UV analytical method developed in Section 2.4.2 and Section 2.4.3.2, an UPLC-ESI-MS system was also investigated. However, the LC conditions developed with the non-volatile ion-paring reagent (1-heptanesulfonic acid) are not compatible with MS systems. The use of volatile solvents and additives in chromatographic separation is essential for mass spectrometry, because undesirable build-up from non-volatile buffer deposits interfere with ESI ionization (Naegele, 2011). HILIC mobile phases tend to contain a higher organic solvent fraction (Section 2.1.2.2), which are more compatible with MS detection, leading to higher detector signals. Consequently, HILIC mode was investigated for HPO chromatography. A mixture of three HPO compounds was used to develop the HILIC method. These three HPO compounds ionised nicely in the ESI source as $[M + H]^+$ ions in positive ion mode for CP20 (140), CP94 (168) and CP102 (184) respectively in acidic (pH 3) and neutral (pH 7) conditions (Figure 2.11). Surprisingly, the three HPOs also ionised even more effectively under basic (pH 9) conditions in positive ion mode (Figure 2.12). In negative ion mode, the HPO mixtures did not readily ionise. Hence, ESI positive ion mode was applied throughout the remaining study.

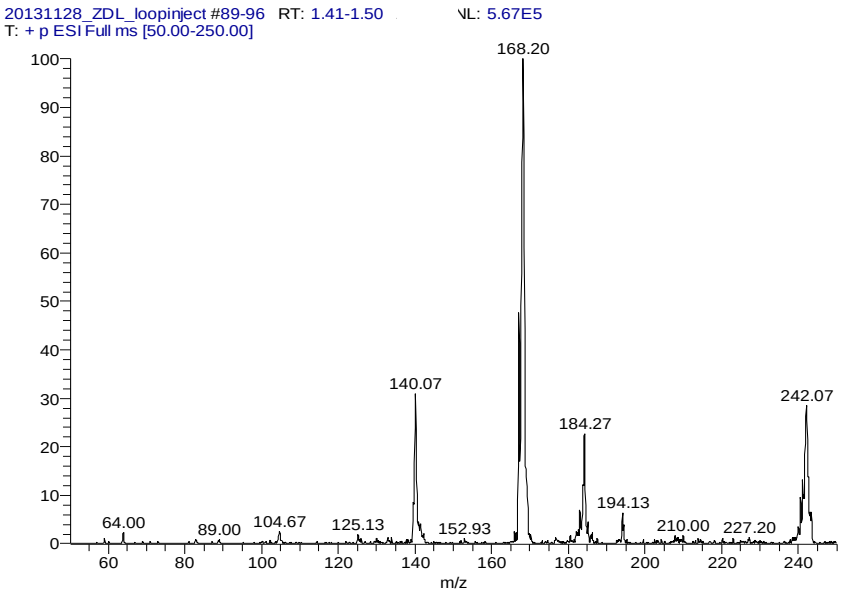

Figure 2.11 Mass spectrum of 50 µg/mL of three HPOs (CP20, CP94 and CP102) mixture solution introduced by loop injection at acidic (pH 3) and neutral (pH 7) conditions.

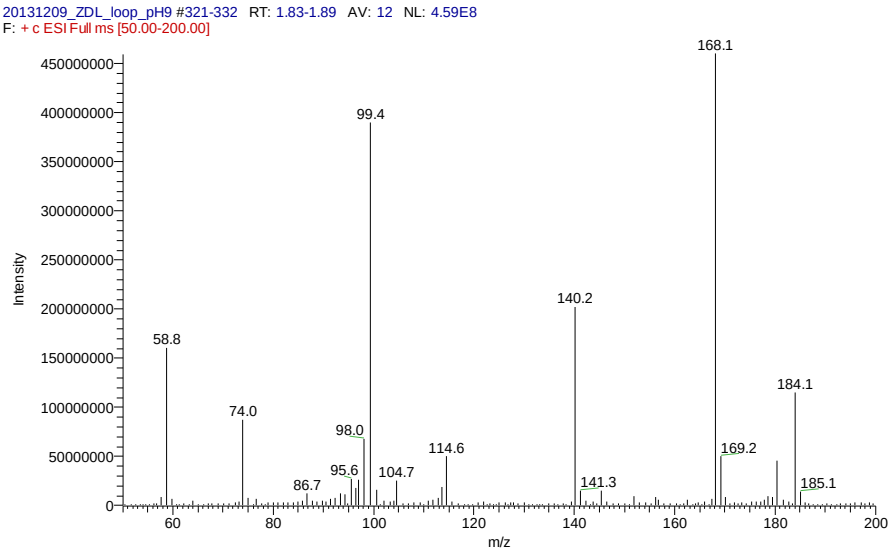

Figure 2.12 Mass spectrum of 50 µg/mL of three HPOs (CP20, CP94 and CP102) mixture solution introduced by loop injection at basic (pH 9) condition.

However, chromatography of HPOs on HILIC columns with BEH HILIC (un-bonded), Amide (bonded) and zwitterionic ZIC-HILIC phases at acidic, neutral and basic conditions did not show any promising retention and separation, see for example (Figure 2.13 to 2.16). Problems associated with HPO chromatography on HILIC phases might result from solute-metal interactions. Metal contamination, such as Fe^{2+}/Fe^{3+}, originating from the corrosion of stainless steel frits in the presence of acidic mobile phases, can complex with HPO iron chelators (Ma and Carr, 2007). Addition of iron chelating agents in the mobile phase, such as EDTA, has been reported to improve HPO chromatography when using LC-UV as the analytical tool (Epemolu et al., 1990). However, EDTA is a non-volatile buffer, not compatible with mass spectrometry, in addition, the solubility of EDTA is poor when ACN concentration is more than 85% and therefore has limited use in HILIC (Heaton and McCalley, 2016). Furthermore, because the HILIC retention mechanism is a combination of mixed modes (Section 2.1.2.2), HPO compounds, containing more than one ionisable group, might interact with the HILIC phase in a combination of complex modes, which could lead to undesirable secondary interactions and result in deterioration of chromatographic peaks.

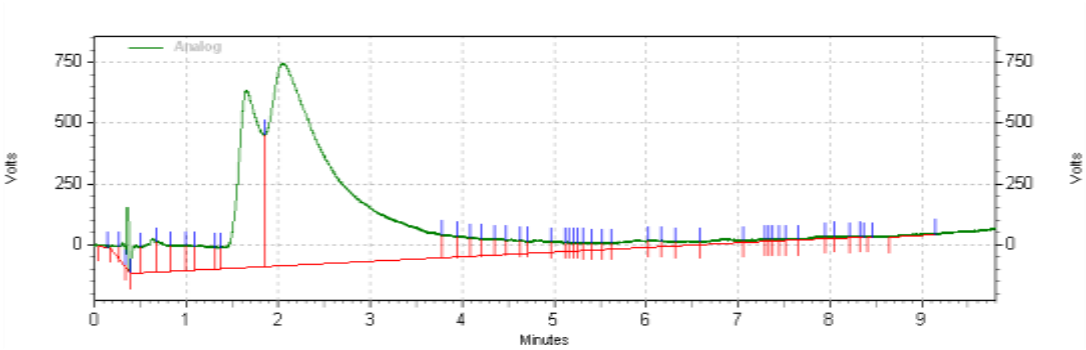

Figure 2.13 UPLC-MS chromatography of 5 µg/mL of CP20, CP94 and CP102 mixture solution in 95/5 v/v ACN/H_2O injected onto Acquity UPLC BEH HILIC column eluted with acidic (pH 3) MPs.
MPs at acidic condition (pH 3) consisted (A) 95/5 v/v ACN/H_2O + 0.125% HCOOH + 10mM $HCOONH_4$ and (B) 5/95 v/v ACN/H_2O + 0.125% HCOOH + 10mM $HCOONH_4$

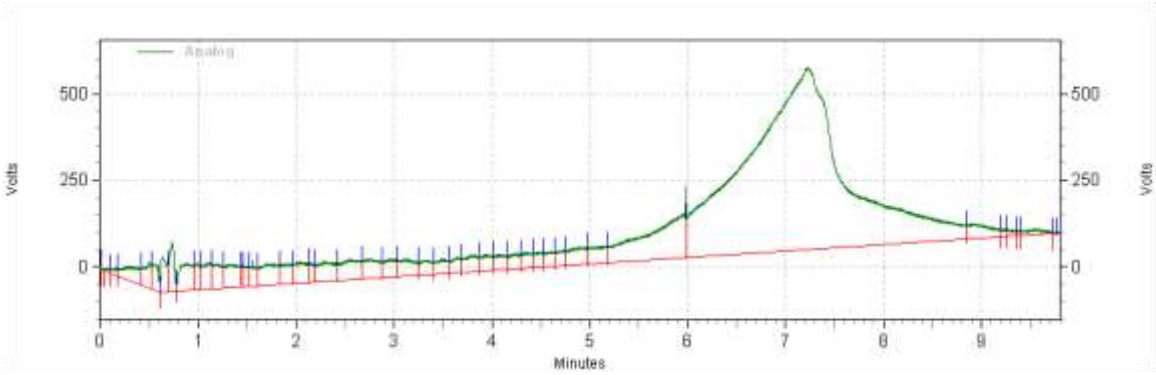

Figure 2.14 UPLC-MS chromatography of 5 µg/mL of CP20, CP94 and CP102 mixture solution in 95/5 v/v ACN/H_2O injected onto Acquity UPLC BEH Amide column eluted with acidic (pH 3) MPs.
MPs at acidic condition (pH 3) consisted (A) 95/5 v/v ACN/H_2O + 0.125% HCOOH + 10mM $HCOONH_4$ and (B) 5/95 v/v ACN/H_2O + 0.125% HCOOH + 10mM $HCOONH_4$

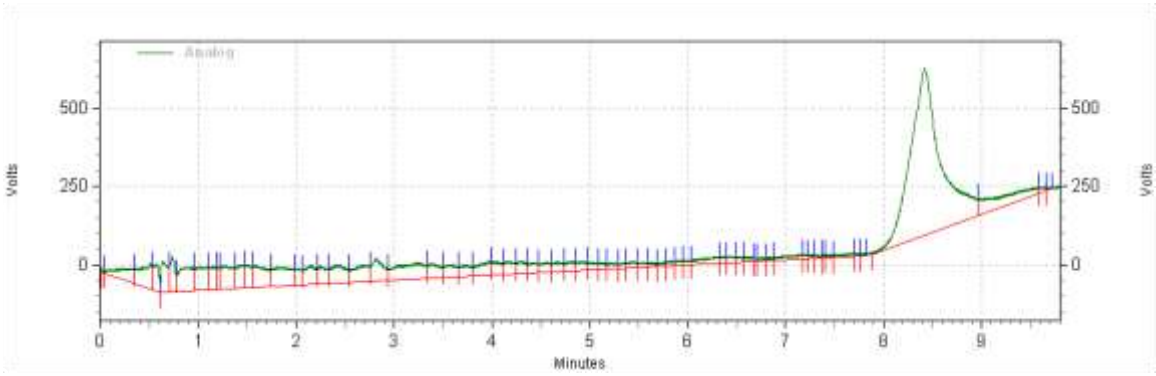

Figure 2.15 UPLC-MS chromatography of 5 g/mL of CP20, CP94 and CP102 mixture solution in 95/5 v/v ACN/H2O injected onto Acquity UPLC BEH Amide column eluted with neutral (pH 7) MPs.
MPs at neutral condition (pH 7) consisted of (A) 95/5 v/v ACN/H_2O + 10mM CH_3COONH_4 and (B) 5/95 v/v ACN/H_2O + 10mM CH_3COONH_4.

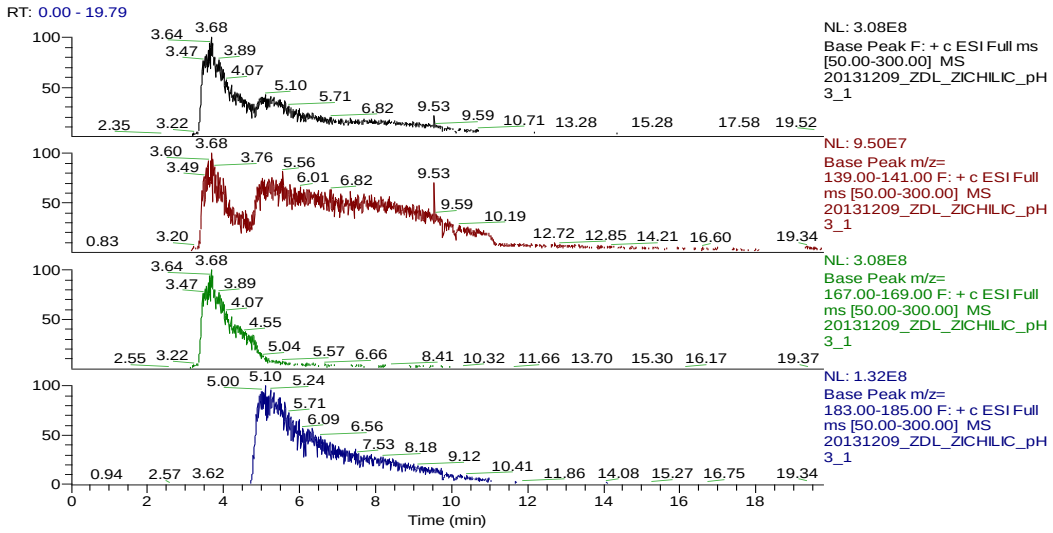

Figure 2.16 UPLC-MS chromatography of 5 µg/mL of CP20, CP94 and CP102 mixture solution in 95/5 v/v ACN/H2O injected onto SeQuant ZIC- HILIC column eluted with acidic (pH 3) MPs.
MPs at acidic condition (pH 3) consisted (A) 95/5 v/v ACN/H_2O + 0.125% HCOOH + 10mM $HCOONH_4$ and (B) 5/95 v/v ACN/H_2O + 0.125% HCOOH + 10mM $HCOONH_4$

2.5 Summary

In order to investigate the *in vitro* metabolic profiles of HPO compounds, a microsomal incubation protocol of Phase I+II metabolic reactions has been developed. The conditions of some essential elements in the incubation mixtures were investigated to achieve the optimal catalysing activity of microsomal enzymes. In order to disrupt the concealed UGTs activity due to the enzyme latency, both Triton-X 100 and the pore-forming peptide alamethicin were titrated into the microsomal incubation mixture to overcome UGT latency. Consequently, alamethicin was adopted as an ideal agent at an optimal concentration of 25μg/mg because of its ability to enhance UGT activity in a substrate and enzyme source independent manner. In addition, the resulting *in vitro* metabolic profiles of the corresponding HPOs were comparable with those of previous *in vivo* studies. Taking into account that there might be deconjugation of newly formed glucuronide by endogenous β-glucuronidase hydrolysis, a commonly used inhibitor, D-saccharic acid 1,4-lactone, was also added the reaction mixture. In this work, it did not show any effect on enhancing the glucuronidation conversion. Hence, D-saccharic acid 1,4-lactone was not included in the protocol.

After examining the ideal concentrations of the above reagents to generate the optimal conditions for HPO microsomal incubation, we decided to substitute these tedious incubation procedures with more efficient *in vitro* drug metabolism commercial kit. The kit is manufactured by Corning Ltd-Life Sciences and contains the same concentrations of key elements as our optional incubation protocol. The results obtained with this kit are described in Chapter 3.

In order to analyse HPO microsomal incubation samples, HPLC-UV using a polymer reversed phase column eluted with mobile phases containing an ion-paring additive was initially applied. This system successfully resolved HPO compounds from the microsomal matrix, characterised by symmetrical and sharp chromatographic peaks. Further quantitative analysis of the parent HPO depletion over the time of microsomal incubation demonstrated a comparable *in vitro* metabolic profile with the previously obtained *in vivo* data. In order to further verify the above results, mass spectrometry offered as a sensitive and specific tool. Since the non-volatile buffers used in the above HPLC-UV method cannot be interfaced with ESI-MS, HILIC analytical columns with ESI-MS-compatible mobile phases were investigated as alternatives.

Unfortunately, none of the HILIC phases investigated in the study serves as a reliable method to establish well resolved good chromatography of HPOs. As a consequence, a reliable analytical method based on UPLC-ESI-MS was sought to further investigate the *in vitro* microsomal metabolism of HPOs and this is described in Chapter 3.

CHAPTER THREE

Development of a high throughput bio-analytical method for the *in vitro* hepatic metabolism study of novel hydroxypyridinones

Chapter 3 Development of a high throughput bio-analytical method for the *in vitro* hepatic metabolism study of novel hydroxypyridinones

3.1 Introduction

A series of novel 3-hydroxypyridin-4-one analogues have been designed based on the structural modification of the lead iron chelator CP20/deferiprone, in order to optimise the physiochemical properties and stereochemical orientations, which might improve the iron chelation efficacy. The investigation on their *in vitro* metabolic profile using human liver microsomal incubation approach has provided the hepatic metabolism information and has facilitated the selection of candidate compound which might possess the better oral availability and improved pharmacokinetic characters leading to an enhanced iron chelation efficacy. A high throughput bio-analytical method was sought to screen the metabolic profiles of the investigated compounds

3.2 Materials

Hydroxypyridinones

CP20, CP94, CP102, CP365, CP364, CP21 were synthesised in King's College London. CN128 (Batch No. 20121228) and CN126 were synthesised in Zhe Jiang University, China. The purity of CN128 was certificated as 98.77%. CP20 analogues (CP669, CP69, CP616, CP28, CP679, CP617) and pegylated HPOs (C11, C21, 6d, C31, K31 K8, K5, K7, K6) were synthesised by Y.Y.Xie and J.P.Li in King's College London. CM1 was synthesised in Chiang Mai University, Thailand.

Chemicals

All solvents and reagents were purchased from Fisher Scientific Ltd (Loughborough,Leicestershire,UK). Pentadecafluorooctanoic acid (PFOA, analytical grade) was purchased from Fluorochem LTD (Hadfield, UK).

Biological materials

Male rat liver microsomes (20 mg/mL in 0.5mL), UltraPool™ human Liver microsomes, 150 mixed gender pooled (20 mg/mL in 0.5mL) were purchased from Corning Ltd-Life Sciences (Ewole, UK). NADPH-regenerating system A (consisting of 31 mM NADP+, 66 mM glucose-6-phosphate and 66 mM $MgCl_2$ in water), NADPH-regenerating system B (consisting of 40 U/mL glucose-6-phosphate dehydrogenase in 5mM sodium citrate), UDP reaction mix solution A (consisting of 25 mM UDP-glucuronic acid in water) and UDP-regenerating system B (consisting of 250 mM Tris–HCl, 40 mM $MgCl_2$ and 0.125 mg/mL alamethicin in water) were also purchased from Corning Ltd-Life Sciences (Ewole, UK). Rabbit serum (Cat No. R4505-100mL) was purchased from Sigma (Dorset, UK).

3.3 Instrumentation

A Waters® Xevo TQ tandem quadrupole mass spectrometer (Waters, Elstree, UK) equipped with an ESI interface, corporate with an Ultra Performance LC system (Waters, Elstree, UK), equipped with a binary solvent delivery system, an Acquity auto-sampler was used throughout this study.

3.4 LC-MS method development

3.4.1 Liquid Chromatography

The LC analysis was performed on a Waters® Acquity Ultra Performance LC system (Waters, Elstree, UK), equipped with a binary solvent delivery system, an auto-sampler. The chromatography was performed on an Agilent Poroshell 120 EC-C_{18} column, 2.1 x 50mm, 2.7µm (Agilent, Lakeside, UK). The mobile phases were composed of (A) 1g pentadecafluorooctanoic acid (PFOA, $CF_3(CF_2)_6COOH$) in 0.1% formic acid, 95% Optima® H_2O, 5% Optima® ACN and (B) 1g PFOA in 0.1% formic acid, 95% Optima® ACN, 5% Optima® H_2O. The UPLC eluting conditions were optimised as follows: linear gradient from 30% to 90% B (0–4 min), isocratic at 90% B (4–5.5 min), linear gradient from 90% to 30% B (5.5–5.6 min), isocratic at 30% B (5.6–9 min). The flow rates of 0.2, 0.5, 0.7 mL/min for a total run time of 9 min were attempted for optimising the chromatographic separation. 0.5 mL/min was found to be the

optimal flow rate. The column and the auto-sampler were maintained at 45 °C and 15 °C, respectively. Three cycles of seal wash were performed including a strong wash, a weak wash and a sample syringe wash. Each wash cycle consisted of 50% of strong solvent (50/50 v/v ACN/MeOH) and 50% of weak solvent (95/5 v/v H_2O/ACN). The injection volume of the standards and sample was 5µL. Samples were introduced from HPLC vials placed in the ANSI-48 vial 2mL holder sample bed layout or a Waters® Acquity UPLC 700µL round 96- well sample plates (Waters, Elstree, UK) in the ANSI-96 well 1mL bed layout of the autosampler.

3.4.2 Mass spectrometry

Mass spectrometry was operated on a Waters® Xevo TQ tandem quadrupole mass spectrometer using an ESI operated in positive ion mode. The desolvation gas (N_2) was set to 650 L/hr at temperature of 400 °C. The cone gas flow was 5 L/hr. The capillary voltage was set to 2.00 kV. Argon was used as the collision gas, the collision gas flow was set at 0.15 mL/min. LM/HM resolution 1 and 2 were both 3/15, ion energy 1 and 2 were both 0.5. Data acquisition was carried out in the MS/MS, Multiple Reaction Monitoring (MRM) mode. Data were processed using the MassLynx V 4.1™ software.

3.4.3 MS/MS (MRM) method development

3.4.3.1 Optimisation of MS and MS/MS parameters

Manual optimisation was performed to preliminarily optimise the MS parameters and to select the appropriate diagnostic ions. 1µg/mL of pure standard solution of the HPO compound in a mixture of 0.1% formic acid in 50/50 v/v ACN/water was directly infused with a flow rate of 200µL/min from the integrated fluidics. The precursor ion spectrum was monitored in the “Mass Tune” of MassLynx™ by setting a mass span of 150 centered on the mass of the infused compound. The cone voltage, capillary voltage, desolvation temperature were adjusted to achieve the highest signal intensity of the HPO compound. The collision energy was increased until the HPO precursor ion was fragmented to several product ions and the fragmented product ion with the most abundance was observed. The product ion spectrum of the precursor HPO ion fragmentation showed the most intense fragmented product ion at the optimised collision

energy.

3.4.3.2 MRM method development

The IntelliStart™ system was used to tune the standard HPO sample and develop the MRM method for the investigated compounds. The standard solution of individual HPO (1μg/mL) was introduced by the direct infusion with a flow rate of 200μL/min from the integrated fluidics. The "sample tuning and develop method" process has optimised cone voltage and collision energy. The cone voltage was adjusted over a range of 2-100 V, and the collision energy was optimised over a range of 2-80 V. The procedure has also searched for precursors and fragmented ions. The MS_1 and MS_2 resolutions were 1.0 and 0.75. Multiple MRM transitions were generated to provide qualitative and confirmatory information for the targeted compound in the HPO biological samples. The dwell time of the MRM transitions was 35 ms with the pause time of 5 ms.

3.4.3.3 Selection of the MRM transition for quantification

In addition to the manual optimisation and the IntelliStart™ "sample tune and method development", the CS ChemDraw Ultra (Cambridge Soft Co.) was used to further analyse the fragmentation pathways. The MRM transition used for quantification was selected and applied for the quantification of metabolic conversion of the HPO biological samples.

3.4.3.4 Quantification method.

The TargetLynx™ software was used for the quantification. In the chromatographic peaks of the investigated compounds, a TargetLynx™ quantification method was created by defining the compound and calibration properties, including the compound name and the retention time etc. In a TargetLynx™ method editor, the parameters were stored and applied to all samples of the same compound. The integration of the peak was accomplished by ApexTrack™. A calibration curve was developed with the calibration curve standards. The concentrations of unknown samples were calculated from the fitted calibration curve.

3.5 *In vitro* metabolic stability incubation method using liver microsomes

To investigate phase I metabolism, the following was spiked into an enpendorf tube: 50µL of 0.1mM HPO compound (prepared in HPLC H_2O), 250µL of 0.2 M phosphate buffer (pH 7.4), 25µL of NADPH regenerating system A, 5µL of NADPH regenerating system B and 145µL of H_2O. The combined components were then pre-incubated at 37 °C for 10 min, after which 25µL of cold human liver microsomes were added to initiate metabolism, giving a final concentration of 1mg/mL protein. The mixture was then incubated at 37 °C in a thermostat incubator for 24 h with gentle shaking to prevent protein sedimentation. The reactions were terminated by spiking in 400µL 4% phosphoric acid to remove protein, followed by spiking in 100µL of 100µM internal standard. Samples were mixed evenly by the vortex mixer and followed by centrifuge at 14,000rpm in a Spectrafuge™ 16M microcentrifuge (Labnet International Inc., NJ, USA) for 10min. The supernatants were collected for the further solid phase extraction.

Phase I+II metabolism was performed alongside Phase I using the same experimental procedure as described above, with the exception of 145µL water, with 40µL of UDP reaction mix solution A and 100µL of UDP reaction mix solution B and 5µL of water.

Blank sample was prepared by substituting microsomal protein with water. Phase I and Phase I+II microsomal incubates for each HPO compound were prepared in triplicate.

3.6 The development of a sample clean-up method using the Solid Phase Extraction (SPE)

3.6.1 Apparatus

The Oasis® MAX (Mixed-mode Anion-eXchange, 1 cc Flangeless Vac syringe cartridge, 10 mg sorbent per cartridge, 30 µm particle size, Waters, Elstree, UK) with an exchange capacity of 0.25 mol/kg and the Oasis® MCX (Mixed-mode Cation-eXchange, 1 cc Flangeless Vac syringe cartridge, 10 mg sorbent per cartridge, 30 µm particle size, Waters, Elstree, UK) with an

exchange capacity of 1 mol/kg were applied on a Visiprep solid phase extraction vacuum manifold (Sigma-Aldrich, UK). An Oasis® 96-well MCX µElution plate (2 mg sorbent per well, 30 µm Particle Size, Waters, Elstree, UK) with an exchange capacity of 1 mol/kg was applied on a high throughput Supelco® SPE PlatePrep vacuum manifold (Sigma-Aldrich, Poole, UK).

3.6.2 SPE sorbent selection

3.6.2.1 Sample preparation

The Phase I+II metabolism of CP20 was investigated in rat liver microsomes following the procedure, which was described in the Section 3.5. A series of CP20 standard solutions were prepared in the rabbit serum in a total volume of 500µL. Serial dilutions of the standard solution CP20 (10µg/mL) in the rabbit serum were performed to provide a set of stock standard solutions with the following concentrations 1000, 500, 250, 125, 62.5, 31.3, 15.6, 7.80, 3.90, 1.95ng/mL. A stock solution of CP21 (IS, 4200ng/mL) in the rabbit serum was also prepared.

3.6.2.2 Sample pre-treatment

The sample was pre-treated by a 1:1 dilution with acidified water diluent for the MCX sorbent and with basified water diluent for the MAX sorbent. The acidified water diluent was 4% phosphoric acid prepared by diluting 47 mL 85% phosphoric acid to 1 L final volume with water. The basified water diluent was 5% ammonium hydroxide prepared by diluting 142mL 35% ammonium hydroxide to 1 L final volume with water. 500µL sample microsomal incubates and 500µL acidified or basified water diluent were spiked into an eppendorf tube. 500 µL CP20 standards in the rabbit serum solutions, 10µL CP21 (IS, 4200ng/mL) and 450µL acidified or basified water diluent were spiked into an eppendorf tube. Samples were subjected to the SPE using the Oasis® syringe cartridge with different sorbents.

3.6.2.3 SPE elution procedure

An Oasis® MCX cartridge or an Oasis® MAX cartridge was placed on the Supelco® 24 port Visiprep vacuum manifold. The cartridge was conditioned with MeOH, equilibrated with water. The diluted acidified or basified sample was loaded on the cartridge. The vacuum valve was

switched on slowly and gradually increased to provide a pressure of 5 mmHg in order to load the entire sample onto the sorbent bed. Then the vacuum pump was disconnected. Formic acid (2%, 1mL), prepared by diluting formic acid (≥ 95%) 20mL to 1L final volume with water, or ammonium hydroxide (5%, 1mL), prepared by diluting ammonium hydroxide (35%) 142 mL to 1L final volume with water, was applied as the initial wash solvent. The vacuum was switched on, set to 10 mm Hg and pulled for another half a minute to eliminate the residual wash solvent; the vacuum line was then disconnected. 100% MeOH (1mL) was applied to elute most of the proteins and phospholipids from the matrix. The vacuum was switched on, set to 10 mm Hg and pulled for another half a minute to eliminate the residual wash solvent, then the vacuum released and the waste fluid discarded. An eppendorf tube was placed under the cartridge. Ammonium hydroxide in methanol (5%, 1mL), prepared by diluting ammonium hydroxide (35%, 142mL) to 1 L final volume with methanol, or formic acid in methanol (2%, 1mL), prepared by diluting formic acid (≥ 95%, 20mL) to 1 L final volume with methanol, was applied as the elution solvent. The vacuum valve was switched on slowly, gradually increased to 5 mm Hg and pulled for another 30 sec to collect all elution solvent. This step was repeated a second time. The sample was evaporated to dryness in a Genevac EZ-2 series evaporator (Genevac Ltd, Suffolk, UK) and reconstituted in 100µL mobile phase. The sample was stored at -80 °C deep freezer before the analysis by LC-MS.

3.7 Validation of the bio-analytical method

3.7.1 Sample preparation

Calibration curve standards

Serial dilutions of the standard solution CN128 (100ng/mL) in rabbit serum were conducted to give a set of stock standard solutions with the concentrations over the range 100, 50, 25, 12.5, 6.25, 3.125, 1.5625, 0.7813, 0.3906, 0.1953ng/mL. A stock solution of CP21 (IS, 420ng/mL) in rabbit serum was also prepared. 50µL CN128 stock standard solution, 10µL CP21 stock solution (both in rabbit serum) and 40µL 4% phosphoric acid were spiked into one single well of the 96 well plate and transferred onto the 96-well MCX µElution plate for the SPE. The SPE

elution steps and post-sample treatments were the same as those using the Oasis® MCX cartridge, apart from that 200μL was used instead of 1mL for the elution solvents at each elution step and a Waters® Acquity UPLC 700μL round 96- well sample collection plate (Waters, Elstree, UK) was used to collect the final eluents (Refer to Section 3.6.2.3).

Sample sets 1,2,3

Three sets of standard samples were prepared to evaluate the assay accuracy, precision, recovery, and matrix effect. The first sample set (set 1) was prepared to evaluate the MS/MS response for the neat standards of CN128 and CP21 (IS) spiked in the LC-MS mobile phase. The second set (set 2) was prepared in the rabbit serum extracts and CN128 and CP21 (IS) spiked after extraction. The third set (set 3) was prepared in the rabbit serum, but CN128 and CP21 (IS) were spiked before extraction. The SPE elution steps and post-sample treatments were the same as those for the CN128 calibration curve standards in rabbit serum.

Set 1. The solutions were prepared using neat solutions of CN128 and CP21 in the LC-MS mobile phase. A set of stock standard solutions with concentrations 75, 40, 1.5625, 0.7813, 0.3906, 0.1953ng/mL were prepared by diluting from the 100ng/mL CN128 standard solution in the mobile phase. A stock solution of CP21 (IS, 420ng/mL) was also prepared in the mobile phase. 50μL of CN128 stock standard solution, 10μL of CP21 stock solution (both in the LC-MS mobile phase) and 40μL of 4% phosphoric acid were spiked into one single well of the 96 well plate.

Set 2. Rabbit serum (60μL) was acidified by 40μL of 4% phosphoric acid. After the MCX SPE extraction and evaporation to dryness in a Genevac EZ-2 series evaporator (Genevac Ltd, Suffolk, UK). The samples were reconstituted by spiking 50μL of CN128 stock standard solution and 10μL of CP21 stock solution (both in mobile phase and the concentrations same as in Set 1) and 40μL mobile phase into the dried well.

Set 3. The solutions were prepared by using CN128 and CP21 in the rabbit serum with concentrations the same as those in Set 1. 50μL of CN128 stock standard solution, 10μL of CP21 stock solution (both in rabbit serum) and 40μL of 4% phosphoric acid were spiked into

one single well of the 96 well plate.

QC samples

A set of QC samples using the pure standard compounds CN128 and CP21 were prepared in the rabbit serum. The sample preparation procedure and SPE were the same as that in sample Set 3. The QCL concentrations were set as 1.5625, 0.7813, 0.3906, 0.1953 ng/mL; the QCM concentration was 40 ng/mL; the QCH was 75 ng/mL.

Calibration curve standards, samples from sets 1-3 and QC samples were analysed in a Waters® Acquity UPLC-Xevo MS system in ESI+ mode. The order of injection was as follows: calibration curve standards were injected first (from a low to a high concentrations), followed by QC samples, then samples from Set 1, Sets 2 and Set 3 injected from low to high concentrations. Samples were analysed within inner-days (n=3) and intra-days (n=3). The matrix effect during the LC-MS analysis of CN128 and CP21 was assessed. In addition, precision, accuracy, linearity, limit of detection, limit of quantification of the method and recovery of analytes were also determined. Due to the batch difference of the 96-well MCX µElution plate, a fluorescent HPO compound with the same binding mechanism to the SPE sorbent was used to monitor the efficiency of the sample clean-up of the investigated HPOs.

3.7.2 Method validation

The assay was validated in accordance with the guidance of the International Conference on Harmonisation (ICH) (ICH).

Assessment of recovery (RE), matrix effect (ME) and progress efficiency (PE)

The recovery (RE) was determined by comparing the mean peak areas of CN128 and CP21 obtained in Set 3 to those in Set 2 (Equation 3.2); The matrix effect (ME) was evaluated by comparing the mean peak areas of CN128 and CP21 obtained in Set 2 to those in Set 1 (Equation 3.1); The progress efficiency (PE) was assessed by comparing the mean peak areas of CN128 and CP21 obtained in Set 3 to those in Set 1 (Equation 3.3)

ME (%) = Set 2 / Set 1 × 100 (Equation 3.1)

RE (%) = Set 3 / Set 2 × 100 (Equation 3.2)

PE (%) = Set 3 / Set 1 × 100 (Equation 3.3)

Precision and Accuracy

The precision of the method was determined by the replicate analyses (n= 9, each sample was analysed in triplicate over three consecutive days) of Set 1, 2, 3 samples containing CN128 and CP21, which was indicated by CV % of mean peak areas of CN128, CP21 and mean peak area ratio of CN128/CP21. The inner-day and intra-day precision was assessed for the CN128 calibration curve standards in rabbit serum by the triplicate analysis of each standard concentration over three consecutive days. CV % of peak areas of CN128, CP21 and peak area ratio of CN128/CP21 was used to evaluate the inner-day and intra-day precision. The accuracy of the method was evaluated by replicate analysis (n=9) of QC samples (CN128 and CP21), which was expressed by

[(Mean observed concentration) / (Nominal concentration)]× 100.

Linearity

The calibration curve was plotted as concentrations versus the response (the concentration ratio vs the peak area ratio of CN128/CP21). The goodness to fit was evaluated by its correlation coefficient and intercept value calculated in the statistical study, which was represented by linear regression equation. The slope and y-intercept values were obtained from the regression equations. The correlation coefficient (r^2) was calculated by the method of least square to confirm linearity of the regression line. In addition, an analysis of the deviation of the slopes of the regression lines was also used to evaluate the reproducibility of the method.

Limit of Detection (LOD) and Limit of Quantification (LOQ)

The detection limit was set as the dilution showing a signal-to-noise ratio of more than 3. The limit of quantification was not determined based on a signal-to-noise ratio (although this ratio exceeded 10), but was set as the lowest standard on the calibration curve that exhibits

acceptable accuracy and precision (a precision of 20% and an accuracy of 80-120%)

3.8 Screening for metabolism conversion of novel hydroxypyridinones

Serial dilutions of the standard solution of each HPO (100ng/mL) in the rabbit serum were conducted to give a set of stock standard solutions with the concentrations falling in the range 1000, 500, 250, 125, 62.5, 31.25, 15.625, 7.813, 3.906, 1.953ng/mL. A stock solution of CP21 (IS, 4200ng/mL) in the rabbit serum was also prepared. 50μL of CN128 stock standard solution, 10μL of CP21 stock solution (both in the rabbit serum) and 40μL of phosphoric acid (4%) were spiked into one single well of the 96 well plate and transferred onto the 96-well MCX μElution plate for the SPE. The SPE elution steps and post-sample treatments were the same as those using the Oasis® MCX cartridge, apart from 200μL was used instead of 1mL for the wash solvents and a Waters® Acquity UPLC 700μL round 96- well sample collection plate (Waters, Elstree, UK) was used to collect the final eluents (Refer to Section 3.6.2.3). Eighteen HPO compounds were screened for their metabolic stability using the human liver microsomes (HLMs) model. The metabolic stability results of CP20, CP94 and CP102 using the rat live microsomes (RLMs) and the HLMs were used as the control groups. The incubation procedure was detailed in the Section 3.5. The incubates were subjected to the SPE sample clean-up method developed in the Section 3.6, then introduced to the LC-MS system optimised in the Section 3.4. The results of metabolic stability were expressed as percentage of parent HPO disappearance, represented in Equation 3.4.

$$\%\ Parent\ compound\ disappearance = \left\{1 - \left[\frac{Parent\ compound\ concentration\ (Sample\ with\ microsomes)}{Parent\ compound\ concentration\ (Blank\ without\ microsomes)}\right]\right\} \times 100$$

Equation 3.4

3.9 Results and Discussion

3.9.1 Hydroxypyridinones (HPOs) investigated in the metabolism study

CP20, CP94 and CP102 were used as control groups as their metabolic profiles were well established *in vivo* (Section 2.4.1). Two chiral HPOs (CN128 and CN126), which are enantiomers, and CM1 (Pangjit et al., 2015) have been identified as new lead compounds. A group of closely related CP20 analogues (CP669, CP69, CP616, CP28, CP679, CP617) was synthesised in order to investigate whether it is possible to reduce the tendency to be extensively metabolised (Xie et al., 2016). Pegylation of iron chelators has been reported in recent years and one such chelator, deferitazole (Hider et al., 2015), has recently been successfully investigated in Phase 2 clinical trials (Neufeld et al., 2012). The advantage of polyethylene glycol (PEG) is that PEG provides favorable biological properties, good solubility in both aqueous and organic milieu, good flexibility and high hydration that increases its hydrodynamic volume(Veronese and Mero, 2008). A series of 1-, 2-, 6- substituted pegylated HPOs were sythesised and their susceptibility towards metabolism has also been investigated (Li et al., 2015a).

Table 3.1 HPOs chemical structure

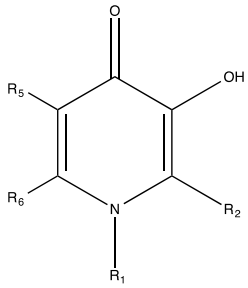

HPOs	R_1	R_2	R_5	R_6
CP20/Deferiprone	$-CH_3$	$-CH_3$	−H	−H
CP94	$-CH_2CH_3$	$-CH_2CH_3$	−H	−H
CP102	$-CH_2CH_2OH$	$-CH_2CH_3$	−H	−H
CP364	$-CH_3$	$-CH_2OH$	−H	−H
CP365	$-CH_2CH_3$	$-CH_2OHCH_3$	−H	−H
CP21	$-CH_2CH_3$	$-CH_3$	−H	−H
CN128	$-CH(C_6H_5)CH_2OH$	$-CH_3$	−H	−H
CN126	$-CH(C_6H_5)CH_2OH$	$-CH_3$	−H	−H
CM1	$-(CH_2)_6NHCOCH_3$	$-CH_3$	−H	−H
CP28	−H	$-CH_3$	−H	−H
CP679	−H	−H	$-CH_3$	−H
CP669	$-CH_3$	−H	$-CH_3$	−H
CP69	$-CH_3$	−H	−H	$-CH_3$
CP616	−H	$-CH_3$	$-CH_3$	−H
CP617	$-CH_3$	$-CH_3$	$-CH_3$	−H
C11	$-CH_2(CH_2OCH_2)_2CH_2NHCOCH_3$	$-CH_3$	−H	−H
C21	$-(CH_2)_2(CH_2OCH_2)_3(CH_2)_2NHCOCH_3$	$-CH_3$	−H	−H
6d	$-CH_2(CH_2OCH_2)_2CH_2NHCOCH_2CH_3$	$-CH_2CH_3$	−H	−H
C31	$-(CH_2)_2O(CH_2)_2OCH_3$	$-CH_3$	−H	−H
K31	$-(CH_2)_2O(CH_2)_2OH$	$-CH_3$	−H	−H
K8	$-CH_3$	$-CH_2OCH_2O(CH_2)_2OCH_3$	−H	$-CH_3$
K5	$-CH_3$	$-CH_2O(CH_2)_2O(CH_2)_2OCH_3$	−H	$-CH_3$
K7	$-CH_3$	−H	−H	$-CH_2OCH_2O(CH_2)_2OCH_3$
K6	$-CH_3$	−H	−H	$-CH_2O(CH_2)_2O(CH_2)_2OCH_3$

3.9.2 LC-MS/MS (MRM) method development

As the quantitative analysis of the parent drug metabolic stability was the major information sought, the analytical strategy selected for this analysis is to produce high throughput and therefore the analytical method should be as efficient and fast as possible. The quantitative determination of HPO compounds in the complex matrix (microsomal metabolism incubates and serum samples) requires a method with very high selectivity and sensitivity for the substance. Therefore, triple quadrupole (QqQ) was used in the Multiple Reaction Monitoring (MRM) mode with great sensitivity, selectivity and efficiency, where the precursor ion was isolated in the first quadrupole (Q1) and after fragmentation in the collision cell (Q2) a specific fragment ion is isolated in the last quadrupole (Q3), was adopted for the metabolites analysis of the HPO compounds investigated. This transition from precursor to fragment ion gives sufficient specificity and sensitivity for quantification (Kostiainen et al., 2003).

In order to obtain the optimum performance, a standard solution of the individual HPO at a concentration of 1µg/mL was introduced by direction infusion into the ESI source before the mass spectrometry. The positive ionisation mode was also selected for both HPO compounds and their metabolites, as the conjugate metabolites (glucuronides included) are usually ionised in positive ionisation with electrospray (+ESI) (Keski-Hynnila et al., 2002). The MS parameters of the instrument, such as the cone voltage, capillary voltage, desolvation temperature etc, were adjusted for the highest signal intensity of the precursor ion in the precursor ion spectrum. The subsequent optimisation of the collision energy provided the highest intensity for the main fragment product ion in the product ion spectrum.

The setting of the MRM transition channels for the monitoring of target analytes is generally selected with the consideration of the signal intensities and structure specificities of the product ions (Konstantinou, 2006). The IntelliStart^{TM} "sample tune and method development" determined the optimum cone voltage over the range of 2-100 V for the HPO. For instance, the optimum cone voltage to generate the most intense signal intensity (Figure 3.1 a) for the precursor ion of CN128 ($[M + H]^+$= 260.28) was 28 V (Figure 3.1 b). With this optimised cone

Compound Name: CN128

Transition 1: ES+, m/z 260.28 > 125.92

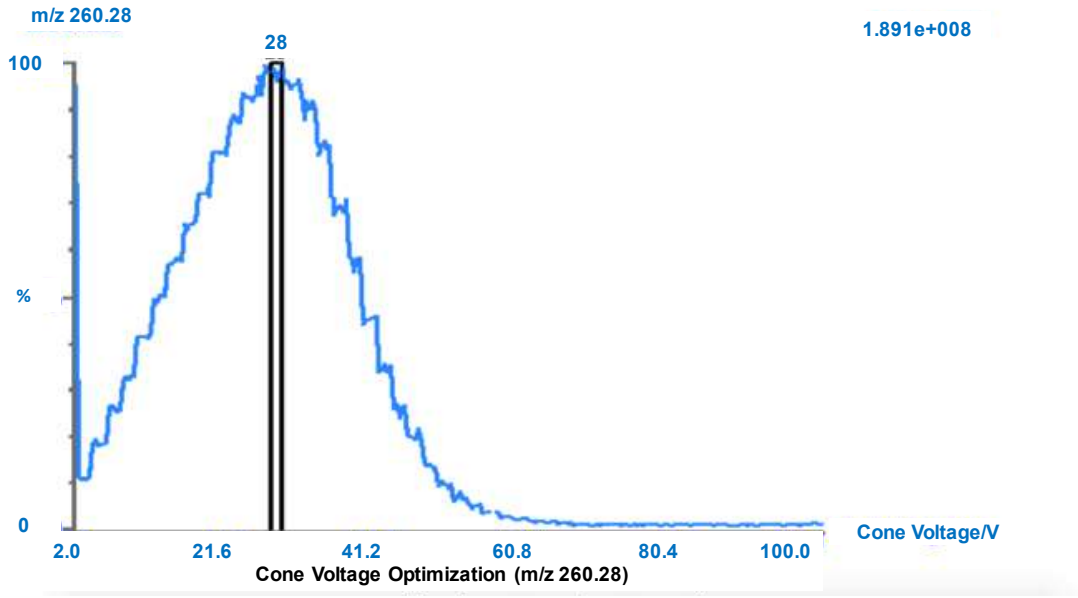

(a)

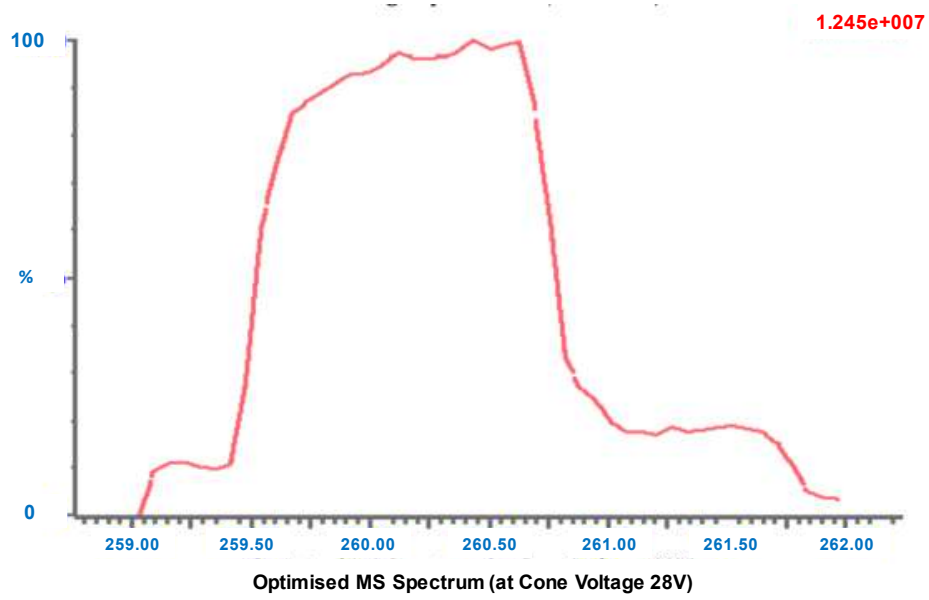

(b)

Figure 3.1 Optimisation of the cone voltage by IntelliStart™ "sample tune and method development"

(a) The plot of signal intensity of the precursor ion vs cone voltage (2-100 V)
(b) The optimised precursor ion spectrum of signal intensity vs m/z (259.02 - 262.00) at the optimum cone voltage of 28 V

voltage, the application of collision energy over the range of 2-80 induced the fragmentation of the precursor ion [M + H]+ 260.28 (Figure 3.2 a). The emerging most intense fragmented ion selected for the product ion was the ion with the m/z of 125.92 in the product ion spectrum when increasing collision energy with an optimum intensity at 18 V (Figure 3.2 b).

With the optimised MS conditions for cone and collision energy voltages, a MRM transition was generated with two characteristic ions as the precursor and the product ions. In the case of CN128 (Figure 3.1 and 3.2), the MRM transition selected was m/z 260.28 > 125.92.

The MRM transitions for each HPO compound were generated using the aforementioned method and were summarised in Table 3.2.

Compound Name: CN128

Transition 1: ES+, m/z 260.28 > 125.92

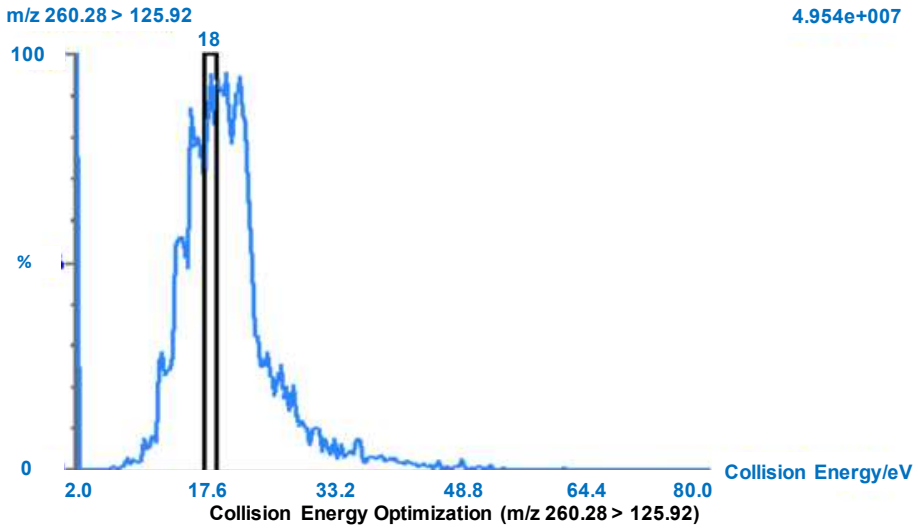

(a)

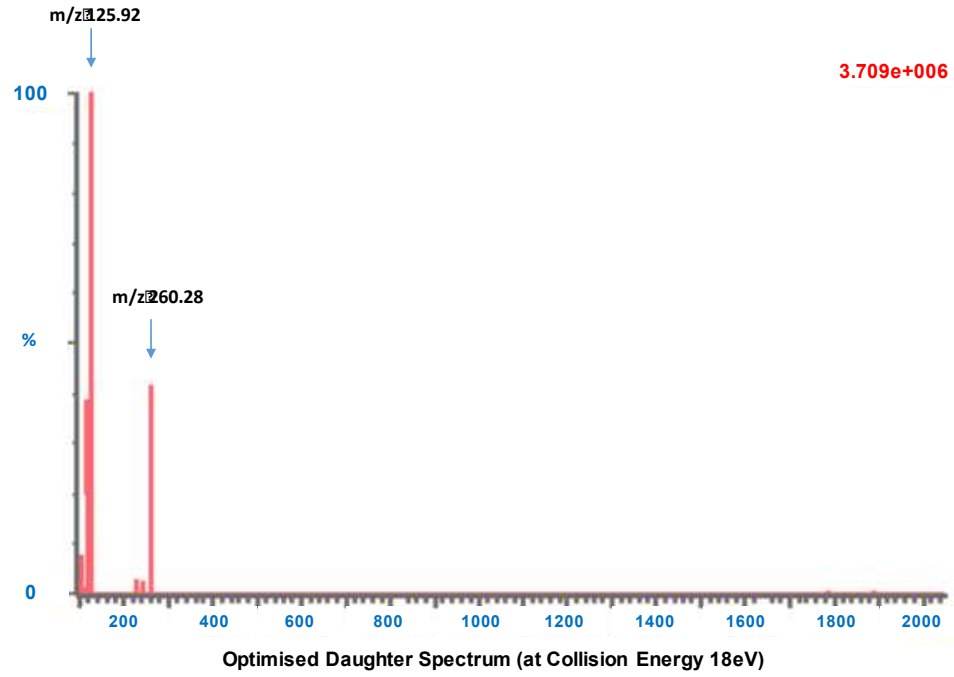

(b)

Figure 3.2 Optimisation of the collision energy voltage by IntelliStart™ "sample tune and method development"

(a) The plot of signal intensity of the product ion vs collision energy voltage (2-80 V)
(b) The optimised product ion spectrum of signal intensity vs m/z (100 - 2000) at the optimum collision energy of 18 V

Table 3.2 MRM transitions of HPOs generated by IntelliStart™

Compound	Precursor m/z	Cone Voltage (V)	Product m/z	Collision Energy (V)
CP20	140.00	18	52.97	22
	140.00	18	94.01	20
CP94	168.03	4	139.92	18
	168.03	4	152.95	18
CP102	184.09	32	124.94	22
	184.09	32	111.91	22
CP364	155.90	6	41.89	24
	155.90	6	81.89	22
CP365	183.90	6	109.91	26
	183.90	6	124.10	22
CP21	154.10	32	125.95	18
	154.10	32	138.89	18
CN128	260.28	28	125.92	18
	260.28	28	117.00	20
CN126	260.21	28	125.98	20
	260.21	28	116.99	18
CM1	267.01	6	125.91	26
	267.01	6	99.99	24
	267.01	6	54.97	28
	267.01	6	71.91	22
CP28	126.00	30	79.92	18
	126.00	30	52.95	22
	126.00	30	66.89	22
CP679	125.94	14	52.95	22
	125.94	14	72.92	16
	125.94	14	52.96	16
CP669	139.84	6	140.63	18
	139.84	6	110.03	22
	139.84	6	124.75	28
	139.84	6	106.18	26
CP69	140.03	4	66.57	22
	140.03	4	93.93	20
	140.03	4	66.96	22
	140.03	4	52.95	22
CP616	140.03	26	52.95	22
	140.03	26	93.99	18
	140.03	26	66.96	22

Compound	Precursor m/z	Cone Voltage (V)	Product m/z	Collision Energy (V)
CP669	139.97	4	66.57	18
	139.97	4	66.96	22
	139.97	4	93.93	28
	139.97	4	52.95	26
CP617	153.90	4	66.89	22
	153.90	4	108.00	20
	153.90	4	92.89	24
C11	298.97	8	125.92	32
	298.97	8	239.84	22
	298.97	8	214.00	24
	298.97	8	151.97	26
C21	370.99	8	272.05	24
	370.99	8	311.99	26
	370.99	8	125.92	40
	370.99	8	204.05	30
6d	327.35	30	271.05	22
	327.35	30	99.92	28
	327.35	30	139.84	32
C31	227.87	4	125.98	20
	227.87	4	102.93	16
	227.87	4	151.96	20
	227.87	4	200.00	16
K31	213.98	6	125.92	18
	213.98	6	151.90	18
	213.98	6	185.95	16
	213.98	6	107.94	30
K8	258.22	16	151.89	14
	258.22	16	123.95	28
	258.22	16	58.95	24
K5	271.90	4	151.90	16
	271.90	4	123.97	28
	271.90	4	108.73	46
K7	244.22	22	155.92	26
	244.22	22	137.95	18
	244.22	22	109.95	24
K6	257.89	4	109.96	24
	257.89	4	137.96	20
	257.89	4	155.87	30
	257.89	4	123.90	24

Multiple MRM transitions per analyte were applied in order to confirm the presence of the desired HPO compound (Table 3.2). To quantify the analyte in the biological samples, one transition was selected based on the comparisons between the signal intensities of the integrated peaks (Table 3.3). Therefore, other MRM transitions were just used to obtain confirmatory or qualitative information in addition to the quantitative data. The MRM transitions selected for quantification were also analysed by the ChemDraw software. The fragment pathways for each MRM transition could be analysed to determine whether the fragmentated ion was stable and specific to the precursor ion.

Table 3.3 The MRM transition selected for quantification

Compound	Parent m/z	Cone Voltage	Daughters	Collision Energy
CP20	140.00	18	52.97	22
CP94	168.03	4	139.92	18
CP102	184.09	32	124.94	22
CP364	155.90	6	41.89	24
CP365	183.90	6	109.91	26
CP21	154.10	32	125.95	18
CN128	260.28	28	125.92	18
CN126	260.21	28	125.98	20
CM1	267.01	6	54.97	28
CP28	126.00	30	52.95	18
CP679	125.94	14	52.95	22
CP669	139.97	4	52.95	26
CP69	140.03	4	52.95	22
CP616	140.03	26	52.95	22
CP617	153.90	4	66.89	22
C11	298.97	8	125.92	32
C21	370.99	8	125.92	40
6d	327.35	30	271.05	22
C31	227.87	4	125.98	20

Compound	Parent m/z	Cone Voltage	Daughters	Collision Energy
K31	213.98	6	125.92	18
K8	258.22	16	123.95	28
K5	271.90	4	151.90	16
K7	244.22	22	109.95	24
K6	257.89	4	137.96	20

Two examples of fragmentation pathways analysed by the ChemDraw software are illustrated in Figure 3.3 and 3.4, the collision energy applied in the ESI-MS/MS (MRM) induced the cleavage of the heteroatom-carbon bond. The charge was stabilised on the heteroatom cleaved moiety, fragmented ion mass was the m/z of precursor ion $[M + H]^+$ minus the leaving group plus two mass unite (two protons), which obeyed the "+2" rule of ESI-MS-MS fragmentation pattern(Weissberg and Dagan, 2011). The cleavage occurred possibly at the C-N bond of CN128 precursor ion with a m/z of 260.31 and produce a fragmented ion with a m/z of 126.13, which correspond to the MRM transition 260.28 > 125.92 generated by IntelliStart™ (Table 3.3). The same fragmentation pattern was also observed on the pegylated HPO (K31), which followed the pathway of 214.24 > 126.13 and corresponded to the MRM transition 213.98 > 125.92 developed by IntelliStart™ (Table 3.3).

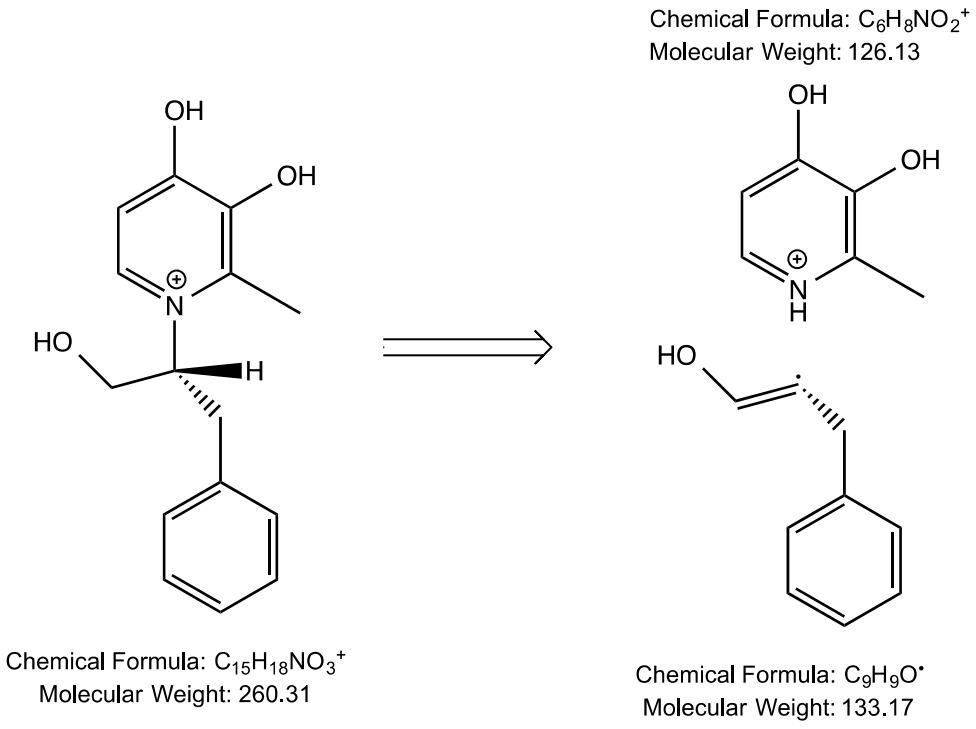

Figure 3.3 The fragmentation pathway of CN128
Precursor ion > Product ion: 260.31 > 126.13

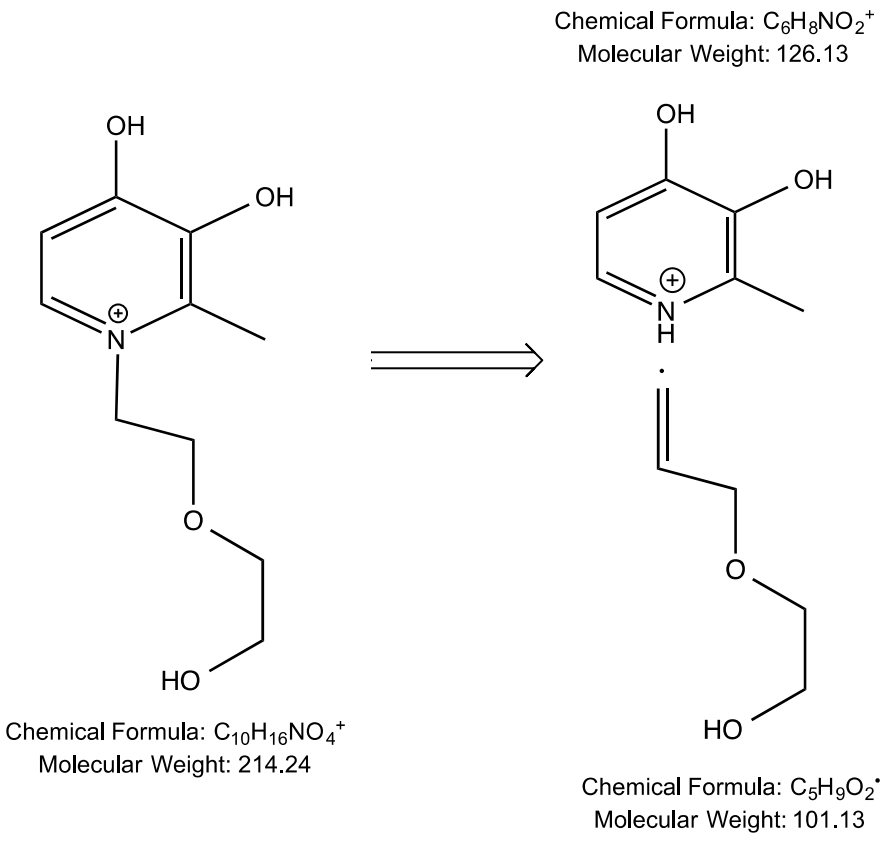

Figure 3.4 The fragmentation pathway of K31
Precursor ion > Product ion: 214.24 > 126.13

By monitoring the specific MRM transition in Table 3.3, each HPO compound investigated was identified and integrated (Appendix V), the metabolic conversion of the parent HPO compound was evaluated by quantifying the percentage of parent drug elimination over the time-course of the *in vitro* microsomal incubation (Section 3.8). The accurate quantitative determination of the HPO compound using LC/ESI/MRM in the biological sample is essential for studying their metabolic profile. However, it could be hampered by interferences from the in-source fragmentation or the fragmentation occurred in the collision cell of their biotransformation metabolites (Korfmacher, 2005). Glucuronides are the metabolite class that is most commonly labile to the in-source fragmentation in the ESI source (Yan et al., 2003). In addition, in the MS/MS (MRM mode), Q1 and Q3 are set at the selected m/z values for glucuronide and its parent molecule respectively to detect the glucuronide (Trontelj, 2012). Thereby, an increase in the signal of the parent ion will occur, which causes the over-estimation of the parent drug. In consequence, an adequate chromatographic separation of the glucuronic conjugate from its parent drug is essential (Jemal and Xia, 1999). Because most of the investigated HPO parent compounds are hydrophilic (Table 3.4, milogP values), they are prone to co-elute with their metabolites at the beginning of the chromatography. Consequently, a volatile ion-paring agent, which is compatible with the MS conditions, was added in the mobile phases. A perfluorinated carboxylic acid, pentadecafluorooctanoic acid (PFOA) was selected (Gao et al., 2006), in order to increase the retention time of the analytes and thereby achieve a good separation.

Table 3.4 The pKa and milogP values of HPO

	p*K*a$_1$	p*K*a$_2$	miLogP		p*K*a$_1$	p*K*a$_2$	miLogP		p*K*a$_1$	p*K*a$_2$	miLogP
CP20	3.65	9.76	-0.60	CP28	3.64	9.73	-0.56	C11	3.39	9.74	-1.67
CP94	3.81	9.93	0.35	CP679	3.31	9.49	0.33	C31	3.42	9.80	-0.82
CP102	3.37	9.80	-0.66	CP669	3.31	9.34	0.56	K31	3.43	9.75	-1.34
CP364	3.06	9.19	-1.25	CP69	3.64	9.13	-0.28	K5	3.26	9.33	-0.49
CP365	3.15	8.93	-0.64	CP616	3.43	10.27	0.55	K7	3.20	8.63	-0.54
CP21	3.65	9.88	-0.23	CP617	3.37	10.32	0.78	K6	3.19	8.67	-0.71
CN128	3.26	9.90	0.56					C31	3.42	9.80	-0.82
CN126	3.26	9.90	0.56								
CM1	3.52	9.80	0.10								

p*K*a$_1$ carbonyl group, p*K*a$_2$ hydroxyl group (Chen, 2013), milogP (Molinspiration, 2015)

In positive ESI mode, an abundant fragment [M + H − 176]+ was detected in most cases after glucuronide fragmentation. The neutral loss of 176 Da corresponds to a monodehydrated glucuronic acid. Therefore, the MRM transitions set for HPO-glucuronides were $[M + H - 176]^+ > [M + H]^+$ for the conjugate which the glucuronide acid moiety directly bound to the nucleophilic site on the HPO aglycon. Since both Phase I and Phase II substrates were incubated in the microsomes. The conjugation could also occur at the functional group introduced from Phase I reaction, such as oxidation. Hence, another MRM transition was set as $[M + H + 16 - 176]^+ > [M + H]^+$ to identify the glucuronides of the mono-hydroxylated HPO (Figure 3.5).

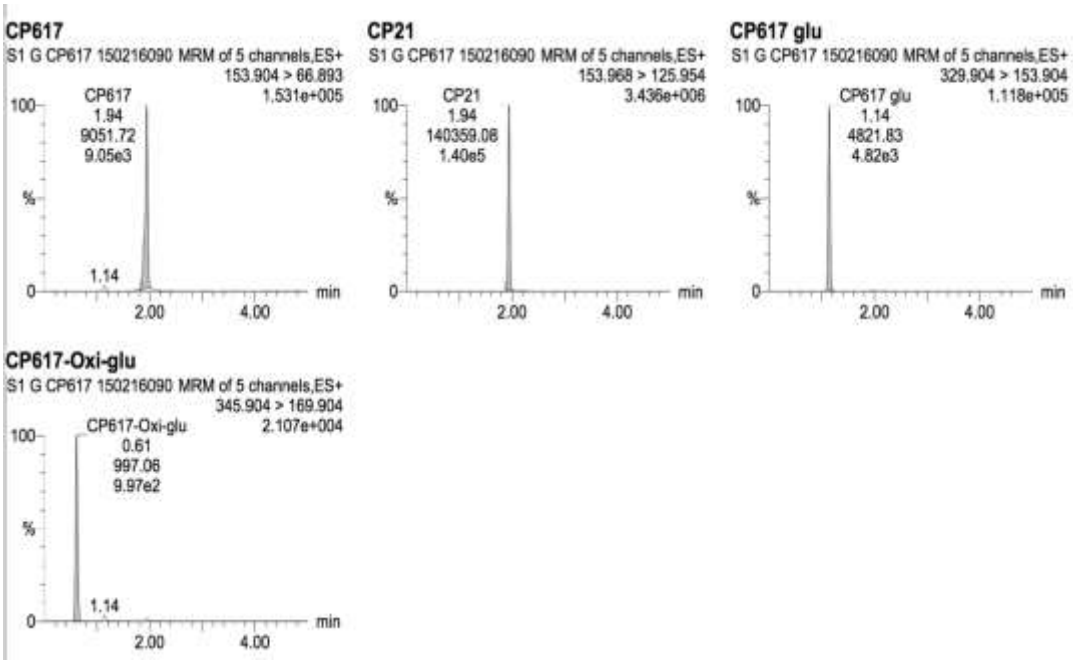

Figure 3.5 MRM chromatographs of CP617 Phase I+II microsomal incubate

3.9.3 Sample clean-up method (SPE) development

The biological matrix components in rabbit serum (mainly phospholipids) and microsomal incubation matrix (microsomal proteins), co-elute with the target analytes and impact the MS response, particularly affecting the efficiency and reproducibility of the electrospray ionisation process (Chambers et al., 2007). In addition, the microsomal incubation media is a chemical complex, in which buffer is also suspected as the main cause for ionisation suppression due to its high concentration and high ionic strength (Zheng et al., 2002).

The main goal to develop a sample clean-up method is to achieve the elimination of matrix components in order to reduce ion suppression during LC-MS analysis, to decrease method variability, to increase sample detection sensitivity and to improve the reproducibility of the further LC-MS analytical system performance (Waters, 2015). The analytes of interest, such as HPO parent compounds and their possible metabolites in sample solutions can bind to the solid phase sorbent with a greater affinity than the matrix components. Thus, the matrix components are washed away. A stronger elution solvent is then used to elute the analytes from the sorbent and collect them for further LC- MS analysis (Trontelj, 2012).

The retention of the possible metabolites on a solid phase sorbent can be facilitated by a number of mechanisms, from reverse phase to ion exchange, depending on the ionisation and lipophilic properties of the parent compounds(Roškar and Lušin, 2012).

The predicted log partition coefficient values (milogP) of HPOs are presented in Table 3.4, and indicate the lipophilicity of the investigated HPOs (Molinspiration, 2015). Negative milogP values of the pegylated HPOs and most of the CP20 analogues indicate that they are all relatively hydrophilic. Consequently, the ion exchange sorbent is preferred over the reversed phase as the mechanism of retention for the sample clean-up by the SPE. The ionisable functional groups of HPO parent compounds and their possible metabolites can interact with the ion exchange sorbent at controlled pH conditions. The elution procedure during SPE using an ion exchange sorbent includes a rigorous washing step with a strong solvent (such as 100%

methanol, Section 3.6.2.3) in order to elute the phospholipids in the serum sample and proteins in the microsomal incubates, without any detrimental effect on the recovery of analytes of interest. Buffer in the microsomal media, which is soluble in water, is also washed away from the SPE sorbent by aqueous solutions. Thus, minimal matrix effects can be achieved by such stepwise elution.

The investigated HPOs contain two ionisable functional groups, the 3-hydroxyl and 4-carbonyl group, with two p*K*a values (Table 3.4, Figure 3.6). The p*K*a values of 4-carbonyl falls between 3.06 ~ 3.81(pKa_1), while the p*K*a values of the 3-hydroxyl group falls in the range 8.67~10.32 (pKa_2). The presence of the acidic carboxylic group on glucuronic moiety has a p*K*a value (pKa_3) around 3 (Farrell et al., 2011). Therefore, at the pH value ≤ 1 or ≥ 12, the HPO compounds and their metabolites will be completely ionised (protonated or deprotonated respectively) and will possess a positive or a negative net charge respectively (Figure 3.6).

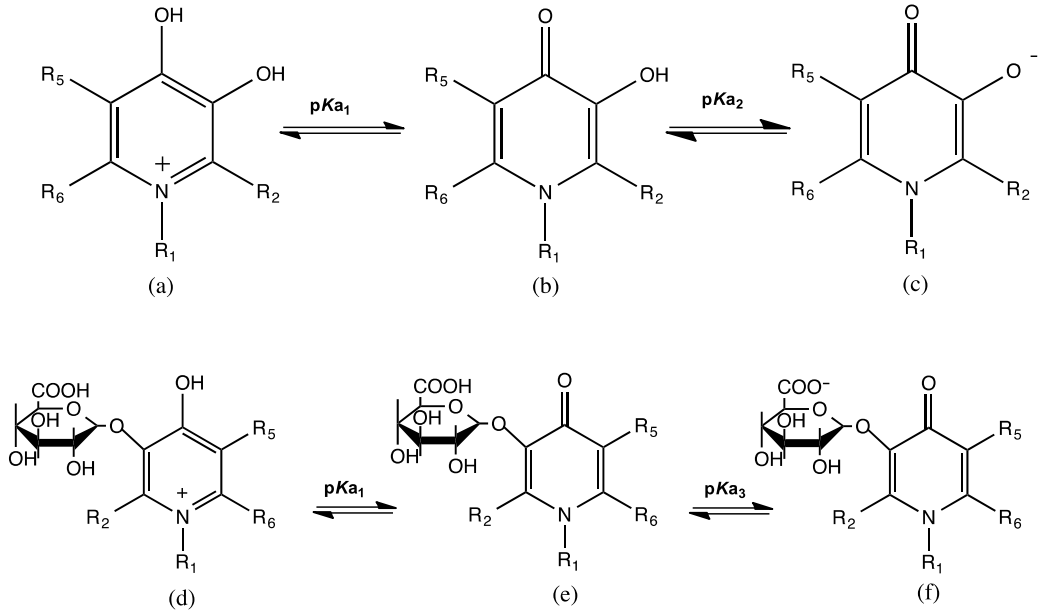

Figure 3.6 The protonation equilibria for HPOs
pKa_1 carbonyl group (3.06~3.81), pKa_2 hydroxyl group (8.67~10.32), pKa_3 carboxylic group (~3)

Four kinds of ion exchange sorbents are available from the Waters Oasis® SPE products (Waters, 2015). The Mixed-mode Weak Cation-eXchange (WCX) sorbent with a carboxylic acid ion-exchange functional group (p*K*a = 5), which is deprotonated at pH ≥ 7 and possess a negative charge (Figure 3.7 a). However, the net charge of most HPOs is neutral over the pH range 7 to10 and partially negatively charged over the pH range 10 to12 (Figure 3.6 b and c). The glucuronide possesses a negative net charge at pH ≥ 7 (Figure 3.6 f). Therefore the WCX is not applicable for the retention of the analytes of interest.

The Mixed-mode Weak Anion-eXchange (WAX) sorbent with a piperazine ion exchange functional group (p*K*a = 6) is be protonated at pH ≤ 4 and contain one positive charge (Figure 3.7 b). The HPO compounds and their glucuronides are partially positively charged when pH ≤ 4 and completely protonated at pH ≤ 1 (Figure 3.6 a and d). Hence, the WAX sorbent is also not feasible for the extraction of the investigated compounds.

At pH 1, the carbonyl group of the parent HPOs is protonated (Figure 3.6 a). The carboxylic group on glucuronic moiety and the carbonyl group of the HPO-glucuronide are also protonated (Figure 3.6 d). Consequently, The Mixed-mode Cation-eXchange (MCX) sorbent with the negatively charged sulfonic acid functional group (p*K*a<1) (Figure 3.7 c) will provide a strong cation-exchange interaction with the positively charged nitrogen atom of the parent HPOs and their glucuronide conjugates.

At pH 12, the hydroxyl group of the parent HPOs is deprotonated (Figure 3.6 c). The carboxylic group on glucuronic moiety of the HPO glucuronide is also deprotonated (Figure 3.6 f). Hence, the positively charged quaternary-amine functional group on the Mixed-mode Anion-eXchange (MAX) sorbent (Figure 3.7 d) can offer strong anion-exchange interaction with the negatively charged deprotonated functional groups of the parent HPOs and their glucuronide conjugates.

Based on the above analysis, the MAX and MCX sorbents were selected for investigating the extraction efficiency of the microsomal incubates containing the HPOs and their metabolites.

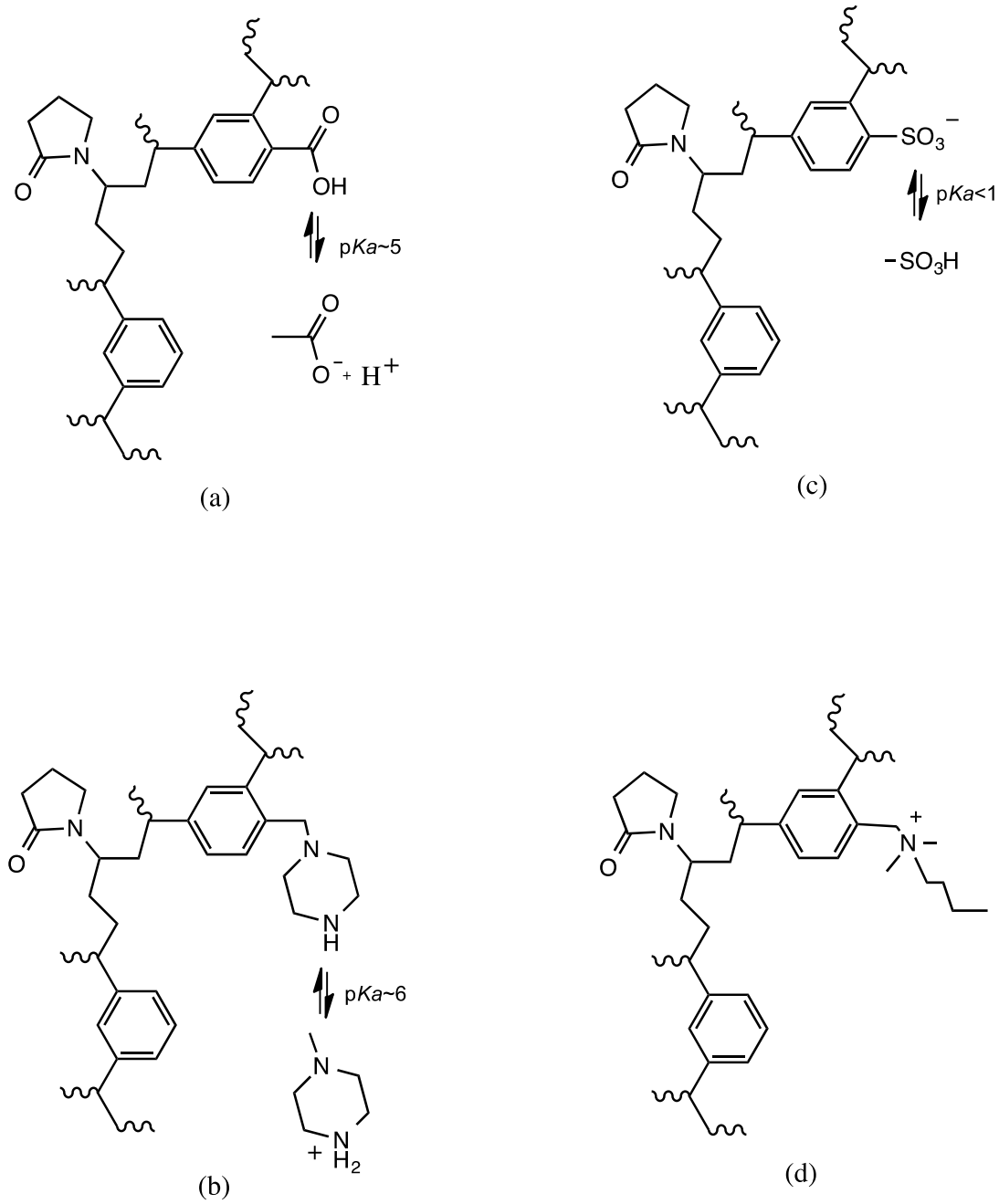

Figure 3.7 Four Oasis® ion-exchange SPE sorbents
Modified from Waters Oasis® sample extraction products brochure(Waters, 2015)
(a) WCX (b) WAX (c) MCX (d) MAX

The SPE procedures of the MCX and the MAX sorbents were detailed in in Section 3.6.2. Prior to SPE, the biological samples (the rabbit serum solutions and microsomal incubates) were pre-treated with acidified or basified diluent for two purposes. Firstly, it is used to ionise the functional groups of the analytes, which interact with the ion exchange sorbents. Secondly, at those pH conditions, the ionisation states of amino acid side chains were altered, thereby changing protein charge distributions and hydrogen-bonding requirements, causing protein precipitation and aggregation (Voet et al., 2013). The pre-treated samples were then subjected to the SPE elution steps. The initial washing step using 2% formic acid (MCX) or 5% ammonium hydroxide (MAX) was used to ionise the functional group on the sorbent so as to enable the ion-exchange interaction between the ionised analytes and the sorbent. The following rigorous washing step with 100% methanol was an essential step to eliminate the endogenous phospholipids in the rabbit serum and microsomal proteins, which could cause ion suppression when subjected to the LC-MS analysis. The final washing step with 5% ammonium hydroxide (MCX) or 2% formic acid (MAX) in methanol was used to convert the electrical polarity of the analytes bound to the sorbents by changing the pH, thus the analytes of interest were no longer bound by the sorbents. The final eluent, containing the clean-uped analytes, was collected, evaporated and reconstituted in the relevant mobile phase before being subjected to the LC-MS analysis

The efficiency of the SPE sample clean-up by the MAX and MCX sorbents was assessed by comparing the signal response of the targeted compounds and the cleanliness of the matrix background of the SPE eluents of CP20 Phase I+II microsomal incubates, when subjected to the LC-MS analysis. A UPLC system with a reverse phase analytical column was employed to separate the possible metabolites from the parent compound CP20 in the SPE eluents by employing a linear gradient elution with the ion pairing agent in the mobile phases (Section 3.4.1). The triple quadruple (QqQ) MS system using the MRM scanning mode was employed for the parent drug CP20 and its metabolite detection in the SPE eluents (Section 3.4.3, 3.9.2). The MRM chromatographs (ion signal intensity vs time) with specific MRM transitions demonstrated that the targeted compounds were present in the SPE eluents of CP20 Phase I+II microsomal incubates. The identification of the parent compound CP20 and the 2-methyl hydroxylated

metabolite of CP20 was facilitated by applying the specific MS fragmentation pathway (MRM) established by the direct infusion of the authentic chemical synthesised standards CP20 and CP364 (Section 3.4.3, 3.9.2). Although the authentic standards of HPO glucuronides could not be obtained, the abundant fragmentation [M + H − 176]+ of a glucuronide in the ESI positive mode in most cases offered evidence to set the MRM transition for the CP20 glucuronide metabolite as a loss of mass 176 (Section 3.9.2). Hence, the MRM transition was set as m/z 316>140.

The MRM chromatographs of the CP20 Phase I+II microsomal incubate MAX SPE eluent in Figure 3.8 illustrated that the glucuronide conjugate of CP20 eluted at 0.96 min at the MRM trace 316>140 (a); the 2-methyl hydroxylated CP20 (CP364) was not extracted efficiently at the MRM transition 155.90 > 41.89 (b), while the parent compound CP20 eluted at 2.20 min at the MRM trace 139.996>52.969 (c).

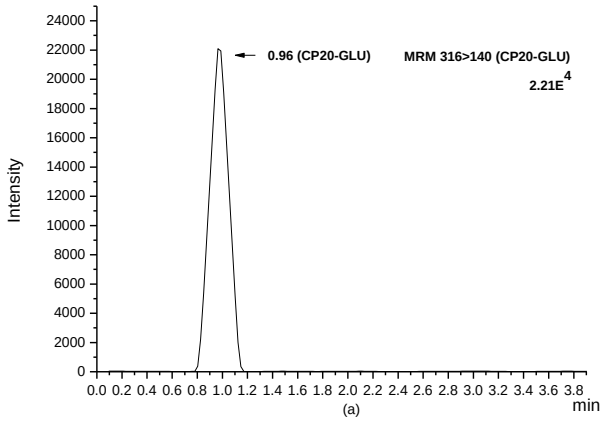

Figure 3.8 The MRM chromatographs of the MAX SPE eluent of CP20 Phase I+II microsomal incubation
(ion signal intensity vs time (min))
(a) The MRM trace 316>140 (CP20-GLU)

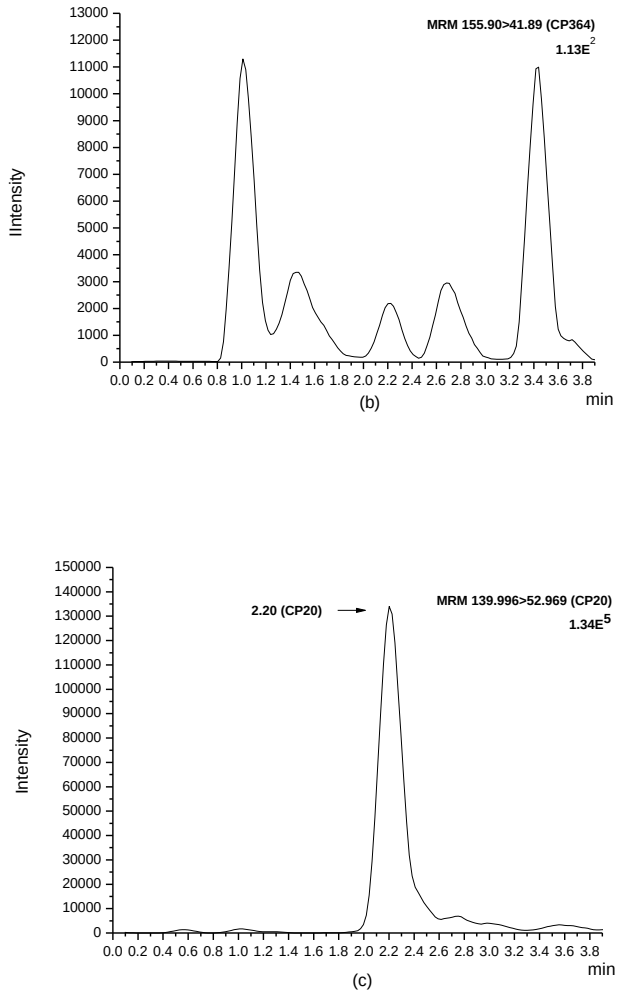

Figure 3.8 The MRM chromatographs of the MAX SPE eluent of CP20 Phase I+II microsomal incubation
(ion signal intensity vs time (min))
(b) The MRM trace 155.90 > 41.89 (CP364) (c) The MRM trace139.996>52.969 (CP20)

The MRM chromatographs of the CP20 Phase I+II microsomal incubate MCX SPE eluent in Figure 3.9 demonstrated that the glucuronide conjugate of CP20 was found to elute at 0.99 min at the MRM trace 316>140 (a); the 2-methyl hydroxylated CP20 was also extracted and eluted at 1.63 min (b). The parent compound CP20 eluted at 2.25 min at the MRM trace 139.996>52.969 (c).

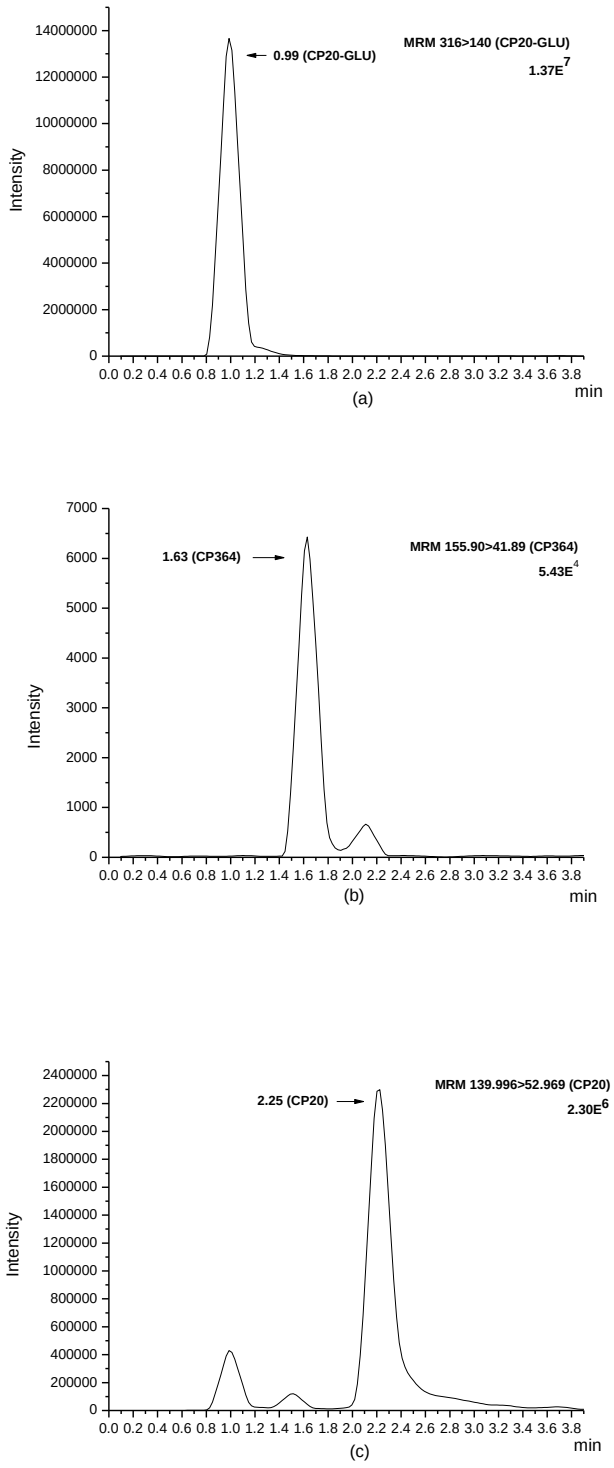

Figure 3.9 The MRM chromatographs of the MCX SPE eluent of CP20 Phase I+II microsomal incubation

(ion signal intensity vs time (min))

The MRM trace 316>140 (CP20-GLU) (b) The MRM trace 155.90 > 41.89 (CP364) (c) The MRM trace139.996>52.969 (CP20)

The MRM chromatographs (Figure 3.8, 3.9) demonstrated good chromatographic separation of the 2-methyl hydroxylated metabolites and glucuronide from the parent molecule CP20. In addition, a clean background was achieved after sample clean-up using both the MAX and the MCX SPE procedures, which indicated that most of the matrix components have been washed away during the SPE procedures. By comparison of the signal response of investigated compounds after the MAX and MCX SPE clean-up. The signal intensity of the CP20 glucuronide after the MCX clean-up was three magnitudes higher than that after the MAX clean-up; $1.37x10^7$ compared with $2.21x10^4$. The signal intensity of the CP20 after the MCX clean-up was one magnitude higher than that after the MAX clean-up; $2.30x10^6$ compared with $1.34x10^5$. The MCX SPE also extracted the 2-methyl hydroxylated CP20 efficiently, while the MAX SPE failed to retain it. Thus, the MCX SPE has a higher recovery of CP20 and its glucuronide and hydroxylated metabolites compared to the MAX SPE, and is therefore a more suitable sample clean-up mechanism for the HPO microsomal incubates. Based on the results of the sorbent comparison study above, the MCX SPE was selected as the optimal ion exchange sorbent to develop the clean-up procedure of the Phase I+II microsomal incubates of CP20.

The percentage of the HPO parent compound elimination after microsomal incubation was used to assess the metabolic stability of the parent compound and the concentrations of the parent compound before and after microsomal incubation was obtained from a calibration curve conducted with a series of same HPO standards in rabbit serum (Section 3.8). Thus, a suitable sample clean-up method was also required for calibration standard samples in the rabbit serum. A calibration of with CP20 standards (1.95 to 1000 ng/mL) in the rabbit serum was assessed to develop the calibration standard sample clean-up method (Section 3.6.2.1, Figure 3.10). The MCX SPE elution was applied for the sample clean-up and subjected to the LC/MS (Figure 3.11).

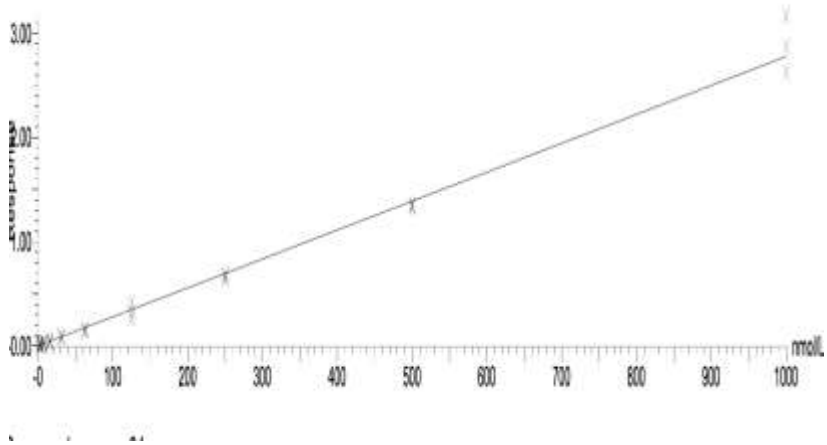

Figure 3.10 The calibration curve of the MCX SPE eluents of standards CP20 in rabbit serum
(peak area ratio of CP20/CP21 vs Concentrations).

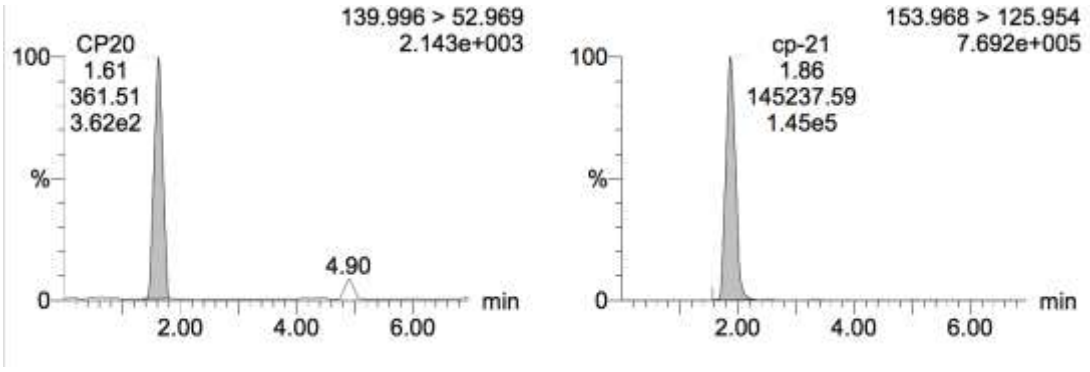

(a)

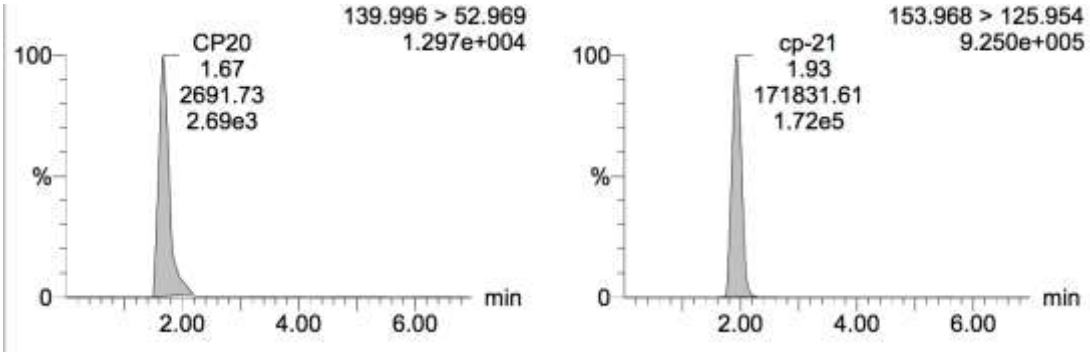

(b)

Figure 3.11 The MRM chromatographs of the MCX SPE eluents of standards CP20 and IS (CP21, 210 ng/mL) in the rabbit serum
(a) CP20 0.098 ng/mL, (b) CP20 31.25 ng/mL

A structural analogue of the investigated HPOs, CP21, was used as the internal standard (IS) in the calibration curve standard rabbit serum samples and was also included in the microsomal incubates in the metabolic stability screen of the investigated HPOs. It was added to the biological matrix prior to the extraction procedure to correct for any variations occurring during the SPE extraction, chromatography separation and the mass spectrometric detection (Rosenfeld, 2009). The concentration of the CP21 was 210 ng/mL, which was between 1/3 and 1/2 of the ULOQ of the analyte, at which concentration, the MS sensitivity could achieve a high S/N with the high sensitivity (Xu and Madden, 2012). On the other hand, the IS concentration was not so high that the peak area ratios of CP20/CP21 for the lower concentrations standards were too low (Figure 3.11 a). A good chromatographic separation of CP20 from CP21 was achieved at the MRM transitions 139.996 > 52.969 and 153.968 > 125.954, illustrated in the MRM chromatographs (Figure 3.11). In addition, The MCX SPE offered an efficient sample clean-up as a neat background was obtained.

In summary, the MCX was selected as the sorbent chemistry for the sample clean-up of the CP20 microsomal incubates and the CP20 calibration curve standards in the rabbit serum samples. The other investigated HPOs and their metabolites have the similar chemical physiological properties (Table 3.4, Figure 3.6), which share the same ionisation pattern at acidic pH when interacting with the ion-exchange MCX sorbent, therefore, the MCX sorbent was also selected as the clean-up method for the microsomal incubates and the calibration curve standards in the rabbit serum samples of other HPOs in this study. Furthermore, in order to enhance the throughput in the labor-intensive screening of the HPOs metabolic stability, the MCX µElution SPE plate format was adopted instead of the SPE cartridge format.

3.9.4 Validation of the bio-analytical method

The established LC-MS/MS (MRM) assay (Section 3.4) with the SPE sample clean-up treatment (Section 3.6) has been proposed to be an efficient quantitative bio-analysis with a high throughput, due to the high sensitivity and selectivity of MRM mode and the elimination of matrix effect impact by the sample clean-up procedures. Hence, the matrix effect, recovery,

precision, accuracy, linearity, limit of detection and limit of quantification were assessed for this bio-analytical method. One of the investigated HPO compounds CN128 and the internal standard CP21 was selected for the method validation (Section 3.9.1, Table 3.1). Rabbit serum was chosen as the biological matrix instead of human liver microsomes for the cost-effectiveness. The assay was validated in accordance with the guidance of the International Conference on Harmonisation (ICH) (ICH).

Matrix effect, Recovery and Process efficiency

The co-eluting matrix components may reduce or enhance the ion intensities of the analytes and affect the reproducibility and accuracy of the assay (Matuszewski et al., 2003). Thus three sets of samples were investigated to determine the matrix effect, recovery of the sample from SPE extraction, process efficiency of the assay, with reference to Section 3.7.1 (Sample sets 1,2,3) and Section 3.7.2 (Equation 3.1, 3.2, 3.3) respectively, in the triplicate analysis over three successive days.

The matrix effect was examined by comparing the MS/MS (MRM) response (mean peak area) of CN128 or CP21 at the given concentrations spiked post-extraction into the serum extract (Set 2) to the MS/MS (MRM) response of the same analyte prepared in the LC-MS mobile phase (Set 1) multiplied by 100. An example of the MRM chromatograph of sample Set 1 is illustrated in Figure 3.12 a, b; CN128 or CP21 eluted at identical retention times with different ion intensities among the three sets of samples examined. The mean values of the matrix effect were 97% and 94% for CN128 and CP21 respectively (Table 3.5, Columns G and H). A value of 100% indicates that the response in the plasma extracts (Set 2) and the neat mobile phase (Set 1) is the same and no potential matrix effect is observed. Thus, a value of > 100% indicates ionisation enhancement, and a value of < 100% indicates ionisation suppression. Hence the mean values of matrix effect of CN128 and CP21 have indicated that very small ion suppression was observed under the SPE and LC-MS/MS conditions.

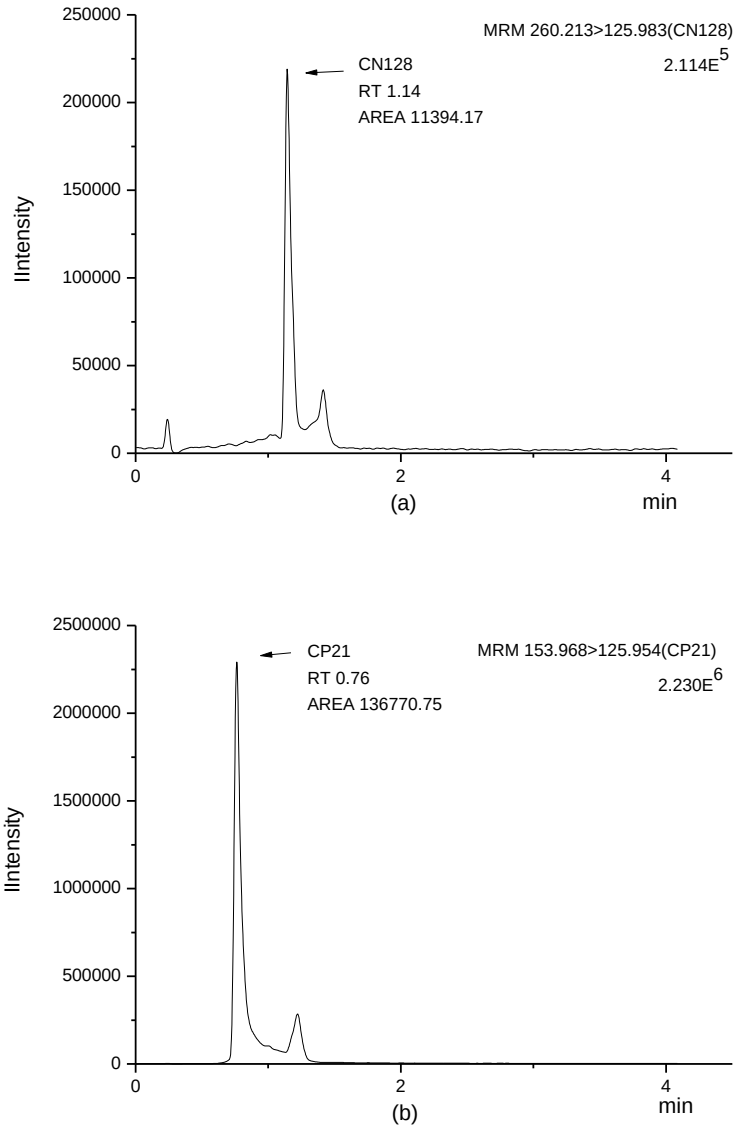

Figure 3.12 The MRM chromatographs of the MCX SPE elutent of Set 1
(ion signal intensity vs time (min))
(a) The MRM trace 260.213>125.983 (CN128) (b) The MRM trace 153.968 > 125.954 (CP21)

Table 3.5 Matrix Effect (ME), Recovery (RE) and Process Efficiency (PE)

Norminal Conc. (ng/mL)	Mean Peak Area (x104, n=9)						ME[a] (%)		RE[b] (%)		PE[c] (%)	
	CN128			CP21								
	Set 1	Set 2	Set 3	Set 1	Set 2	Set 3	CN128	CP21	CN128	CP21	CN128	CP21
0.0977	0.7	0.7	0.7	16.4	15.4	14.5	94	94	94	94	94	89
0.1953	1.2	1.1	1.1	16.2	16.0	13.8	99	86	94	86	94	85
0.3906	2.1	2.0	1.9	14.2	14.1	13.6	99	96	90	96	90	96
0.7815	3.9	3.7	3.8	14.8	14.5	13.9	98	96	98	96	98	94
20	104.7	103.1	98.8	15.5	14.5	13.6	93	93	94	94	94	88
37.5	168.0	166.9	154.4	15.7	15.6	15.1	99	97	92	97	92	96
Mean							97	94	94	94	94	89
%RSD							2.8	4.3	2.8	4.3	2.8	5.1
Column	**A**	**B**	**C**	**D**	**E**	**F**	**G**	**H**	**I**	**J**	**K**	**L**

[a] Matrix effect: The ratio of the MS/MS (MRM) response (mean peak area) of CN128 or CP21 at the given concentrations spiked post-extraction into the serum extract (Set 2) to the MS/MS (MRM) response (mean peak area) of the same analyte prepared in the LC-MS mobile phase (Set 1) multiplied by 100.
[b] Recovery: The ratio of the MS/MS (MRM) response (mean peak area) of CN128 or CP21 at the given concentrations spiked pre-extraction into the serum extract (Set 3) to the MS/MS (MRM) response (mean peak area) of the same analyte spiked post-extraction into the serum extract (Set 2) multiplied by 100.
[c] Process efficiency: The ratio of the MS/MS (MRM) response (mean peak area) of CN128 or CP21 at the given concentrations spiked pre-extraction into the serum extract (Set 3) to the MS/MS (MRM) response (mean peak area) of the same analyte prepared in the LC-MS mobile phase (Set 1) multiplied by 100.

The recovery of CN128 and CP21 extracted from the rabbit serum using the developed SPE method (Section 3.6) was assessed by determining the ratio of the MS/MS (MRM) response (mean peak area) of CN128 or CP21 at the given concentrations spiked pre-extraction into the serum extract (Set 3) to the MS/MS (MRM) response (mean peak area) of the same analyte spiked post-extraction into the serum extract (Set 2) multiplied by 100. The recovery values for CN128 and CP21 were both 94% (Table 3.5, Columns I and J), which have represented good recovery of the SPE method used for sample extraction.

The progress efficiency was also included to evaluate the efficiency of the SPE extraction for CN128 and CP21 in rabbit serum. By comparing the MS/MS (MRM) response (mean peak area) of CN128 or CP21 spiked into the rabbit serum, followed by extraction, reconstitution in the LC-MS mobile phase, and LC-MS analysis with the corresponding peak areas of the same compound analysed directly in the mobile phase, the efficiency of the SPE extraction procedure can be determined. Owing to the observed small ionisation suppression for both CN128 and

CP21 due to the matrix effect (97% and 94%, respectively, Table 3.5, columns G and H), the process efficiency values (Set 3 / Set 1 × 100) were ≤ 100 (94% and 89%, respectively, Table 3.5, columns K and L). The value of the process efficiency has indicated a reliable and efficient extraction method developed for sample clean-up.

The low % RSD values (Table 3.5, Columns G to L), which are typically less than about 5%, have demonstrated only small variations among the matrix effect, recovery and progress efficiency assessed at the investigated concentrations for both CN128 and CP21, which indicates the reproducibility and robust of the method.

Precision and accuracy

Precision of the bio-analysis of Sample Set 1, Set 2 and Set 3 was evaluated in the triplicate analysis over three successive days, which was expressed as the coefficient of variation (%) in determining peak areas of CN128, peak areas of CP21 and peak area ratios (CN128/CP21) for each sample set. The precision values (CV, %) obtained for peak areas of CN128, peak areas of CP21 and peak area ratios of CN128/CP21 for Sample set 1 were ranging from 2.5-5.5%, 4.2-5.4% and 3.5-5.1% respectively (Table 3.6, Columns A, D, G); for Sample set 2 fell in the range 4.6-12.4%, 6.7-13.5% and 6.7-11.8% respectively (Table 3.6, Columns B, E, H); for Sample set 3 were within the range of 5.8-10.7%, 5.9-10.4% and 5.6-11.3% respectively (Table 3.6, Columns C, F, I). The precision value determined for these sample sets at each concentration was less than 15%, and consequently achieved the precision acceptance criteria based on the ICH guideline and indicates the reliability of the established bio-analysis method. The accuracy of the method was assessed by the quality control sample (QCs) from triplicate analysis over three successive days. The high QC concentration (QCH) should be in the upper quartile of the calibration curve. The mid QC concentration (QCM) is near the middle (~ 50%) of the calibration range (Li et al., 2013). Hence, the QCH was set at the concentration of 75 ng/mL and the QCM concentration was selected at 40 ng/mL, according to the calibration curve standard concentration range investigated 0.1953 ~ 100 ng/mL. Four low concentrations (1.5625, 0.7813, 0.3906, 0.1953 ng/mL) at the low concentration range of the calibration curve were selected as the QCL sample. The accuracy values were expressed as [(mean observed

concentration)/ (nominal concentration)] × 100. The accuracy values (%) of the QC samples ranging from 90-107% (Table 3.6, column J) were less than 15% variation of their corresponding nominal concentration, which satisfies the accuracy acceptance criteria according to the ICH guideline.

Table 3.6 Precision (CV, %) of determining peak areas of CN128, peak areas of CP21 and peak area ratios (CN128/CP21) in Sample Set 1, Set 2 and Set 3 and Accuracy (%) determined from QC samples.

	Precision (CV, %, n=9)									
Nominal Conc. (ng/mL)	Peak area CN128			Peak area CP21			Peak area ratio CN128/CP21			Accuracy (%)[d]
	Set 1[a]	Set 2[b]	Set 3[c]	Set 1[a]	Set 2[b]	Set 3[c]	Set 1[a]	Set 2[b]	Set 3[c]	
0.0977	5.5	7.9	9.5	4.5	6.9	10.4	3.5	7.5	10.6	95
0.1953	5.3	7.9	10.7	5.4	6.7	9.9	5.1	7.6	7.1	90
0.3906	4.9	6.3	8.7	4.8	7.2	8.5	4.5	6.8	6.5	97
0.7815	4.5	12.4	5.9	4.2	9.7	6.7	4.0	10.5	11.3	105
20	3.8	4.9	6.7	4.6	8.4	5.9	3.5	6.7	5.6	107
37.5	2.5	4.6	5.8	4.5	13.5	6.5	3.7	11.8	10.6	101
0.0977	5.5	7.9	9.5	4.5	6.9	10.4	3.5	7.5	10.6	95
Column	**A**	**B**	**C**	**D**	**E**	**F**	**G**	**H**	**I**	**J**

[a] in neat LC-MS mobile phases. [b] CN128 and CP21 spiked post-extraction into the serum extract. [c] CN128 and CP21 spiked pre-extraction into the serum extract. [d] Determined from QC samples, expressed as [(mean observed concentration)/ (nominal concentration)] × 100, observed concentrations were calculated from the calibration curves

The inter-day and the intra-day precision were determined as the coefficient of variation of the triplicate analysis of calibration curve standards (Section 3.7.1, Calibration curve standards). The precision values (CV, %) obtained for peak areas of CN128, peak areas of CP21 and peak area ratios of CN128/CP21 at each concentration of the inter-day analysis fell in the range 1.2-11.1%, 2.0-15.0% and 1.2-14.2% respectively (Table 3.7, Columns A, B, C); of the intra-day analysis was within the range of 1.5-11.7%, 1.7-9.3% and 1.4-14.4% respectively (Table 3.7, Columns D, E, F). According to the ICH guideline, the acceptance criteria for method precision is ≤15%. Thus, the precision values determined for the triplicate analysis of calibration curve standards over three days validation demonstrate the robustness and reproducibility of the developed method.

Table 3.7 Inter-day and intra-day precision

Nominal Conc. (ng/mL)	Inter-day (CV, %, n=3)			Intra-day (CV, %, n=3)		
	Peak area CN128	Peak area CP21	Peak area ratio CN128/ CP21	Peak area CN128	Peak area CP21	Peak area ratio CN128/ CP21
0.0977	1.7	2.0	2.9	3.2	1.7	3.6
0.1953	3.9	8.0	14.2	11.1	4.2	1.9
0.3906	6.0	15.0	9.7	9.4	8.5	11.1
0.7813	9.5	11.7	5.7	11.7	8.3	14.4
1.5625	6.4	12.8	6.4	4.1	7.9	4.6
3.125	11.1	14.5	5.5	8.5	9.2	3.2
6.25	10.4	10.0	2.2	8.0	7.4	1.4
12.5	1.2	8.5	7.5	1.5	9.3	7.8
25	10.3	10.0	1.2	8.3	8.3	4.2
50	2.7	7.6	5.0	2.9	6.5	4.6
Columns	**A**	**B**	**C**	**D**	**E**	**F**

Linearity

Good linearity was obtained for the calibration curves plotted within inter-day (n=3) and intra-day (n=3) validation, which was assessed by the correlation coefficient r^2 values of 0.991377, 0.980759 and 0. 988663 (Table 3.8, Column C, Figure 3.13). The % RSD of the mean slope values of the calibration curves was 4.5% (Table 3.8, column A). The %RSD values demonstrated only small variations during the inner-day and intra-day validation and implied that the overall system performance was robust, reproducible and reliable.

Table 3.8 Linearity of the calibration curve

Day	Slope (Mean, n=3)	Intercept (Mean, n=3)	Regression Coefficient (r^2)
1	0.357586	0.0136156	0.991377
2	0.327511	0.0180073	0.980759
3	0.337598	0.0165789	0.988663
Mean	0.340898		
%RSD	4.5		
column	**A**	**B**	**C**

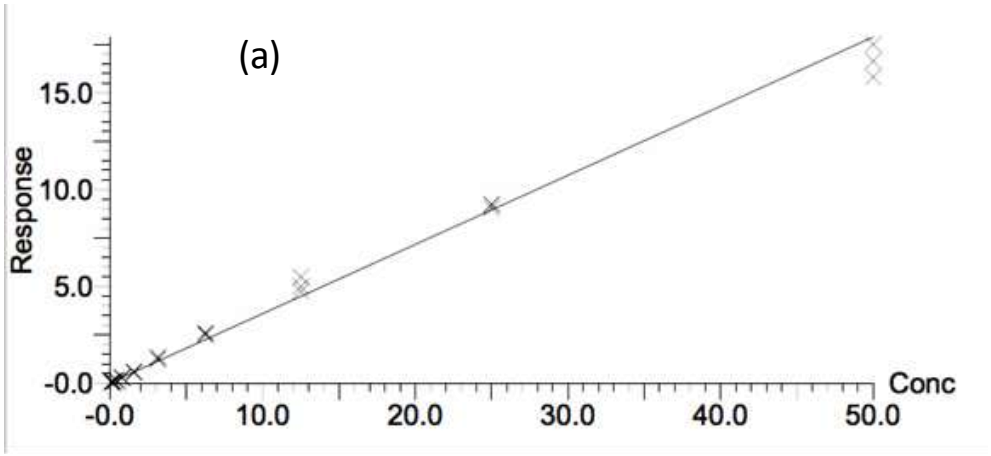

(a) Day 1 validation: Calibration curve Y = 0.357586 X + 0.01361; Curve type: Linear; Weighting 1/x

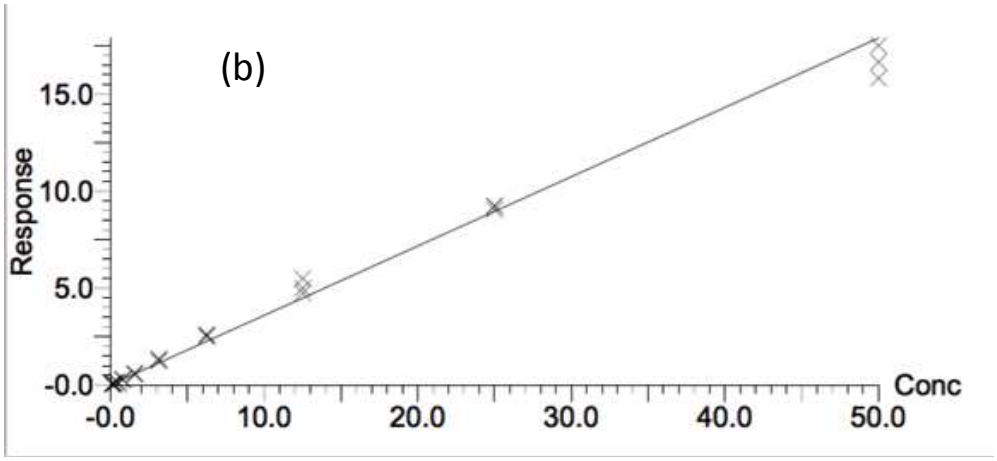

(b) Day 2 validation: Calibration curve Y = 0.327511 X + 0.0180073; Curve type: Linear; Weighting 1/x

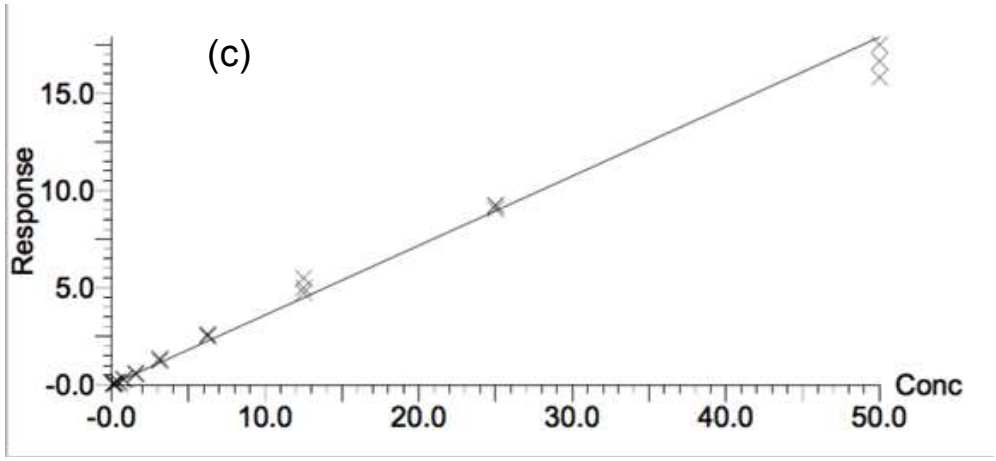

(c) Day 3 validation: Calibration curve Y = 0.337598 X + 0.0165789; Curve type: Linear; Weighting 1/x

Figure 3.13: Calibration curve of the MRM response
Mean peak area ratios of CN128/CP21 vs Concentrations (Three days method validation).

Limit of Detection (LOD) and Limit of Quantification (LOQ)

As defined in Section 3.7.2, LOD is set as the concentration showing a signal-to-noise ratio of more than 3, which was 0.02931 ng/mL for the developed method. LOQ was set as the lowest standard concentration on the calibration curve that exhibits acceptable precision and accuracy (a precision of 20% and an accuracy of 80-120%). The precision determined for the triplicate analysis of calibration curve standards over three days validation at the concentrations of calibration standards were all less than 15% and with the accuracy ranging between 90-107% as discussed before. Thus the LOQ is the lowest standard concentration of CN128, which is 0.0977 ng/mL.

3.9.5 Screening for metabolic conversion of novel HPO compounds

3.9.5.1 Metabolic conversion of CP20/deferiprone, CP94 and CP102

As previously discussed, the extensive glucuronidation pathway of CP20/deferiprone and CP94 observed in humans result in limited iron chelation efficacy. Particularly the formation of glucuronide at the 3-hydroxyl group will inactivate the pharmacological activity. Therefore, a series of 3-hydroxypyridin-4-one compounds with modifications on the ring substitution has been screened for their metabolic profiles in the liver microsomal incubations in order to select the alternative candidate compound for CP20/deferiprone.

The percentages of Phase I and Phase I+II metabolism biotransformation have been evaluated for 18 novel HPO compounds (Section 3.9.1, Table 3.1). The reactions were incubated in the presence of human liver microsomes together with the cofactors: NADPH (the cofactor for CYPs-dependent metabolism) and UDPGA (the cofactor for UGTs-dependent glucuronidation) (Section 3.5). The sample clean-up and LC-MS analysis utilised the methods discussed in the previous sections (Section 3.9.2 and 3.9.3). The percentages of metabolism biotransformation for CP20/deferiprone, CP94 and CP102 have been assessed in both rat and human liver microsomes, which were used as control groups, as their metabolism profiles have been previously subjected to extensive investigation (For chemical structures, refer to Section 3.9.1,

Table 3.1). CP20/deferiprone is substantially metabolised by both rat and human liver microsomes, fortified with both NADPH and UDPGA. The percentages of CP20/deferiprone metabolised after Phase I+II microsomal incubation were found to be 46% and 90% respectively, suggesting extensive loss of the parent compound by glucuronidation conjugation (Figure 3.14, Table 3.9 Row A and B). In contrast, CP20/deferiprone was moderately metabolised by both rat and human microsomes in the presence of NADPH (Phase I cofactor). The percentages of CP20/deferiprone metabolised under these conditions were 19% and 25% respectively (Figure 3.14, Table 3.9 Row A and B). The metabolic pathway of CP20 is illustrated in Scheme 3.1.

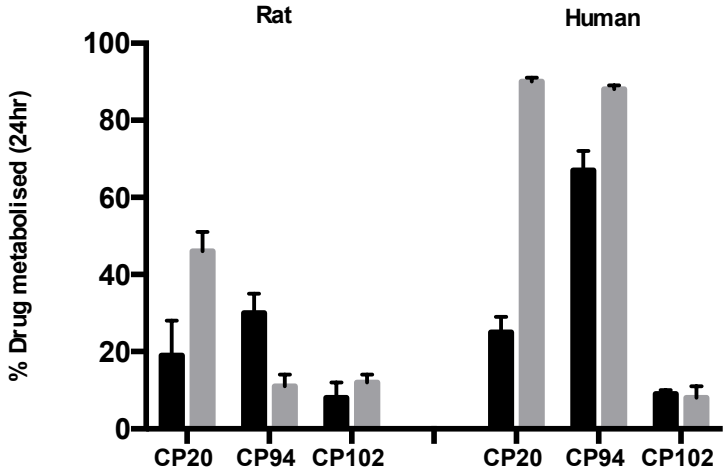

Figure 3.14 Metabolic conversions of CP20, CP94, and CP102 in human and rat liver microsomes
Black: Phase I; Grey: Phase I+II

Table 3.9 Metabolic conversions of CP20, CP94, CP102 in human and rat liver microsomes

	% Drug metabolised (24 hr) (Mean ± SD, n=3)		
HPOs	**Phase I**	**Phase I+II**	**Row**
CP20/deferiprone RLMs	19 ± 9	46 ± 5	A
CP20/deferiprone HLMs	25 ± 4	90 ± 1	B
CP94 RLMs	30 ± 5	11 ± 3	C
CP94 HLMs	67 ± 5	88 ± 1	D
CP102 RLMs	8 ± 4	12 ± 2	E
CP102 HLMs	9 ± 1	8 ± 3	F

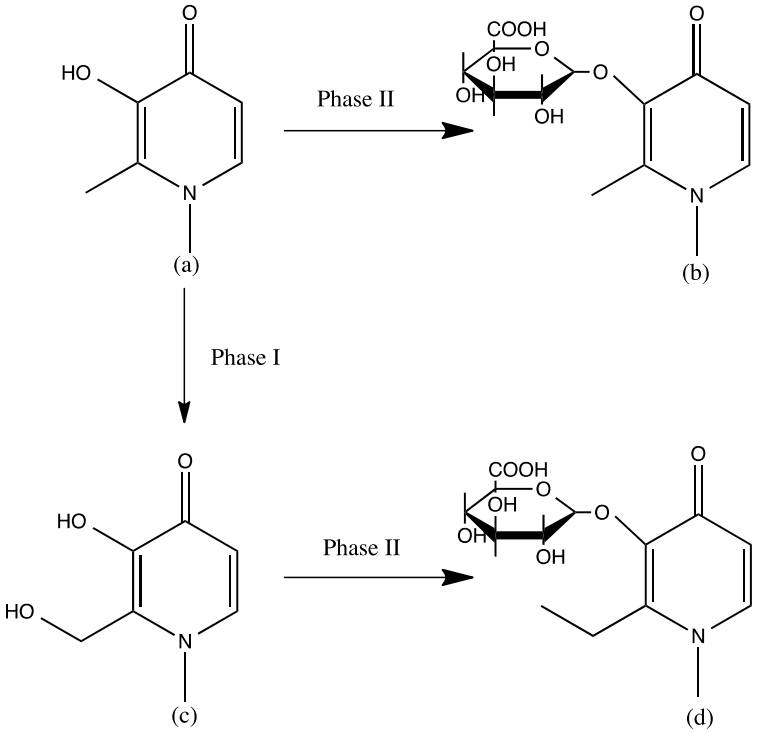

Scheme 3.1 Metabolic pathways of CP20

(a) CP20;
(b) 3-O- glucuronide conjugate of CP20;
(c) CP20-2-hydroxymethyl metabolite;
(d) Glucuronide conjugate of CP20-2-hydroxymethyl metabolite.

The Phase I metabolism pathway represents the major route of metabolism for CP94, when the incubation was performed in rat liver microsomes (Scheme 3.2). The percentage of CP94 elimination in the Phase I reaction was 30% compared with 11% in the Phase I+II reaction (Figure 3.14, Table 3.9 Row C). CP94 was found to undergo extensive glucuronidation conjugation in human liver microsomes; only 12% of the parent compound remained intact after Phase I+II incubation reaction (Figure 3.14, Table 3.9 Row D). The Phase I metabolic pathway of CP94 has led to considerable conversion of the parent compound (67%, Table 3.9 Row D), which indicates that the extensive glucuronidation occurs on the hydrophilic site introduced by Phase I metabolic pathway. This metabolic pathway is shown in Scheme 3.2. CP102 has previously been demonstrated to be resistant to both Phase I and Phase II (glucuronidation) (Singh et al., 1996). This was confirmed in this study where the percentages of parent compound conversion in both Phase I and Phase I+II were minor, 8% and 12% respectively in rat liver microsomes and 9% and 8% respectively in human liver microsomes (Figure 3.14, Table 3.9 Row E and F). In summary, the metabolic profiles for CP20/deferiprone, CP94 and CP102 reported in this work were in a good agreement with the previous studies (Section 2.4.1). These findings further suggest that the system developed in this work to screen the metabolic conversion of a series of novel HPO compounds is both reliable and robust.

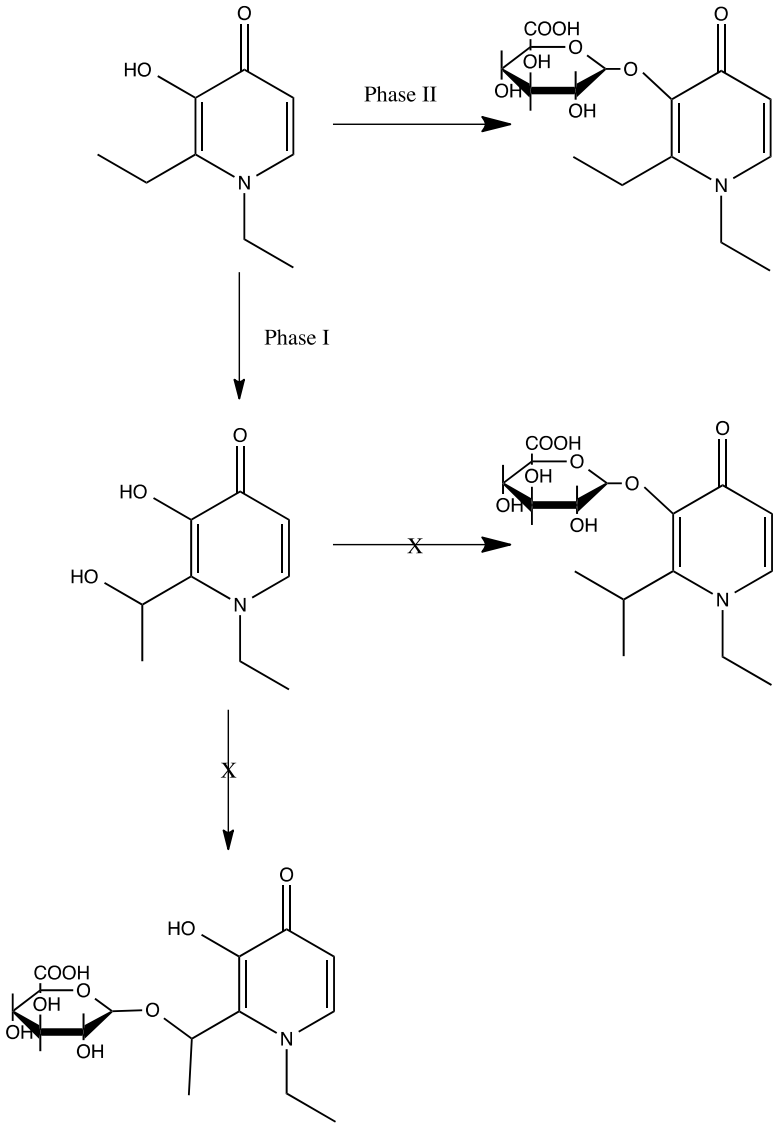

Scheme 3.2 Metabolic pathways of CP94

(a) CP94;
(b) 3-O- glucuronide conjugate of CP94 (the major metabolite in man);
(c) CP94-2-(1'-hydroxyethyl) metabolite (the major metabolite in rat)

3.9.5.2 Metabolic conversion of CN128 and CN126

CN128 and CN126 are two enantiomers of a chiral HPO compound, (R) and (S)-3-hydroxy-1-(1-hydroxy-3-phenylpropanyl)-2-methylpyridin-4(1H)-one (For chemical structures, refer to Section 3.9.1, Table 3.1, p74). It has been reviewed that metabolising enzymes often display a preference for one enantiomer of a chiral drug over the other, resulting in enantioselectivity (Lu, 2007). The enantioselective metabolism has been reported with both the CYP-mediated and UGT-mediated Phase I and II metabolism respectively (Sten et al., 2006, Kaminsky and Zhang, 1997). Consequently, although these two enantiomers share essentially the same physicochemical properties, their interaction with metabolising enzymes could be different at the binding step and/or at the catalytic step, resulting in different affinities and/or reactivities, which could produce metabolites distinguished in nature and/or extent (Lu, 2007). Indeed, CN128 and CN126 were found to display enantioselective metabolism profiles (Figure 3.15 and Table 3.10). The two enantiomers are eliminated to different degrees, when mediated by CYPs and UGTs enzymes, in both Phase I and Phase II reactions. CN126 was substantially metabolised to a higher extent compared with CN128, 89 % and 38 % (Figure 3.15, Table 3.10, Rows E and D). The extent of parent drug glucuronidation of CN126 in human liver microsomes was almost identical to that of CP20/deferiprone and CP94, 90% and 88% respectively (Table 3.10, Rows A and B). Glucuronidation of CN128 indicates that it is much more resistant to UGTs when compared with its enantiomer CN126, CP20/deferiprone and CP94, implying better chelation efficacy. With respect to the CYP-mediated Phase I reaction, the metabolism has also displayed a preference for one enantiomer over the other; where CN128 was found to be metabolised by 18% as compared to 31% for CN126 (Figure 3.15, Table 3.10, Rows D and E). The possible pathway of metabolic biotransformation is presented in Scheme 3.3. The metabolic pathway of CN126 is listed in Appendix VI-I. In consequence, the (R)-enantiomer HPO, CN128, has displayed reduced metabolic elimination when compared with the (S)-enantiomer CN126.

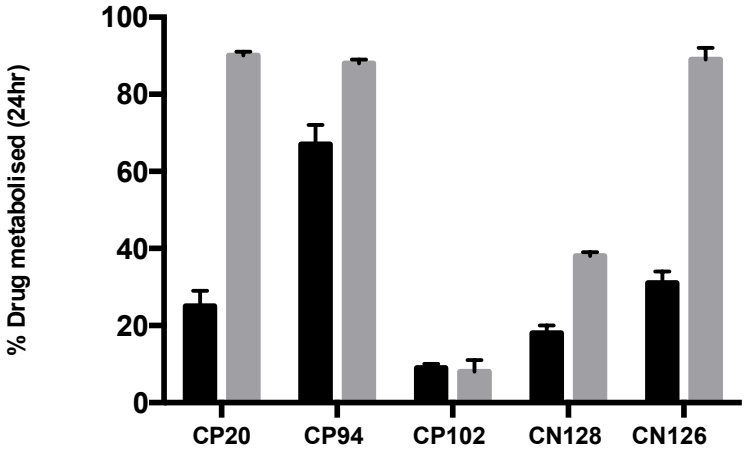

Figure 3.15 Metabolic conversions of CN128, CN126 in human liver microsomes
Metabolic conversions of CP20/deferiprone, CP94, CP102 in human liver microsomes were taken from Figure 3.14
Black: Phase I; Grey: Phase I+II

Table 3.10 Metabolic conversions of CN128, CN126 in human liver microsomes
Metabolic conversions of CP20/deferiprone, CP94, CP102 in human liver microsomes were taken from Table 3.9

	% Drug metabolised (24 hr) (Mean ± SD, n=3) in HLMs		
HPOs	**Phase I**	**Phase I+II**	**Row**
CP20/deferiprone	25 ± 4	90 ± 1	A
CP94	67 ± 5	88 ± 1	B
CP102	9 ± 1	8 ± 3	C
CN128	18 ± 2	38 ± 1	D
CN126	31 ± 3	89 ± 3	E

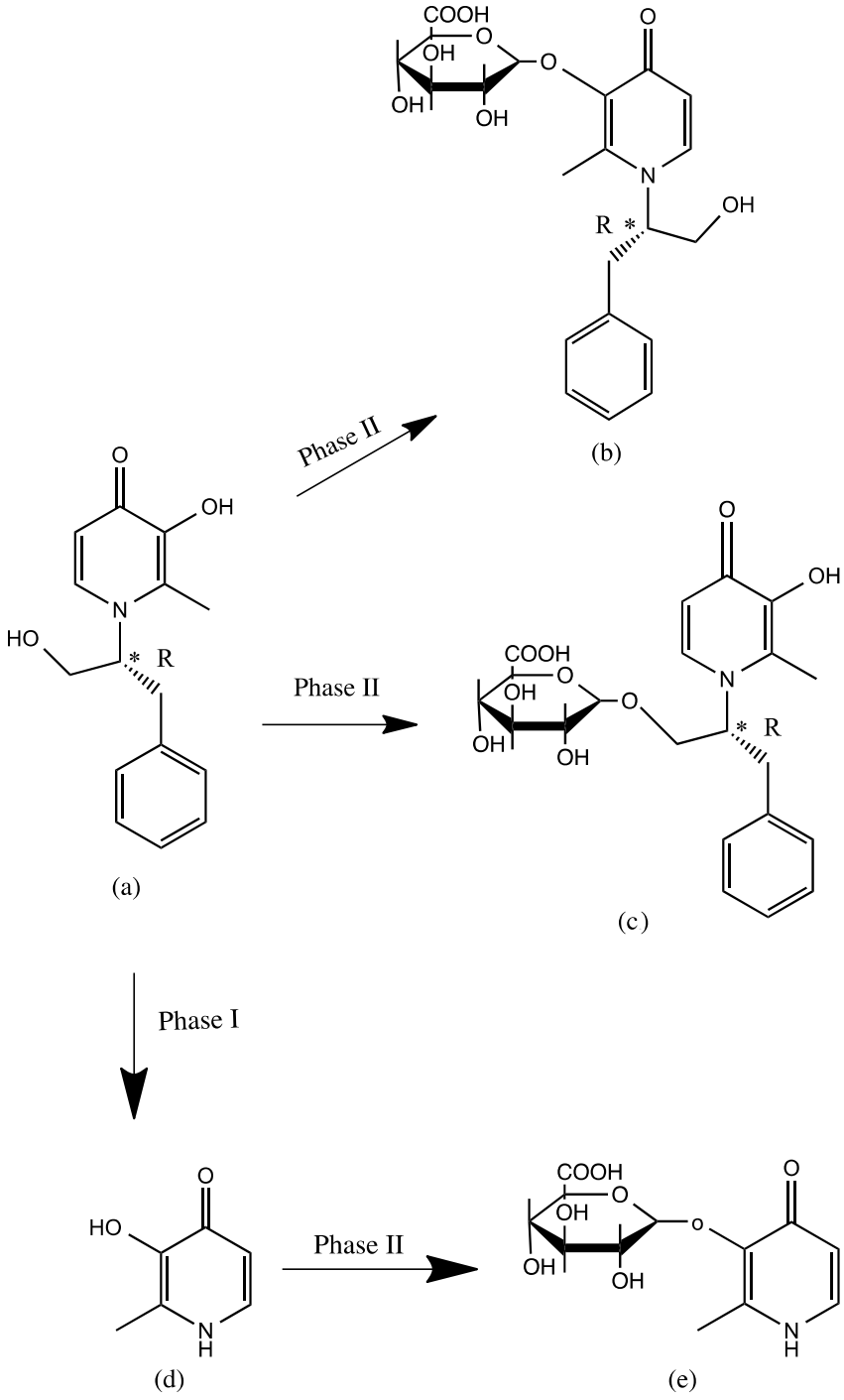

Scheme 3.3 Metabolic pathways of CN128

(a) CN128;
(b) 3-O-glucuronide conjugate of CN128;
(c) CN128-1-(1-O-glucuronide) conjugate;
(d) N-dealkylated metabolite of CN128;
(e) 3-O-glucuronide conjugate of N-dealkylated metabolite of CN128

3.9.5.3 Metabolic conversion of CM1

Another novel HPO compound, CM1, with the ω-acetamido-6-alkyl substituent at the position-1 of the hydroxypyridinone ring has also been investigated for its *in vitro* metabolic clearance during human liver microsomal incubation (For chemical structures, refer to Section 3.9.1, Table 3.1, p74). The percentage of parent compound elimination by UGTs metabolising enzyme was less than those of CP20/deferiprone and CP94, 69% compared with 90% and 88% (Figure 3.16, Table 3.11, Rows D, A and B). The extent of Phase I metabolism reaction was minor, only 4% of the parent drug was converted by the CYP enzymes (Figure 3.16, Table 3.11 Row D). The probable metabolic pathway is illustrated in Scheme 3.4.

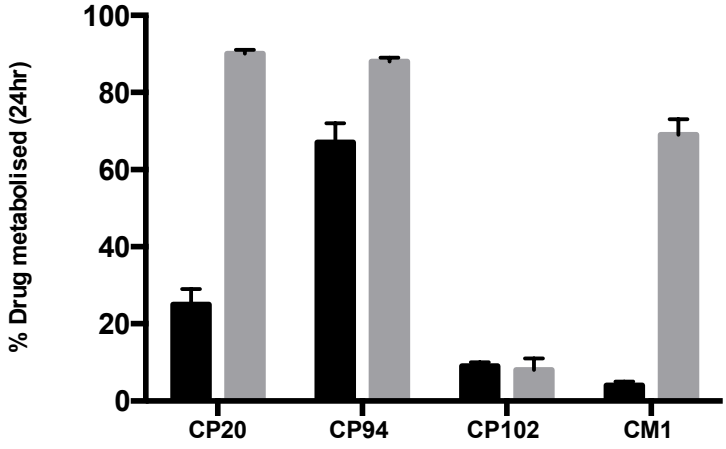

Figure 3.16 Metabolic conversion of CM1 in human liver microsomes
Metabolic conversions of CP20/deferiprone, CP94, CP102 in human liver microsomes were taken from Figure 3.14
Black: Phase I; Grey: Phase I+II

Table 3.11 Metabolic conversion of CM1 in human liver microsomes
Metabolic conversions of CP20/deferiprone, CP94, CP102 in human liver microsomes were taken from Table 3.9

	% Drug metabolised (24 hr) (Mean ± SD, n=3) in HLMs		
HPOs	**Phase I**	**Phase I+II**	**Row**
CP20/deferiprone	25 ± 4	90 ± 1	A
CP94	67 ± 5	88 ± 1	B
CP102	9 ± 1	8 ± 3	C
CM1	4 ± 1	69 ± 4	D

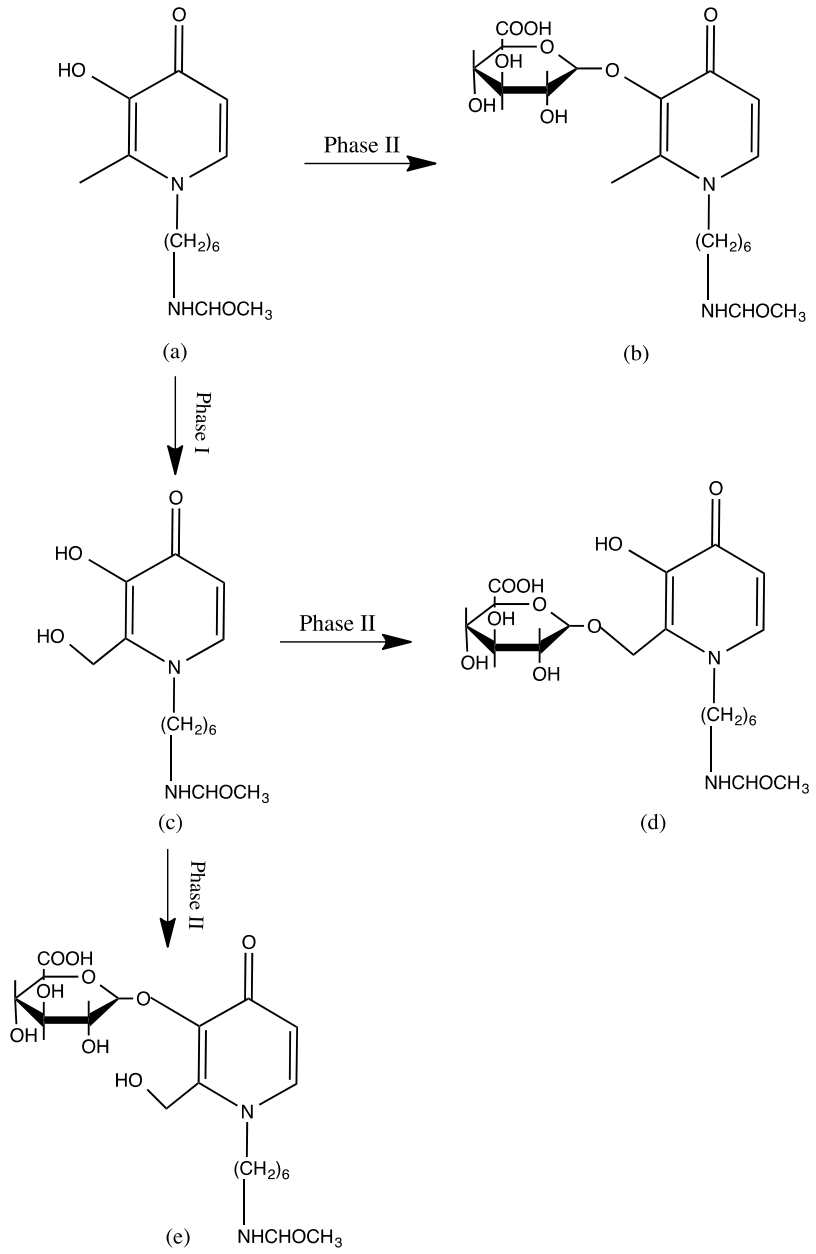

Scheme 3.4 Possible metabolic pathways of CM1

(a) CM1;
(b) 3-O-glucuronide conjugate of CM1;
(c) CM1-2-hydroxymethyl metabolite;
(d) Glucuronide of 2-hydroxymethyl conjugate of CM1;
(e) 3-O-glucuronide conjugate of CM1-2-hydroxymethyl metabolite

3.9.5.4 Metabolic conversion of close analogues of CP20

A series of mono-, di- and tri- methyl substituted analogues at *ortho*-, *meta*- and *para*-positions with respect to the phenolic group of 3-hydroxypyridin-4-one ring have been investigated for the effect of the substitution patterns on the drug metabolism profiles in the human liver microsomes (For chemical structures, refer to Section 3.9.1, Table 3.1, p74). Regioselectivity in drug metabolism has been reported previously. For instance, a regioselective oxidation by CYPs-dependent monooxygenase was observed with preferential insertion of oxygen at *meta-para* unsubstituted carbon atoms rather than the *ortho-meta* unsubstituted position, by altering the chloride substitution patterns of the polychlorinated biphenyls (Borlakoglu et al., 1990). The conjugation reaction mediated by the UGT enzymes also demonstrated regioselectivity, where glucuronides were formed to different extents depending on the isomers of *ortho*-, *meta*- and *para*-xylene (Corn, 1993). Hence, it was of great interest to investigate the impact of varying the methyl substitution patterns on the 3-hydroxypyridin-4-one ring on the metabolic profiles. Similar to both CP20/deferiprone and CP94, the major route of metabolism of this series of methyl-substituted analogues was found to be glucuronidation. The parent drug elimination percentage incubated in the human liver microsomes with UDPGA cofactor fell in the range from 73% to 98% (Table 3.12, Rows D to I, Figure 3.17) in comparison to 90% and 88% for CP20/deferiprone and CP94 (Table 3.12, Rows A and B, Figure 3.17). This regioselective attack by the UGT enzymes was not apparent for this series of analogues. The 2,5- and 1,6- dimethyl HPOs (CP616 and CP69) displayed a slightly reduced of glucuronidation conjugation (73% and 79%, Table 3.12, Rows E and D). Concerning the biotransformation of parent compounds by the Phase I pathway, the 1, 6- dimethyl and 1, 2, 5- tri-methyl, CP69 and CP617, demonstrated similar extents of oxidative metabolism (28% and 29% respectively, Table 3.12, Rows D and F, Figure 3.17) compared with that of CP20/deferiprone (25%, Table 3.12, Row A, Figure 3.17), while CP669, the 1, 5- dimethyl substituted HPO, displayed a slightly higher degree of Phase I biotransformation (39%, Table 3.12, Row G, Figure 3.17). The degree of Phase I metabolism of another 2, 5- di-methyl substituted HPO, CP616, demonstrated a slightly reduced extent (16%, Table 3.12, Row E) compared with that of CP20/deferiprone. The two mono-methyl substituted HPO analogues, 2- methyl and 5- methyl HPOs, CP28 and CP679 experience the lowest degree of Phase I metabolic conversion (11% and 10%, Table 3.12, Rows H and I, Figure 3.17)

and the extent was comparable with that of CP102 (9%, Table 3.12, Row C, Figure 3.17). The likely metabolic pathway of one compound of this series of analogues, CP28, is presented in Scheme 3.5. For other compounds of this series, their metabolic pathways are listed in Appendix VI-II.

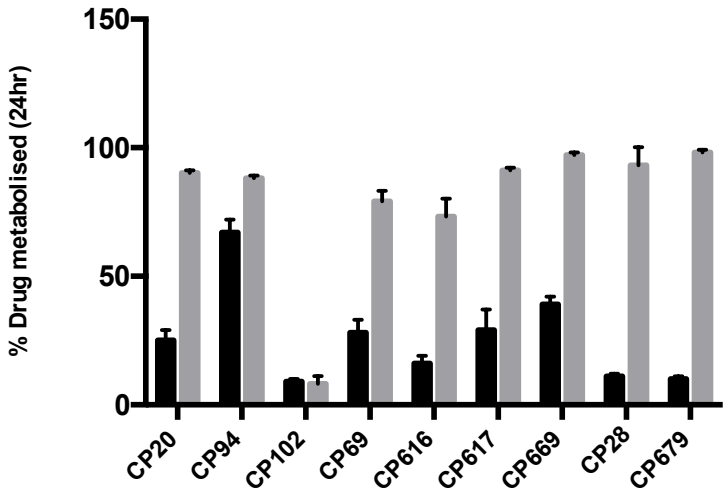

Figure 3.17 Metabolic conversions of CP69, CP616, CP617, CP669, CP28 and CP679 in human liver microsomes

Metabolic conversions of CP20/deferiprone, CP94, CP102 in human liver microsomes were taken from Figure 3.14
Black: Phase I; Grey: Phase I+II
Chemical structures are given in Section 3.9.1, Table 3.1

Table 3.12 Metabolic conversions of CP69, CP616, CP617, CP669, CP28 and CP679 in human liver microsomes

Metabolic conversions of CP20/deferiprone, CP94, CP102 in human liver microsomes were taken from Table 3.9

	% Drug metabolised (24 hr) (Mean ± SD, n=3) in HLMs		
HPOs	**Phase I**	**Phase I+II**	**Row**
CP20/deferiprone	25 ± 4	90 ± 1	A
CP94	67 ± 5	88 ± 1	B
CP102	9 ± 1	8 ± 3	C
CP69	28 ± 5	79 ± 4	D
CP616	16 ± 3	73 ± 7	E
CP617	29 ± 8	91 ± 1	F
CP669	39 ± 3	97 ± 1	G
CP28	11 ± 1	93 ± 7	H
CP679	10 ± 1	98 ± 1	I

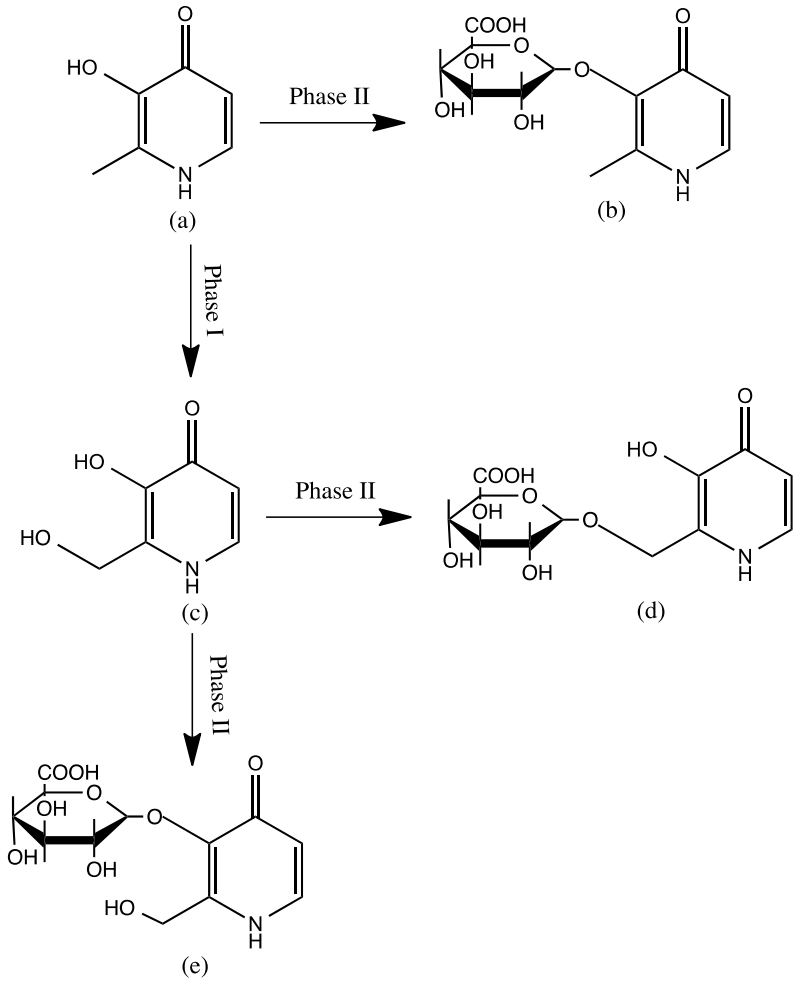

Scheme 3.5 Metabolic pathways of CP28

(a) CP28;
(b) 3-O-glucuronide conjugate of CP28;
(c) CP28-2-hydroxymethyl metabolite;
(d) Glucuronide of 2-hydroxymethylconjugate of CP28;
(e) 3-O-glucuronide conjugate of CP28-2-hydroxymethyl metabolite

3.9.5.5 Metabolic conversion of pegylated hydroxypyridinones

As previously discussed, pegylation has provided advantageous biological properties, improving the pharmacokinetic character and efficacy of iron chelators (Veronese and Mero, 2008). The series of 1-, 2-, 6- substituted pegylated HPOs (Section 3.9.1, Table 3.1) were incubated in the human liver microsomes in order to study the influence of the presence of pegylated groups on the metabolic profiles (For chemical structures, refer to Section 3.9.1, Table 3.1, p74). Comparable with the CP20/deferiprone and CP94, K8 and K5, where the pegylated function is *ortho* with respect to the phenolic group, demonstrated marked glucuronidation with 80% and 97% parent drug disappearance (Figure 3.18, Table 3.13 Rows H and I). In contrast there is a reduction of glucuronidation in both K7 and K6 with 40% and 26% parent drug conjugated by glucuronidation (Figure 3.18, Table 3.13 Rows J and K), where the pegylated group is para with respect to the phenolic group. The rate of glucuronidation is further reduced ranging from 20 % to 38% (Table 3.13 Rows D to G), when the pegylated function is placed on the N-atom of the ring (C11, C21, C31, K31).

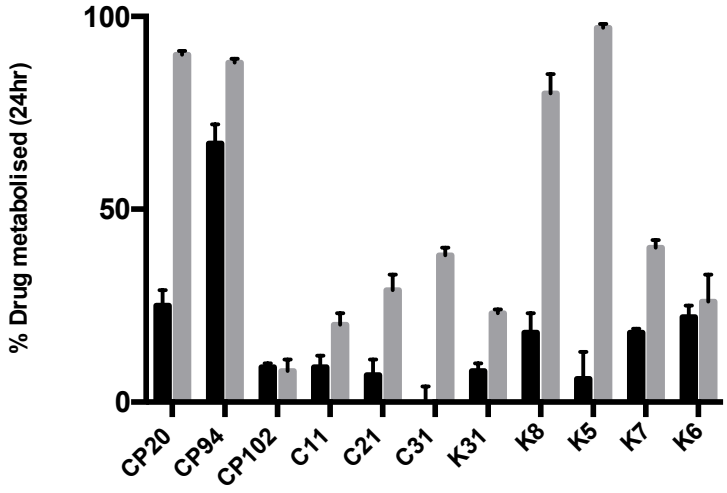

Figure 3.18 Metabolic conversions of pegylated HPOs in human liver microsomes
Metabolic conversions of CP20/deferiprone, CP94, CP102 in human liver microsomes were taken from Figure 3.14
Black: Phase I; Grey: Phase I+II

With regard to Phase I metabolic pathway, K8, K7 and K6, where the pegylated group is on the *ortho-, para*- position with respect to phenolic group, were transformed by CYPs to a similar extent (18%, 18% and 22%, Table 3.13, Row H, J and K, Figure 3.18) to that of CP20/deferiprone (25%, Table 3.13, Row A, Figure 3.18). In contrast, C11, C21, C31, K31, where the pegylated function is at the position-1 of the ring, and K5, where the pegylated group is *ortho*- to the phenolic group were metabolised to a reduced extent, with C31 experiencing no detectable phase I metabolic pathway (Table 3.13, Row D to G and I, Figure 3.18).

Table 3.13 Metabolic conversions of pegylated HPOs in human liver microsomes
Metabolic conversions of CP20/deferiprone, CP94, CP102 in human liver microsomes were taken from Table 3.9

	% Drug metabolised (24 hr) (Mean ± SD, n=3) in HLMs		
HPOs	**Phase I**	**Phase I+II**	**Row**
CP20/deferiprone	25 ± 4	90 ± 1	A
CP94	67 ± 5	88 ± 1	B
CP102	9 ± 1	8 ± 3	C
C11	9 ± 3	20 ± 3	D
C21	7 ± 4	29 ± 4	E
C31	0 ± 4	38 ± 2	F
K31	8 ± 2	23 ± 1	G
K8	18 ± 5	80 ± 5	H
K5	6 ± 7	97 ± 1	I
K7	18 ± 1	40 ± 2	J
K6	22 ± 3	26 ± 7	K

As both Phase I and Phase II metabolic conversions were both markedly reduced for C11, this chelator was selected for further investigation, whereby C11 was incubated in the presence of human liver microsomes fortified only with UDPGA in the absence of NADPH. Under these conditions, direct Phase II glucuronidation can be observed without any prior Phase I oxidative metabolism. There was virtually no direct glucuronidation on the parent compound observed (Figure 3.19, Table 3.14), indicating that the glucuronidation of C11 occurs after some degree of oxidative metabolic modification (Scheme 3.6). Metabolic pathways of other compounds from this series are listed in Appendix VI-III.

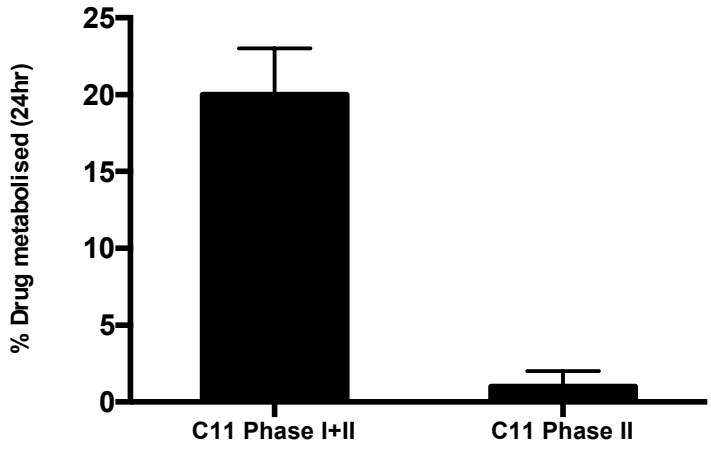

Figure 3.19 Phase I+II and Phase I metabolic conversion of C11 in human liver microsomes
Black: Phase I; Grey: Phase I+II

Table 3.14 Phase I+II and Phase I metabolic conversion of C11 in human liver microsomes

	% Drug metabolised (24 hr) (Mean ± SD, n=3) in HLMs	
HPOs	**Phase I+II**	**Phase II**
C11	20 ± 3	1 ± 1

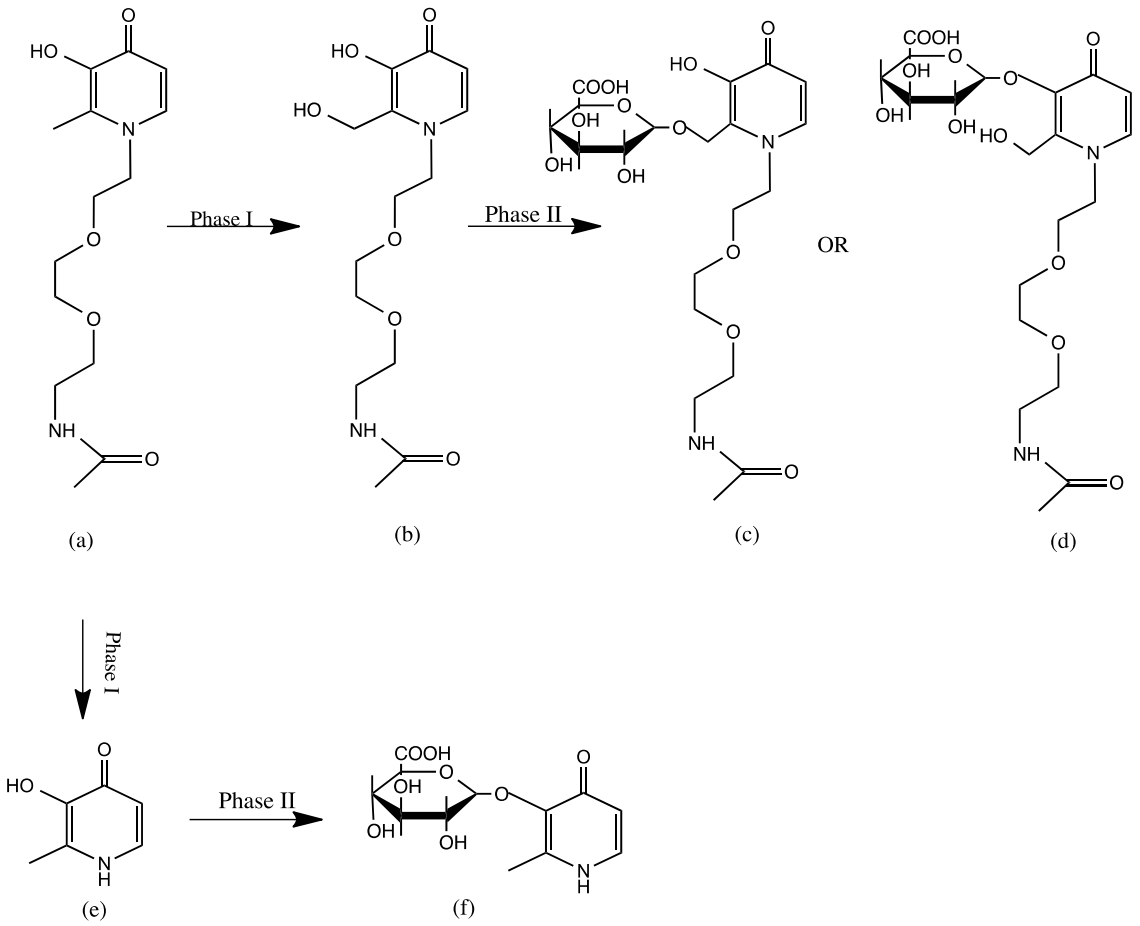

Scheme 3.6 Metabolic pathways of C11

(a) C11;
(b) C11-2-hydroxymethyl metabolite;
(c) Glucuronide of 2-hydroxymethyl conjugate of C11;
(d) 3-O-Glucuronide conjugate of C11-2-hydroxymethyl metabolite;
(e) N-dealkylated metabolite of C11;
(f) 3-O-glucuronide conjugate of N-dealkylated metabolite of C11

As the loss of C11 by both Phase I and II metabolising enzymes was found to be much less substantial than that of CP20/deferiprone, the study has been extended to its less hydrophilic analogue (6d, Table 3.1). Unfortunately both Phase I and phase II metabolic conversions were found to be more substantial compared with those of C11. (Figure 3.20, Table 3.15). Consequently, the substitution with pegylated groups at different positions on the HPO ring has introduced regioselective metabolic profiles, with some of the candidates displaying reduced degree of metabolism.

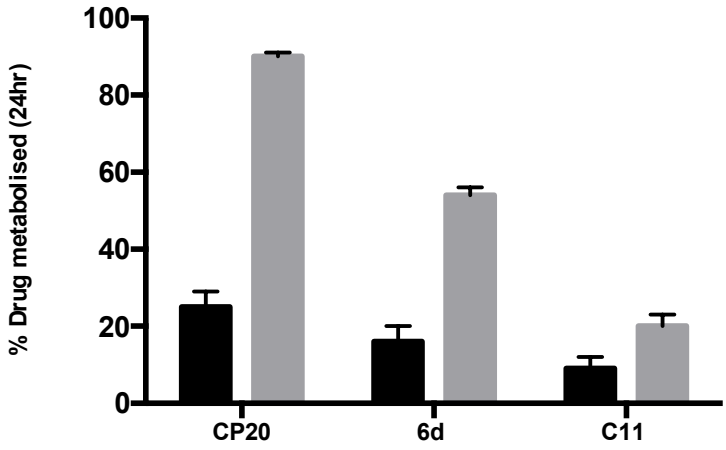

Figure 3.20 Metabolic conversion of C11 and 6d in human liver microsomes
Metabolic conversion of CP20/deferiprone in human liver microsomes were taken from Figure 3.14
Black: Phase I; Grey: Phase I+II

Table 3.15 Metabolic conversion of C11 and 6d in human liver microsomes
Metabolic conversion of CP20/deferiprone in human liver microsomes were taken from Table 3.9

	% Drug metabolised (24 hr) (Mean ± SD, n=3) in HLMs		
HPOs	**Phase I**	**Phase I+II**	**Row**
CP20/deferiprone	25 ± 4	90 ± 1	A
C11	9 ± 3	20 ± 3	B
6d	16 ± 4	54 ± 2	C

3.10 Summary

A rapid, sensitive and selective bio-analytical method for simultaneous screening and quantification of novel 3-hydroxypyridin-4-one analogues has been developed and validated. The method is useful for the investigation of metabolic profiles of hydroxypyridinones. The high throughput sample clean-up pre-treatment of biological samples using a mixed-mode cation exchange (MCX) solid phase extraction to concentrate and purify parent compounds and their metabolites is coupled to a quantitative method using ultra performance liquid-chromatography (UPLC) coupled with a tandem quadrupole mass spectrometer (TQ-MS) operated in the multiple reaction monitoring (MRM) acquisition mode. The UPLC and MS/MS (MRM) conditions have been optimised and established. This new approach is suitable for high sample throughput and has been applied to the screening and quantification of Phase I and Phase II metabolic biotransformations and clearance of a range of novel 3-hydroxypyridin-4-one compounds.

The modification of methyl substitution patterns does not further optimise deferiprone/CP20 properties regarding to glucuronidation. Another HPO, CM1, suffered a slightly lesser extent of glucuronidation compared with CP20 in HLMs. Large decreases of the extent of glucuronidation were observed in most of the pegylated HPOs and one of the chiral enantiomers CN128. The reduced metabolic elimination of these parent HPOs by the liver metabolism enzymes will enhance the iron chelation efficacy of the compounds. However, the pegylated side chain increases the hydrophilicity of the hydroxypyridinones, when compared with CP20/deferiprone, the milogP values all being negative (Section 3.9.2, Table 3.4). The lipid solubility of the free ligand HPOs is desirable for access to intracellular iron by permeating the membranes by non-facilitated diffusion. The reduced lipophilicity of the pegylated HPOs is likely to reduce the rate of penetration of the cell membranes. Consequently, CN128, with ideal physicochemical properties and metabolic profiles, was subjected to a further detailed efficacy study. Although the glucuronidation rate of CM1 was not reduced to a large extent, this HPO was also investigated in the efficacy study due to its ideal physicochemical properties.

CHAPTER FOUR

Efficacy study of 3-hydroxypyridin-4-ones

Chapter 4 Efficacy study of 3-hydroxypyridin-4-ones

4.1 Introduction

An *in vivo* animal model is essential in order to establish the iron chelation activity of iron chelators, including absorption from the gastrointestinal tract in the intact organism. We have adopted the *in vivo* ^{59}Fe-ferritin-labelled non-iron overloaded rat model to evaluate the oral availability and iron mobilisation from the major iron overload site, the liver (Liu et al., 1999c). We have compared two lead chelators, CN128 and CM1 (Figure 4.1) with CP20/deferiprone. CN128 was selected for the efficacy study due to its slow rate of metabolism in the liver (Chapter 3, Section 3.9.5.2). CM1 possessed suitable physicochemical characteristics to act as a candidate of an ideal iron chelator, which possesses high affinity and selectivity for iron(III) and a suitable partition coefficient for both the ligand and iron complex to permeate cell membranes (Pangjit et al., 2015). All the animal work in this project has been conducted under the animal license PPL 70/6954, and carried out under the regulations of Animals (Scientific Procedures) Act 1986. The efficacy study of CN128 involved collaboration with the Medicinal Chemistry Research Group of the Institute of Pharmacy, Zhejiang University, China in order to provide preclinical efficacy data of CN128 for Phase I clinical trial. The efficacy study of CM1 was collaborated with Chiang Mai University, Thailand.

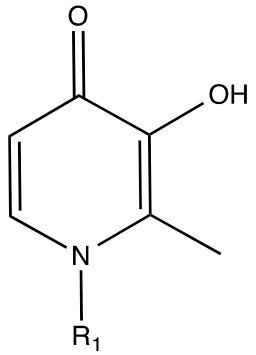

HPO	R_1
CN128	$-CH(C_6H_5)CH_2OH$
CM1	$-(CH_2)_6NHCOCH_3$

Figure 4.1 Chemical structures of CN128 and CM1

4.2 Materials and apparatus

Hydroxypyridinones

CN128,(R)-3-hydroxy-1-(1-hydroxy-3-phenylpropanyl)-2-methylpyridin-4(1H)-one (hydrochloride form) and CP20/deferiprone, 1,2-dimethyl-3-hydroxypyridin-4-one (hydrochloride form) were designed and synthesised by the Medicinal Chemistry Research Group of Institutie of Pharmacy, Zhejiang University, China. Ferriprox™ (film coated CP20/deferiprone tablets, 500mg) was purchased Apotex Inc. Canada; CM1, 1-(N-acetyl-6-aminohexyl)-3-hydroxypyridin-4-one (free base form) was synthesised in Chiang Mai University, Thailand.

Animal experiments

Male (230 to 300g) and female (210 to 220g) young adult (7 weeks) Sprague-Dawley rats (Harlan UK Ltd., Oxon, UK); Buprenorphine (Archimedes Pharma Ltd Reading, UK); Liquid isoflurane (Aesica Queenborough Ltd, Kent, UK); Euthatal (Merial S.A.S, Toulouse, France); Rodent vascular access port with pre-attached silastic catheter, 3 Fr; Huber needle (Harvard Apparatus, Kent, UK); Plastipack™ syringes (BD, NJ, US); Neolus® hypodermic needles (Terumo, Leuven, Belgium); Feeding needles, FNC-12-4, curved, 12 gauge, 3.9 inches (Kent Scientific Corporation, Torrington, US); Most of the surgical tools and facilities were kindly provided by Dr. Manasi Nandi research group, King's College London

Analytical experiments

^{59}Fe radionuclide (Perkin Elmer, Cambridge, UK); Sephadex® G-25 disposable PD-10 desalting columns (Sigma-Aldrich, Dorset, UK); T25 digital Ultra-Turrax homogenizer (IKA, Staufen, Germany); Sorvall RT7 centrifuge (GMI, Inc., Minnesota, US); Compugamma CS gamma counter (LKB Wallac, Victoria, Australia); Optima™ L-90K ultra centrifuge (Beckman Coulter Inc., UK); Sodium acetate anhydrous, sodium phosphate，sodium ammonium sulphate, sodium carboxymethyl cellulose (NaCMC) (Sigma-Aldrich Company Ltd, Dorset, England).

4.3 Methods

4.3.1 ^{59}Fe labeled ferritin rat model

Three batches of ^{59}Fe labeled ferritin were prepared in order to accomplish the project.

4.3.1.1 Implantation of catheter into the right jugular vein of rats (Day 1)

Five adult male SD rats were anaesthetised with 2-3% inhaled isofluoran and placed on a heated mat. 20μg/kg buprenorphine was administered by intramuscular (i.m.) injection in order to provide postoperative analgesia. The body weights and doses of analgesia are listed in Table 4.1

Table 4.1: Animals body weight and analgesia administration record

Batch No.					
1		2		3	
B.W. (g)	Buprenorphine (μg)	B.W. (g)	Buprenorphine (μg)	B.W. (g)	Buprenorphine (μg)
263.9	5.3	280.2	5.6	285.0	5.7
259.8	5.2	278.3	5.6	287.5	5.8
276.4	5.5	293.8	5.9	275.5	5.5
254.6	5.1	282.2	5.6	280.2	5.6
252.0	5.0	281.2	5.6	290.3	5.8

The dorsal and ventral neck regions were shaved and a 1.5 cm incision is made at both sides. The dorsal incision was 1 cm left to the midline of the body, the ventral incision was on the midline. A skin-tunneling needle passed subcutaneously over the right shoulder from the ventral to the dorsal incision site. A vascular access port catheter was threaded subcutaneously to the ventral neck region, leaving the saline filled port at the right side of the dorsal incision site. The catheter was cut to the appropriate length and flushed with 50 IU/ml heparin in clinical grade saline (0.9%). The right jugular vein was carefully isolated with two suture threads, and the anterior portion completely occluded. A small incision was made with a 23-gauge needle and the catheter insert posteriorly for approximately 1 cm past the suture and secured in place. The ventral neck region was sutured and the region sterilised. The port portion of the catheter was placed subcutaneously at the dorsal incision site and the incision site sutured and sterilised. The jugular veins of five male 230 to 240g male adult SD rats were cannulated and implanted with catheters. Animals were recovered in a heated chamber (30°C for 1-2 hours) before placed

in the holding room.

4.3.1.2 Packed red blood cell preparation and administration into animals (Day 2)

Packed red blood cells (RBCs) were prepared from adult male SD rats (250 to 300g) anaesthetised as in Section 4.3.1.1. Approximately 10ml of blood was removed from each rat and added to 80ml of 20mM phosphate buffered saline (PBS) at pH 7.4, containing 2mM citrate at 4°C. The diluted blood was centrifuged in Sorvall RT7 centrifuge (2500 rpm) for 5 min at 4°C. The supernatant was carefully decanted; the RBCs were washed with PBS several times. The combined packed red blood cells were approximately 10 to 20 mL and kept in the incubator at 37°C. 24 hours post vascular access port catheters implantation, no animals displayed any visual clinical signs of distress or infection. Animals were re-anaesthetised with inhaled isofluorane 2-3% and the catheter line was flushed with heparinised saline followed by 3ml of warmed packed red blood cells (0.5ml/min) using a Huber needle followed by a further heparinised saline flush. Animals were recovered in a heated chamber (30°C for 1-2 hours) and returned to the holding room.

4.3.1.3 ^{59}Fe labeling (Day 3)

24 hours post red blood cell infusion; animals did not display any visual clinical signs of distress or infection. Animals were re-anaesthetised with inhaled isofluorane 2-3% and the catheter line flushed with heparinised saline. 200 µCi of ^{59}Fe in 0.25ml of sodium citrate (50mM, pH7.0), prepared by diluting the stock solution (1mCi ^{59}Fe 50µl in sodium citrate, 50mM, pH7.0) five times, was administered via the access port and flushed through with heparinised saline. Animals recovered were placed in a designated holding room for further 24 hours.

All the surgical operations were performed with the help of Dr. Anna Star.

4.3.1.4 Purification of ^{59}Fe ferritin (Day 4)

Animals were sacrificed and the livers were removed. The weights of livers were recorded (Table 4.2). The combined livers were homogenised in 4vol (w/v) of sodium acetate (0.25M pH 4.8), the volumes of sodium acetate used were listed in Table 4.2.

Table 4.2: Animal liver weight and volume of sodium acetate (NaAc)

Batch No.		
1	**2**	**3**
Liver weight (g)	**Liver weight (g)**	**Liver weight (g)**
10.60	9.41	13.63
10.20	11.48	12.80
10.80	8.30	12.40
11.20	9.30	14.10
12.00	10.24	NA
Total Liver weight(g)	**Total Liver weight(g)**	**Total Liver weight(g)**
54.8	48.7	52.9
Volume of NaAc(mL)	**Volume of NaAc(mL)**	**Volume of NaAc(mL)**
219.2	194.8	211.6

The homogenate was heated from 20°C to 70°C for 20 min and maintained 70 to 75°C for 10 min on a heated magnetic plate. After cooling to 10°C, the coagulated proteins were removed by centrifugation at 2500 g for 15min at 4°C (Sorvall RT7 centrifuge). The supernatant containing tissue ferritin was precipitated by half saturated sodium ammonium sulphate (every 325ml was treated with 95g sodium ammonium sulphate to obtain a 50% saturated solution), and left to stand for 30min at 4°C in an ice-bath. The resulting precipitate was separated by centrifugation at 3500 g for 15min at 4°C (Sorvall RT7 centrifuge). The precipitate was dissolved in 15ml sodium acetate (0.25M, pH 4.8) (sample solution). Undissolved precipitate was removed by passing through PD-10 columns (Sephadex G25). The process using PD-10 columns was described as follows: a PD-10 column was firstly conditioned with 2 mL sodium acetate (0.25M, pH 4.8); 1mL sample solution was loaded on the PD-10 column; followed by a wash step with 3 mL sodium acetate (0.25M, pH 4.8) to wash out the undissolved precipitate. The tissue ferritin was collected by eluting the column with 4ml sodium acetate (0.25M, pH 4.8). The combined eluent from all the PD-10 columns was 70ml in total. The combined eluent was super-centrifuged at 4°C for 2h at 100,000g (Optima^{TM} L-90K ultra centrifuge). The resulting precipitate was dissolved in 10ml sodium phosphate solution (50mM, pH 7.4) and stored at 4°C.

10μL of the solution was subjected to a Compugamma CS gamma counter to measure the initial radioactivity (Table 4.3). The purified ^{59}Fe ferritin solution was used for the following HPO efficacy study.

Table 4.3: Initial radioactivity of ^{59}Fe-ferritin stock solution

Radioactivity	Batch No. 1	2	3
Counts per Min/10μL	17268	47562	12345
μCi/mL	75	206	54

4.3.1.5 HPO preparation

Two milliliters of stock solution of CN128 hydrochloride form (M.W. 296) at five dosages were prepared in water, which were 75μmol/kg b.w., 150μmol/kg b.w., 300μmol/kg b.w., 600μmol/kg b.w., 1200μmol/kg b.w.. The sample amount weighed in each stock solution (2mL) corresponded to the dose administered to a 300g b.w. animal. The oral gavage volumes to each animal were calculated by the equation: (Animal b.w.／300g) x 2mL. The stock solutions of CM1 free base form (M.W. 266), at three doses of 75μmol/kg b.w., 150μmol/kg b.w., 300μmol/kg b.w., were prepared in 50% propanediol and oral administered to rats in the same manner as CN128. Ferriprox^{TM}, film coated CP20/deferiprone tablets, was initially used as the positive control. Twenty tablets were weighed together and the average weight of tablets was calculated, which was 822g. According to the “QC analysis report” provided from China, the purity of the active ingredient in a tablet (500g CP20/deferiprone in one tablet) is 98.8%. Thus the percentage of CP20/deferiprone in each tablet was obtained from (Amount of CP20/deferiprone in the tablet／Mean weight of the tablet)×100%, which was [(500g×98.8%)／822g]×100% equal to 60%. The amount of ferriprox^{TM} tablet administered to achieve the equivalent dose investigated for CN128 was converted by (Dose investigated／Percentage of CP20/deferiprone in the tablet). Tablets were crushed to fine powder and each dose was prepared in 5% sodium carboxymethyl cellulose (NaCMC). A fine suspension was formed after sonication for 30min. The supernatant after centrifugation for 5min was used for administration. CP20/deferiprone (free base form, M.W. 139) stock solutions were later used as positive control and prepared at doses equivalent

to CN128, which were suspended in 50% propanediol and sonicated until totally dissolved. Due to the insolubility of high doses (600μmol/kg b.w. and 1200μmol/kg b.w.), the suspensions were titrated with concentrated hydrochloric acid until a clear solution was achieved. Water was used as negative control throughout the study.

4.3.1.6 Procedures for the efficacy study

Rats were fasted overnight. 1μCi of ^{59}Fe-ferritin was injected intravenously through the rat tail vein. One hour later, rats were administered with CN128 by oral gavage at five doses. Positive control rats were administered with ferriprox^{TM} or CP20 crude drug at the same doses as CN128. Negative control rats were administered with an equivalent volume of water. Rats were placed in separate metabolic cages with urine and faeces collected separately and were allowed free access to food 1 hr after oral gavage. There was no restriction of water throughout the study period. The investigation was terminated 24 hrs after the ^{59}Fe-ferritin administration; the rats were killed by intraperitoneal (i.p.) injection of 1ml euthatal. The liver and gastrointestinal tract (including its contents and the faeces) were removed. Urine and faeces were collected from metabolic cages. Samples were subjected to gamma counting. The calculations of “Iron mobilisation,” “Efficacy” and “Total recovery” are represented by equations 4.1, 4.2 and 4.3.

$$\text{Iron mobilisation}(\%) = \frac{\text{Activity}_{\text{(gut and faeces)}}}{\text{Activity}_{\text{(gut and faeces)}} + \text{Activity}_{\text{(liver)}}} \times 100 \qquad \text{Equation 4.1}$$

$$\text{Efficacy}\ (\%) = \text{Iron mobilisation}(\%) - \text{Control}(\%) \qquad \text{Equation 4.2}$$

$$\text{Total recovery}(\%) = \frac{\text{Activity}_{\text{(gut and faeces)}} + \text{Activity}_{\text{(liver)}}}{\text{Activity}_{\text{(total)}}} \times 100 \qquad \text{Equation 4.3}$$

$\text{Activity}_{\text{(total)}}$ was obtained from the initial radioactivity of the purified ^{59}Fe-ferritin (Section 4.3.1.4, Table 4.3) multiplied by the decay factors demonstrated in “^{59}Fe decay table “(PerkinElmer).

Each study group included five animals administered with five doses of CN128 (one animal per each dose), five animals administered with corresponding doses of ferriprox^{TM} or

CP20/deferiprone crude drug as a positive control (one animal per each dose) and one animal administered with water as a negative control. Ten groups of SD rats (half male and half female) were investigated for the whole project. Injection dose of ^{59}Fe-ferritin was adjusted daily according to the "^{59}Fe decay table "(half life 44.51 days) throughout the study.

4.3.1.7 Statistical analysis

The statistical significance of difference was determined for the "iron mobilization" and "efficacy" among different iron chelators, using "GraphPad Prism 5.0" software (LaJolla, CA, USA).

4.3.2 Recovery of deferiprone/CP20 in the ferriprox™ suspension

Known amounts of CP20/deferiprone standard compound were suspended in 5% NaCMC and appeared as clear solutions. Solutions were further diluted 100 folds before subjecting to HPLC-UV analysis. A Hewlett-Packard HPLC (Agilent Technologies Ltd., Shropshire, UK) equipped with UV-Vis detector was used and coupled with a polymer PLRP column (250mm×4.6mm, 5μm) (Polymer Laboratories Ltd, Shropshire, UK). Mobile phase was consisted of 1-heptane sulfonic acid (5mM, pH 2) and acetonitrile. The elution flow rate was 1.0 ml/min with a gradient of 2%–40% CH_3CN in 20 min and post-run was followed for 5 min at 2% CH_3CN. A calibration curve (Concentration vs Peak area) of the CP20/deferiprone standard solutions was conducted by Origin 8 (OriginLab Corporation, Northampton, USA). The supernatant of a ferriprox™ suspension, in which the theoretical CP20/deferiprone content is equivalent to a CP20/deferiprone dose of 75μmol/kg b.w. administered to a 300g rat, was diluted 100 folds and injected into HPLC-UV. The peak area of the effective component CP20/deferiprone in this supernatant of ferriprox™ suspension was integrated and the concentration of CP20/deferiprone in the suspension was obtained by back calculation from the calibration curve of deferirpone standards. The recovery of CP20/deferiprone in the fine sonicated ferriprox™ suspension was calculated as (Observed concentration／Theoretical concentration) x 100%.

4.4 Results and discussion

4.4.1 Efficacy study of CN128

As iron overload develops, proportionally more iron is found in parenchymal cells, predominantly in hepatocytes; the most important source of rapidly chelatable intracellular iron is a transient low molecular weight iron pool, namely labile iron pool (Porter et al., 1989a). Hence, in the established *in vivo* model, mobilisation of iron from liver parenchymal cells by the investigated chelating agents is to be measured. Consequently, this specific labile iron pool is targeted allowing the study of the site of action of new candidate iron chelators. Using a radio iron probe allows the precise labeling of the iron pool to study the site of action and route of excretion; ^{59}Fe labeled ferritin taken up by hepatocytes was used to label this iron pool (Hershko et al., 1973). Thus, optimal ^{59}Fe-ferritin labeling of the labile iron pool in the hepatocytes is crucial. ^{59}Fe-ferritin when injected via the rat tail vein is rapidly removed to the hepatocyte (Liu et al., 1999c). It is then broken down by lysosomal degradation to constituent amino acids and ^{59}Fe, the latter entering the labile iron pool (LIP). Over a period of 1 to 2 h, the labeled iron pool is removed to endogenous ferritin. Hence, there is a time window, about 1h after the administration of ^{59}Fe-ferritin, that the LIP in hepatocytes contain a high content of ^{59}Fe in transit before storage in endogenous ferritin, where oral active iron chelators can mobilise and scavenge ^{59}Fe (Liu et al., 1999c). Efficient liver clearance of ^{59}Fe-ferritin can be achieved 1h after injection with the majority of radiolabel being located in the liver representing as a significantly enhanced gamma radiation counts values of the liver above the detection limit. Thus, test HPO compounds were administered 1 h after the administration of ^{59}Fe-ferritin. The increase in gut content and faeces radiation counts, which resulted from biliary excretion, was reflected by a commensurate decrease in liver counts. Different ligands have different pharmacokinetic profiles, which in turn lead to different iron excretion time profiles. The peak of iron excretion varies with different ligands in the previous investigation within 24 hrs (Liu et al., 1999c). Therefore, collections of excreted iron were made over a 24 h period. There was no appreciable iron excretion by the urinary route induced by the investigated compounds. Three parameters were examined to evaluate the oral availability, iron mobilisation capacity of an iron chelator and system reliability, which are “Iron mobilisation,” “Efficacy” and “Total recovery” (Section 4.3.1.6).

Water was used as the vehicle solvent for CN128 hydrochloride form, which is the simplest vehicle for drug administration. Ferriprox™ tablets contain a number of inert materials, known as additives or excipients including diluent, adhesive, disintegrents and lubricants. Hence, given that sodium carboxymethyl cellulose (NaCMC) has been widely used as drug vehicle, crushed ferriprox™ tablets were suspended in 5% NaCMC and sonicated to a fine suspension. However, when administering the suspension to rats, blockage of oral gavage needle often occurred and hindered the effective oral administration, which was mainly due to the sediment of tablet additives leading to uneven suspension. Thus, the supernatants of the above suspensions were used instead. Consequently, the recovery of CP20/deferiprone in the supernatant of a ferriprox™ suspension, in which the theoretical CP20/deferiprone content is equivalent to a CP20/deferiprone dose of 75μmol/kg b.w. administered to a 300g rat, was back-calculated from the CP20/deferiprone standards calibration curve (Figure 4.2) using the method described in Section 4.3.2.

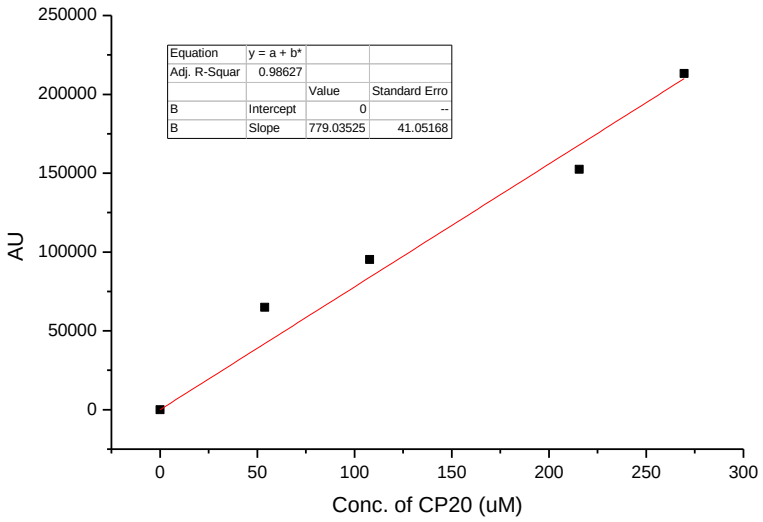

Figure 4.2 Calibration curve of CP20/deferiprone standards

The concentration of the CP20/deferiprone in the above suspension was 51.9 μM/L, while the theoretical CP20/deferiprone concentration is 215.6 μM/L. Therefore, the recovery of CP20/deferiprone in the supernatant of the above ferriprox^{TM} suspension was determined as only 24%. Hence, using the supernatant of the tablet suspension in 5% NaCMC led to under-evaluation of CP20/deferiprone efficacy. Consequently, we decided to use CP20/deferiprone crude drug (free base form) as the positive control. It has been reported that 50% 1,2-propanediol can be used in man for oral administration of drugs (Liu, 1997). Thus it was adopted as the vehicle for the CP20/deferiprone crude drug and concentrated hydrochloric acid was used to assist dissolution at the high doses. These sample solutions all appeared as clear solutions. It is this preparation of CP20/deferiprone crude drug that was used as the positive control during the efficacy studies.

A preliminary experiment was designed to examine the effectiveness of the ^{59}Fe ferritin animal model. The dose of 300μmol/kg b.w. was selected. The iron mobilisation of CN128 was found to be 30.7 %, which was nearly 4.5 fold more than that of CP20 (7.2 %) (Figure 4.3, Table 4.4). The efficacy of CN128 (28.1 %) was almost 6 fold more than that of CP20 (4.5 %) (Figure 4.4, Table 4.4). Hence, CN128 at dose of 300μmol/kg presented significantly improved oral availability and iron scavenging efficacy compared with CP20/deferiprone at the equivalent dose.

The standard deviations (SD) of the values of “Iron mobilisation,” “Efficacy” and “Total recovery” for eight groups of rats assessed in the above preliminary study were low, which fell in a range of 2.8% to 5.2% (Table 4.4). Thus the method was considered to be consistent and reliable. The total recovery of ^{59}Fe in the liver, gut contents and faeces were 80.3 % and 75.4 % for CP20 and CN128 groups respectively (Table 4.4), indicating the success of radio-iron labeling in the targeted hepatic iron pool.

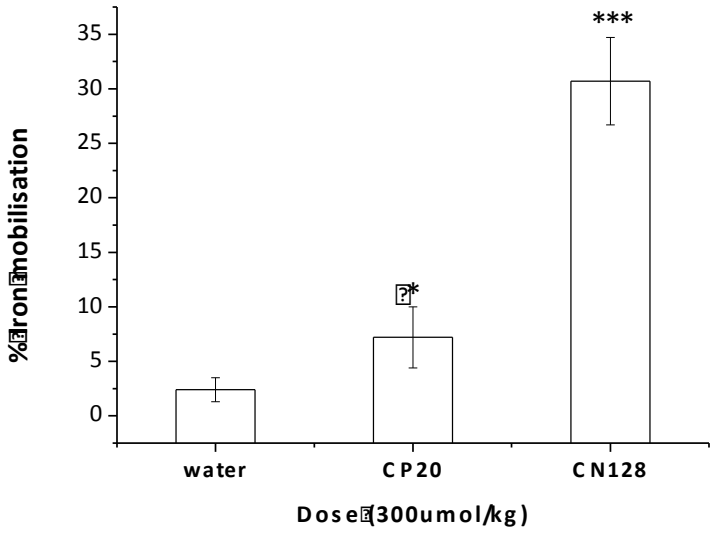

Figure 4.3 Iron mobilisation of CN128 and controls at dose 300 µmol/kg (N=8) in preliminary experiment

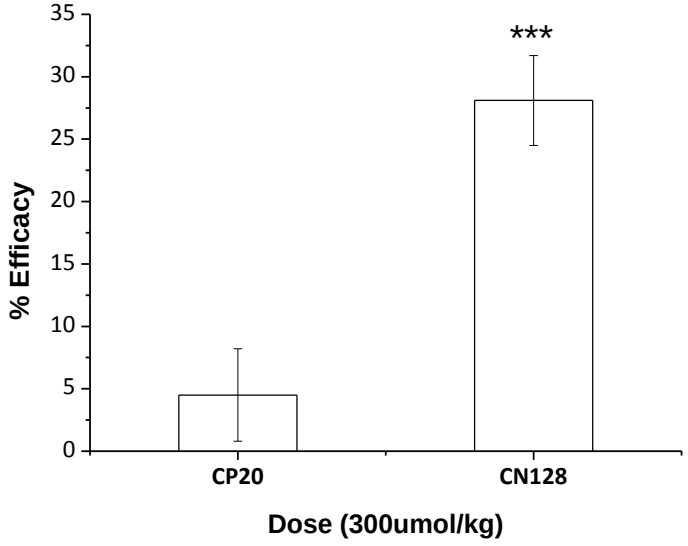

Figure 4.4 Efficacy of CN128 and controls at dose 300 µmol/kg (N=8) in preliminary experiment

Table 4.4 Iron mobilisation, efficacy, and recovery of CN128 and CP20 in preliminary experiment

Chelator	Dose (µmol/kg)	Iron mobilisation % Mean ± SD	Efficacy % Mean ± SD	Total recovery % Mean ± SD	No.
CP20/deferiprone	300	7.2 ± 2.8	4.5 ± 3.7	80.3 ± 4.5	8
CN128	300	30.7 ± 4.0	28.1 ± 3.6	75.4 ± 5.2	8

A dose response study of CN128 in rats was further investigated to establish the magnitude of the iron chelation effect of CN128 as a function of the dose, which would provide valuable information for identification of optimal dosage regimens (Appendix VI). From the dose response study, increasing iron mobilisation efficacy has been observed when the administered doses of CN128 increased from 75μmol/kg b.w, to 1200μmol/kg b.w. Compared with CP20/deferiprone, the iron mobilisation capacity has been significantly improved at equivalent doses (Figure 4.5).

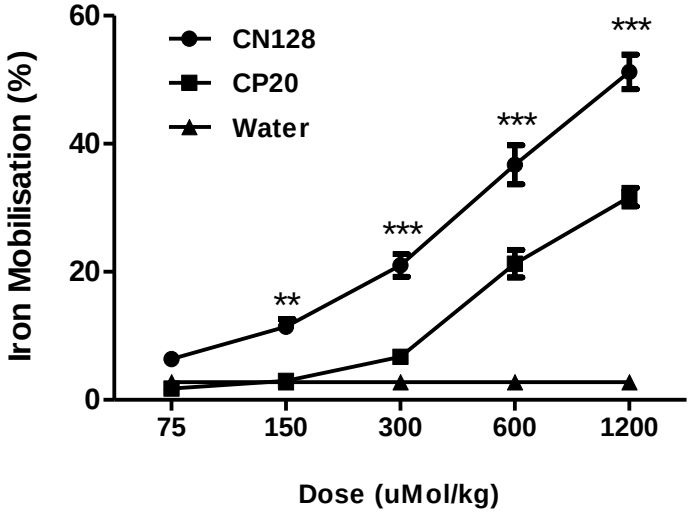

Figure 4.5 Iron mobilisation of CN128 in a dose response study

Efficient iron mobilisation from the liver was observed in CP20 groups when administered dose increased to 600 μmol/kg (18.9%), which has resulted in comparable iron scavenge capacity with CN128 administered at a dose of 300 μmol/kg (18.3%) (Figure 4.6; Table 4.5). At the dose of 150μmol/kg b.w., CP20 had an extremely low efficacy (0.6%) in contrast to CN128, which was 15 times more efficacious (8.7%) (Figure 4.6; Table 4.5). The results have demonstrated that the dose used for inducing the efficient iron mobilisation could be reduced when CN128 used as a chelating agent. The total recovery values demonstrated the reliability of the assay system (Table 4.5).

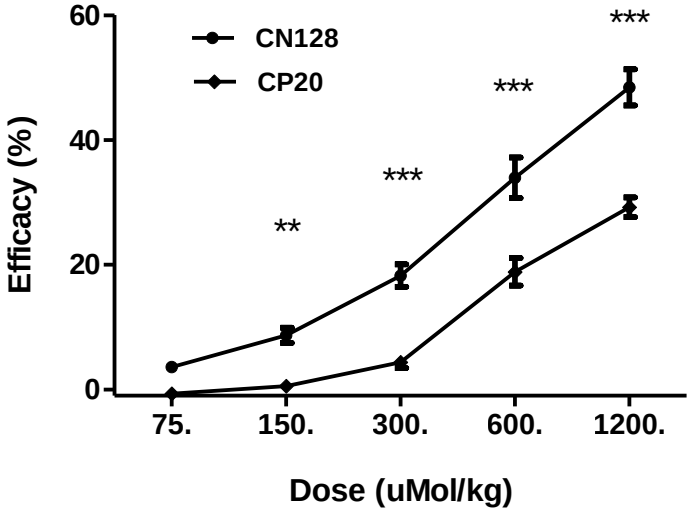

Figure 4.6 Efficacy of CN128 in a dose response study

Table 4.5 Dose response study of CN128

Chelator	Dose (μmol/kg)	Dose (mg/kg)	Iron mobilisation % Mean ± SD	Efficacy % Mean ± SD	Total recovery % Mean ± SD	No.
CN128	75	22	6.4 ± 1.7	3.6 ± 1.7	73.1 ± 6.7	10
CP20	75	10	1.8 ± 0.7	−0.7 ± 0.8	64.0 ± 14.2	10
CN128	150	44	11.4 ± 3.6	8.7 ± 3.9	71.5 ± 18.2	10
CP20	150	21	3.0 ± 1.3	0.6 ± 1.2	68.8 ± 12.7	10
CN128	300	89	21.0 ± 5.3	18.3 ± 5.7	70.6 ± 22.0	10
CP20	300	42	6.7 ± 2.7	4.4 ± 2.8	72.6 ± 14.2	10
CN128	600	177	36.7 ± 9.2	33.9±10.2	69.4 ± 19.6	10
CP20	600	83	21.3 ± 6.5	18.9 ± 7.0	64.6 ± 11.3	10
CN128	1200	354	51.2 ± 8.1	48.5 ± 9.1	72.8 ± 17.9	10
CP20	1200	167	31.7 ± 4.3	29.2 ± 5.0	66.0 ± 12.8	10

The impact of sex difference of animals on the efficacy of iron mobilisation has also been investigated. There was no substantial variation between the male and female groups at all five doses administered (Figure 4.7).

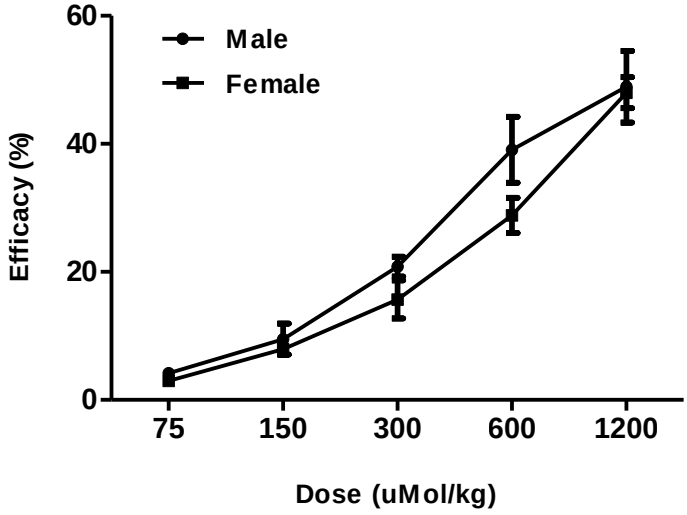

Figure 4.7 Sex differences in efficacy of CN128

4.4.2 Efficacy study of CM1

CM1 was selected as another candidate iron chelator and its iron-scavenging efficacy was evaluated in the same *in vivo* model. A dose response study has also been investigated for CM1. At a dose of 450 μmol/kg, CM1 was demonstrated to be 2.5 times more efficacious than deferiprone/CP20 (18.6% compared with 7.5%, Table 4.6) in iron mobilisation from the liver, when administered to rats via the oral gavage (Figure 4.8 and 4.9). Although there was a decrease in efficacy of both CM1 and CP20 when the dose was reduced to 150 μmol/kg, CM1 was found to be four times more effective than CP20 (2.6% compared with 0.6%, Table 4.6).

Thus a second new orally active iron chelator CM1 was identified in this study. The results also suggested that a reduced dose could be applicable. The total recovery values in this study confirmed the reliability of the animal model (Table 4.6)

Table 4.6 Dose response study of CM1

Chelator	Dose (µmol/kg)	Dose (mg/kg)	Iron mobilisation % Mean ± SD	Efficacy % Mean ± SD	Total recovery % Mean ± SD	No.
CM1	75	20	2.2 ± 0.7	0.5 ± 0.6	75.2 ± 7.7	6
CP20	75	10	1.6 ± 0.6	-0.7 ± 0.6	80.0 ± 10.5	6
CM1	150	40	4.3 ± 1.5	2.6 ± 1.4	75.5 ± 11.2	6
CP20	150	21	3.0 ± 1.7	0.6 ± 1.6	68.5 ± 10.4	6
CM1	450	120	20.5 ± 13	18.6 ± 6.0	71.8 ± 12.0	6
CP20	450	63	10.1 ± 2.8	7.5 ± 2.8	76.2 ± 12.4	6

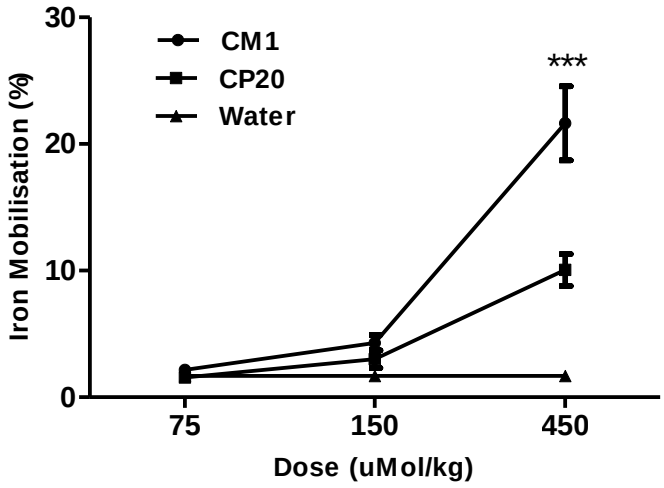

Figure 4.8 Iron mobilisation of CM1 in a dose response study

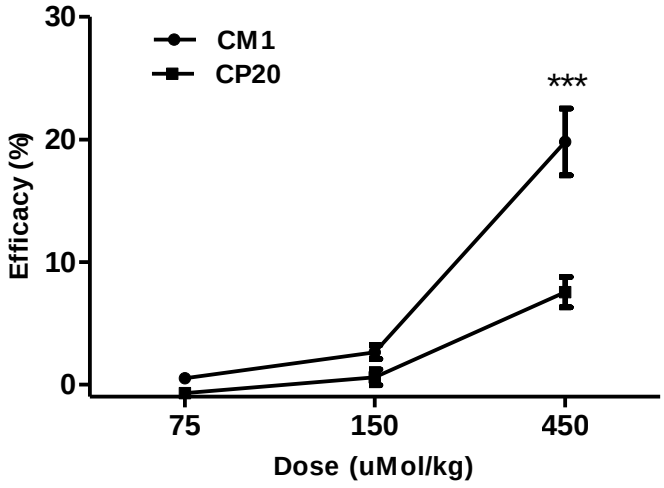

Figure 4.9 Efficacy of CM1 in a dose response study

The effect of sex difference on the iron mobilisation efficacy has also been investigated. Interestingly, with CM1, a significant difference between male and female groups was observed at the dose of 450 μmol/kg; the male group displaying 2.5 times enhanced efficacy in iron mobilisation when compared with the female group (Figure 4.10, Table 4.7).

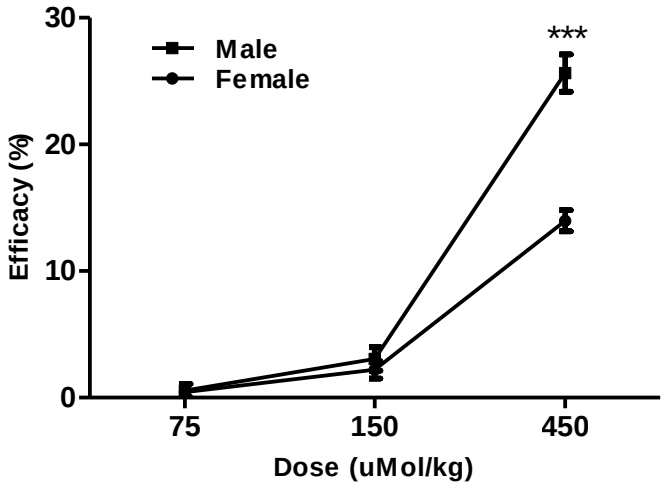

Figure 4.10 Sex differences in efficacy of CM1

Table 4.7 Sex differences in efficacy of CM1

Sex	Dose (μmol/kg)	Dose (mg/kg)	Efficacy % Mean ± SD	Total Recovery % Mean ± SD	No.
Male	75	20	0.5 ± 0.6	75.2 ± 7.7	3
Female	75	20	-0.7 ± 0.6	80.0 ± 10.5	3
Male	150	40	2.6 ± 1.4	75.5 ± 11.2	3
Female	150	40	0.6 ± 1.6	68.5 ± 10.4	3
Male	450	120	18.6 ± 6.0	71.8 ± 12.0	3
Female	450	120	7.5 ± 2.8	76.2 ± 12.4	3

4.5 Summary

The established *in vivo* rat ^{59}Fe-ferritin model has provided a useful procedure to investigate the iron mobilisation efficacy of iron chelators, by specifically labeling the major iron overloaded site with radio iron, namely, the liver parenchymal cell (hepatocytes). Both CN128 and CM1 have displayed the efficient mobilisation of iron from the liver and excreted iron via the biliary route to faeces. Both CN128 and CM1 have demonstrated improved efficacy in iron mobilisation when compared with deferiprone/CP20. The iron mobilisation capacities were most enhanced at the lower doses of 150 μmol/kg for both compounds. Particularly, CN128 displayed superior efficacy at this low dosage, which was 15 times more efficacious compared with CP20. The efficient iron removal from the liver when chelators were introduced by oral gavage has also demonstrated that both compounds are orally active. The impact of sex difference on the iron mobilisation of CM1 has initiated additional considerations when using iron chelaters to treat patients of different gender. Both compounds were identified as potential candidates as alternatives of CP20/deferiprone for clinical use. The *in vivo* results indicate that they could be used for treatment of iron overload patients at a reduced dose to that adopted for CP20/deferiprone.

The excellent efficacy that has been demonstrated in our *in vivo* model for CN128 was further investigated in Zhejiang University, China (Xin, 2016). It has been reported from China that CN128 is also efficient in iron chelation in the iron overloaded *Cebus* monkey model. The iron output was promoted by oral administration of CN128 and CP20 to *Cebus* monkeys. Enhanced iron output was observed when the dose of CN128 administered increased from 75 μmol/kg to 600 μmol/kg. Optimal iron output was observed when CN128 was administered at a dose of 300 μmol/kg, which was 2.5 times more than that of CP20 (Figure 4.11, Table 4.8). In addition, chronic toxicity tests have indicated that CN128 lacks the ability to trigger of agranulocytosis (Hoffbrand et al., 2003), which has been reported in deferiprone/CP20. Cytotoxicity studies using white cells, hepatocytes and cardiomyocytes have also been studied for CM1, which was reported to be effectively non-toxic (Pangjit et al., 2015).

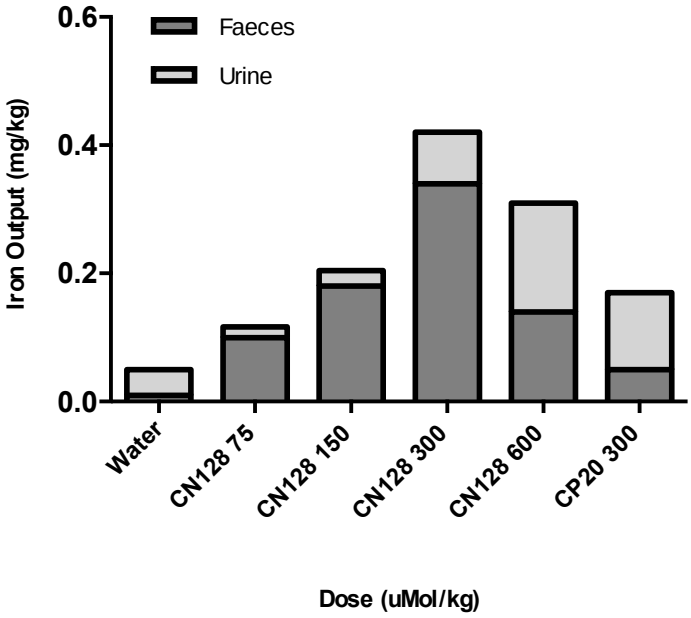

Figure 4.11 Iron output in urine and faeces of Cebus monkey after oral administration of CN128 and CP20 (Xin, 2016)

Table 4.8 Iron output in urine and faeces of Cebus monkey after single dosing of CN128 and CP20 (Xin, 2016)

Chelator	Dose (μmol/kg)	Dose (mg/kg)	Urine iron output (mg/kg)	Faeces iron output (mg/kg)	No.
CN128	75	22	0.017	0.100	6
CN128	150	44	0.024	0.180	6
CN128	300	89	0.080	0.340	6
CN128	600	177	0.170	0.140	6
CP20	300	42	0.120	0.050	6

CHAPTER FIVE

Conclusion and Remarks

Chapter 5 Conclusion and Remarks

5.1 Systemic iron overload

Several inherited diseases are associated with iron overload from the hyperabsorption of iron from the diet, for instance, hereditary haemochromatosis, which is common in Northern Europe and North America. These patients develop the symptoms of iron overload typically in the fourth or fifth decade of life. Because the patients are not anaemic, hereditary haemochromatosis can be successfully treated by phlebotomy (Pietrangelo, 2006). β-Thalassemia major is fatal in the absence of regular blood transfusion, which in turn is associated with systemic iron overload. With non-chelated transfused patients, death generally occurs in the second decade of life as a result of infection or heart disease (Rund and Rachmilewitz, 2005). More recently transfusion has also been introduced for the treatment of sickle cell anemia, owing to its beneficial effects in the treatment of crises and in the reduction of the incidence of stroke. However, as with β-thalassemia major, regular transfusion induces iron overload (Lucania et al., 2011). Thalassemia and sickle cell genes are widely dispersed in tropical and subtropical regions of the world (Weatherall, 2008). Iron absorption may also be enhanced secondary to anemia in patients with β-thalassaemia intermedia, which is also a common disease in South East Asia (Rund and Rachmilewitz, 2005). In contrast to hereditary haemochromatosis, patients suffering from the various haemoglobinopathies outlined above are anaemic and so are not treatable by phlebotomy. Unless these disorders of iron overload can be prevented by chelation therapy, toxic and potentially lethal levels of iron are deposited in the liver, heart and endocrine organs.

5.2 Clinically useful chelators

There are currently three iron chelators available for clinical use, Desferrioxamine (DFO), CP20/deferiprone (DFP) and Deferasirox (DFS).

Desferrioxamine (DFO), a natural siderophore, binds iron(III) extremely tightly, leading to the formation of a stable iron(III) complex (Dhungana et al., 2001), which promotes RE and

hepatocellular iron excretion via both urinary and biliary routes in rats (Hershko, 1978). DFO is effective in preventing complications associated with iron overload in patients with thalassemia major (Brittenham et al., 1994). Unfortunately DFO is not orally active and has to be administered parenterally over prolonged time periods because of its rapid renal clearance. Patient compliance with this regimen is frequently poor (Pippard et al., 1978). Furthermore, even in well-chelated patients, NTBI is still present for a large percentage of the treatment period and therefore gradually loads the heart and endocrine tissues. A large proportion of patients treated with DFO suffer from serious cardiovascular adverse effects (Borgna-Pignatti et al., 2006).

Deferasirox (DFS), a lead compound developed by Novartis, can penetrate membranes easily and possesses good oral availability due to its extreme hydrophobicity (Zhou et al., 2012). DFS has been demonstrated to be efficient at removing liver iron from regularly transfused patients (Cappellini et al., 2010) but is apparently less effective at removing cardiac iron (Wood et al., 2010). By virtue of a high proportion of both the free ligand and the iron complex binding to albumin (greater than 98%), the ligand possesses low toxicity despite its strong lipophilic character (Weiss et al., 2006). Kidney toxicity is the prevalent side effect of this chelator (Rafat et al., 2009), although there is also a high incidence of rashes (Sharma et al., 2015).

CP20/deferiprone (DFP) was the first orally active iron chelator extensively investigated for iron overload chelation therapy. It is a small molecule facilitating good oral absorption by the gastrointestinal tract. DFP is less effective in mobilising iron from hepatocellular iron stores as compared with DFS. However, it is efficient in readily removing iron from cardiac tissue (Pepe et al., 2011). Roughly 60% of DFP is bound to albumin, so there is free DFP available to enter cells and scavenge iron (Seyed Dorraji et al., 2014). Agranulocytosis and neutropenia are the most serious side effects of CP20/deferiprone. Fortunately, both symptoms are reversible on discontinuation of DFP treatment (Hoffbrand et al., 2003)

5.3 Chelators under development

Clearly, at the present time, there is no ideal iron chelator available that is relatively free of toxic side effects. Consequently there is a requirement for the identification of new iron chelating agents with superior iron chelating efficacy / toxicity ratios. Desferrithiocin (DFT) (Figure 5.1 a) is a siderophore isolated from *Streptomyces antibioticus*. It binds iron(III) with a high affinity (pFe^{3+} = 20.4) and forms a 2:1 complex using a phenolate oxygen, a carboxylate oxygen, and a nitrogen atom as ligands at physiological pH (Bergeron et al., 2014). The compound was shown to be an excellent iron chelating agent when administered orally to rodents (Bergeron et al., 1991) and *Cebus apella* primates (Bergeron et al., 1993). However, the predominant side effect associated with DFT is nephrotoxicity (Bergeron et al., 1993). Nevertheless, the remarkable oral bioavailability and iron-chelating efficacy initiated a successful structure−activity investigation aimed at ameliorating DFT-induced nephrotoxicity.

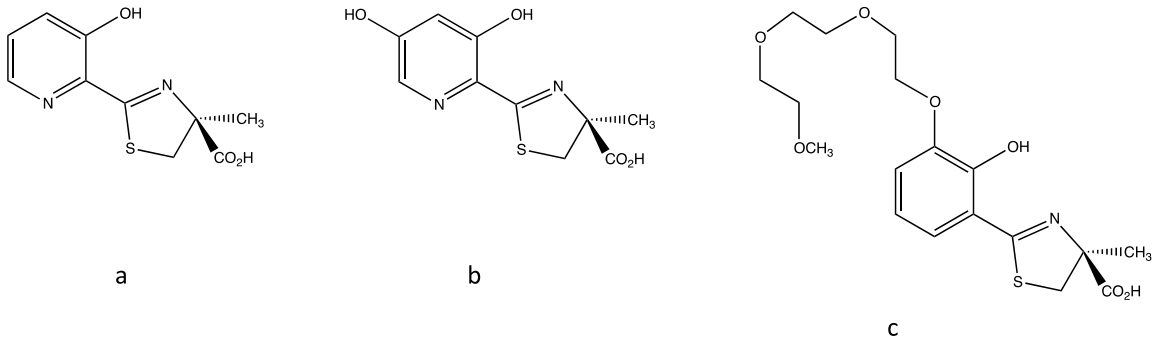

Figure 5.1 Chemical structures of Desferrithiocin (DFT) and analogues
a. Desferrithiocin, b. Deferitrin, c. Deferitazole

A range of such DFT analogues has been investigated and one of these compounds, Deferitrin (Figure 5.1 b) was identified with ameliorated nephrotoxicity. This led to a Phase I human clinical trial by Genzyme. The Initial results were promising when the drug was given s.i.d. (Donovan et al., 2005). However, when the ligand was given b.i.d., unacceptable renal toxicity was observed and the trials were terminated (Galanello et al., 2007). In a further attempt to

develop a chelator lacking such side effects, a series of polyether analogs of desferrithiocin was prepared (Bergeron et al., 2006). A polyether derivative, deferitazole (formerly FBS0701, Figure 5.1 c), was identified as a lead chelator. Deferitazole forms a stable complex with iron(III) with high selectivity under biological conditions. The affinity constant and pFe^{3+} values of deferitazole (log β_2 33.1, pFe^{3+} 22.3) are similar to those of deferasirox (Exjade) (log β_2 36.9, pFe^{3+} 22.5) (Hider et al., 2015). It has been demonstrated to possess 4-fold higher iron chelation efficacy with no observable renal toxicity when compared with deferasirox in preclinical studies (Bergeron et al., 2008). It was subsequently entered into phase I and II clinical trials sponsored by Ferrokin Biosciences and initially promising iron chelating and scavenging was reported (Rienhoff et al., 2011, Neufeld et al., 2012). However, the compound has not been moved to Phase III trial due to neurotoxicity experienced by some of phase II patients (Hider R.C., 2016, pers. comm.)

As discussed in the introduction, we have investigated a range of novel HPOs, but in particular an enantiomer pairs (Chapter 1, Section 1.8), CN128 and CN126 (Figure 5.2). Usually the development of chiral compounds as iron chelating agents is avoided because of the necessity of obtaining a single stereoisomer product rather than a racemic mixture. With most synthetic routes, racemic mixtures are produced, which must be resolved into the two enantiomeric components. However, the synthesis involved in the preparation of the chiral HPOs discussed in this thesis is relatively simple and yields chirally homogenous samples. The synthetic method is characterised by the following steps: Compound I is reacted with compound II to give 3-benzyl-protected maltol (Compound III), and then reacted with different chiral amino alcohols (Compound IV) to get chiral 3-benzyloxypyridin-4-ones (Compound V), finally compound V is deprotected under palladium catalysed carbon as hydrogenation catalyst to form the compound VI (Scheme 5.1, (Hider R. C., 2014). The chiral amino alcohols are prepared from the corresponding D- and L- amino acids by catalytic reaction.

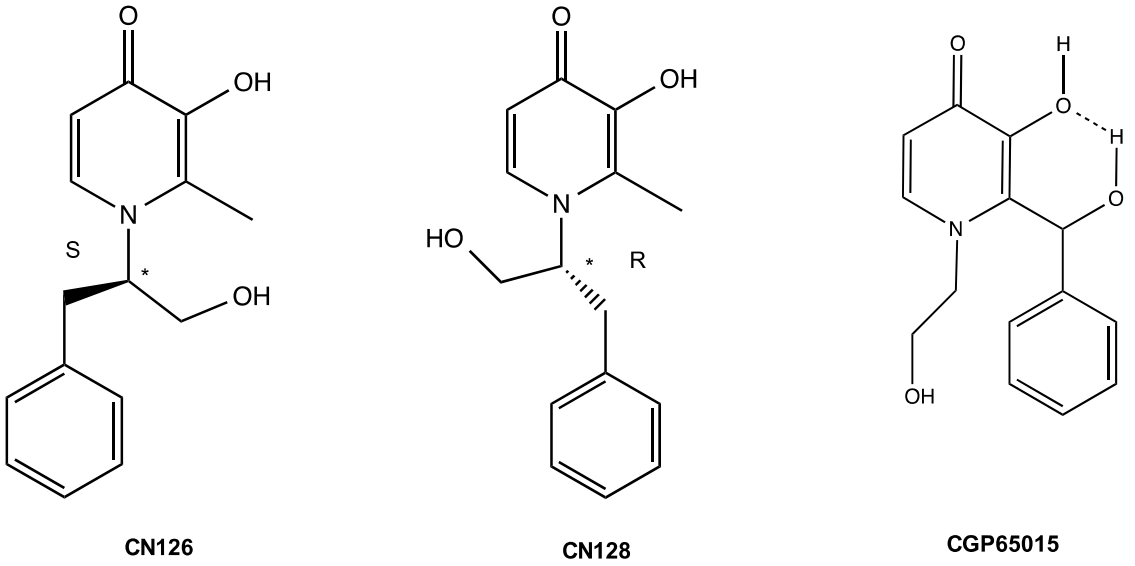

Figure 5.2 Chemical structures of CN128, CN126 and CGP65015

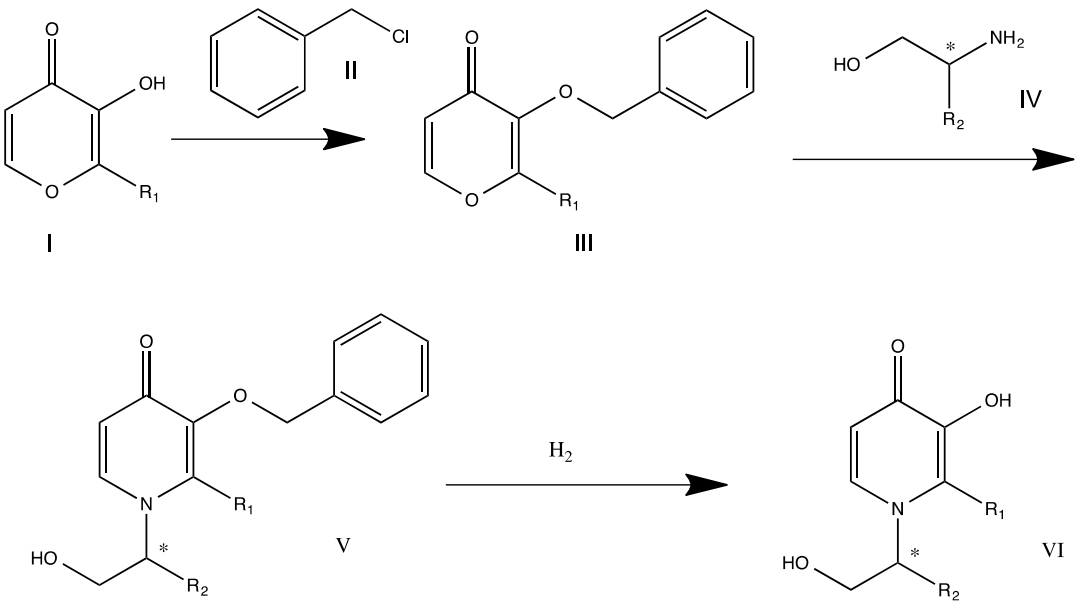

Scheme 5.1 Synthesis of chiral HPOs

As mentioned in the introduction, CGP65015 is the high pFe3+ bidentate hydroxypyridinone developed by Novartis. It is interesting to note the similarities in the structures of CN128 and CGP65015 (Figure 5.2), they have very similar physical parameters, however whereas CN128 is prepared directly from a chiral intermediate (the amino alcohol [IV]) and is over 99% chirally pure, CGP65015 is prepared as a racemic mixture (Lowther et al., 1999, Zbinden, 1997) and has never been resolved into the two pure enantiomeric forms. It was for this reason that Ciba (Basel, Switzerland) did not continue to develop this molecule.

5.4 New lead HPO iron chelators

In this thesis, I have demonstrated the high efficacy of CN128 in iron mobilisation studies over a wide range of doses in an *in vivo* rat ^{59}Fe-ferritin model. Markedly enhanced efficacy was achieved at lower doses than those typically adopted clinically with CP20/deferiprone.

In order for an international pharmaceutical company to take a novel drug into man, there must be a strong “composition of matter”, patent. Unfortunately, CM1, the pegylated HPOs and the closely related CP20/deferiprone analogues are all covered by earlier patents. In contrast, the concept of using enantiomeric pairs has enabled us to obtain Chinese (Yu Y.P., 2011) and European (Hider R. C., 2014) patents.

Further chronic toxicity tests in mice and primates have demonstrated that the *in vivo* toxicity of CN128 is relatively low, in many tests, CN128 was found to be much less toxic than CP20/deferiprone. Significantly no influence on the white cell count in primates was observed with CN128 (Xin, 2016). This data has been submitted to the Chinese FDA. It is planned to initiate a combined Phase I/ Phase II clinical trial early in 2017.

5.5 Development of new system for monitoring HPO metabolism

In order to efficiently monitor the hepatic metabolic profiles of HPOs, we have established an *in vitro* metabolic model using human hepatic microsomes. A sensitive and selective bio-analytical method with high throughput has been developed and validated for the quantification of the

hepatic metabolic depletion of HPOs in the human microsomal incubates. This method includes a solid phase extraction sample clean-up procedure, a UPLC system collaborated into a tandem quadrupole mass spectrometer (TQ-MS) operated in the multiple reaction monitoring (MRM) acquisition mode. This method enabled us to select a promising candidate compound demonstrating markedly reduced glucuronidation compared with CP20/deferiprone, which was subjected to an *in vivo* rat ^{59}Fe-ferritin model for its efficacy study. However, it would have been ideal if we had obtained the metabolic data from rat microsomal incubations. However, we decided to adopt human mirosomes for the major study as this clearly will relate better to further clinical studies, so as to extrapolate the metabolic profiles to the efficacy data.

REFERENCES

References

ABBOUD, S. & HAILE, D. J. 2000. A novel mammalian iron-regulated protein involved in intracellular iron metabolism. *J. Biol. Chem.,* 275**,** 19906-12.

AISEN, P., WESSLING-RESNICK, M. & LEIBOLD, E. A. 1999. Iron metabolism. *Curr. Opin. Chem. Biol.,* 3**,** 200-206.

AJIOKA, R. S., PHILLIPS, J. D. & KUSHNER, J. P. 2006. Biosynthesis of heme in mammals. *Biochim. Biophys. Acta, Mol. Cell. Res.,* 1763**,** 723-736.

AL-REFAIE, F. N., SHEPPARD, L. N., NORTEY, P., WONKE, B. & HOFFBRAND, A. V. 1995. Pharmacokinetics of the oral iron chelator deferiprone (L1) in patients with iron overload. *Brit. J. Haematol.,* 89**,** 403-408.

ANDERSON, L. J., HOLDEN, S., DAVIS, B., PRESCOTT, E., CHARRIER, C. C., BUNCE, N. H., FIRMIN, D. N., WONKE, B., PORTER, J., WALKER, J. M. & PENNELL, D. J. 2001. Cardiovascular T2-star (T2*) magnetic resonance for the early diagnosis of myocardial iron overload. *Eur. Heart J.,* 22**,** 2171-2179.

ANDREWS, N. C. 1999. Disorders of Iron Metabolism. *N. Eng. J. Med.,* 341**,** 1986-1995.

ASCENZI, P., BOCEDI, A., VISCA, P., ALTRUDA, F., TOLOSANO, E., BERINGHELLI, T. & FASANO, M. 2005. Hemoglobin and heme scavenging. *IUBMB Life,* 57**,** 749-59.

BAKER, E., BAKER, S. M. & MORGAN, E. H. 1998. Characterisation of non-transferrin-bound iron (ferric citrate) uptake by rat hepatocytes in culture. *Biochim. Biophys. Acta -Gen. Subjects,* 1380**,** 21-30.

BERGERON, R., STREIFF, R., CREARY, E., DANIELS, R. J., KING, W., LUCHETTA, G., WIEGAND, J., MOERKER, T. & PETER, H. 1993. A comparative study of the iron-clearing properties of desferrithiocin analogues with desferrioxamine B in a Cebus monkey model. *Blood,* 81**,** 2166-2173.

BERGERON, R. J., WIEGAND, J., DIONIS, J. B., EGLI-KARMAKKA, M., FREI, J., HUXLEY-TENCER, A. & PETER, H. H. 1991. Evaluation of desferrithiocin and its synthetic analogs as orally effective iron chelators. *J. Med. Chem.,* 34**,** 2072-2078.

BERGERON, R. J., WIEGAND, J., MCMANIS, J. S. & BHARTI, N. 2014. Desferrithiocin: a search for clinically effective iron chelators. *J. Med. Chem.,* 57**,** 9259-91.

BERGERON, R. J., WIEGAND, J., MCMANIS, J. S., BHARTI, N. & SINGH, S. 2008. Design, synthesis, and testing of non-nephrotoxic desazadesferrithiocin polyether analogues. *J. Med. Chem.,* 51**,** 3913-23.

BERGERON, R. J., WIEGAND, J., MCMANIS, J. S., VINSON, J. R. T., YAO, H., BHARTI, N. & ROCCA, J. R. 2006. (S)-4,5-Dihydro-2-(2-hydroxy-4-hydroxyphenyl)-4-methyl-4-thiazolecarboxylic Acid Polyethers: A Solution to Nephrotoxicity. *J. Med. Chem.,* 49**,** 2772-2783.

BERNHARDT, P. V. 2007. Coordination chemistry and biology of chelators for the treatment of iron overload disorders. *Dalt. Trans.***,** 3214-3220.

BEUTLER, E. 2007. Iron storage disease: facts, fiction and progress. *Blood Cells Mol. Dis.,* 39**,** 140-7.

BEUTLER, E., HOFFBRAND, A. V. & COOK, J. D. 2003. Iron deficiency and overload. *Hematology Am. Soc. Hematol. Educ. Program***,** 40-61.

BORGNA-PIGNATTI, C., CAPPELLINI, M. D., DE STEFANO, P., DEL VECCHIO, G. C., FORNI, G. L., GAMBERINI, M. R., GHILARDI, R., PIGA, A., ROMEO, M. A., ZHAO, H. & CNAAN, A. 2006. Cardiac morbidity and mortality in deferoxamine- or deferiprone-treated patients with thalassemia major. *Blood,* 107**,** 3733-3737.

BORLAKOGLU, J. T., DREW, M. G., WILKINS, J. P. & DILS, R. R. 1990. Effects of molecular substitution patterns on the cytochrome P-450-dependent metabolism of 2,2',3,5,5',6- and 2,2',3,4,4',6-hexachlorobiphenyl by rat liver microsomal monooxygenases. *Biochim. Biophys. Acta,* 1036**,** 167-75.

BRISSOT, P., ROPERT, M., LE LAN, C. & LOREAL, O. 2012. Non-transferrin bound iron: a key role in iron overload and iron toxicity. *Biochim. Biophys. Actal.,* 3**,** 403-10.

BRITTENHAM, G. M., GRIFFITH, P. M., NIENHUIS, A. W., MCLAREN, C. E., YOUNG, N. S., TUCKER, E. E., ALLEN, C. J., FARRELL, D. E. & HARRIS, J. W. 1994. Efficacy of deferoxamine in preventing complications of iron overload in patients with thalassemia major. *N. Engl. J. Med.,* 331**,** 567-573.

BROWN, K. 2012. Efficacy study of chiral HPO compounds.

BUSZEWSKI, B. & NOGA, S. 2012. Hydrophilic interaction liquid chromatography (HILIC)—a powerful separation technique. *Anal. Bioanal. Chem.,* 402**,** 231-247.

CABANTCHIK, Z. I., BREUER, W., ZANNINELLI, G. & CIANCIULLI, P. 2005. LPI-labile plasma iron in iron overload. *Best Pract. Res. Clin. Haematol.,* 18**,** 277-87.

CAMASCHELLA, C., ROETTO, A., CALI, A., DE GOBBI, M., GAROZZO, G., CARELLA, M., MAJORANO, N., TOTARO, A. & GASPARINI, P. 2000. The gene TFR2 is mutated in a new type of haemochromatosis mapping to 7q22. *Nat. Genet.,* 25**,** 14-15.

CAPPELLINI, M. D., PORTER, J., EL-BESHLAWY, A., LI, C.-K., SEYMOUR, J. F., ELALFY, M., GATTERMANN, N., GIRAUDIER, S., LEE, J.-W., CHAN, L. L., LIN, K.-H., ROSE, C., TAHER, A., THEIN, S. L., VIPRAKASIT, V., HABR, D., DOMOKOS, G., ROUBERT, B. & KATTAMIS, A. 2010. Tailoring iron chelation by iron intake and serum ferritin: the prospective EPIC study of deferasirox in 1744 patients with transfusion-dependent anemias. *Haematologica,* 95**,** 557-566.

CARPENTER, C. E. & MAHONEY, A. W. 1992. Contributions of Heme and Nonheme Iron to Human Nutrition. *Crit. Rev. in Food Sci.,* 31**,** 333-367.

CASANOVAS, G., MLECZKO-SANECKA, K., ALTAMURA, S., HENTZE, M. W. & MUCKENTHALER, M. U. 2009. Bone morphogenetic protein (BMP)-responsive elements located in the proximal and distal hepcidin promoter are critical for its response to HJV/BMP/SMAD. *J. Mol. Med. ,* 87**,** 471-80.

CAVILL, I. 1999. Iron status as measured by serum ferritin: the marker and its limitations. *Am. J. Kidney Dis.,* 34**,** s12-s17.

CHAMBERS, E., WAGROWSKI-DIEHL, D. M., LU, Z. & MAZZEO, J. R. 2007. Systematic and comprehensive strategy for reducing matrix effects in LC/MS/MS analyses. *J. Chromatogr. B,* 852**,** 22-34.

CHEN, Y. L. 2013. *Prediction of physicochemical properties for Fe3+ chelating agents.* Ph.D. Thesis, King's College London.

CHENG, Y., ZAK, O., AISEN, P., HARRISON, S. C. & WALZ, T. 2004. Structure of the Human Transferrin Receptor-Transferrin Complex. *Cell,* 116**,** 565-576.

CHIRNOMAS, D., SMITH, A. L., BRAUNSTEIN, J., FINKELSTEIN, Y., PEREIRA, L., BERGMANN, A. K., GRANT, F. D., PALEY, C., SHANNON, M. & NEUFELD, E. J. 2009. Deferasirox pharmacokinetics in patients with adequate versus inadequate response. *Blood,* 114**,** 4009-4013.

CHOUDHURY R. 1995. *Metabolism and Pharmacokinetics of 1-Hydroxyalkyl-3-hydroxypyridin-4-one Chelating Agents.* Ph.D. Thesis, King's College, London.

COLEMAN, M. D. 2010. *Human drug metabolism*, Oxford: Wiley-Blackwell.

CORN, M. 1993. *In:* CORN, M. (ed.) *Handbook of Hazardous Materials.* San Diego: Academic Press.

CRISPONI, G., AMBU, R., CRISTIANI, F., MANCOSU, G., NURCHI, V. M., PINNA, R. & FAA, G. 2000. Does iron concentration in a liver needle biopsy accurately reflect hepatic iron burden in β-thalassemia? *Clin. Chem.,* 46**,** 1185-1188.

DE DOMENICO, I., WARD, D. M. & KAPLAN, J. 2007. Hepcidin regulation: ironing out the details. *J. Clin. Invest. ,* 117**,** 1755-1758.

DEJAEGHER, B., MANGELINGS, D. & VANDER HEYDEN, Y. 2008. Method development for HILIC assays. *J. Sep. Sci.,* 31**,** 1438-48.

DEVANUR, L. D., EVANS, R. W., EVANS, P. J. & HIDER, R. C. 2008. Chelator-facilitated removal of iron from transferrin: relevance to combined chelation therapy. *Biochem. J.,* 409**,** 439-447.

DHUNGANA, S., WHITE, P. S. & CRUMBLISS, A. L. 2001. Crystal structure of ferrioxamine B: a comparative analysis and implications for molecular recognition. *J. Biol. Inorg. Chem.,* 6**,** 810-8.

DONOVAN, A., BROWNLIE, A., ZHOU, Y., SHEPARD, J., PRATT, S. J., MOYNIHAN, J., PAW, B. H., DREJER, A., BARUT, B., ZAPATA, A., LAW, T. C., BRUGNARA, C., LUX, S. E., PINKUS, G. S., PINKUS, J. L., KINGSLEY, P. D., PALIS, J., FLEMING, M. D., ANDREWS, N. C. & ZON, L. I. 2000. Positional cloning of zebrafish ferroportin1 identifies a conserved vertebrate iron exporter. *Nature,* 403**,** 776-81.

DONOVAN, J. M., PLONE, M., DAGHER, R., BREE, M. & MARQUIS, J. 2005. Preclinical and clinical development of deferitrin, a novel, orally available iron chelator. *Ann. N. Y. Acad. Sci.,* 1054**,** 492-4.

EPEMOLU, R. O., ACKERMAN, R., PORTER, J. B., HIDER, R. C., DAMANI, L. A. & SINGH, S. 1994. HPLC determination of 1,2-diethyl-3-hydroxypyridin-4-one (CP94), its iron complex [Fe(III)(CP94)3] and glucuronide conjugate [CP94-GLUC] in serum and urine of thalassaemic

patients. *J. Pharm. Biomed. Anal.,* 12**,** 923-30.
EPEMOLU, R. O., SINGH, S., HIDER, R. C. & DAMANI, L. A. 1990. Chromatography of 3-hydroxypyridin-4-ones: novel orally active iron chelators. *J. Chromatogr. A* 519**,** 171-178.
FARRELL, T., POQUET, L., DIONISI, F., BARRON, D. & WILLIAMSON, G. 2011. Characterization of hydroxycinnamic acid glucuronide and sulfate conjugates by HPLC–DAD–MS2: Enhancing chromatographic quantification and application in Caco-2 cell metabolism. *J. Pharmaceut. Biomed. ,* 55**,** 1245-1254.
FEDER, J. N., GNIRKE, A., THOMAS, W., TSUCHIHASHI, Z., RUDDY, D. A., BASAVA, A., DORMISHIAN, F., DOMINGO, R., ELLIS, M. C. & FULLAN, A. 1996. A novel MHC class I-like gene is mutated in patients with hereditary haemochromatosis. *Nat. Genet. ,* 13**,** 399-408.
FINKELSTEIN, J. 2009. Metalloproteins. *Nature,* 460**,** 813-813.
FISHER, M. B., CAMPANALE, K., ACKERMANN, B. L., VANDENBRANDEN, M. & WRIGHTON, S. A. 2000. In vitro glucuronidation using human liver microsomes and the pore-forming peptide alamethicin. *Drug Metab. Dispos.,* 28**,** 560-6.
FLEMING, M. D., ROMANO, M. A., SU, M. A., GARRICK, L. M., GARRICK, M. D. & ANDREWS, N. C. 1998. Nramp2 is mutated in the anemic Belgrade (b) rat: evidence of a role for Nramp2 in endosomal iron transport. *Proc. Natl. Acad. Sci. U S A,* 95**,** 1148-53.
FLEMING, M. D., TRENOR, C. C., 3RD, SU, M. A., FOERNZLER, D., BEIER, D. R., DIETRICH, W. F. & ANDREWS, N. C. 1997. Microcytic anaemia mice have a mutation in Nramp2, a candidate iron transporter gene. *Nat. Genet.,* 16**,** 383-6.
FULCERI, R., BANHEGYI, G., GAMBERUCCI, A., GIUNTI, R., MANDL, J. & BENEDETTI, A. 1994. Evidence for the intraluminal positioning of p-nitrophenol UDP-glucuronosyltransferase activity in rat liver microsomal vesicles. *Arch. Biochem. Biophys.,* 309**,** 43-6.
GALANELLO, R., FORNI, G., JONES, A., KELLY, A., WILLEMSEN, A., HE, X., JOHNSTON, A., FULLER, D., DONOVAN, J. & PIGA, A. A dose escalation study of the pharmacokinetics, safety & efficacy of deferitrin an oral iron chelator in beta thalassaemia patients. Blood, 2007. AMER SOC HEMATOLOGY 1900 M STREET. NW SUITE 200, WASHINGTON, DC 20036 USA, 784A-785A.
GAO, S., BHOOPATHY, S., ZHANG, Z.-P., WRIGHT, D. S., JENKINS, R. & KARNES, H. T. 2006. Evaluation of volatile ion-pair reagents for the liquid chromatography–mass spectrometry analysis of polar compounds and its application to the determination of methadone in human plasma. *J. Pharm. Biomed. Anal.,* 40**,** 679-688.
GARBY, L. & NOYES, W. D. 1959. Studies on hemoglobin metabolism. I. The kinetic properties of the plasma hemoglobin pool in normal man. *J. Clin. Invest.,* 38**,** 1479.
GIARDINA, P. J. & GRADY, R. W. 2001. Chelation therapy in β-thalassemia: An optimistic update. *Semin. in Hematol.,* 38**,** 360-366.
GKOUVATSOS, K., PAPANIKOLAOU, G. & PANTOPOULOS, K. 2012. Regulation of iron transport and the role of transferrin. *Biochim. Biophys. Actal.,* 3**,** 188-202.
GLICKSTEIN, H., EL, R. B., LINK, G., BREUER, W., KONIJN, A. M., HERSHKO, C., NICK, H. & CABANTCHIK, Z. I. 2006. Action of chelators in iron-loaded cardiac cells: Accessibility to intracellular labile iron and functional consequences. *Blood,* 108**,** 3195-203.
GOUCHER, E., KICMAN, A., WOLFF, K., SMITH, N. & JICKELLS, S. 2010. Hydrophilic stationary phases: a practical approach for the co-analysis of compounds with varying polarity in biological matrices. *J. Sep. Sci.,* 33**,** 955-65.
GRADY, R., GRAZIANO, J., WHITE, G., JACOBS, A. & CERAMI, A. 1978. The development of new iron-chelating drugs. II. *J. Pharm. Exp. Ther.,* 205**,** 757-765.
GRAZIANO, J., GRADY, R. & CERAMI, A. 1974. The identification of 2, 3-dihydroxybenzoic acid as a potentially useful iron-chelating drug. *J. Pharm. Exp. Ther. ,* 190**,** 570-575.
GYPARAKI, M., PORTER, J., HIRANI, S., STREATER, M., HIDER, R. & HUEHNS, E. 1987. In vivo evaluation of hydroxypyridone iron chelators in a mouse model. *Acta haematol.,* 78**,** 217-221.
HAGAR, W. & VICHINSKY, E. 2008. Advances in clinical research in sickle cell disease. *Br. J. Haematol.,* 141**,** 346-356.
HALLIWELL, B. & GUTTERIDGE, J. M. 1984. Oxygen toxicity, oxygen radicals, transition metals and disease. *Biochem. J.,* 219**,** 1-14.
HANWELL, M. D., CURTIS, D. E., LONIE, D. C., VANDERMEERSCH, T., ZUREK, E. & HUTCHISON, G. R. 2012. Avogadro: an advanced semantic chemical editor, visualization, and analysis platform. *J. Cheminform.,* 4**,** 1-17.
HARRIS, Z. L., DURLEY, A. P., MAN, T. K. & GITLIN, J. D. 1999. Targeted gene disruption reveals an

essential role for ceruloplasmin in cellular iron efflux. *Proc. Natl. Acad. Sci. U S A,* 96**,** 10812-7.
HEATON, J. C. & MCCALLEY, D. V. 2016. Some factors that can lead to poor peak shape in hydrophilic interaction chromatography, and possibilities for their remediation. *J. Chromatogr. A,* 1427**,** 37-44.
HEINEMANN, I. U., JAHN, M. & JAHN, D. 2008. The biochemistry of heme biosynthesis. *Arch. Biochem. Biophys.,* 474**,** 238-251.
HENTZE, M. W., MUCKENTHALER, M. U. & ANDREWS, N. C. 2004. Balancing acts: molecular control of mammalian iron metabolism. *Cell,* 117**,** 285-297.
HERSHKO, C. 1978. Determinants of fecal and urinary iron excretion in desferrioxamine treated rats. *Blood,* 51**,** 415-423.
HERSHKO, C., COOK, J. D. & FINCH, D. A. 1973. Storage iron kinetics. 3. Study of desferrioxamine action by selective radioiron labels of RE and parenchymal cells. *J. Lab Clin. Med.,* 81**,** 876-86.
HERSHKO, C., KONIJN, A. M., NICK, H. P., BREUER, W., CABANTCHIK, Z. I. & LINK, G. 2001. ICL670A: a new synthetic oral chelator: evaluation in hypertransfused rats with selective radioiron probes of hepatocellular and reticuloendothelial iron stores and in iron-loaded rat heart cells in culture. *Blood,* 97**,** 1115-22.
HIDER R. C., L. Z. D., YU Y.P., LI Z. . 2014. *European patent: EP 2692724B1*.
HIDER R. C., T. G. S., LIU Z. D. . 1998. *International Patent WO98/54138*.
HIDER, R. C. 2002. Nature of nontransferrin-bound iron. *Eur. J. Clin. Invest.,* 32 Suppl 1**,** 50-4.
HIDER, R. C., CHOUDHURY, R., RAI, B. L., DEHKORDI, L. S. & SINGH, S. 1996. Design of orally active iron chelators. *Acta Haematol.,* 95**,** 6-12.
HIDER RC, K. G., SILVER J. 1982. *U.K. Patent: GB- 2118176*.
HIDER, R. C. & KONG, X. 2013. Iron speciation in the cytosol: an overview. *Dalt. Trans.,* 42**,** 3220-9.
HIDER, R. C., KONG, X., ABBATE, V., HARLAND, R., CONLON, K. & LUKER, T. 2015. Deferitazole, a new orally active iron chelator. *Dalt. Trans.,* 44**,** 5197-5204.
HOFFBRAND, A. V., COHEN, A. & HERSHKO, C. 2003. Role of deferiprone in chelation therapy for transfusional iron overload. *Blood,* 102**,** 17-24.
HUYNEN, M. A., SNEL, B., BORK, P. & GIBSON, T. J. 2001. The phylogenetic distribution of frataxin indicates a role in iron-sulfur cluster protein assembly. *Hum. Mol. Genet.,* 10**,** 2463-8.
ICH. *Guidlines: ICH* [Online]. N.P. Available: http://www.ich.org/products/guidelines.html [Accessed 10 Nov. 2015].
JACOBS, A. 1976. An intracellular transit iron pool. *Ciba Found. Symp.***,** 91-106.
JEMAL, M. & XIA, Y. Q. 1999. The need for adequate chromatographic separation in the quantitative determination of drugs in biological samples by high performance liquid chromatography with tandem mass spectrometry. *Rapid Commun. Mass Spectrom.,* 13**,** 97-106.
JEONG, S. Y. & DAVID, S. 2003. Glycosylphosphatidylinositol-anchored ceruloplasmin is required for iron efflux from cells in the central nervous system. *J. Biol. Chem.,* 278**,** 27144-8.
JIA, L. & LIU, X. 2007. The conduct of drug metabolism studies considered good practice (II): in vitro experiments. *Curr. Drug Metab.,* 8**,** 822.
JIAN, W., EDOM, R. W., XU, Y. & WENG, N. 2010. Recent advances in application of hydrophilic interaction chromatography for quantitative bioanalysis. *J. Sep. Sci.,* 33**,** 681-97.
KAMINSKY, L. S. & ZHANG, Z. Y. 1997. Human P450 metabolism of warfarin. *Pharmacol. Ther.,* 73**,** 67-74.
KAUTZ, L., JUNG, G., VALORE, E. V., RIVELLA, S., NEMETH, E. & GANZ, T. 2014. Identification of erythroferrone as an erythroid regulator of iron metabolism. *Nat. Genet. ,* 46**,** 678.
KESKI-HYNNILA, H., KURKELA, M., ELOVAARA, E., ANTONIO, L., MAGDALOU, J., LUUKKANEN, L., TASKINEN, J. & KOSTIAINEN, R. 2002. Comparison of electrospray, atmospheric pressure chemical ionization, and atmospheric pressure photoionization in the identification of apomorphine, dobutamine, and entacapone phase II metabolites in biological samples. *Anal. Chem.,* 74**,** 3449-57.
KONSTANTINOU, I. K. 2006. *Antifouling paint biocides,* Berlin, Springer
KONTOGHIORGHES, G. J., ALDOURI, M. A., HOFFBRAND, A. V., BARR, J., WONKE, B., KOUROUCLARIS, T. & SHEPPARD, L. 1987. Effective chelation of iron in beta thalassaemia with the oral chelator 1, 2-dimethyl-3-hydroxypyrid-4-one. *Br. Med. J. (Clin. Res. Ed.),* 295**,** 1509-1512.
KORFMACHER, W. A. 2005. *Using mass spectrometry for drug metabolism studies,* Boca Raton, FL: CRC Press.

KOSTIAINEN, R., KOTIAHO, T., KUURANNE, T. & AURIOLA, S. 2003. Liquid chromatography/atmospheric pressure ionization–mass spectrometry in drug metabolism studies. *J. Mass Spectrom.,* 38**,** 357-372.

KOZYRAKI, R., FYFE, J., VERROUST, P. J., JACOBSEN, C., DAUTRY-VARSAT, A., GBUREK, J., WILLNOW, T. E., CHRISTENSEN, E. I. & MOESTRUP, S. K. 2001. Megalin-dependent cubilin-mediated endocytosis is a major pathway for the apical uptake of transferrin in polarized epithelia. *Proc. Natl. Acad. Sci. U S A,* 98**,** 12491-6.

KRISTIANSEN, M., GRAVERSEN, J. H., JACOBSEN, C., SONNE, O., HOFFMAN, H.-J., LAW, S. K. A. & MOESTRUP, S. K. 2001. Identification of the haemoglobin scavenger receptor. *Nature,* 409**,** 198-201.

KUMAR, G. N. & SURAPANENI, S. 2001. Role of drug metabolism in drug discovery and development. *Med. Res. Rev.,* 21**,** 397-411.

KUSHNER, J. P., PORTER, J. P. & OLIVIERI, N. F. 2001. Secondary iron overload. *Hematology Am. Soc. Hematol. Educ. Program***,** 47-61.

LAKHAL, S., TALBOT, N. P., CROSBY, A., STOEPKER, C., TOWNSEND, A. R., ROBBINS, P. A., PUGH, C. W., RATCLIFFE, P. J. & MOLE, D. R. 2009. Regulation of growth differentiation factor 15 expression by intracellular iron. *Blood,* 113**,** 1555-1563.

LAULHERE, J. P., LABOURE, A. M. & BRIAT, J. F. 1989. Mechanism of the transition from plant ferritin to phytosiderin. *J. Biol. Chem.,* 264**,** 3629-35.

LEE, M. & ZHU, M. 2011. *Mass spectrometry in drug metabolism and disposition,* Hoboken, N.J.: Wiley.

LEIBOLD, E. A. & MUNRO, H. N. 1988. Cytoplasmic protein binds in vitro to a highly conserved sequence in the 5' untranslated region of ferritin heavy- and light-subunit mRNAs. *Proc. Natl. Acad. Sci. U S A,* 85**,** 2171-2175.

LETT, E., KRISZT, W., DE SANDRO, V., DUCROTOY, G. & RICHERT, L. 1992. Optimal detergent activation of rat liver microsomal UDP-glucuronosyl transferases toward morphine and 1-naphthol: contribution to induction and latency studies. *Biochem. Pharmacol.,* 43**,** 1649-53.

LI, J., LU, Z., KONG, X., MA, Y., ZHANG, X., BANSAL, S. S., ABBATE, V. & HIDER, R. C. 2015a. Design and synthesis of novel pegylated iron chelators with decreased metabolic rate. *Future Med. Chem.*

LI, W., ZHANG, J. & FRANCIS, L. S. 2013. *Handbook of LC-MS Bioanalysis: Best Practices, Experimental Protocols, and Regulations*, John Wiley & Sons.

LI, Z., HAN, J., SUN, S. A., CHEN, K. & TANG, D. Q. 2015b. Hydrophilic Interaction Liquid Chromatography/Mass Spectrometry: An Attractive and Prospective Method for the Quantitative Bioanalysis in Drug Metabolism. *Curr. Drug Metab.*

LILL, R. & MUHLENHOFF, U. 2006. Iron-sulfur protein biogenesis in eukaryotes: components and mechanisms. *Annu. Rev. Cell Dev. Biol.,* 22**,** 457-86.

LIU, D. Y., LIU, Z. D., LU, S. L. & HIDER, R. C. 1999a. Gradient ion-pair high-performance liquid chromatographic method for analysis of 3-hydroxypyridin-4-one iron chelators. *J. Chromatogr. B Biomed. Sci. Appl.,* 730**,** 135-9.

LIU, Z. D. 1997. *Design of orally active iron(III) chelators* Ph.D. Thesis, King's College London.

LIU, Z. D. & HIDER, R. C. 2002. Design of clinically useful iron(III)-selective chelators. *Med. Res. Rev.,* 22**,** 26-64.

LIU, Z. D., KHODR, H. H., LIU, D. Y., LU, S. L. & HIDER, R. C. 1999b. Synthesis, Physicochemical Characterization, and Biological Evaluation of 2-(1‘-Hydroxyalkyl)-3-hydroxypyridin-4-ones: Novel Iron Chelators with Enhanced pFe3+ Values. *J. Med. Chem. ,* 42**,** 4814-4823.

LIU, Z. D., LU, S. L. & HIDER, R. C. 1999c. In vivo iron mobilisation evaluation of hydroxypyridinones in 59Fe-ferritin-loaded rat model. *Biochem. Pharmacol.,* 57**,** 559-566.

LIUZZI, J. P., AYDEMIR, F., NAM, H., KNUTSON, M. D. & COUSINS, R. J. 2006. Zip14 (Slc39a14) mediates non-transferrin-bound iron uptake into cells. *Proc. Natl. Acad. Sci. U S A,* 103**,** 13612-13617.

LOWTHER, N., FOX, R., FALLER, B., NICK, H., JIN, Y., SERGEJEW, T., HIRSCHBERG, Y., OBERLE, R. & DONNELLY, H. 1999. In vitro and in situ permeability of a 'second generation' hydroxypyridinone oral iron chelator: correlation with physico-chemical properties and oral activity. *Pharm. Res.,* 16**,** 434-440.

LU, H. 2007. Stereoselectivity in drug metabolism. *Expert Opin. Drug Metab. Toxicol.,* 3**,** 149-58.

LU, S. L., GOSRIWATANA, I., LIU, D. Y., LIU, Z. D., MALLET, A. I. & HIDER, R. C. 2000. Biliary and urinary metabolic profiles of 1,2-diethyl-3-hydroxypyridin-4-one (CP94) in the rat. *Drug Metab. Dispos.,* 28**,** 873-9.

LU, S. L., LIU, Z. D., LIU, D. Y. & HIDER, R. C. 1998. In - vivo metabolism of 1 - (3′ - hydroxypropyl) - 2 - methyl - 3 - hydroxypyridin - 4 - one (CP41) and 1 - (2′ - hydroxyethyl) - 2 - ethyl - 3 - hydroxypyridin - 4 - one (CP102) by rat. *J. Pharm. Pharmacol.,* 50**,** 199-199.

LUCANIA, G., VITRANO, A., FILOSA, A. & MAGGIO, A. 2011. Chelation treatment in sickle - cell - anaemia: much ado about nothing? *Br. J. Haematol.,* 154**,** 545-555.

LUZZATTO, L. & GOODFELLOW, P. 1989. Sickle cell anaemia. A simple disease with no cure. *Nature* 337**,** 17-8.

MA, L. & CARR, P. W. 2007. Loss of bonded phase in reversed-phase liquid chromatography in acidic eluents and practical ways to improve column stability. *Anal. Chem.,* 79**,** 4681-4686.

MA, Y., ABBATE, V. & HIDER, R. 2015. Iron-sensitive fluorescent probes: monitoring intracellular iron pools. *Metallomics,* 7**,** 212-222.

MATUSZEWSKI, B. K., CONSTANZER, M. L. & CHAVEZ-ENG, C. M. 2003. Strategies for the Assessment of Matrix Effect in Quantitative Bioanalytical Methods Based on HPLC–MS/MS. *Anal. Chem.,* 75**,** 3019-3030.

MCCANCE, R. A. & WIDDOWSON, E. M. 1937. Absorption and excretion of iron. *Lancet,* 230**,** 680-684.

MCKIE, A. T., BARROW, D., LATUNDE-DADA, G. O., ROLFS, A., SAGER, G., MUDALY, E., MUDALY, M., RICHARDSON, C., BARLOW, D., BOMFORD, A., PETERS, T. J., RAJA, K. B., SHIRALI, S., HEDIGER, M. A., FARZANEH, F. & SIMPSON, R. J. 2001. An iron-regulated ferric reductase associated with the absorption of dietary iron. *Science,* 291**,** 1755-9.

MCKIE, A. T., MARCIANI, P., ROLFS, A., BRENNAN, K., WEHR, K., BARROW, D., MIRET, S., BOMFORD, A., PETERS, T. J., FARZANEH, F., HEDIGER, M. A., HENTZE, M. W. & SIMPSON, R. J. 2000. A Novel Duodenal Iron-Regulated Transporter, IREG1, Implicated in the Basolateral Transfer of Iron to the Circulation. *Mol. Cell,* 5**,** 299-309.

MEECH, R. & MACKENZIE, P. I. 1997. Structure and function of uridine diphosphate glucuronosyltransferases. *Clin. Exp. Pharmacol. Physiol.,* 24**,** 907-15.

MIZUTANI, K., TOYODA, M. & MIKAMI, B. 2012. X-ray structures of transferrins and related proteins. *Biochim. Biophys. Actal. - Gen. Sub.,* 1820**,** 203-211.

MOLINSPIRATION. 2015. *Calculation of Molecular Properties and Bioactivity Score* [Online]. Available: http://www.molinspiration.com/cgi-bin/properties [Accessed 19 Oct. 2015].

MUNRO, H. N. & LINDER, M. C. 1978. Ferritin: structure, biosynthesis, and role in iron metabolism. *Physiol. Rev.,* 58**,** 317-96.

NAEGELE, E. 2011. *Making your LC Method Compatible with Mass Spectrometry* [Online]. Available: http://www.agilent.com/cs/library/technicaloverviews/Public/5990--7413EN.pdf [Accessed 15 Nov. 2015].

NEMETH, E., TUTTLE, M. S., POWELSON, J., VAUGHN, M. B., DONOVAN, A., WARD, D. M., GANZ, T. & KAPLAN, J. 2004. Hepcidin regulates cellular iron efflux by binding to ferroportin and inducing its internalization. *Science,* 306**,** 2090-3.

NEUFELD, E. J., GALANELLO, R., VIPRAKASIT, V., AYDINOK, Y., PIGA, A., HARMATZ, P., FORNI, G. L., SHAH, F. T., GRACE, R. F., PORTER, J. B., WOOD, J. C., PEPPE, J., JONES, A. & RIENHOFF, H. Y., JR. 2012. A phase 2 study of the safety, tolerability, and pharmacodynamics of FBS0701, a novel oral iron chelator, in transfusional iron overload. *Blood,* 119**,** 3263-8.

OHGAMI, R. S., CAMPAGNA, D. R., MCDONALD, A. & FLEMING, M. D. 2006. The Steap proteins are metalloreductases. *Blood,* 108**,** 1388-1394.

OLESON, L. & COURT, M. H. 2008. Effect of the beta-glucuronidase inhibitor saccharolactone on glucuronidation by human tissue microsomes and recombinant UDP-glucuronosyltransferases. *J. Pharm. Pharmacol.,* 60**,** 1175-82.

OSTERLOH, K. & AISEN, P. 1989. Pathways in the binding and uptake of ferritin by hepatocytes. *Biochim. Biophys. Acta,* 1011**,** 40-5.

OUDIT, G. Y., SUN, H., TRIVIERI, M. G., KOCH, S. E., DAWOOD, F., ACKERLEY, C., YAZDANPANAH, M., WILSON, G. J., SCHWARTZ, A., LIU, P. P. & BACKX, P. H. 2003. L-type Ca2+ channels provide a major pathway for iron entry into cardiomyocytes in iron-overload cardiomyopathy. *Nat. Med.,* 9**,** 1187-94.

OWEN, D. & KÜHN, L. C. 1987. Noncoding 3' sequences of the transferrin receptor gene are required for mRNA regulation by iron. *EMBO J.,* 6**,** 1287-1293.

PANGJIT, K., BANJERDPONGCHAI, R., PHISALAPHONG, C., FUCHAROEN, S., XIE, Y. Y., LU, Z. D., HIDER, R. C. & SRICHAIRATANAKOOL, S. 2015. Characterisation of a novel oral iron chelator: 1-(N-

Acetyl-6-Aminohexyl)-3-Hydroxy-2-Methylpyridin-4-one. *J. Pharm. Pharmacol.,* 67**,** 703-13.
PARADKAR, P. N., ZUMBRENNEN, K. B., PAW, B. H., WARD, D. M. & KAPLAN, J. 2009. Regulation of mitochondrial iron import through differential turnover of mitoferrin 1 and mitoferrin 2. *Mol. Cell. Biol.,* 29**,** 1007-16.
PATEL, B. K. & HUTT, A. J. 2004. Stereoselectivity in drug action and disposition: an overview. *Chirality in drug design and development. New York: Marcel Dekker Inc***,** 139-190.
PEARSON, P. G. & WIENKERS, L. C. 2009. *Handbook of Drug Metabolism,* New York, Informa Healthcare USA.
PEPE, A., MELONI, A., CAPRA, M., CIANCIULLI, P., PROSSOMARITI, L., MALAVENTURA, C., PUTTI, M. C., LIPPI, A., ROMEO, M. A., BISCONTE, M. G., FILOSA, A., CARUSO, V., QUARTA, A., PITROLO, L., MISSERE, M., MIDIRI, M., ROSSI, G., POSITANO, V., LOMBARDI, M. & MAGGIO, A. 2011. Deferasirox, deferiprone and desferrioxamine treatment in thalassemia major patients: cardiac iron and function comparison determined by quantitative magnetic resonance imaging. *Haematologica,* 96**,** 41-47.
PERKINELMER. *Iron-59 decay table* [Online]. Available: https://ehs.missouri.edu/rad/isotopedata/fe-59decaytable.pdf [Accessed 29 Nov. 2015].
PETTERSEN, E. F., GODDARD, T. D., HUANG, C. C., COUCH, G. S., GREENBLATT, D. M., MENG, E. C. & FERRIN, T. E. 2004. UCSF Chimera--a visualization system for exploratory research and analysis. *J. Comput. Chem.,* 25**,** 1605-12.
PIETRANGELO, A. 2006. Hereditary hemochromatosis. *Biochim. Biophys. Acta - Mol. Cell Res.,* 1763**,** 700-710.
PIGA, A., GAGLIOTI, C., FOGLIACCO, E. & TRICTA, F. 2003. Comparative effects of deferiprone and deferoxamine on survival and cardiac disease in patients with thalassemia major: a retrospective analysis. *Haematologica.,* 88**,** 489-496.
PIPPARD, M., JOHNSON, D. & FINCH, C. 1981. A rapid assay for evaluation of iron-chelating agents in rats. *Blood,* 58**,** 685-692.
PIPPARD, M. J., CALLENDER, S. T. & WEATHERALL, D. J. 1978. Intensive iron-chelation therapy with desferrioxamine in iron-loading anaemias. *Clin. Sci. Mol. Med.,* 54**,** 99-106.
PITT, C., GUPTA, G., ESTES, W., ROSENKRANTZ, H., METTERVILLE, J., CRUMBLISS, A. L., PALMER, R., NORDQUEST, K., HARDY, K. & WHITCOMB, D. 1979. The selection and evaluation of new chelating agents for the treatment of iron overload. *J. Pharm. Exp. Ther.,* 208**,** 12-18.
PIYAMONGKOL, S., MA, Y. M., KONG, X. L., LIU, Z. D., AYTEMIR, M. D., VAN DER HELM, D. & HIDER, R. C. 2010. Amido‐3‐hydroxypyridin‐4‐ones as Iron (III) Ligands. *Chem. Eur. J.* , 16**,** 6374-6381.
PORTER, J. B. 2001. Deferoxamine pharmacokinetics. *Semin. Hematol.,* 38**,** 63-8.
PORTER, J. B., HUEHNS, E. R. & HIDER, R. C. 1989a. The development of iron chelating drugs. *Baillieres Clin. Haematol.,* 2**,** 257-92.
PORTER, J. B., JASWON, M. S., HUEHNS, E. R., EAST, C. A. & HAZELL, J. W. 1989b. Desferrioxamine ototoxicity: evaluation of risk factors in thalassaemic patients and guidelines for safe dosage. *Br. J. Haematol.,* 73**,** 403-9.
PORTER, J. B., SINGH, S., HOYES, K. P., EPEMOLU, O., ABEYSINGHE, R. D. & HIDER, R. C. 1994. Lessons from preclinical and clinical studies with 1,2-diethyl-3-hydroxypyridin-4-one, CP94 and related compounds. *Adv. Exp. Med. Biol.,* 356**,** 361-70.
RAFAT, C., FAKHOURI, F., RIBEIL, J.-A., DELARUE, R. & LE QUINTREC, M. 2009. Fanconi Syndrome Due to Deferasirox. *Amer. J. Kid. Dis.* , 54**,** 931-934.
RAI, B. L., LIU, Z. D., LIU, D. Y., LU, S. L. & HIDER, R. C. 1999. Synthesis, physicochemical properties and biological evaluation of ester prodrugs of 3-hydroxypyridin-4-ones: design of orally active chelators with clinical potential. *Eur. J. Med. Chem.,* 34**,** 475-485.
RAYMOND, K. N. & CARRANO, C. J. 1979. Coordination chemistry and microbial iron transport. *Acc. Chem. Res.,* 12**,** 183-190.
RIENHOFF, H. Y., VIPRAKASIT, V., TAY, L., HARMATZ, P., VICHINSKY, E., CHIRNOMAS, D., KWIATKOWSKI, J. L., TAPPER, A., KRAMER, W., PORTER, J. B. & NEUFELD, E. J. 2011. A phase 1 dose-escalation study: safety, tolerability, and pharmacokinetics of FBS0701, a novel oral iron chelator for the treatment of transfusional iron overload. *Haematologica,* 96**,** 521-525.
ROSENFELD, J. 2009. *Sample preparation for hyphenated analytical techniques*, John Wiley & Sons.
ROŠKAR, R. & LUŠIN, T. T. 2012. *Analytical Methods for Quantification of Drug Metabolites in*

Biological Samples, INTECH Open Access Publisher.
ROUAULT, T. A. 2006. The role of iron regulatory proteins in mammalian iron homeostasis and disease. *Nat. Chem. Biol.,* 2**,** 406-414.
RUND, D. & RACHMILEWITZ, E. 2005. β-Thalassemia. *N. Eng. J. Med.,* 353**,** 1135-1146.
SCHMIDT, P. J., TORAN, P. T., GIANNETTI, A. M., BJORKMAN, P. J. & ANDREWS, N. C. 2008. The Transferrin Receptor Modulates Hfe-Dependent Regulation of Hepcidin Expression. *Cell Metab. ,* 7**,** 205-214.
SCHRIER, S. L. 2002. Pathophysiology of thalassemia. *Curr. Opin. Hematol.,* 9**,** 123-6.
SERGEJEW, T., FORGIARINI, P. & SCHNEBLI, H.-P. 2000. Chelator-induced iron excretion in iron-overloaded marmosets. *Br. J. Haematol. ,* 110**,** 985-992.
SEYED DORRAJI, M. S., PANAHI AZAR, V. & RASOULIFARD, M. H. 2014. Interaction between deferiprone and human serum albumin: Multi-spectroscopic, electrochemical and molecular docking methods. *Eur. J. Pharm. Sci.,* 64**,** 9-17.
SHARMA, A., ARORA, E. & SINGH, H. 2015. Hypersensitivity reaction with deferasirox. *J. Pharmacol. Pharmacother. ,* 6**,** 105-106.
SHAYEGHI, M., LATUNDE-DADA, G. O., OAKHILL, J. S., LAFTAH, A. H., TAKEUCHI, K., HALLIDAY, N., KHAN, Y., WARLEY, A., MCCANN, F. E., HIDER, R. C., FRAZER, D. M., ANDERSON, G. J., VULPE, C. D., SIMPSON, R. J. & MCKIE, A. T. 2005. Identification of an Intestinal Heme Transporter. *Cell,* 122**,** 789-801.
SHINDO, M., TORIMOTO, Y., SAITO, H., MOTOMURA, W., IKUTA, K., SATO, K., FUJIMOTO, Y. & KOHGO, Y. 2006. Functional role of DMT1 in transferrin-independent iron uptake by human hepatocyte and hepatocellular carcinoma cell, HLF. *Hepatol. Res.,* 35**,** 152-62.
SIES, H. & PACKER, L. 2005. *Phase II conjugation enzymes and transport systems*, Gulf Professional Publishing.
SINGH, S., CHOUDHURY, R., EPEMOLU, R. O. & HIDER, R. C. 1996. Metabolism and pharmacokinetics of 1-(2'-hydroxy-ethyl)- and 1-(3'-hydroxypropyl)-2-ethyl-3-hydroxypyridin-4-ones in the rat. *Eur. J. Drug Metab. Pharmacokinet.,* 21**,** 33-41.
SINGH, S., EPEMOLU, R. O., DOBBIN, P. S., TILBROOK, G. S., ELLIS, B. L., DAMANI, L. A. & HIDER, R. C. 1992. Urinary metabolic profiles in human and rat of 1,2-dimethyl- and 1,2-diethyl-substituted 3-hydroxypyridin-4-ones. *Drug Metab. Dispos.,* 20**,** 256-61.
SMITH, A. & MORGAN, W. T. 1981. Hemopexin-mediated transport of heme into isolated rat hepatocytes. *J. Biol. Chem.,* 256**,** 10902-9.
STEN, T., QVISEN, S., UUTELA, P., LUUKKANEN, L., KOSTIAINEN, R. & FINEL, M. 2006. Prominent but reverse stereoselectivity in propranolol glucuronidation by human UDP-glucuronosyltransferases 1A9 and 1A10. *Drug Metab. Dispos.,* 34**,** 1488-94.
SUMMERS, M. R., JACOBS, A., TUDWAY, D., PERERA, P. & RICKETTS, C. 1979. Studies in Desferrioxamine and Ferrioxamine Metabolism in Normal and Iron-Loaded Subjects. *Br. J. Haematol. ,* 42**,** 547-555.
SWARTZ, M. E. 2005. UPLC™: an introduction and review. *J. Liq. Chrom. Relat. Tech.,* 28**,** 1253-1263.
TRAPNELL, C. B., KLECKER, R. W., JAMIS-DOW, C. & COLLINS, J. M. 1998. Glucuronidation of 3'-azido-3'-deoxythymidine (zidovudine) by human liver microsomes: relevance to clinical pharmacokinetic interactions with atovaquone, fluconazole, methadone, and valproic acid. *Antimicrob. Agents Chemother.,* 42**,** 1592-6.
TRONTELJ, J. 2012. Quantification of glucuronide metabolites in biological matrices by LC–MS/MS. *In:* PRASAIN, D. J. (ed.) *Tandem Mass Spectrometry Applications and Principles.* InTech.
UNGER, A. & HERSHKO, C. 1974. Hepatocellular uptake of ferritin in the rat. *Br. J. Haematol.,* 28**,** 169-79.
VASHISHT, A. A., ZUMBRENNEN, K. B., HUANG, X., POWERS, D. N., DURAZO, A., SUN, D., BHASKARAN, N., PERSSON, A., UHLEN, M., SANGFELT, O., SPRUCK, C., LEIBOLD, E. A. & WOHLSCHLEGEL, J. A. 2009. Control of iron homeostasis by an iron-regulated ubiquitin ligase. *Science,* 326**,** 718-21.
VERGA FALZACAPPA, M. V., VUJIC SPASIC, M., KESSLER, R., STOLTE, J., HENTZE, M. W. & MUCKENTHALER, M. U. 2007. STAT3 mediates hepatic hepcidin expression and its inflammatory stimulation. *Blood,* 109**,** 353-8.
VERONESE, F. M. & MERO, A. 2008. The impact of PEGylation on biological therapies. *BioDrugs,* 22**,** 315-29.
VOET, D., VOET, J. G. P., CHARLOTTE, W., JUDITH, G. V. & CHARLOTTE, W. P. 2013. *Fundamentals of biochemistry: life at the molecular level,* Hoboken, NJ: Wiley.

VULPE, C. D., KUO, Y. M., MURPHY, T. L., COWLEY, L., ASKWITH, C., LIBINA, N., GITSCHIER, J. & ANDERSON, G. J. 1999. Hephaestin, a ceruloplasmin homologue implicated in intestinal iron transport, is defective in the sla mouse. *Nat. Genet.,* 21**,** 195-9.

WADA, T., OARA, H., WATANABE, K., KINOSHITA, H. & YACHI, A. 1970. Autoradiographic study on the site of uptake of the haptoglobin-hemoglobin complex. *J. Reticuloendothel. Soc. ,* 8**,** 185.

WALLANDER, M. L., LEIBOLD, E. A. & EISENSTEIN, R. S. 2006. Molecular control of vertebrate iron homeostasis by iron regulatory proteins. *Biochim. Biophys. Acta - Mol. Cell Res. ,* 1763**,** 668-689.

WARD, R. J., FLORENCE, A. L., BALDWIN, D., ABIAKA, C., ROLAND, F., RAMSEY, M. H., DICKSON, D. P., PETERS, T. J. & CRICHTON, R. R. 1991. Biochemical and biophysical investigations of the ferrocene - iron - loaded rat. *Euro. J. Biochem.,* 202**,** 405-410.

WATERS. 2015. *Oasis Sample Extraction Products* [Online]. Available: http://www.waters.com/waters/en_US/Oasis-Sample-Extraction-Products/nav.htm?cid=513209&locale=en_US [Accessed 19/10 2015].

WEATHERALL, D. J. 2008. Genetic variation and susceptibility to infection: the red cell and malaria. *Brit. J. Haematol.,* 141**,** 276-286.

WEISS, H. M., FRESNEAU, M., CAMENISCH, G. P., KRETZ, O. & GROSS, G. 2006. In vitro blood distribution and plasma protein binding of the iron chelator deferasirox (ICL670) and its iron complex Fe-[ICL670]2 for rat, marmoset, rabbit, mouse, dog, and human. *Drug Metab. Dispos.,* 34**,** 971-5.

WEISSBERG, A. & DAGAN, S. 2011. Interpretation of ESI(+)-MS-MS spectra—Towards the identification of "unknowns". *Int. J. Mass Spectrom.,* 299**,** 158-168.

WISH, J. B. 2006. Assessing iron status: beyond serum ferritin and transferrin saturation. *Clin. J. Am. Soc. Nephrol.,* 1**,** S4-S8.

WOOD, J. C. 2007. Magnetic resonance imaging measurement of iron overload. *Curr. Opin. Hematol.,* 14**,** 183.

WOOD, J. C., KANG, B. P., THOMPSON, A., GIARDINA, P., HARMATZ, P., GLYNOS, T., PALEY, C. & COATES, T. D. 2010. The effect of deferasirox on cardiac iron in thalassemia major: impact of total body iron stores. *Blood,* 116**,** 537-543.

XIE, Y. Y., LU, Z., KONG, X. L., ZHOU, T., BANSAL, S. & HIDER, R. 2016. Systematic comparison of the mono-, dimethyl- and trimethyl 3-hydroxy-4(1H)-pyridones - Attempted optimization of the orally active iron chelator, deferiprone. *Eur. J. Med. Chem.,* 115**,** 132-40.

XIN 2016. Unpublished data: "Toxicology report of CN128".

XU, Q. A. & MADDEN, T. L. 2012. *LC-MS in drug bioanalysis,* New York Springer.

YAN, Z., CALDWELL, G. W., JONES, W. J. & MASUCCI, J. A. 2003. Cone voltage induced in-source dissociation of glucuronides in electrospray and implications in biological analyses. *Rapid Commun. Mass Spectrom.,* 17**,** 1433-42.

YU Y.P., H. R. C., LIU Z.D., LI Z. . 2011. *Chinese patent: CN 102190644B*.

ZAKIM, D., GOLDENBERG, J. & VESSEY, D. A. 1973. Effects of metals on the properties of hepatic microsomal uridine diphosphate glucuronyltransferase. *Biochemistry,* 12**,** 4068-4074.

ZBINDEN, P. 1997. *US Patent 5,688,815*.

ZHENG, J. J., LYNCH, E. D. & UNGER, S. E. 2002. Comparison of SPE and fast LC to eliminate mass spectrometric matrix effects from microsomal incubation products. *J. Pharm. Biomed. Anal.,* 28**,** 279-285.

ZHOU, T., MA, Y., KONG, X. & HIDER, R. C. 2012. Design of iron chelators with therapeutic application. *Dalt. Trans.,* 41**,** 6371-6389.

APPENDICES

Appendices

Appendix I

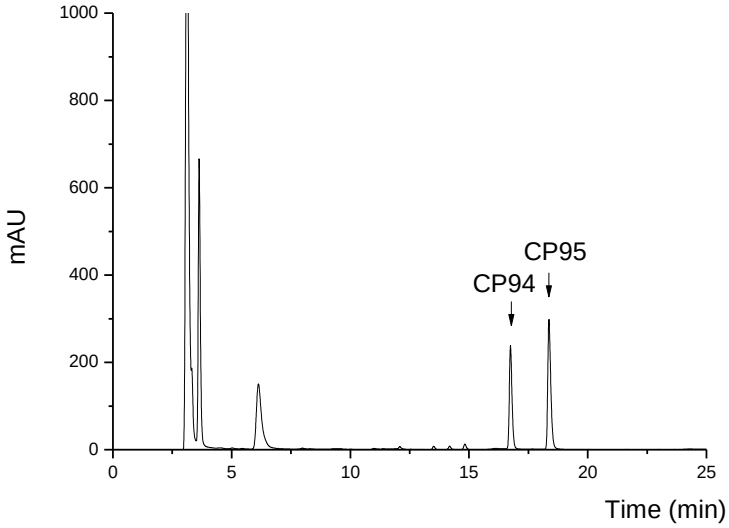

Figure I-1 Chromatography of CP94 rat liver microsomal incubates (NADPH+UDPGA included, alamethicin/microsomal protein ratio: 25 µg/mg).

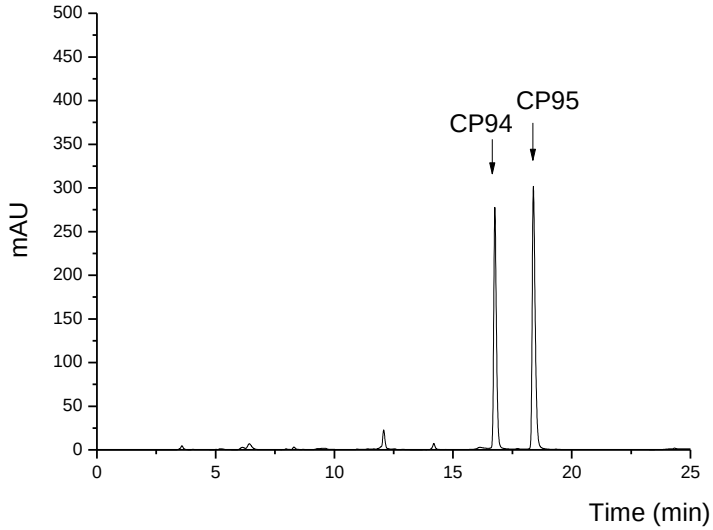

Figure I-2 Chromatography of blank rat liver microsomal incubates (NADPH+UDPGA excluded, alamethicin/microsomal protein ratio: 25 µg/mg).

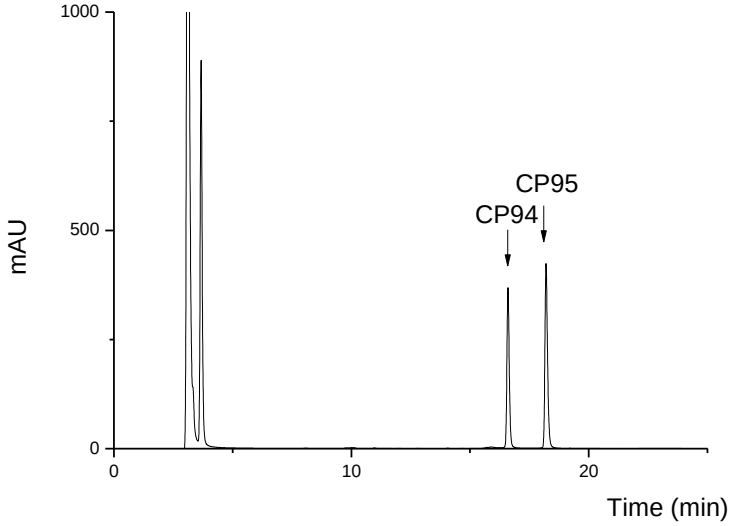

Figure I-3 Chromatography of CP94 rat liver microsomal incubates (NADPH+UDPGA included, alamethicin/microsomal protein ratio: 25 µg/mg) deconjugated by β-glucuronidase.

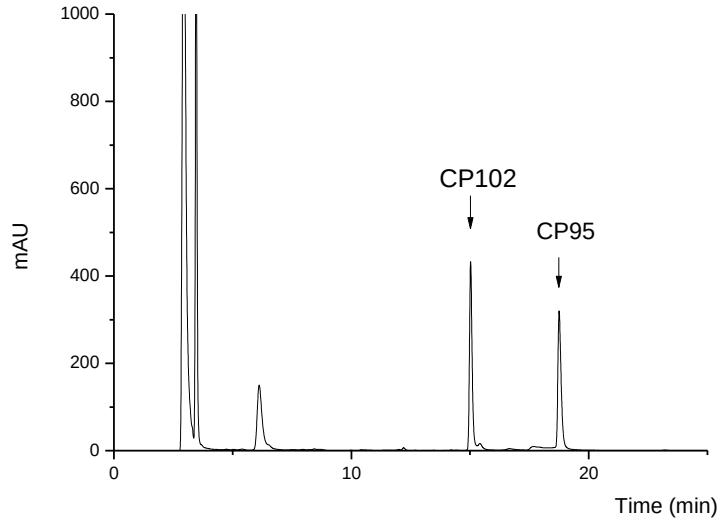

Figure I-4 Chromatography of CP102 rat liver microsomal incubates (NADPH+UDPGA included, alamethicin/microsomal protein ratio: 25 µg/mg).

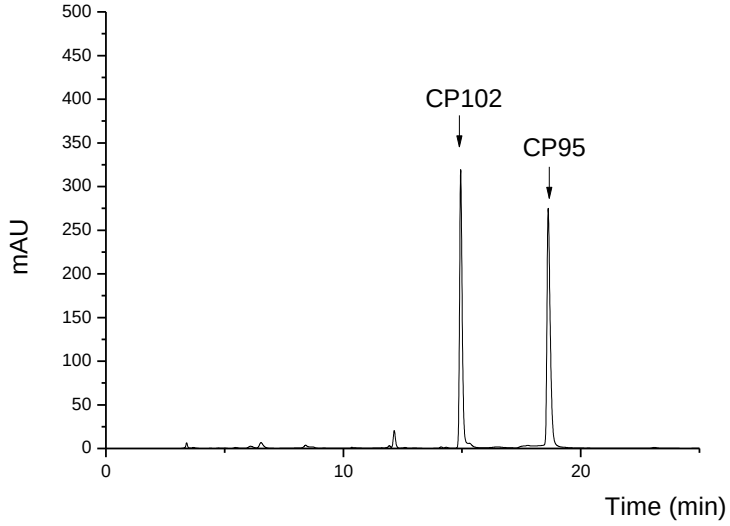

Figure I-5 Chromatography of blank rat liver microsomal incubates (NADPH+UDPGA excluded, alamethicin/microsomal protein ratio: 25 µg/mg).

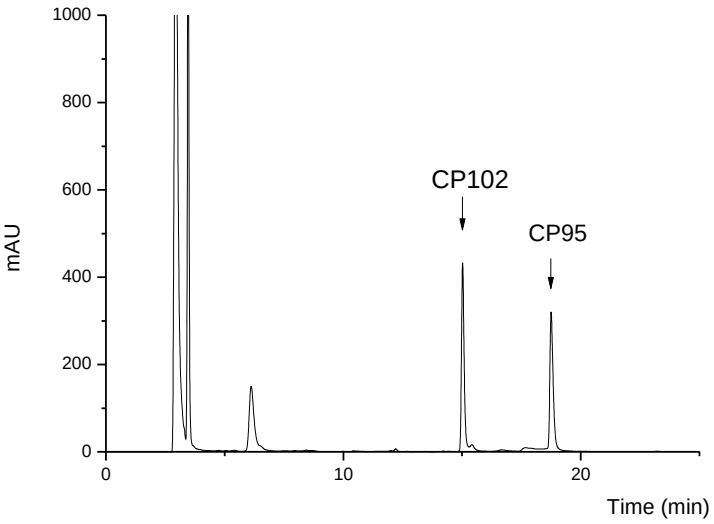

Figure I-6 Chromatography of CP102 rat liver microsomal incubates (NADPH+UDPGA included, alamethicin/microsomal protein ratio: 25 µg/mg) deconjugated by β-glucuronidase.

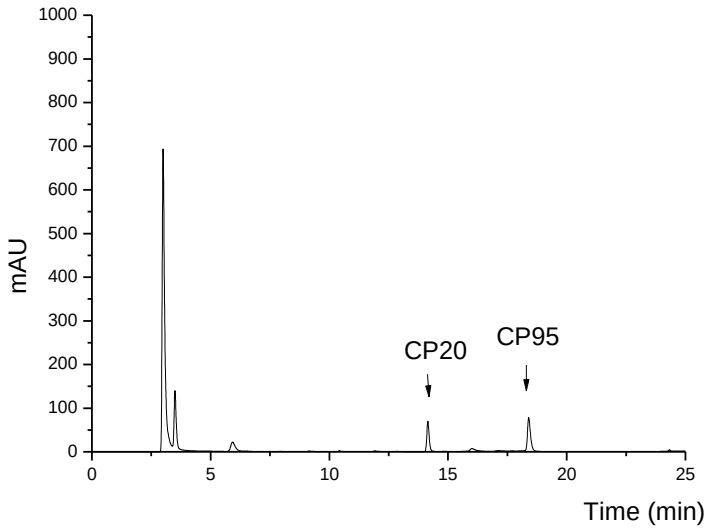

Figure I-7 Chromatography of CP20 human liver microsomal incubates (NADPH+UDPGA included, alamethicin/microsomal protein ratio: 25 µg/mg).

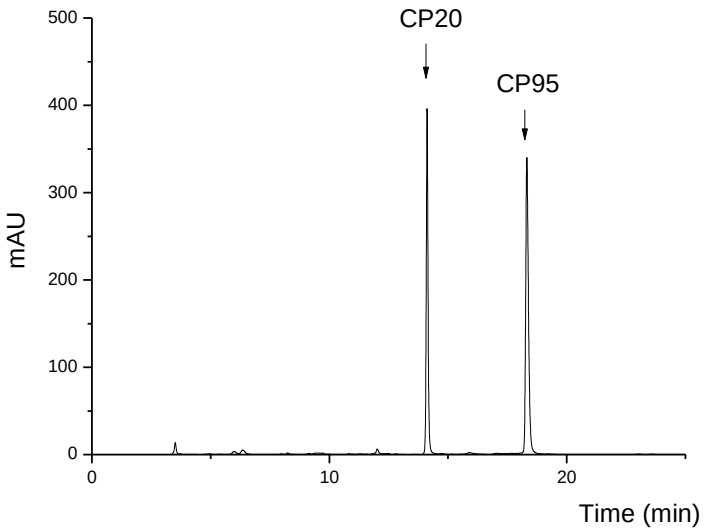

Figure I-8 Chromatography of blank human liver microsomal incubates (NADPH+UDPGA excluded, alamethicin/microsomal protein ratio: 25 µg/mg.

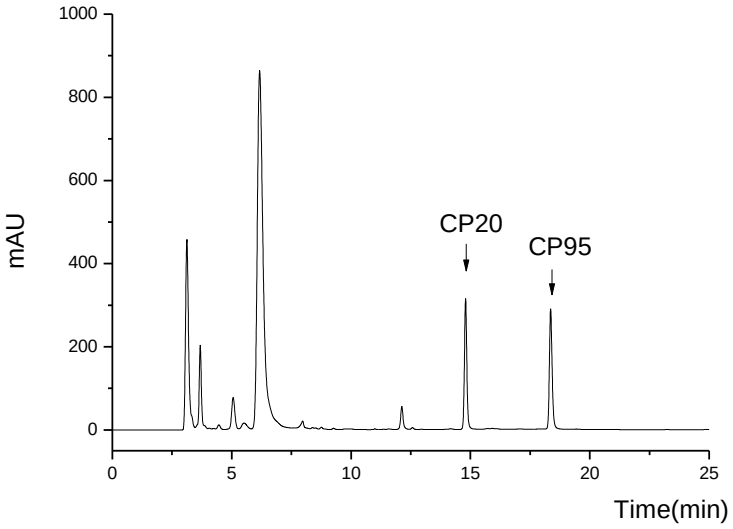

Figure I-9 Chromatography of CP20 human liver microsomal incubates (NADPH+UDPGA included, alamethicin/microsomal protein ratio: 25 µg/mg) deconjugated by β-glucuronidase.

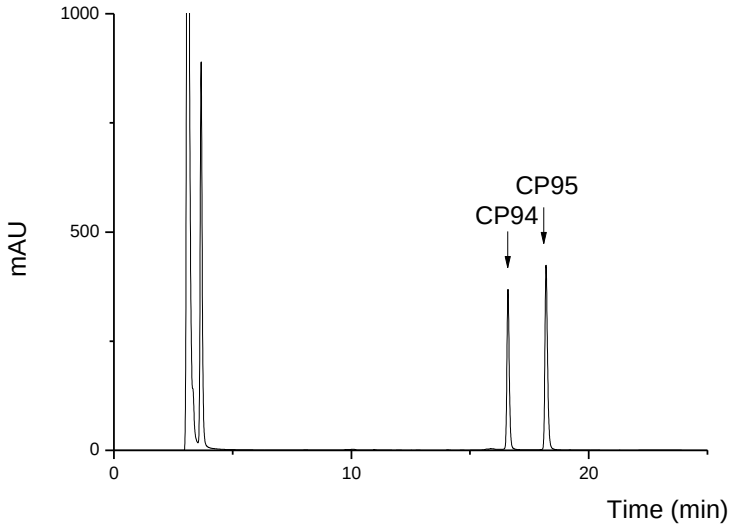

Figure I-10 Chromatography of CP94 human liver microsomal incubates (NADPH+UDPGA included, alamethicin/microsomal protein ratio: 25 µg/mg).

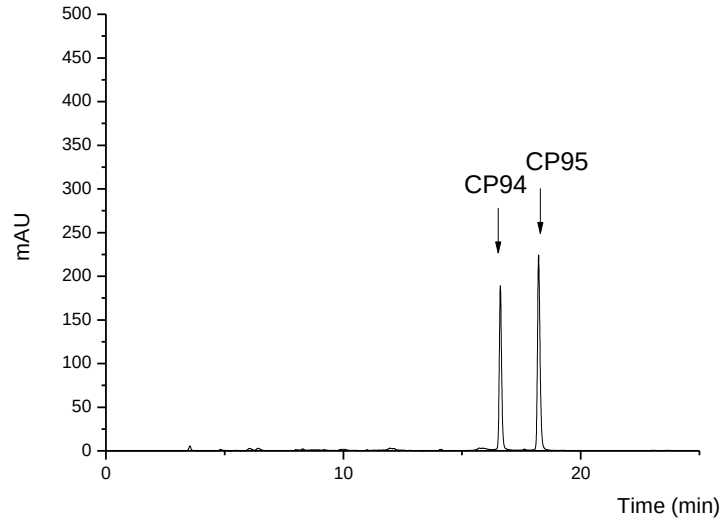

Figure I-11 Chromatography of blank human liver microsomal incubates (NADPH+UDPGA excluded, alamethicin/microsomal protein ratio: 25 µg/mg).

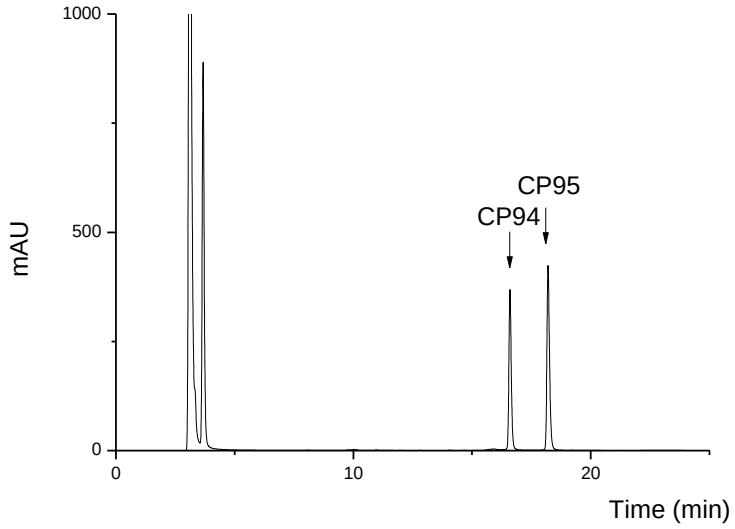

Figure I-12 Chromatography of CP94 human liver microsomal incubates (NADPH+UDPGA included, alamethicin/microsomal protein ratio: 25 µg/mg) deconjugated by β-glucuronidase.

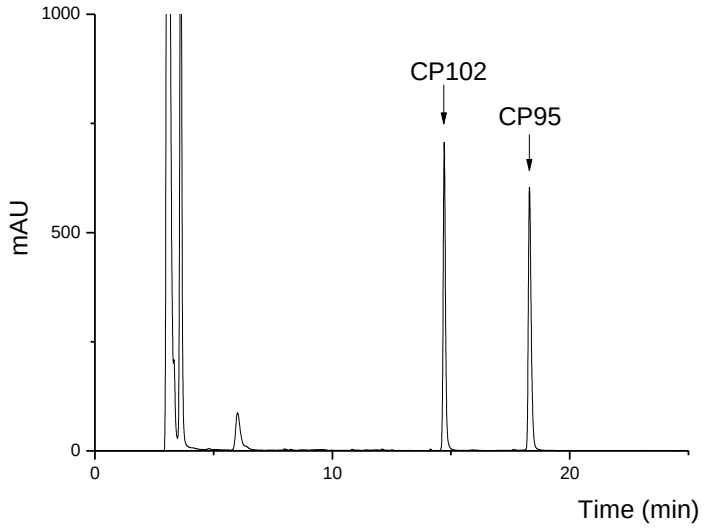

Figure I-13 Chromatography of CP102 human liver microsomal incubates (NADPH+UDPGA included, alamethicin/microsomal protein ratio: 25 µg/mg).

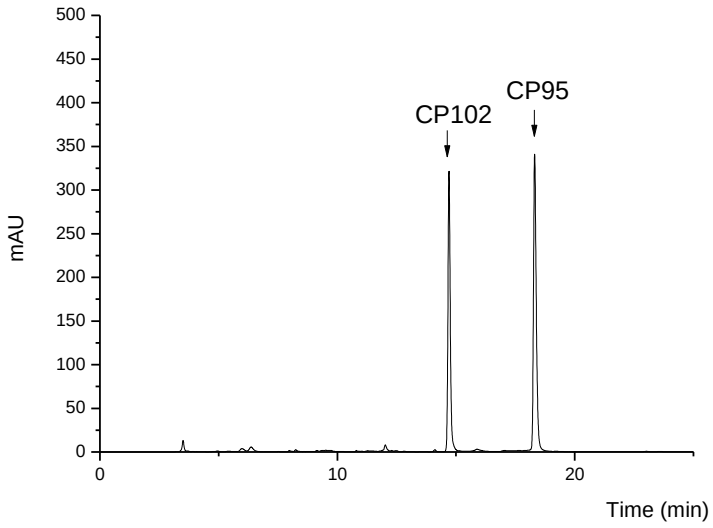

Figure I-14 Chromatography of blank human liver microsomal incubates (NADPH+UDPGA excluded, alamethicin/microsomal protein ratio: 25 µg/mg).

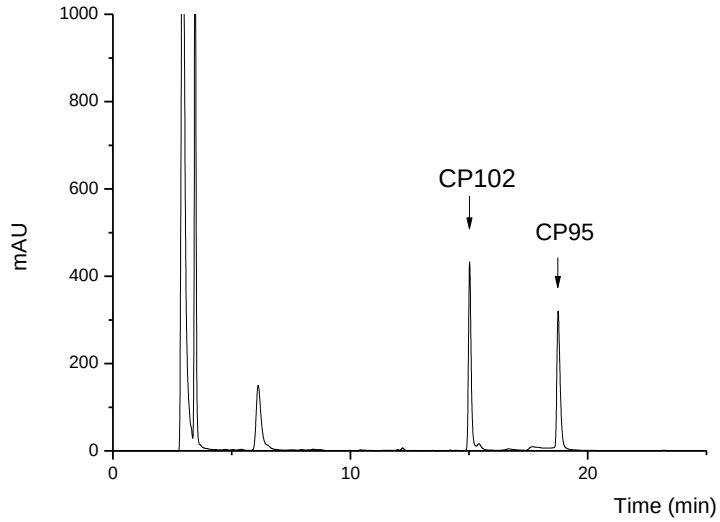

Figure I-15 Chromatography of CP102 human liver microsomal incubates (NADPH+UDPGA included, alamethicin/microsomal protein ratio: 25 µg/mg) deconjugated by β-glucuronidase.

Appendix II

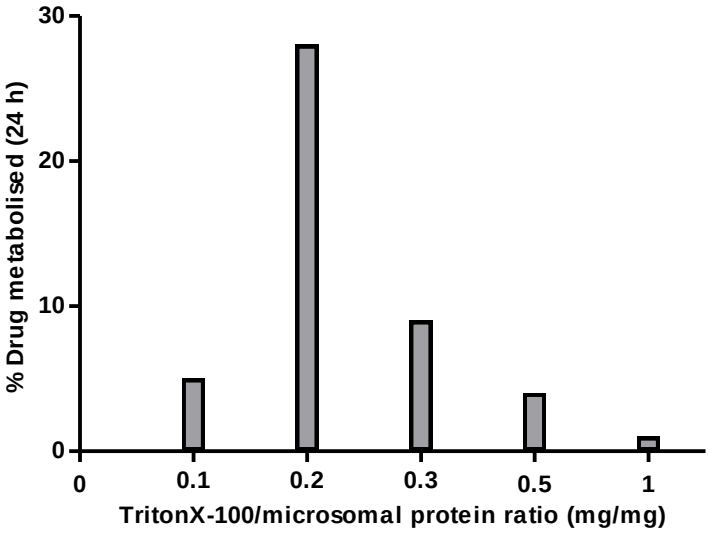

Figure II-1. Percentage of CP20 metabolism by Phase I+II pathway in human liver microsomal incubations titrated with Triton X-100.

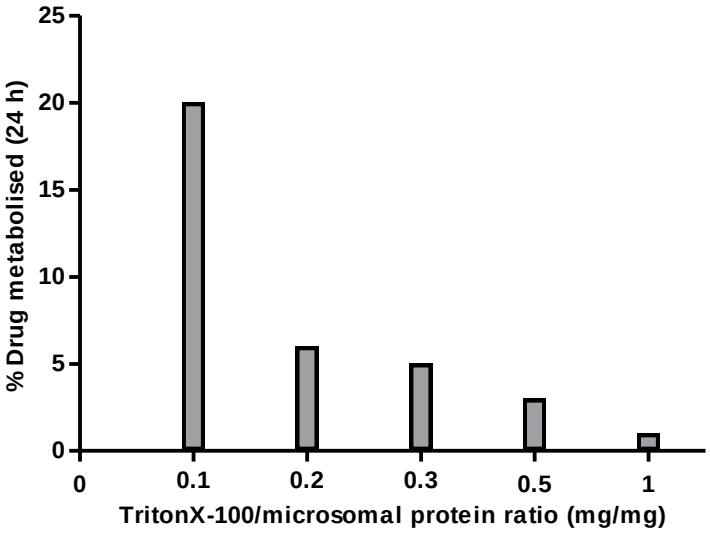

Figure II-2. Percentage of CP94 metabolism by Phase I+II pathway in rat liver microsomal incubations titrated with Triton X-100.

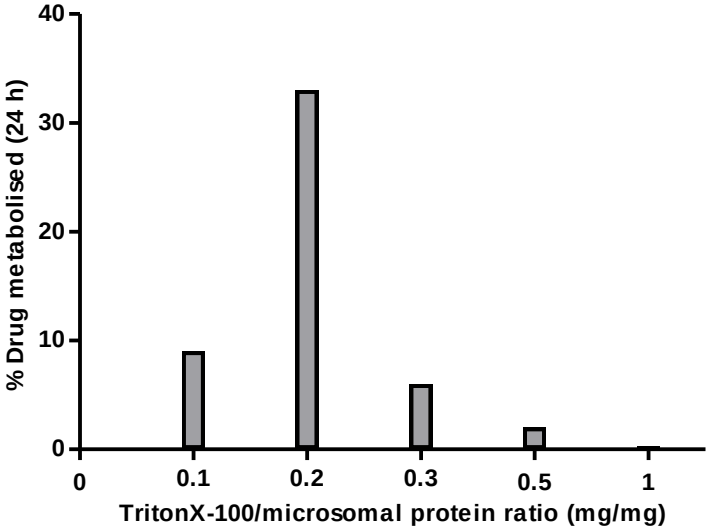

Figure II-3. Percentage of CP94 metabolism by Phase I+II pathway in human liver microsomal incubations titrated with Triton X-100.

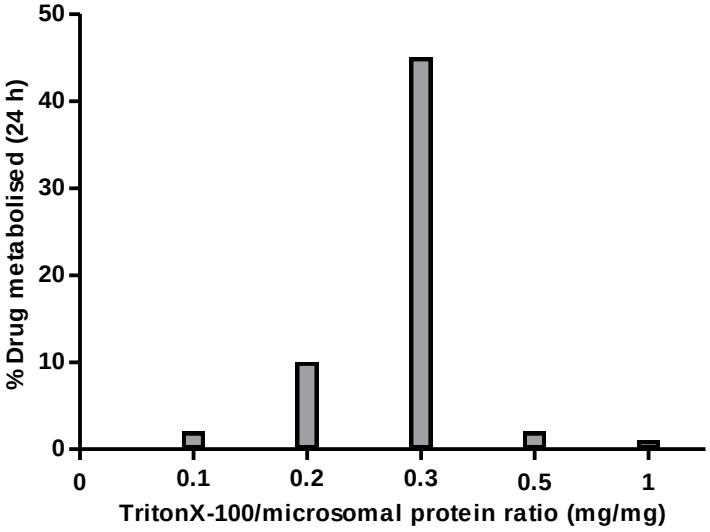

Figure II-4. Percentage of CP102 metabolism by Phase I+II pathway in rat liver microsomal incubations titrated with Triton X-100.

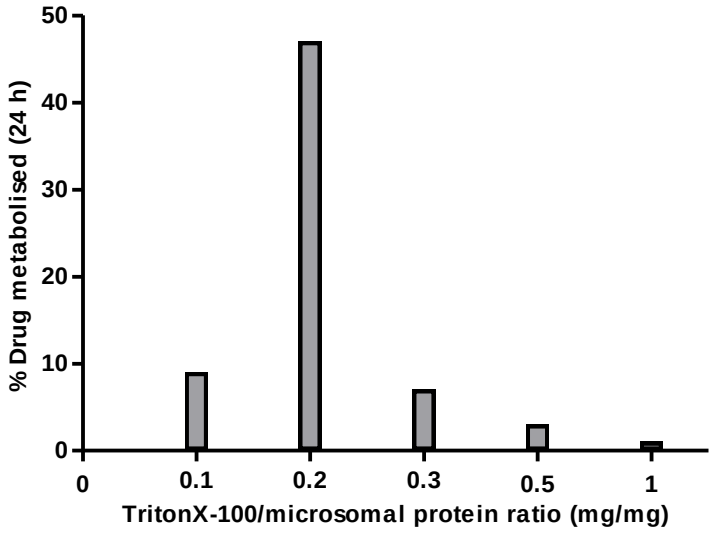

Figure II-5. Percentage of CP102 metabolism by Phase I+II pathway in human liver microsomal incubations titrated with Triton X-100.

Appendix III

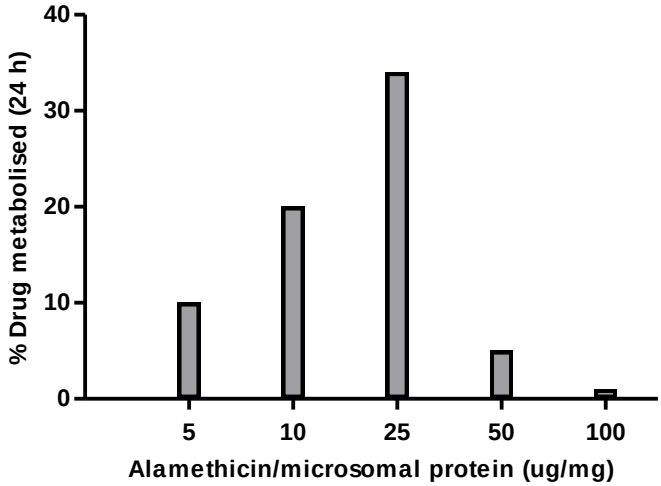

Figure III-1. Percentage of CP20 metabolism by Phase I+II pathway in human liver microsomal incubations titrated with alamethicin.

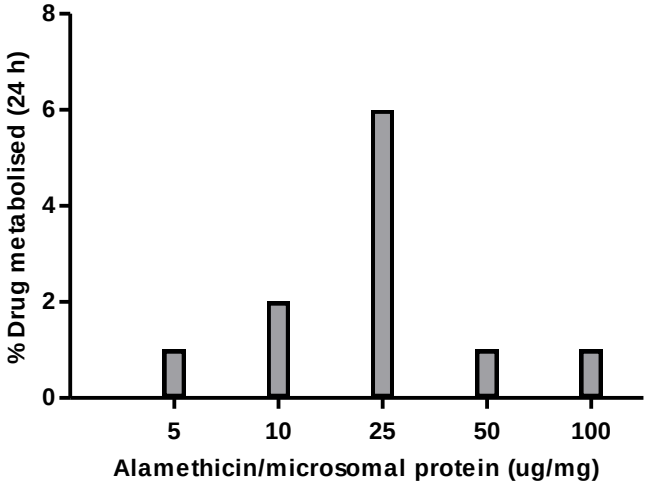

Figure III-2. Percentage of CP94 metabolism by Phase I+II pathway in rat liver microsomal incubations titrated with alamethicin.

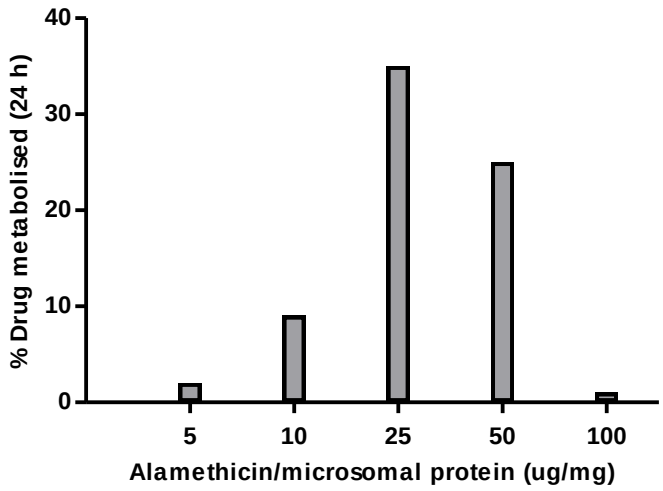

Figure III-3. Percentage of CP94 metabolism by Phase I+II pathway in human liver microsomal incubations titrated with alamethicin.

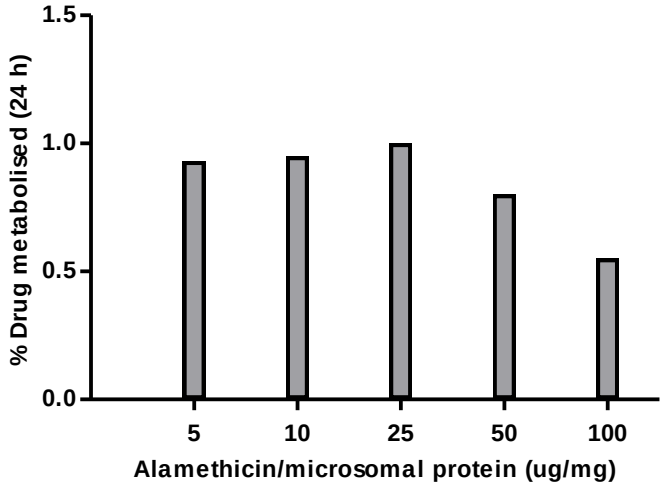

Figure III-4. Percentage of CP102 metabolism by Phase I+II pathway in rat liver microsomal incubations titrated with alamethicin.

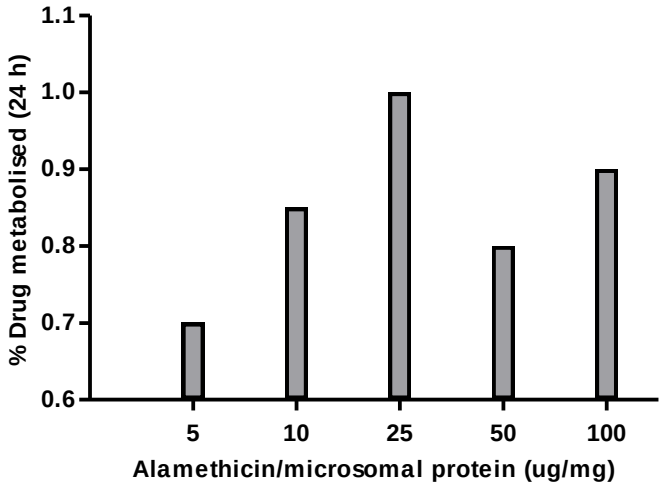

Figure III-5. Percentage of CP102 metabolism by Phase I+II pathway in human liver microsomal incubations titrated with alamethicin.

Appendix IV

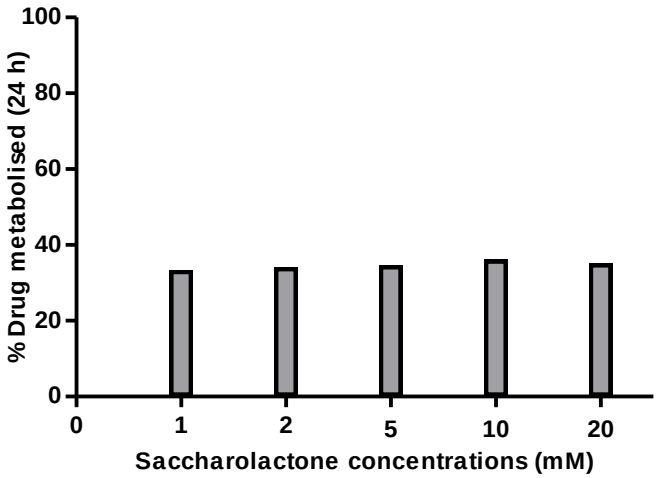

Figure IV-1. Percentage of CP20 metabolism by Phase I+II pathway in human liver microsomal incubates titrated with saccharolactone

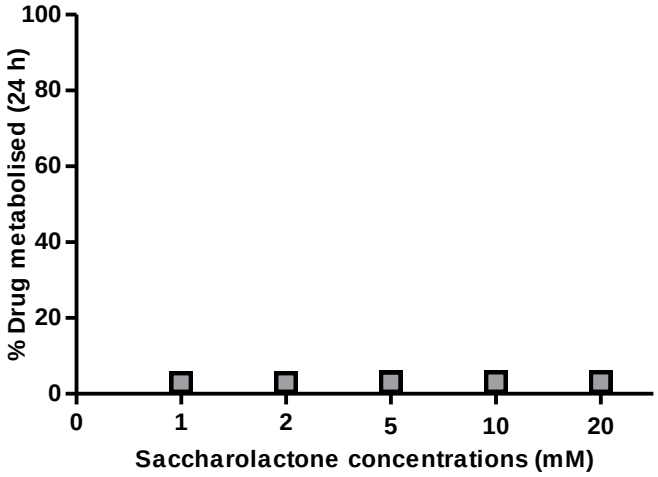

Figure IV-2. Percentage of CP94 metabolism by Phase I+II pathway in rat liver microsomal incubates titrated with saccharolactone

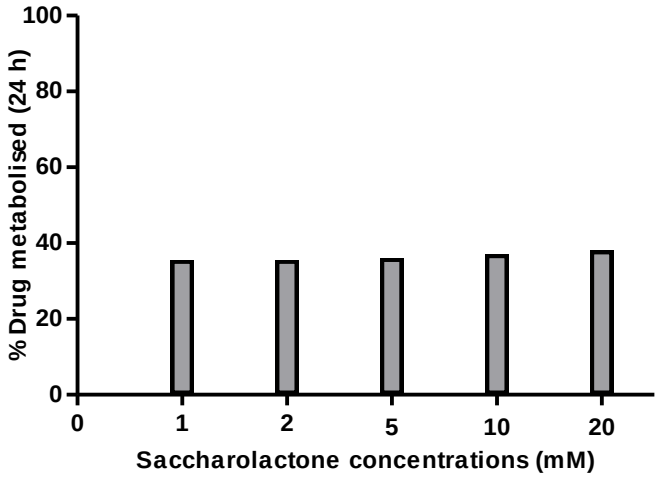

Figure IV-3. Percentage of CP94 metabolism by Phase I+II pathway in human liver microsomal incubates titrated with saccharolactone.

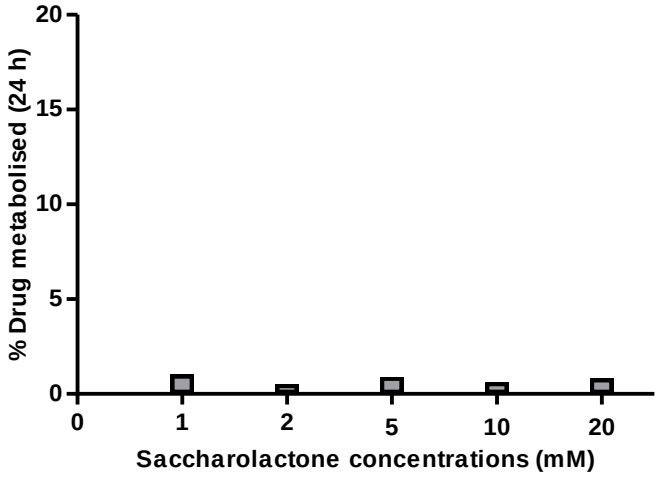

Figure IV-4. Percentage of CP102 metabolism by Phase I+II pathway in rat liver microsomal incubates titrated with saccharolactone.

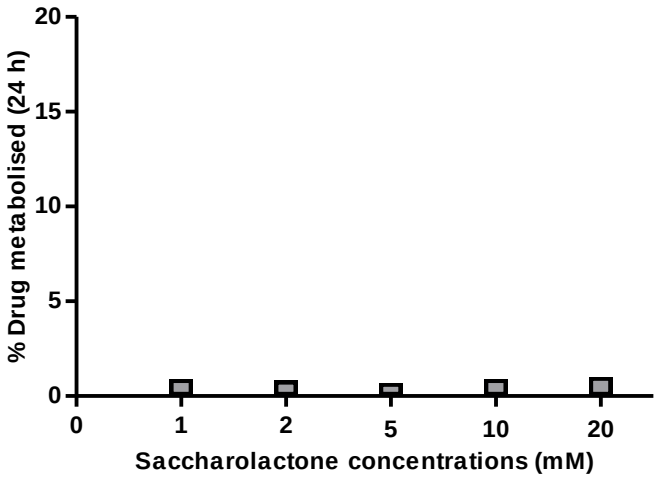

Figure IV-5. Percentage of CP102 metabolism by Phase I+II pathway in human liver microsomal incubates titrated with saccharolactone

Appendix V

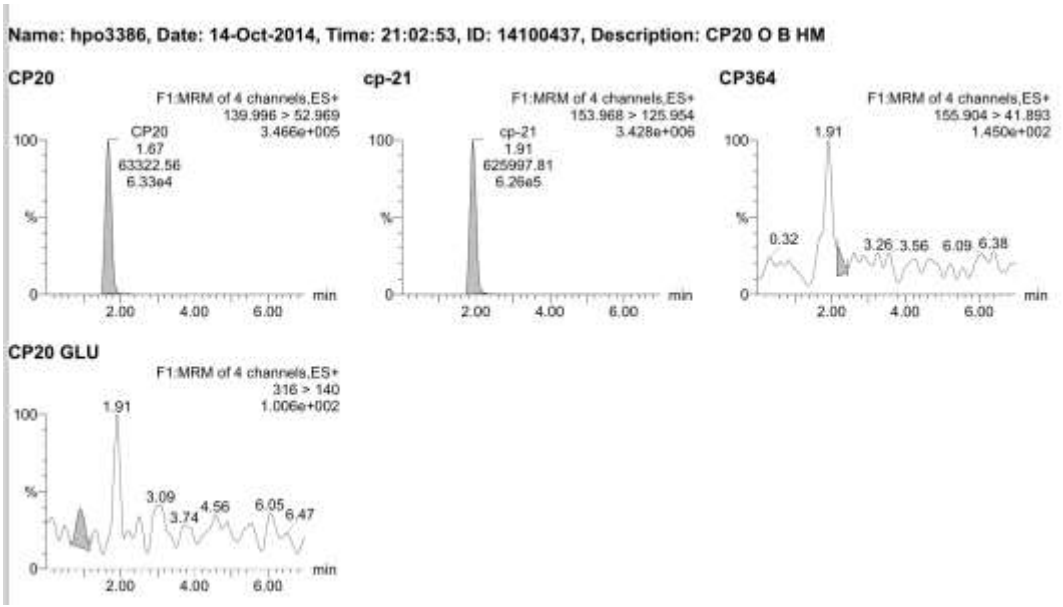

Figure V-1 MRM chromatographs of CP20 Phase I microsomal HLMs blank

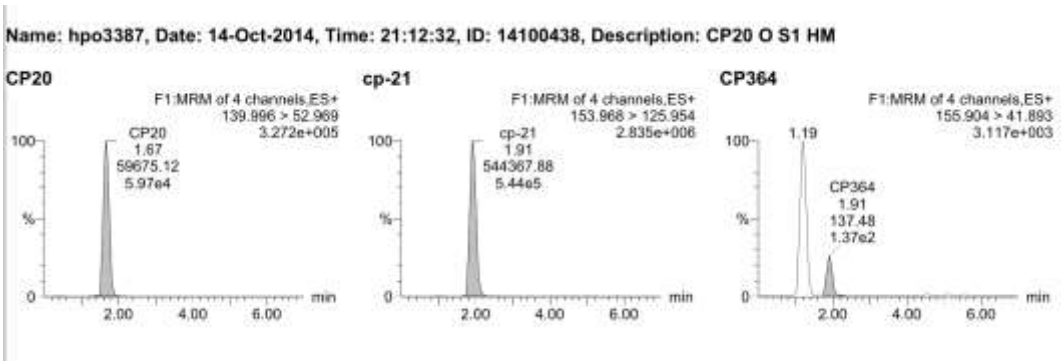

Figure V-2 MRM chromatographs of CP20 Phase I microsomal HLMs sample

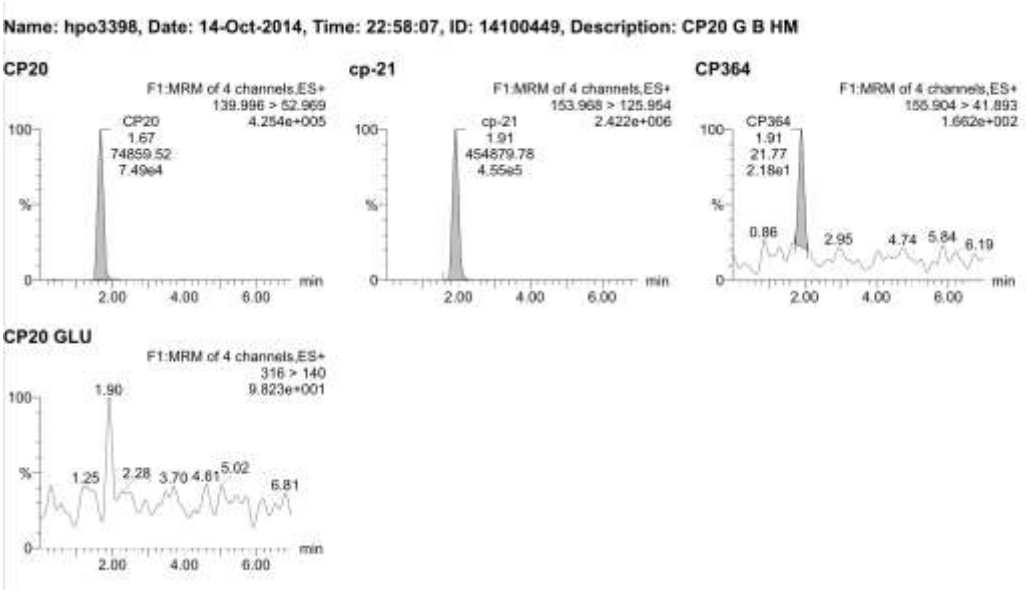

Figure V-3 MRM chromatographs of CP20 Phase I+II microsomal HLMs blank

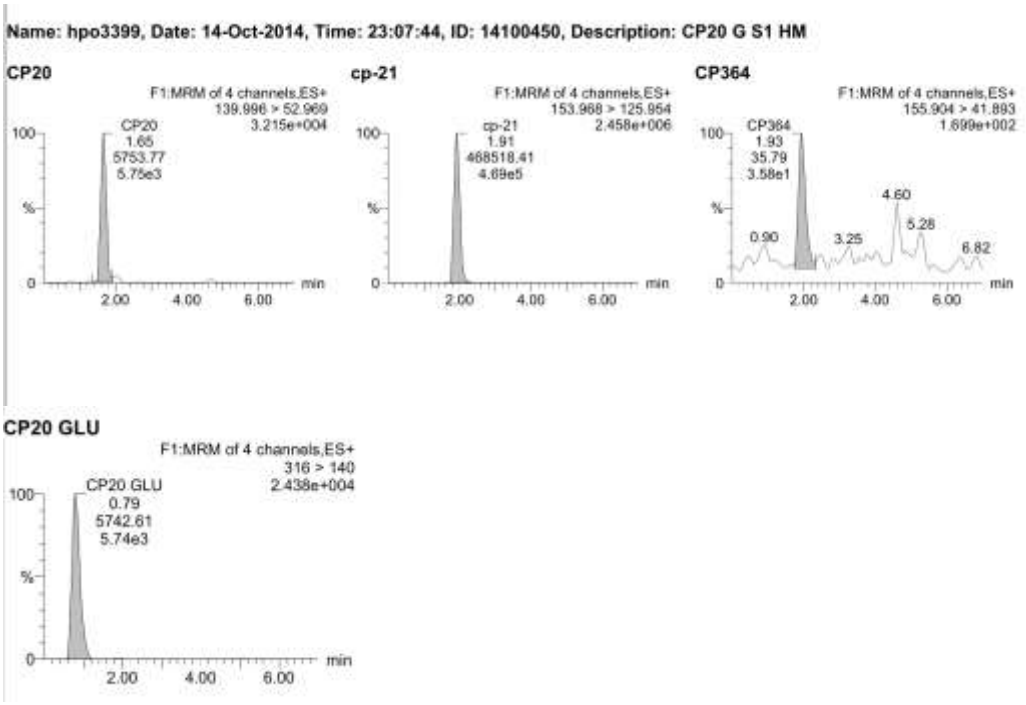

Figure V-4 MRM chromatographs of CP20 Phase I+II microsomal HLMs sample

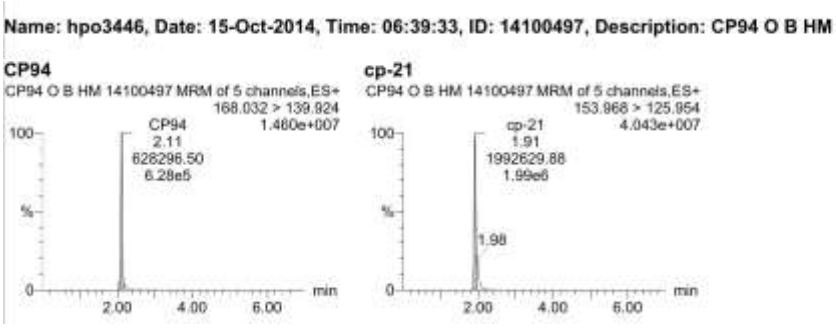

Figure V-5 MRM chromatographs of CP94 Phase I microsomal HLMs blank

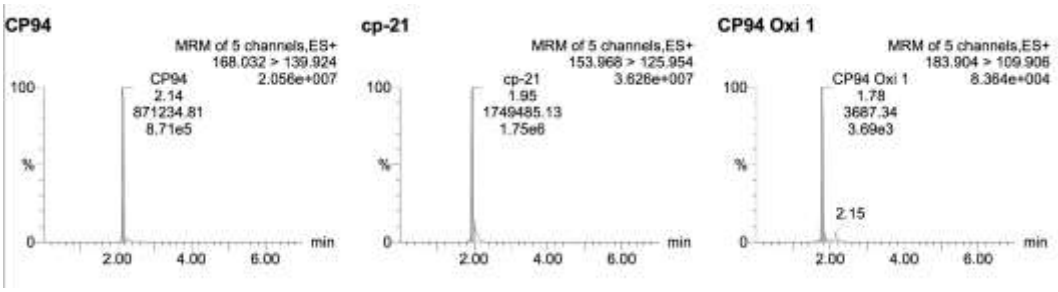

Figure V-6 MRM chromatographs of CP94 Phase I microsomal HLMs sample

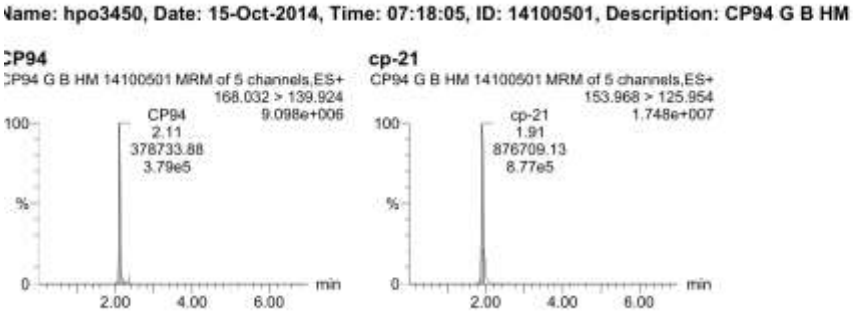

Figure V-7 MRM chromatographs of CP94 Phase I+II microsomal HLMs blank

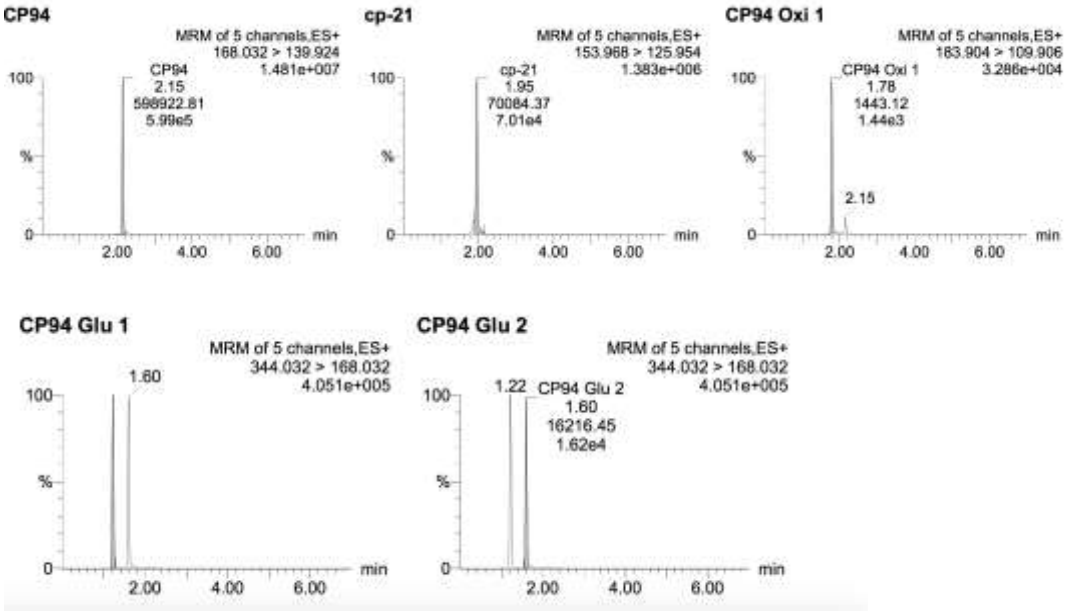

Figure V-8 MRM chromatographs of CP94 Phase I+II microsomal HLMs sample

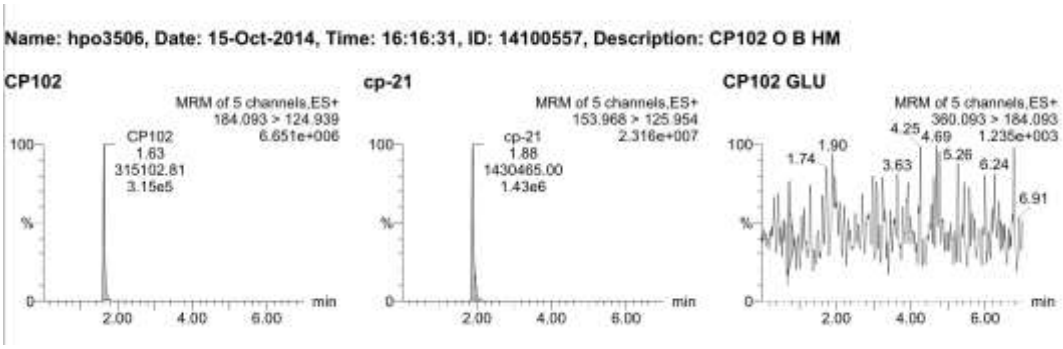

Figure V-9 MRM chromatographs of CP102 Phase I microsomal HLMs blank

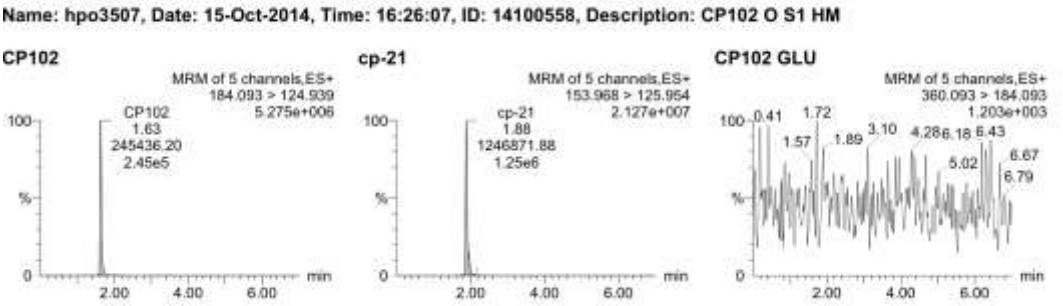

Figure V-10 MRM chromatographs of CP102 Phase I microsomal HLMs sample

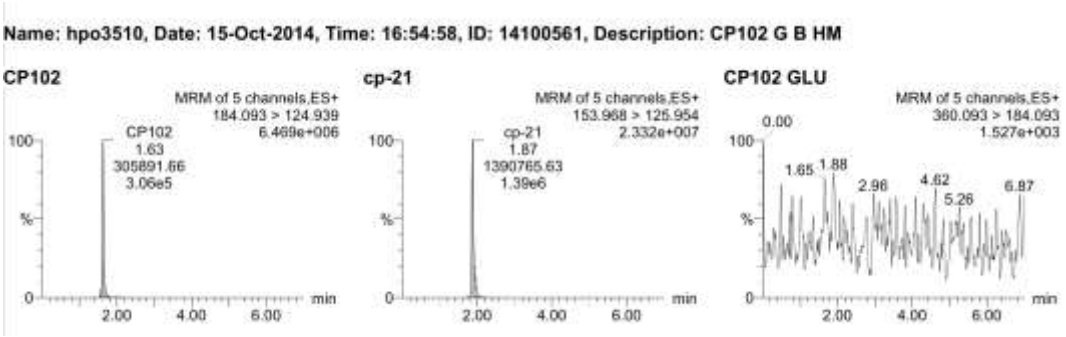

Figure V-11 MRM chromatographs of CP102 Phase I+II microsomal HLMs blank

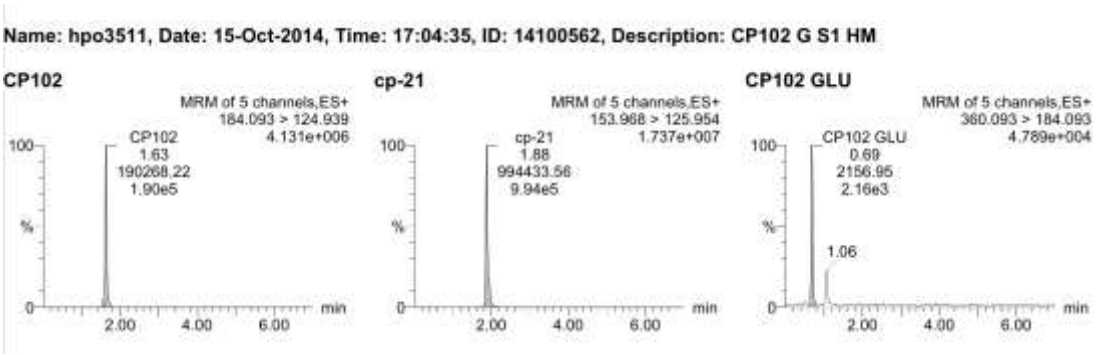

Figure V-12 MRM chromatographs of CP102 Phase I+II microsomal HLMs sample

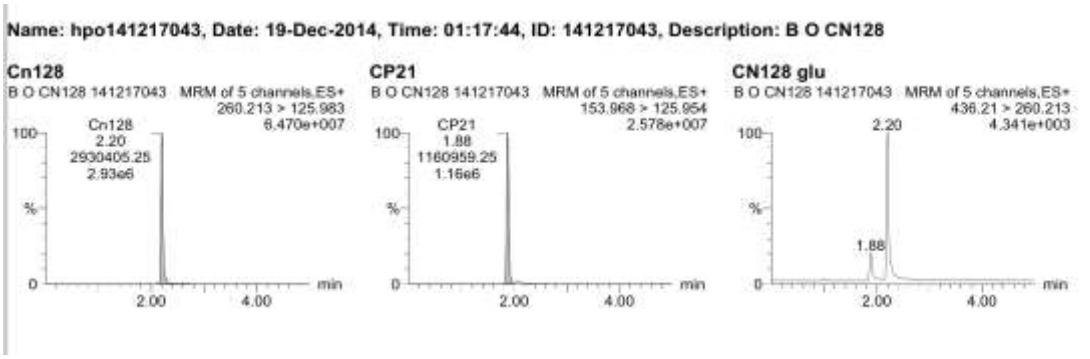

Figure V-13 MRM chromatographs of CN128 Phase I microsomal HLMs blank

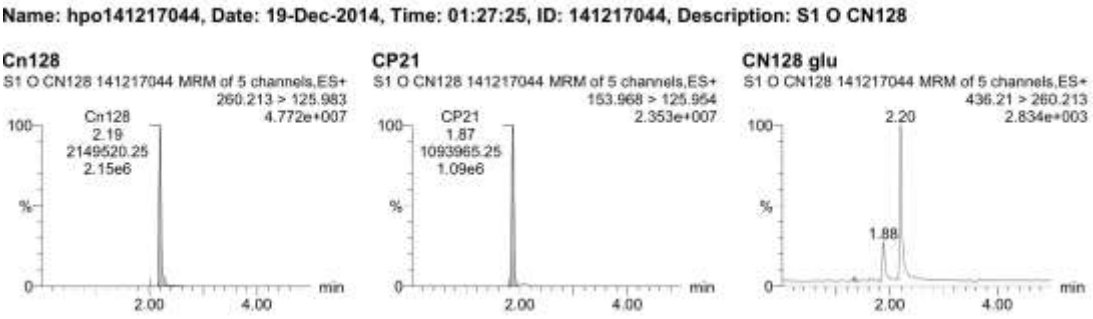

Figure V-14 MRM chromatographs of CN128 Phase I microsomal HLMs sample

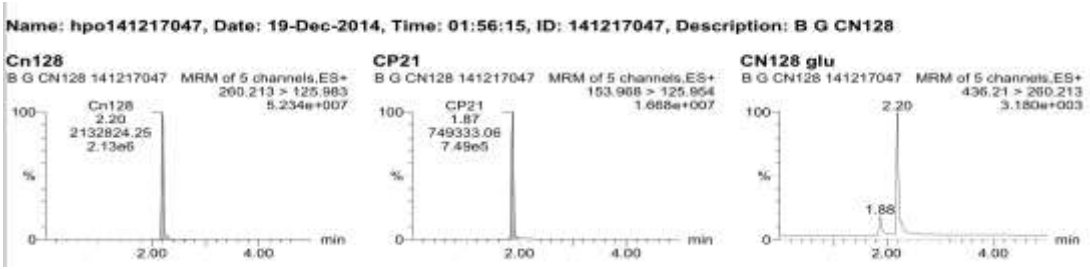

Figure V-15 MRM chromatographs of CN128 Phase I+II microsomal HLMs blank

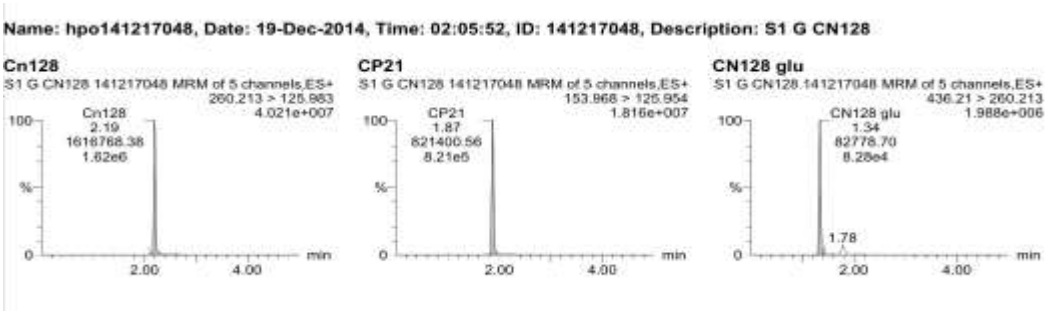

Figure V-16 MRM chromatographs of CN128 Phase I+II microsomal HLMs sample

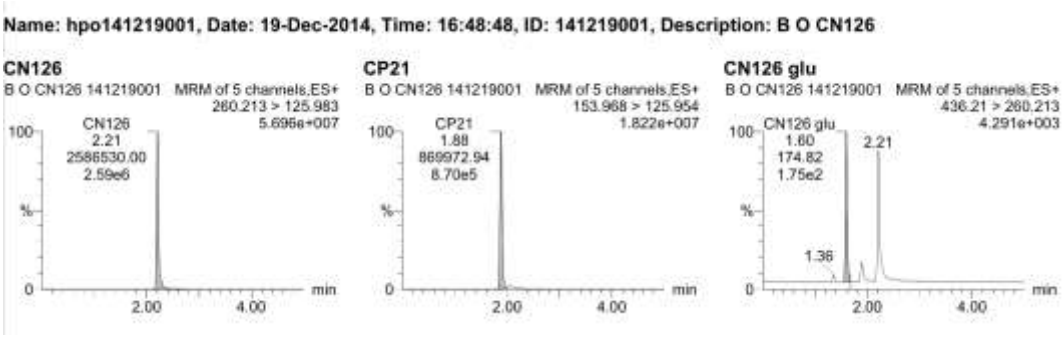

Figure V-17 MRM chromatographs of CN126 Phase I microsomal HLMs blank

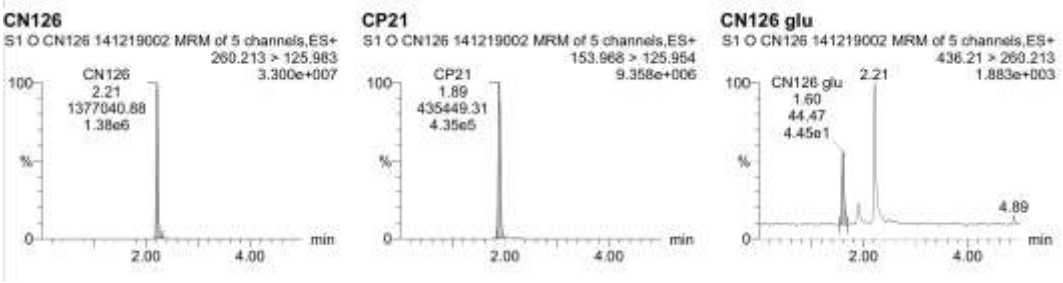

Figure V-18 MRM chromatographs of CN126 Phase I microsomal HLMs sample

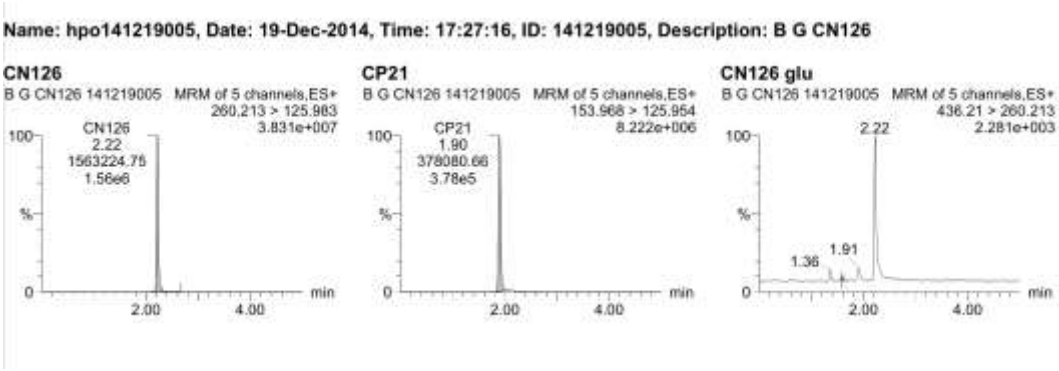

Figure V-19 MRM chromatographs of CN126 Phase I+II microsomal HLMs blank

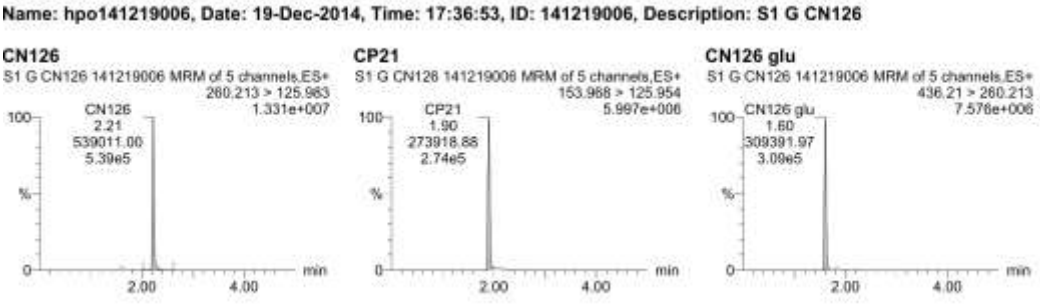

Figure V-20 MRM chromatographs of CN126 Phase I+II microsomal HLMs sample

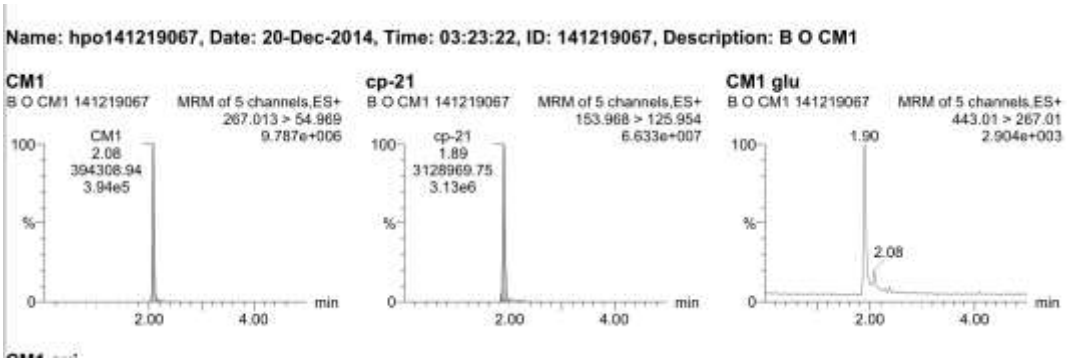

Figure V-21 MRM chromatographs of CM1 Phase I microsomal HLMs blank

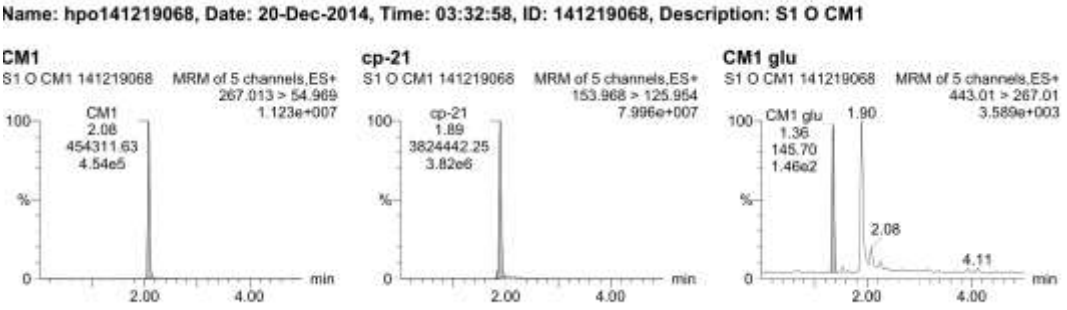

Figure V-22 MRM chromatographs of CM1 Phase I microsomal HLMs sample

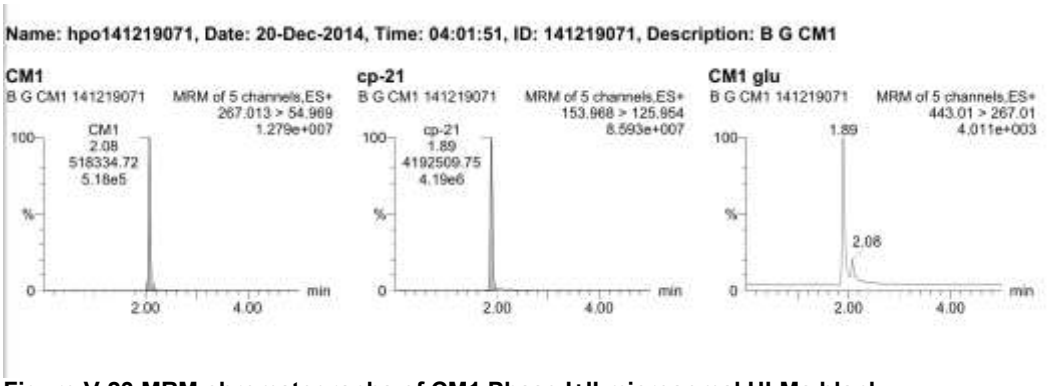

Figure V-23 MRM chromatographs of CM1 Phase I+II microsomal HLMs blank

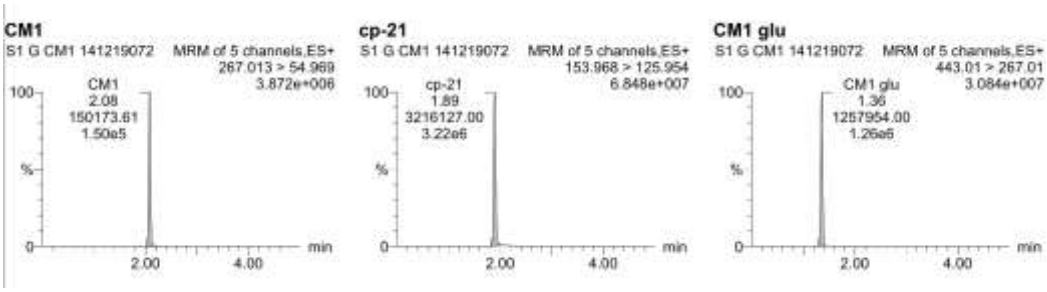

Figure V-24 MRM chromatographs of CM1 Phase I+II microsomal HLMs sample

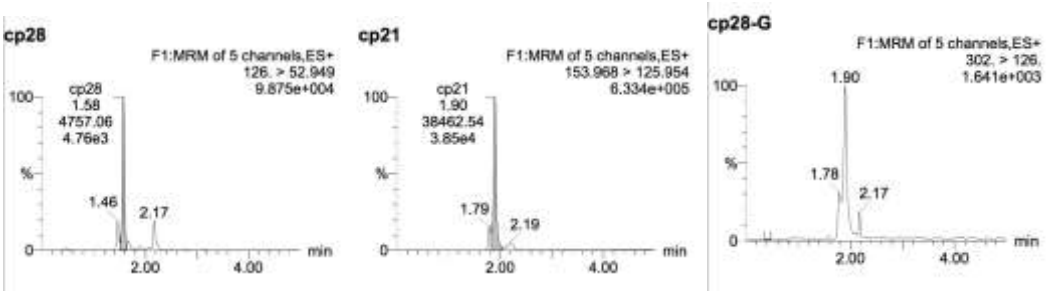

Figure V-25 MRM chromatographs of CP28 Phase I microsomal HLMs blank

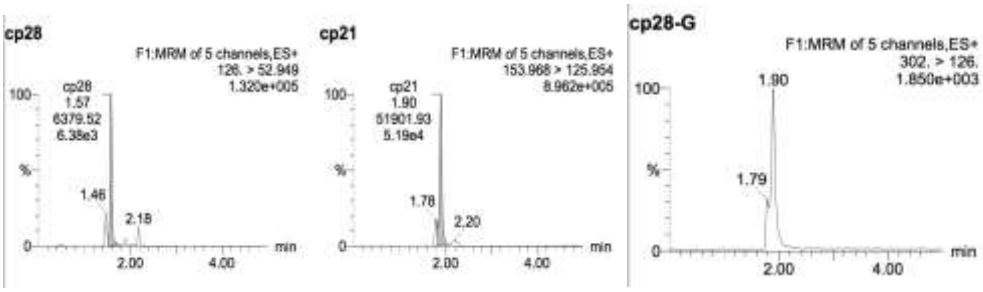

Figure V-26 MRM chromatographs of CP28 Phase I microsomal HLMs sample

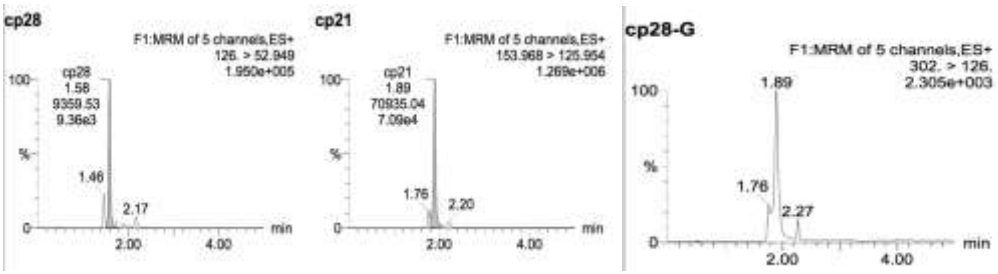

Figure V-27 MRM chromatographs of CP28 Phase I+II microsomal HLMs blank

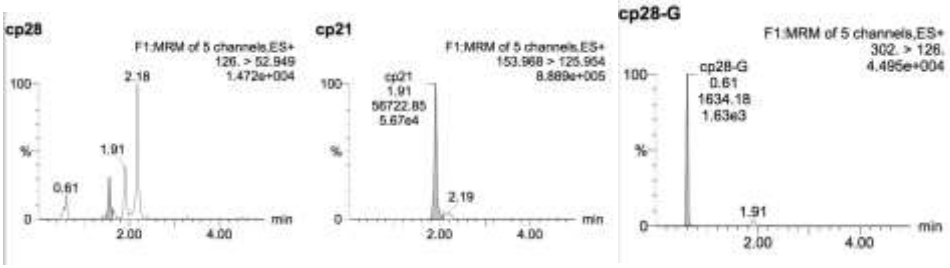

Figure V-28 MRM chromatographs of CP28 Phase I+II microsomal HLMs sample

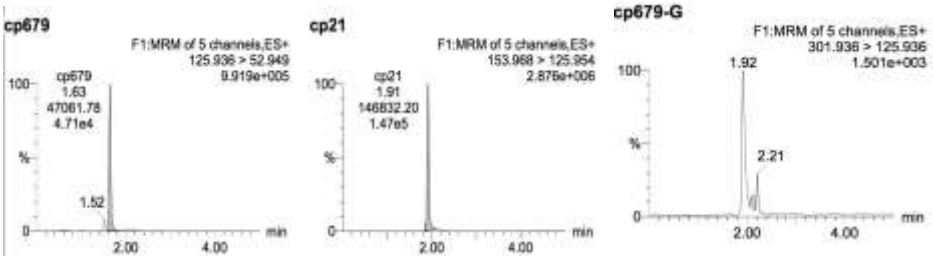

Figure V-29 MRM chromatographs of CP679 Phase I microsomal HLMs blank

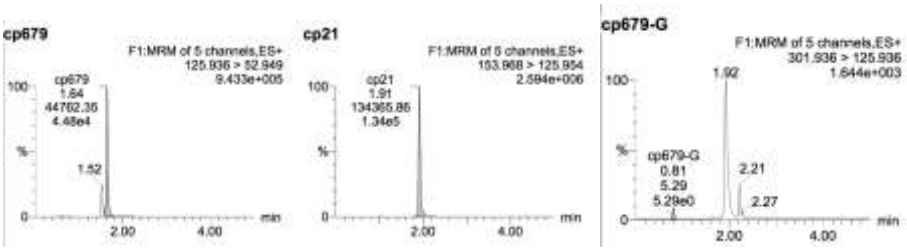

Figure V-30 MRM chromatographs of CP679 Phase I microsomal HLMs sample

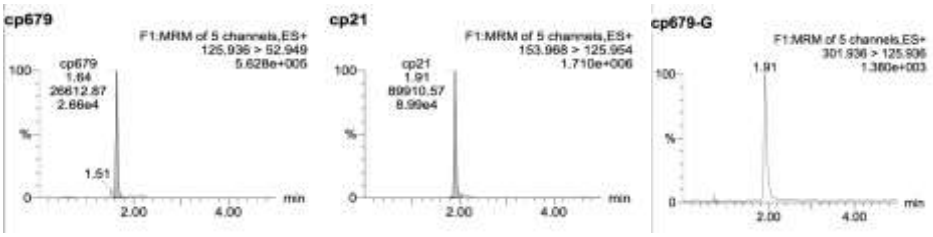

Figure V-31 MRM chromatographs of CP679 Phase I+II microsomal HLMs blank

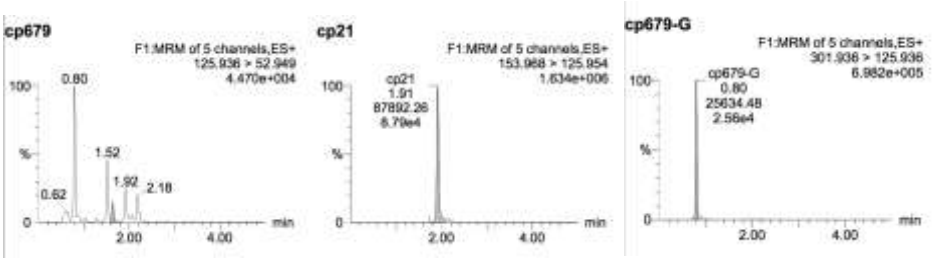

Figure V-32 MRM chromatographs of CP679 Phase I+II microsomal HLMs sample

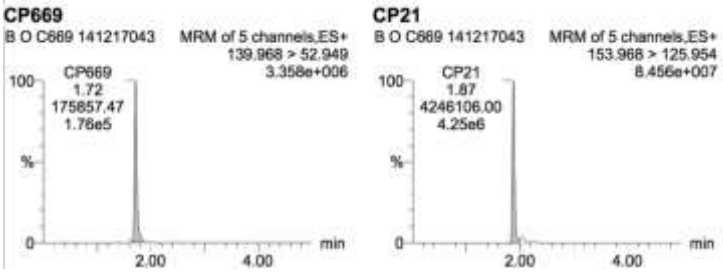

Figure V-33 MRM chromatographs of CP669 Phase I microsomal HLMs blank

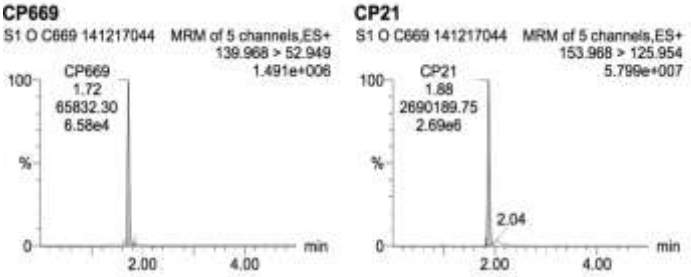

Figure V-34 MRM chromatographs of CP669 Phase I microsomal HLMs sample

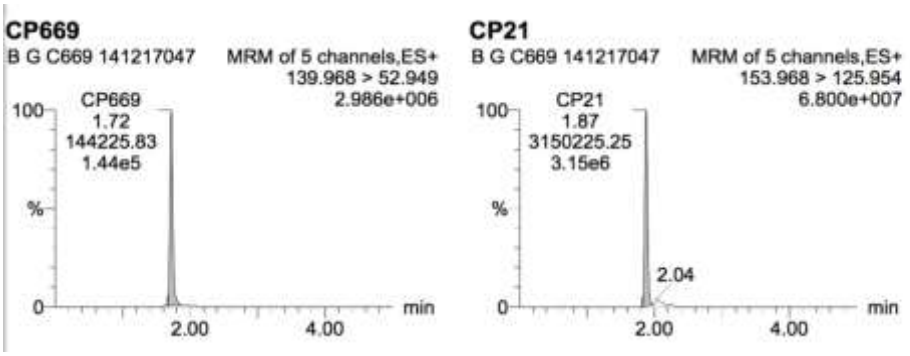

Figure V-35 MRM chromatographs of CP669 Phase I+II microsomal HLMs blank

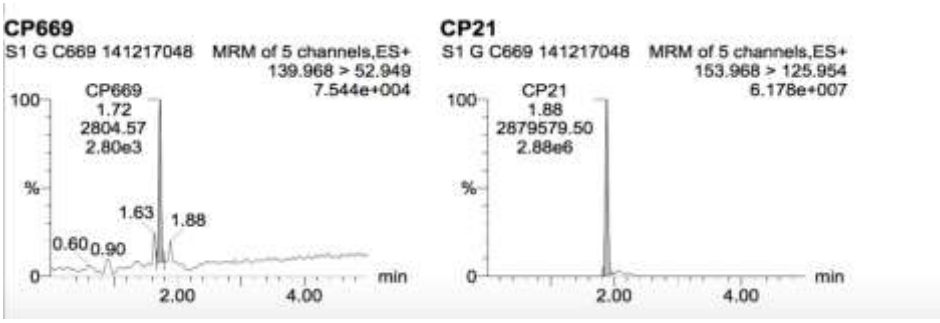

Figure V-36 MRM chromatographs of CP669 Phase I+II microsomal HLMs sample

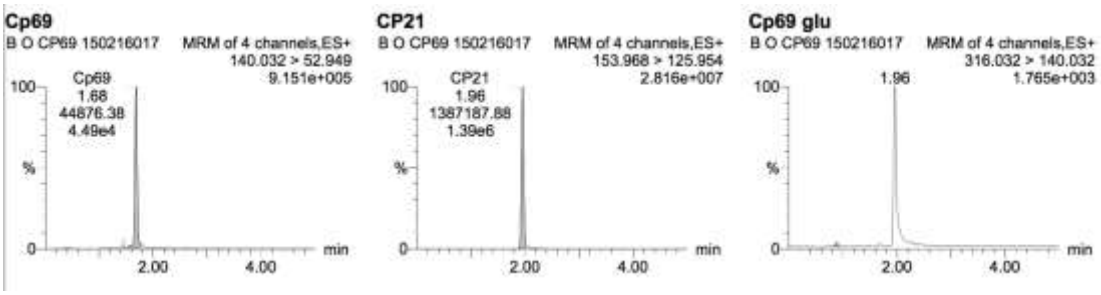

Figure V-37 MRM chromatographs of CP69 Phase I microsomal HLMs blank

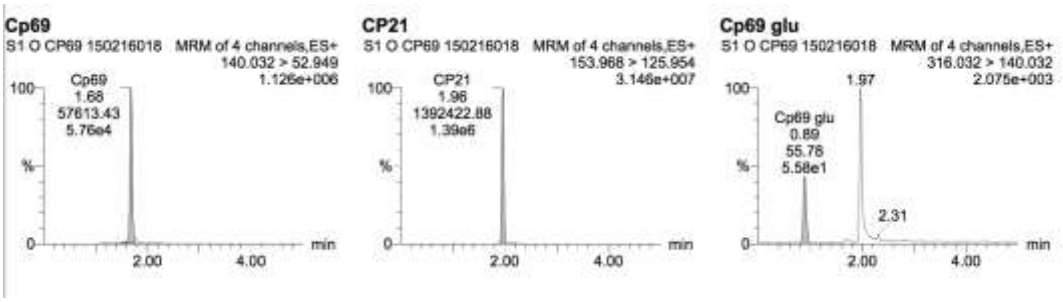

Figure V-38 MRM chromatographs of CP69 Phase I microsomal HLMs sample

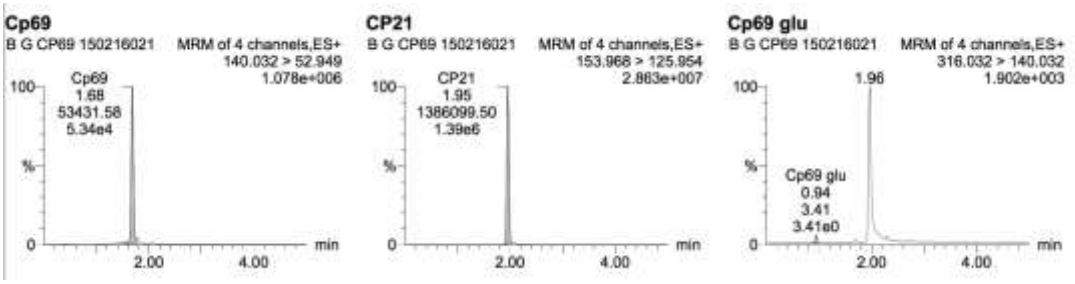

Figure V-39 MRM chromatographs of CP69 Phase I+II microsomal HLMs blank

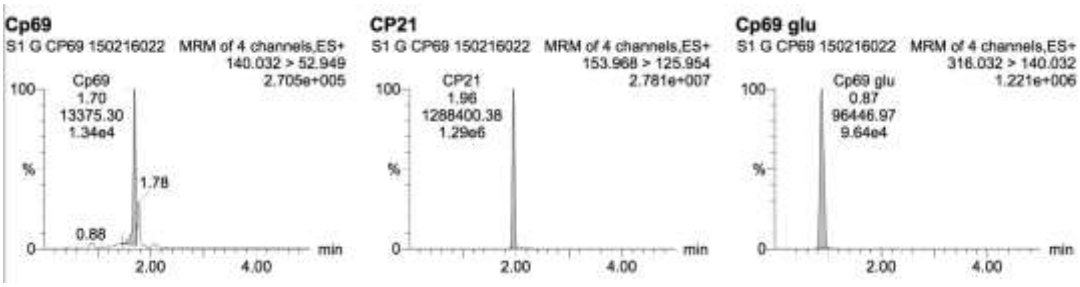

Figure V-40 MRM chromatographs of CP69 Phase I+II microsomal HLMs sample

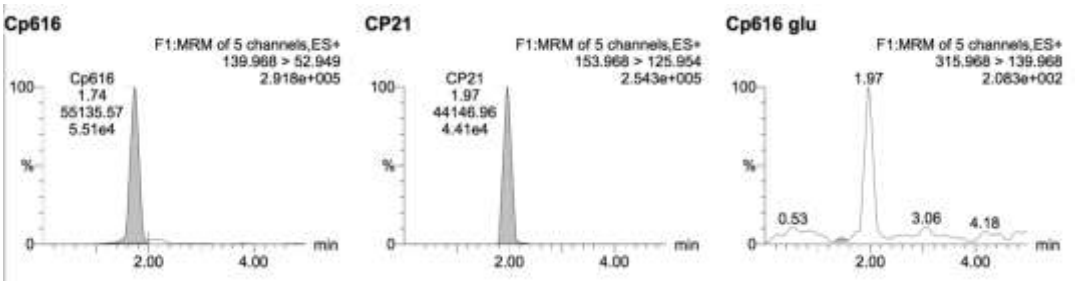

Figure V-41 MRM chromatographs of CP616 Phase I microsomal HLMs blank

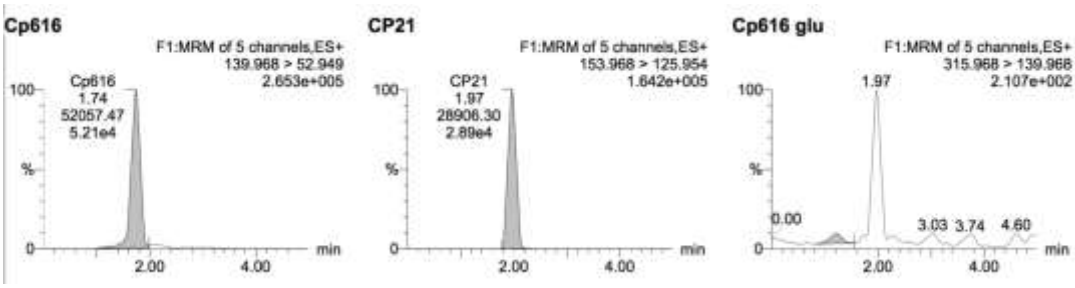

Figure V-42 MRM chromatographs of CP616 Phase I microsomal HLMs sample

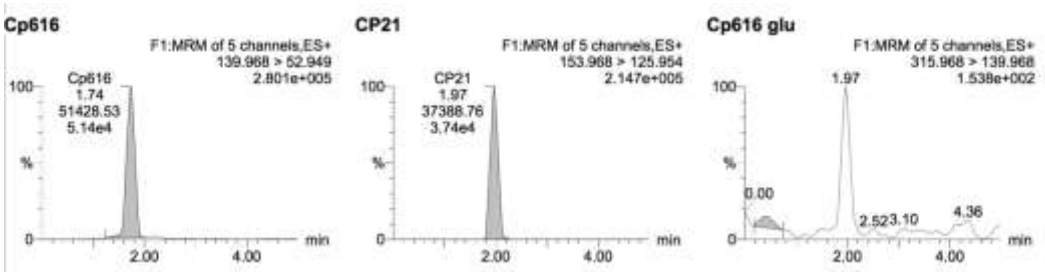

Figure V-43 MRM chromatographs of CP616 Phase I+II microsomal HLMs blank

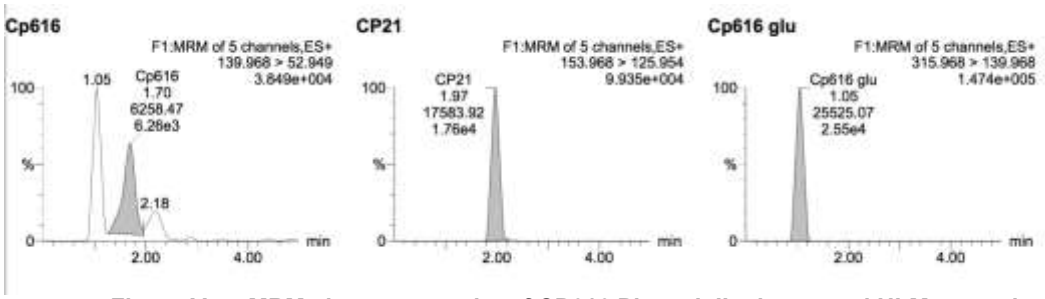

Figure V-44 MRM chromatographs of CP616 Phase I+II microsomal HLMs sample

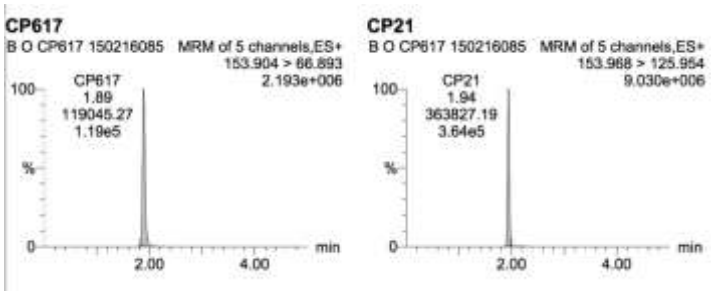

Figure V-45 MRM chromatographs of CP617 Phase I microsomal HLMs blank

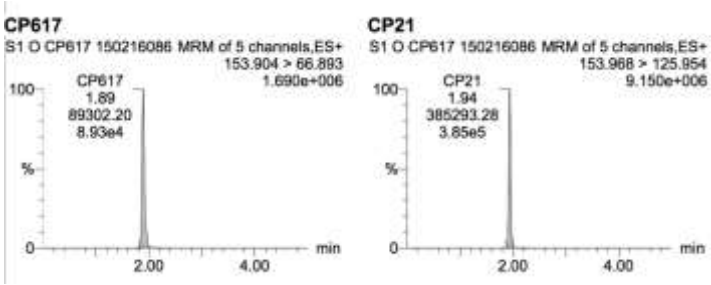

Figure V-46 MRM chromatographs of CP617 Phase I microsomal HLMs sample

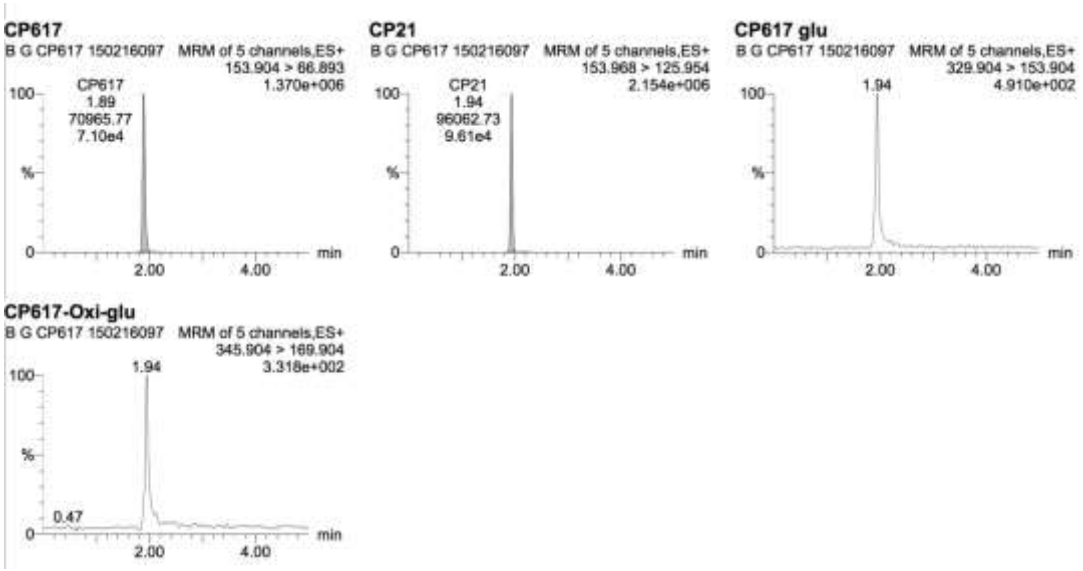

Figure V-47 MRM chromatographs of CP617 Phase I+II microsomal HLMs blank

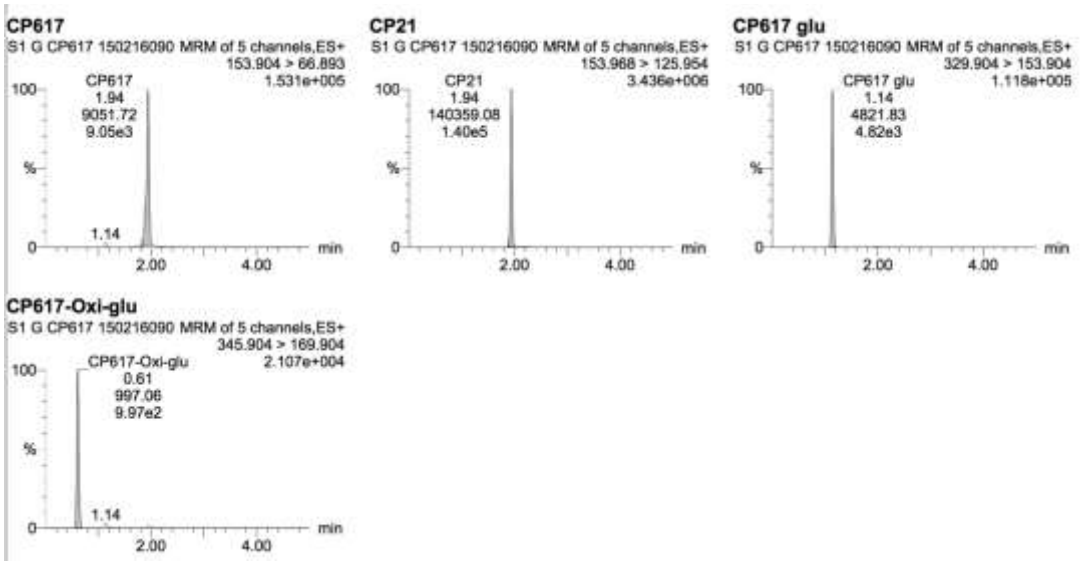

Figure V-48 MRM chromatographs of CP617 Phase I+II microsomal HLMs sample

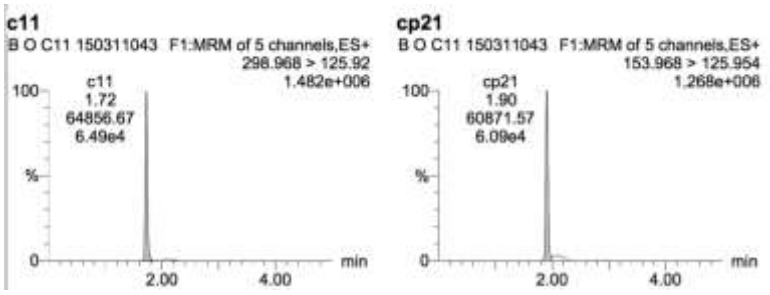

Figure V-49 MRM chromatographs of C11 Phase I microsomal HLMs blank

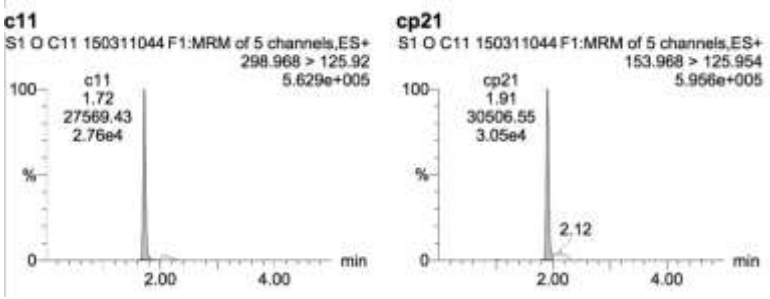

Figure V-50 MRM chromatographs of C11 Phase I microsomal HLMs sample

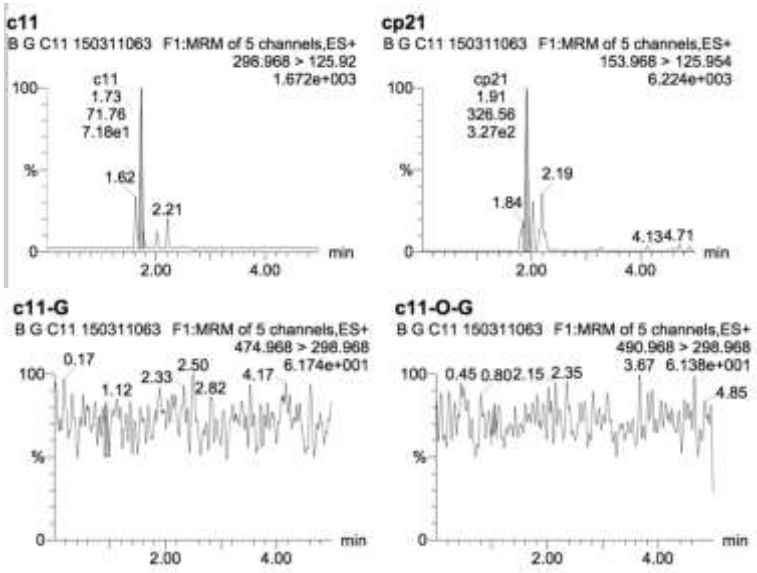

Figure V-51 MRM chromatographs of C11 Phase I+II microsomal HLMs blank

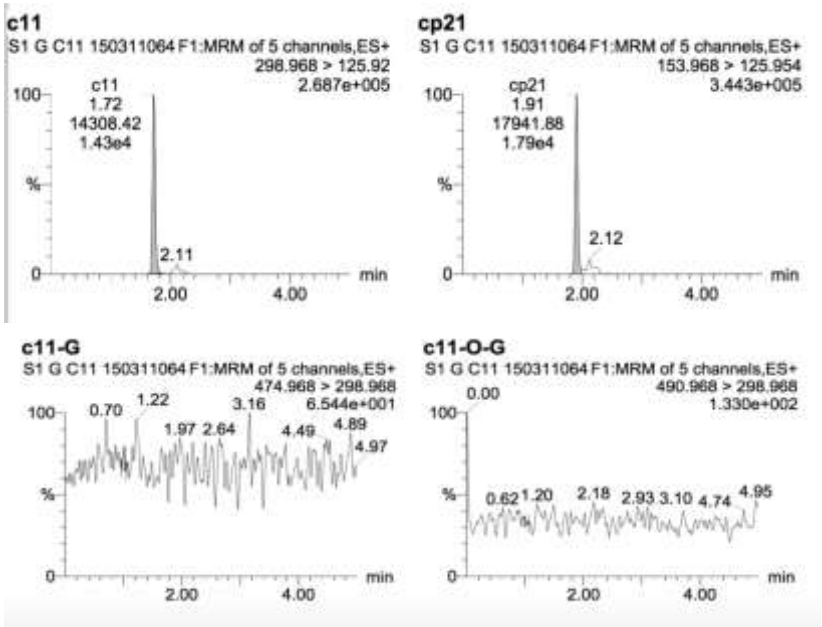

Figure V-52 MRM chromatographs of C11 Phase I+II microsomal HLMs sample

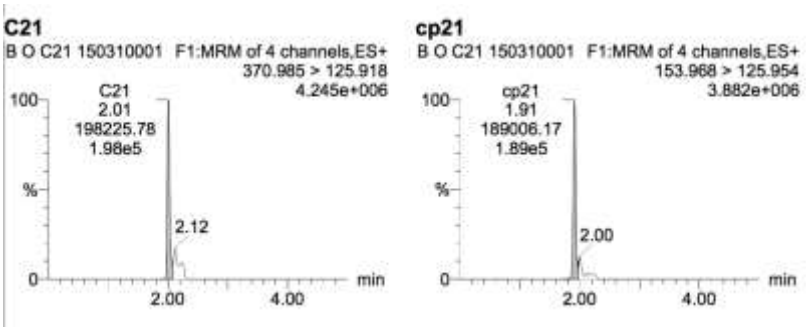

Figure V-53 MRM chromatographs of C21 Phase I microsomal HLMs blank

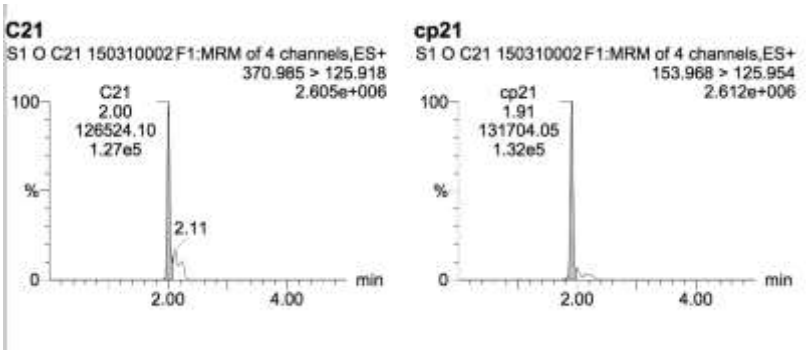

Figure V-54 MRM chromatographs of C21 Phase I microsomal HLMs sample

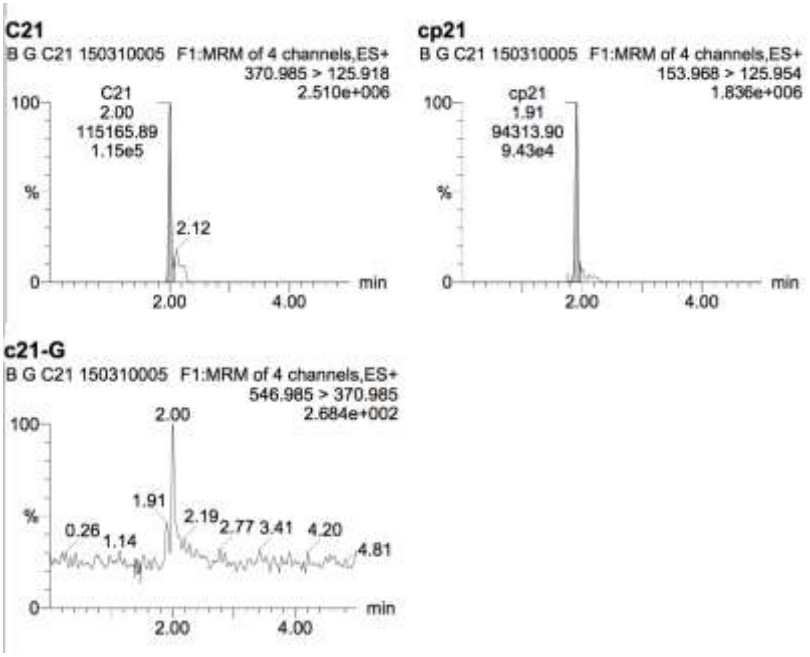

Figure V-55 MRM chromatographs of C21 Phase I+II microsomal HLMs blank

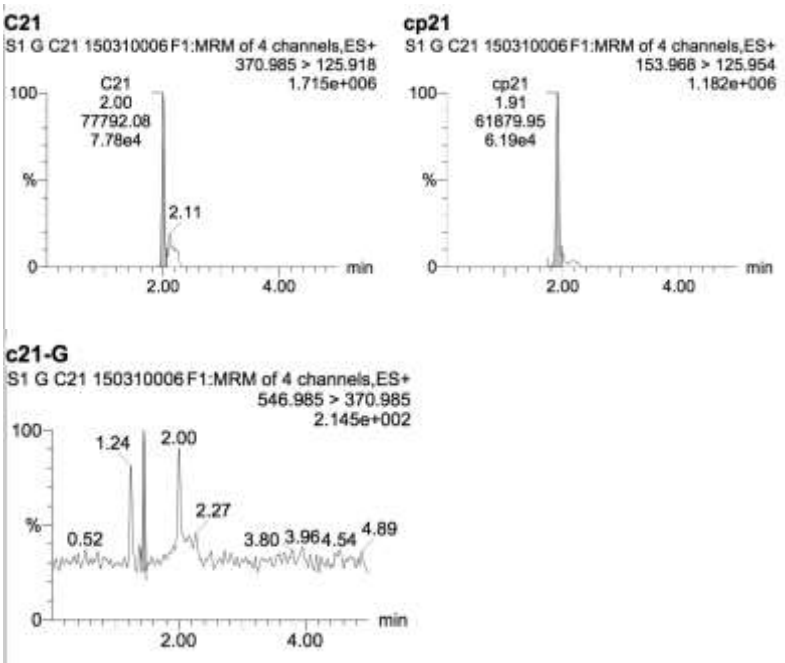

Figure V-56 MRM chromatographs of C21 Phase I+II microsomal HLMs sample

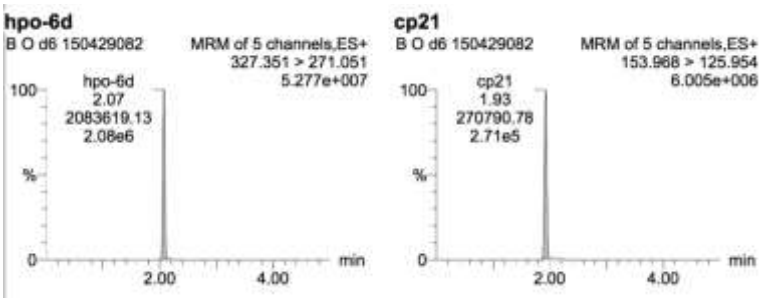

Figure V-57 MRM chromatographs of 6d Phase I microsomal HLMs blank

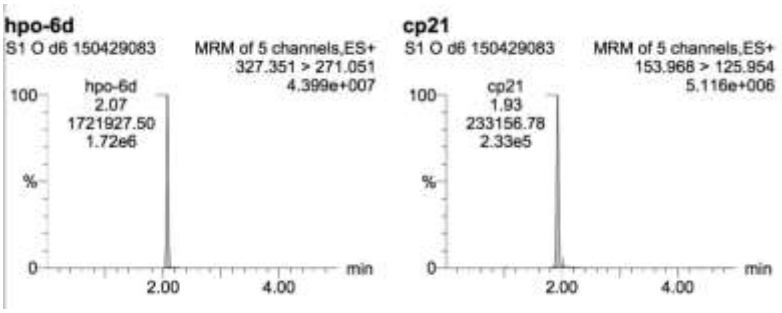

Figure V-58 MRM chromatographs of 6d Phase I microsomal HLMs sample

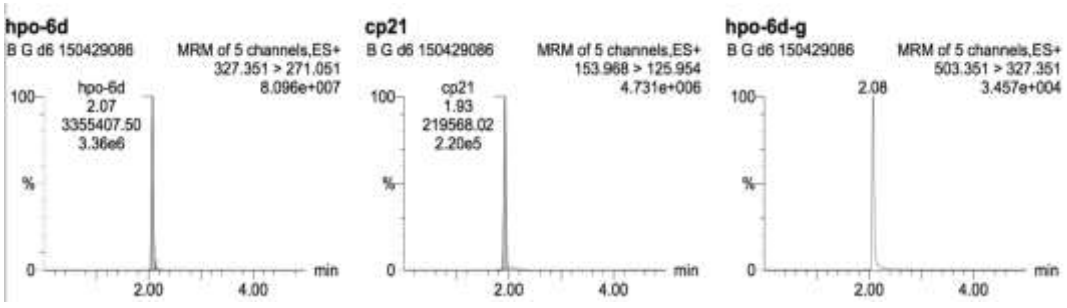

Figure V-59 MRM chromatographs of 6d Phase I+II microsomal HLMs blank

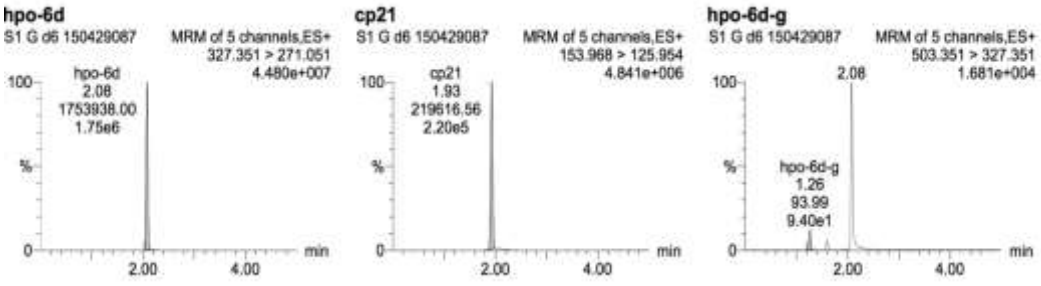

Figure V-60 MRM chromatographs of 6d Phase I+II microsomal HLMs sample

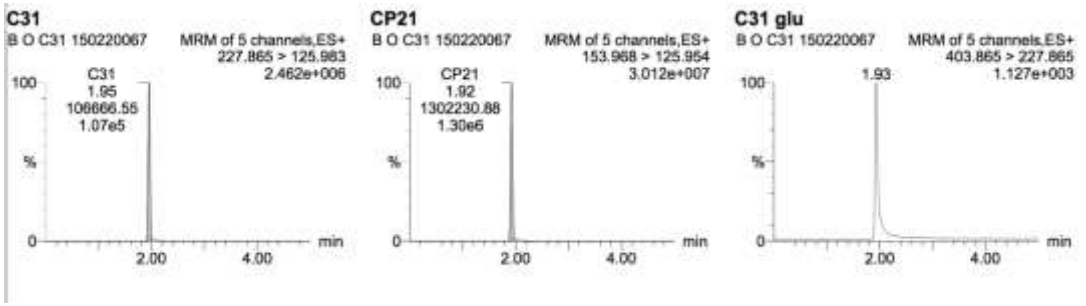

Figure V-61 MRM chromatographs of C31 Phase I microsomal HLMs blank

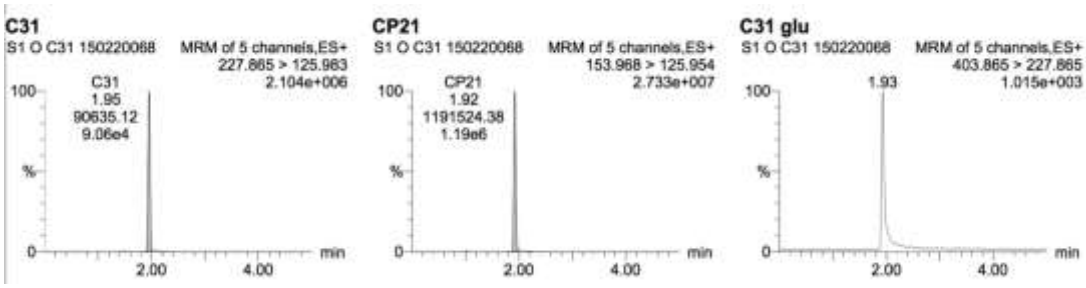

Figure V-62 MRM chromatographs of C31 Phase I microsomal HLMs sample

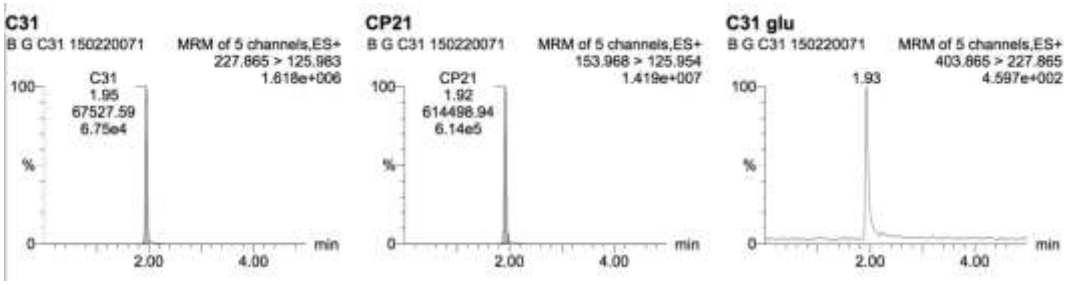

Figure V-63 MRM chromatographs of C31 Phase I+II microsomal HLMs blank

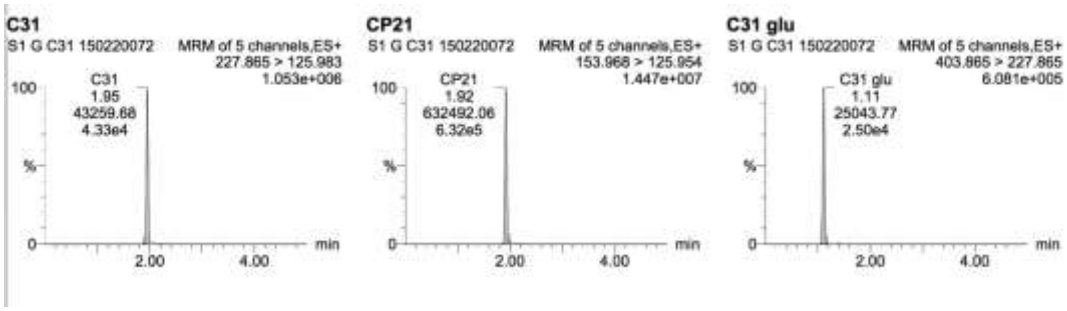

Figure V-64 MRM chromatographs of C31 Phase I+II microsomal HLMs sample

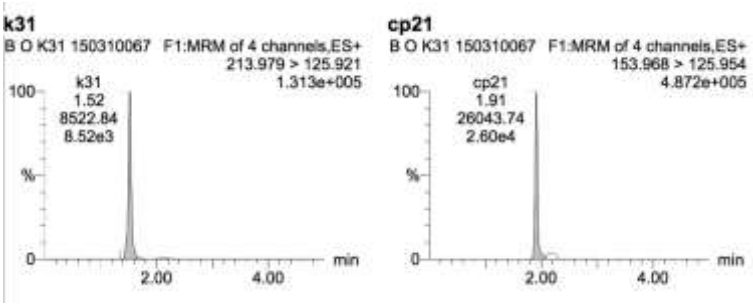

Figure V-65 MRM chromatographs of K31 Phase I microsomal HLMs blank

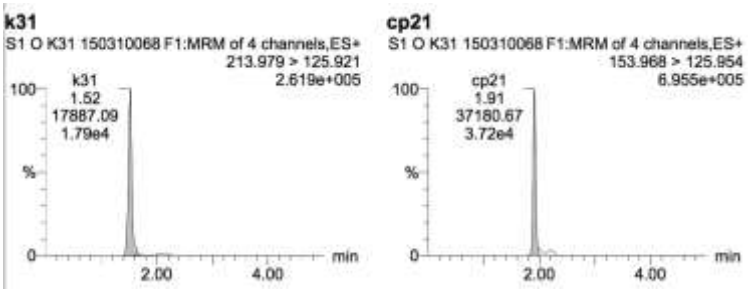

Figure V-66 MRM chromatographs of K31 Phase I microsomal HLMs sample

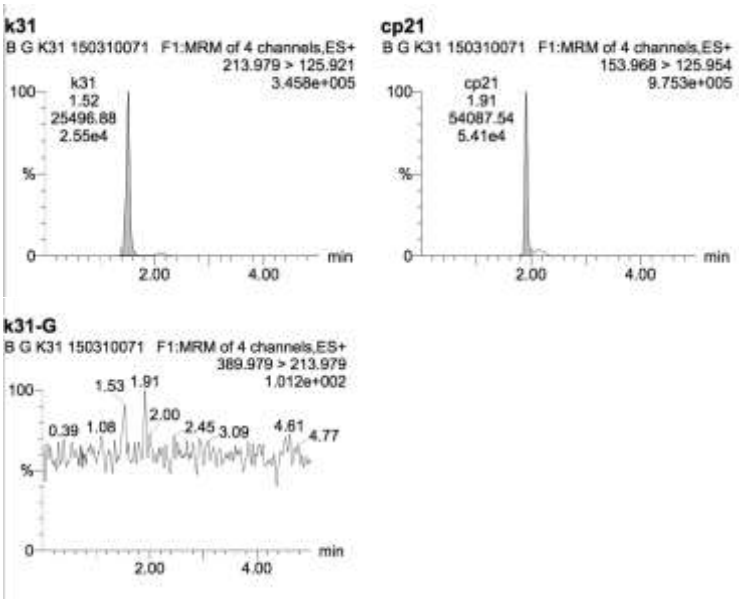

Figure V-67 MRM chromatographs of K31 Phase I+II microsomal HLMs blank

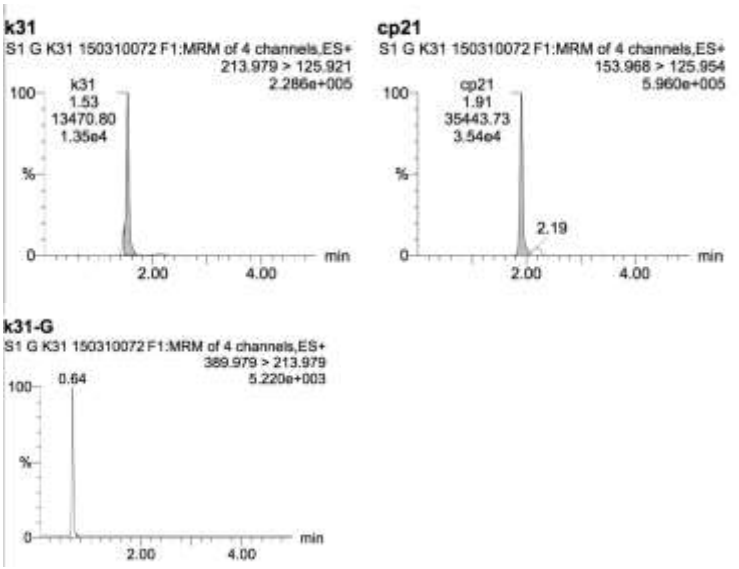

Figure V-68 MRM chromatographs of K31 Phase I+II microsomal HLMs sample

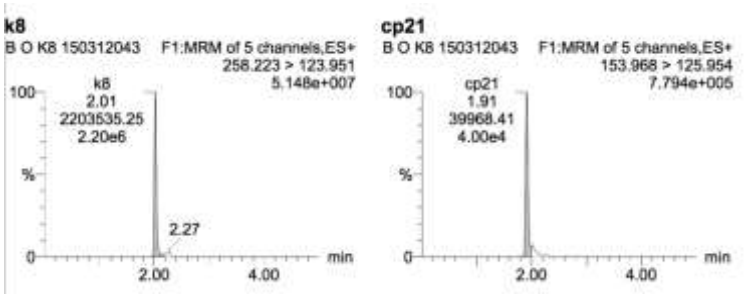

Figure V-69 MRM chromatographs of K8 Phase I microsomal HLMs blank

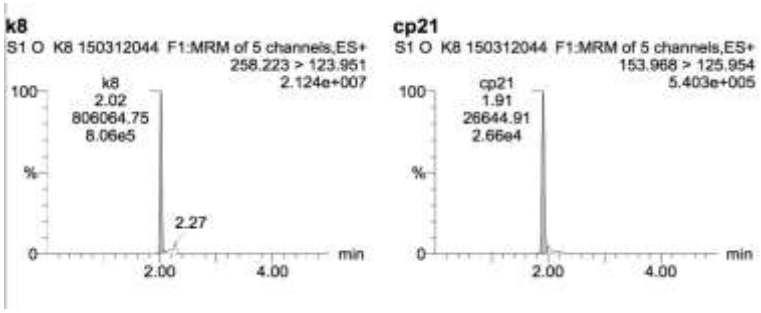

Figure V-70 MRM chromatographs of K8 Phase I microsomal HLMs sample

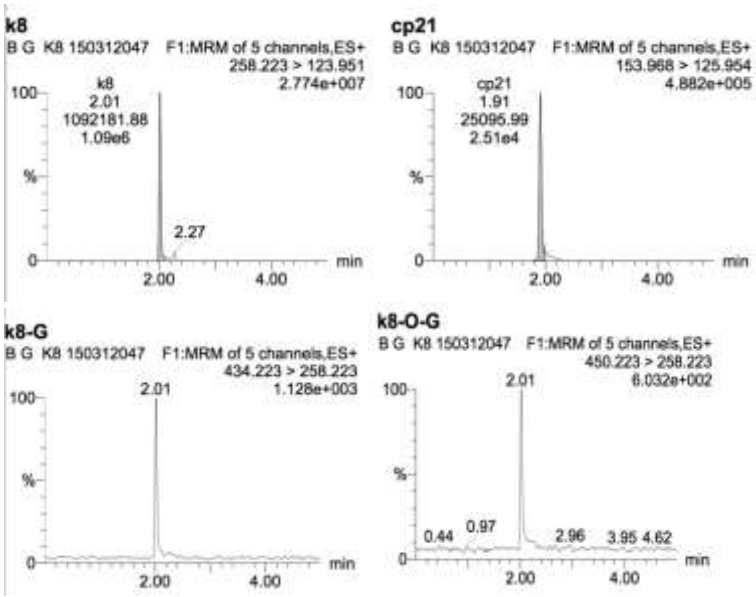

Figure V-71 MRM chromatographs of K8 Phase I+II microsomal HLMs blank

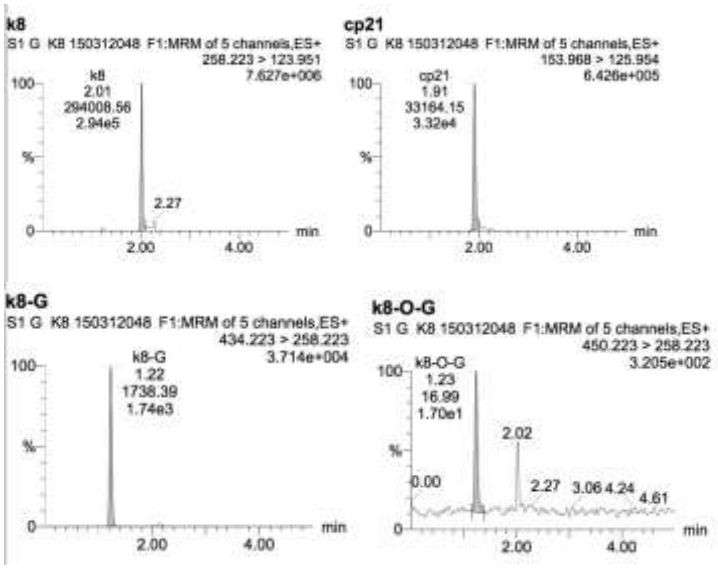

Figure V-72 MRM chromatographs of K8 Phase I+II microsomal HLMs sample

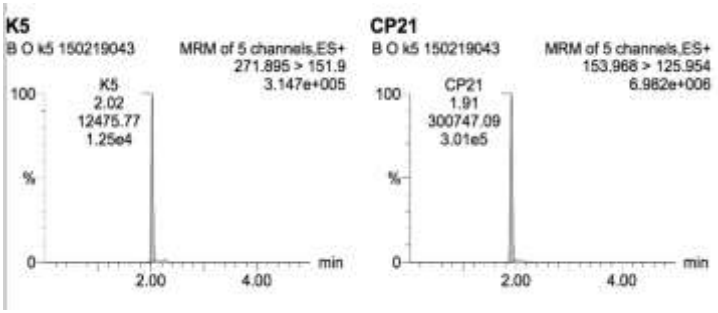

Figure V-73 MRM chromatographs of K5 Phase I microsomal HLMs blank

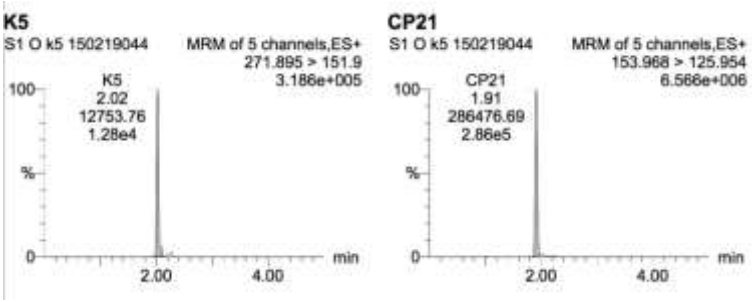

Figure V-74 MRM chromatographs of K5 Phase I microsomal HLMs sample

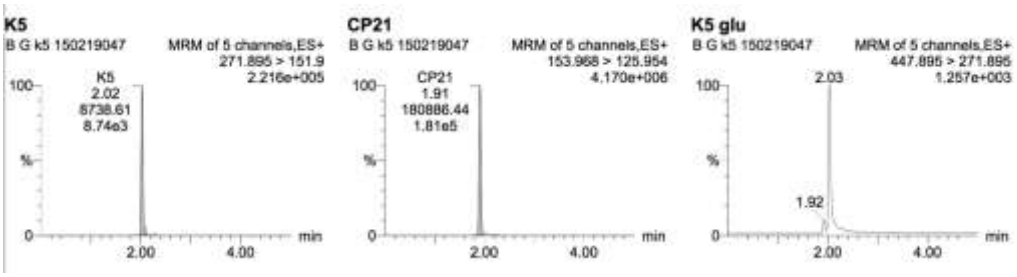

Figure V-75 MRM chromatographs of K5 Phase I microsomal HLMs blank

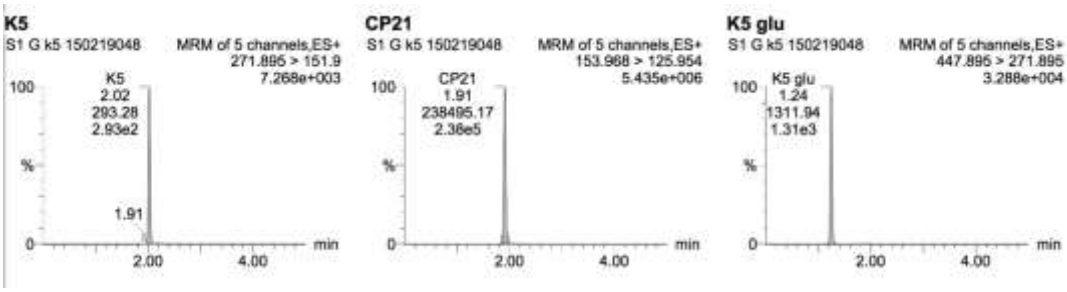

Figure V-76 MRM chromatographs of K5 Phase I+II microsomal HLMs sample

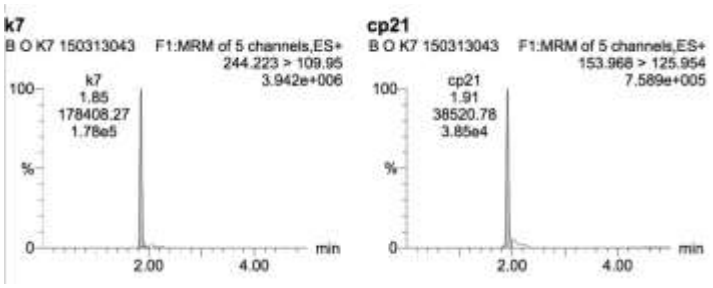

Figure V-77 MRM chromatographs of K7 Phase I microsomal HLMs blank

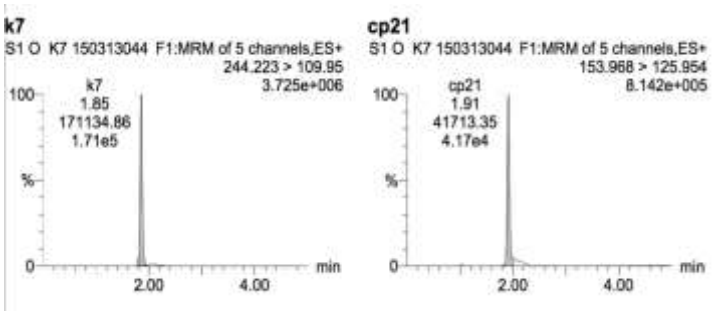

Figure V-78 MRM chromatographs of K7 Phase I microsomal HLMs sample

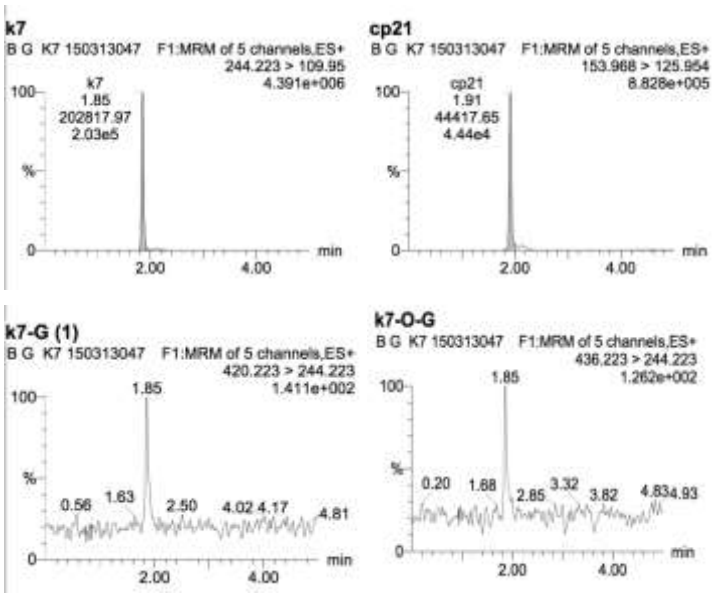

Figure V-79 MRM chromatographs of K7 Phase I+II microsomal HLMs blank

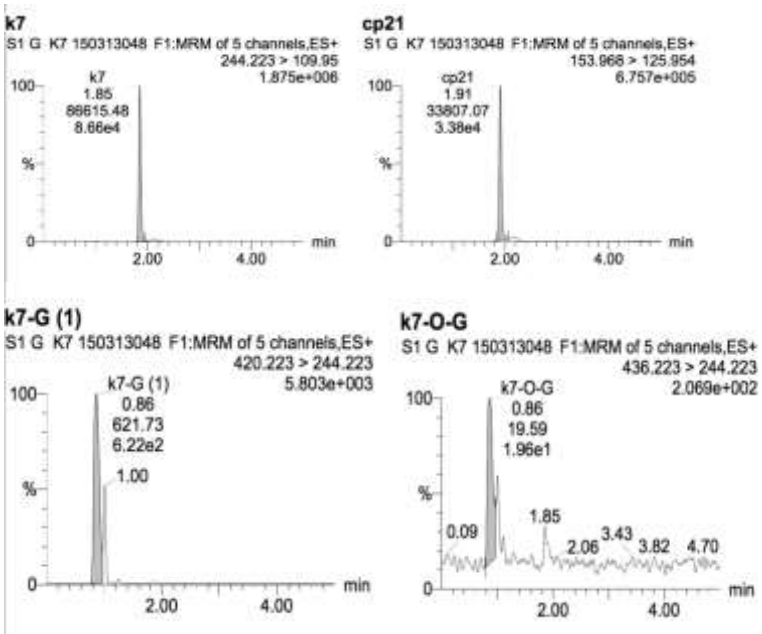

Figure V-80 MRM chromatographs of K7 Phase I+II microsomal HLMs sample

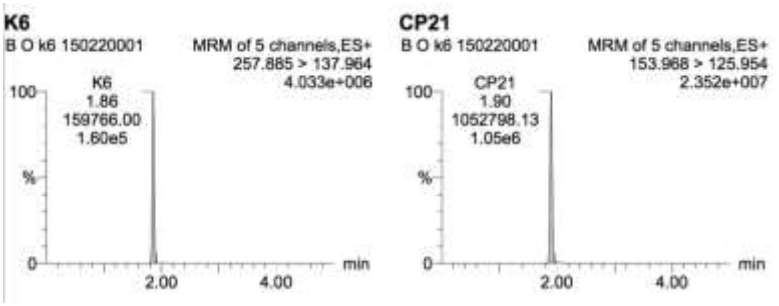

Figure V-81 MRM chromatographs of K6 Phase I microsomal HLMs blank

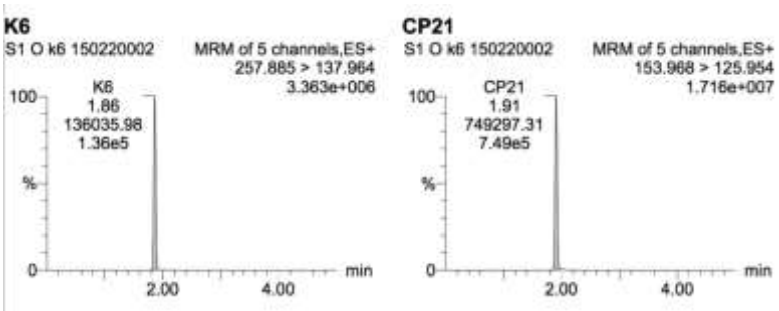

Figure V-82 MRM chromatographs of K6 Phase I microsomal HLMs sample

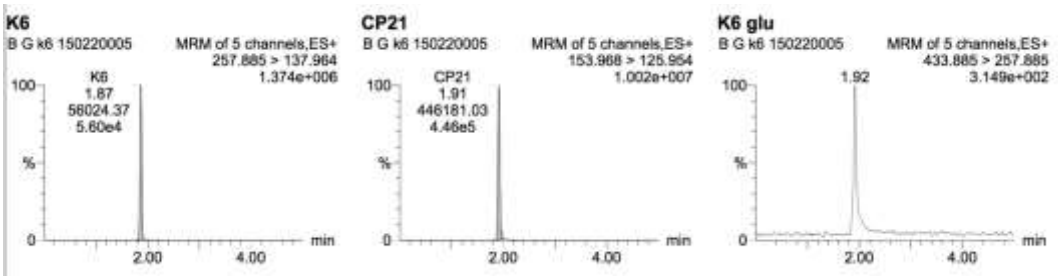

Figure V-83 MRM chromatographs of K6 Phase I+II microsomal HLMs blank

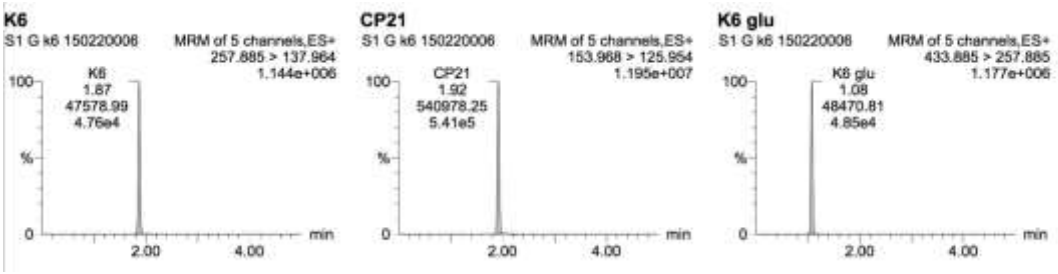

Figure V-84 MRM chromatographs of K6 Phase I+II microsomal HLMs sample

Appendix VI

VI-I Metabolic conversion of CN126

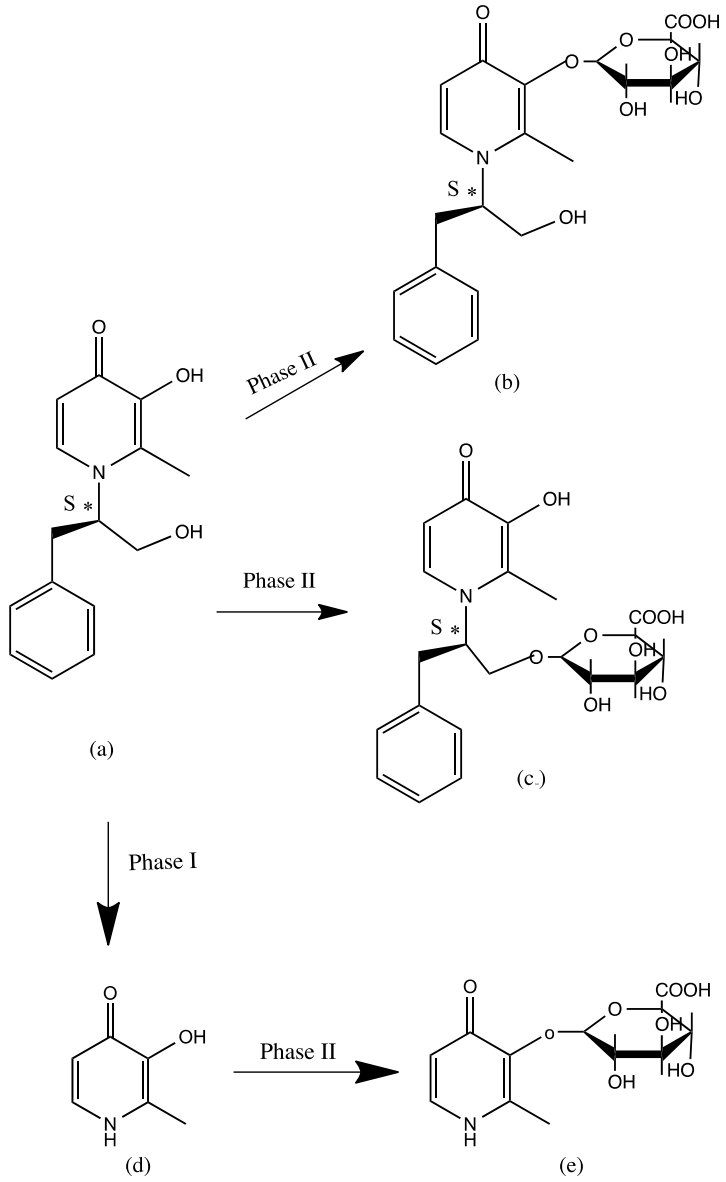

Scheme V-I Metabolic pathways of CN126

(a) CN126;
(b) 3-O-glucuronide conjugate of CN126;
(c) CN126-1-(1-O-glucuronide) conjugate;
(d) N-dealkylated metabolite of CN126;
(e) 3-O-glucuronide conjugate of N-dealkylated metabolite of CN126

VI-II Metabolic conversion of close analogues of CP20

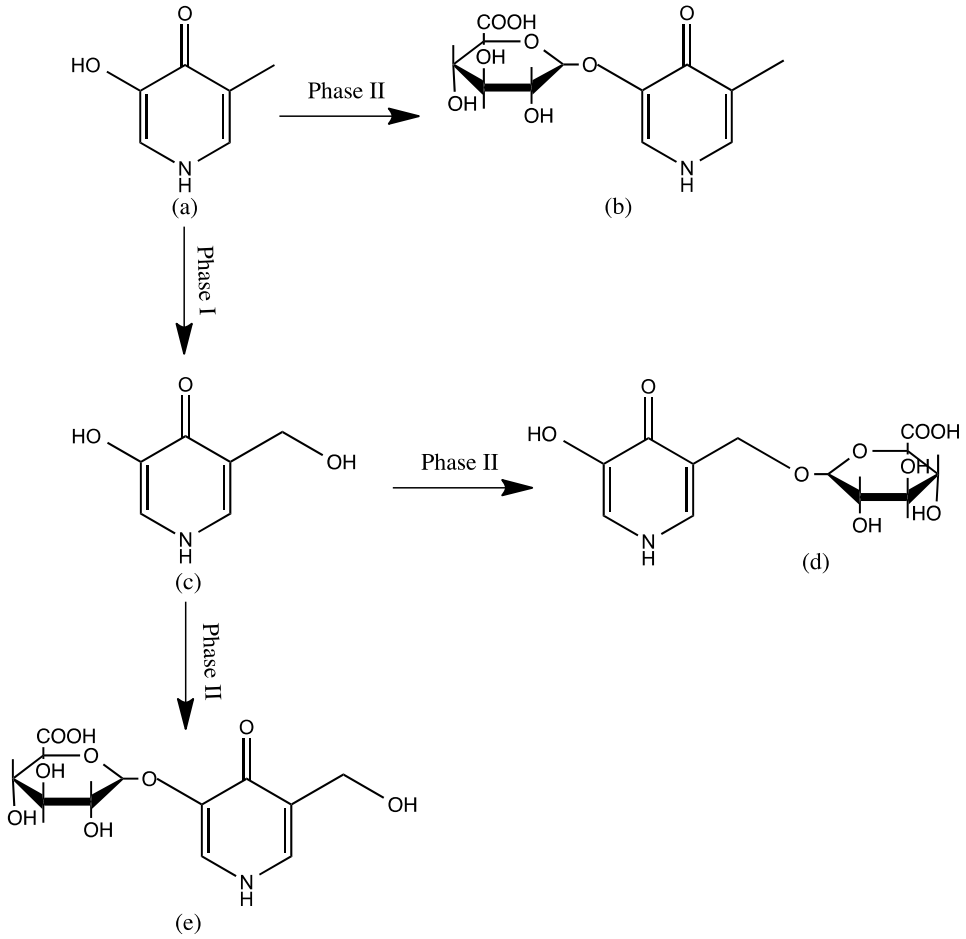

Scheme VI-II-1 Metabolic pathways of CP679

(a) CP679;
(b) 3-O-glucuronide conjugate of CP679;
(c) CP679-5-hydroxymethyl metabolite;
(d) Glucuronide of 5-hydroxymethyl conjugate of CP679;
(e) 3-O-glucuronide conjugate of CP679-5-hydroxymethyl metabolite

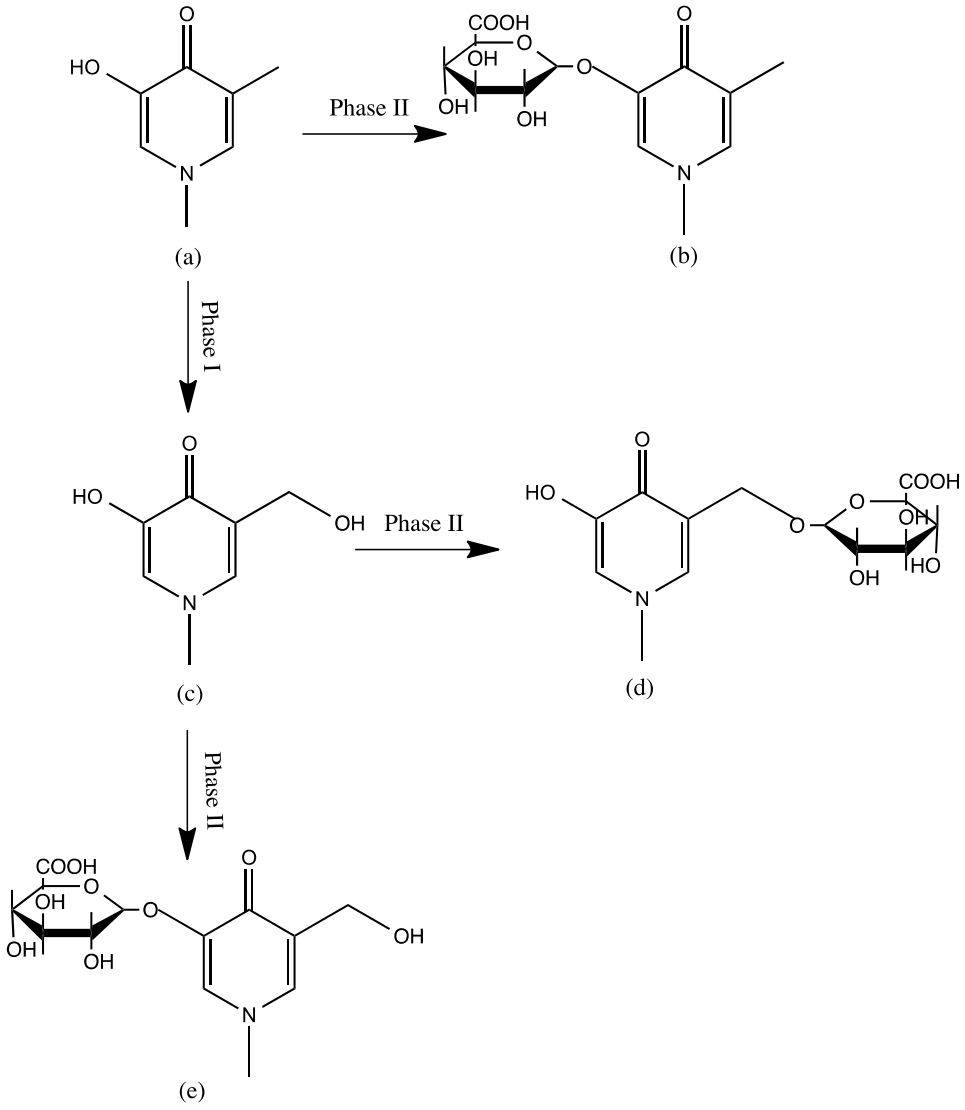

Scheme VI-II-2 Metabolic pathways of CP669

(a) CP669;
(b) 3-O-glucuronide conjugate of CP669;
(c) CP669-5-hydroxymethyl metabolite;
(d) Glucuronide of 5-hydroxymethyl conjugate of CP669;
(e) 3-O-glucuronide conjugate of CP669-5-hydroxymethyl metabolite

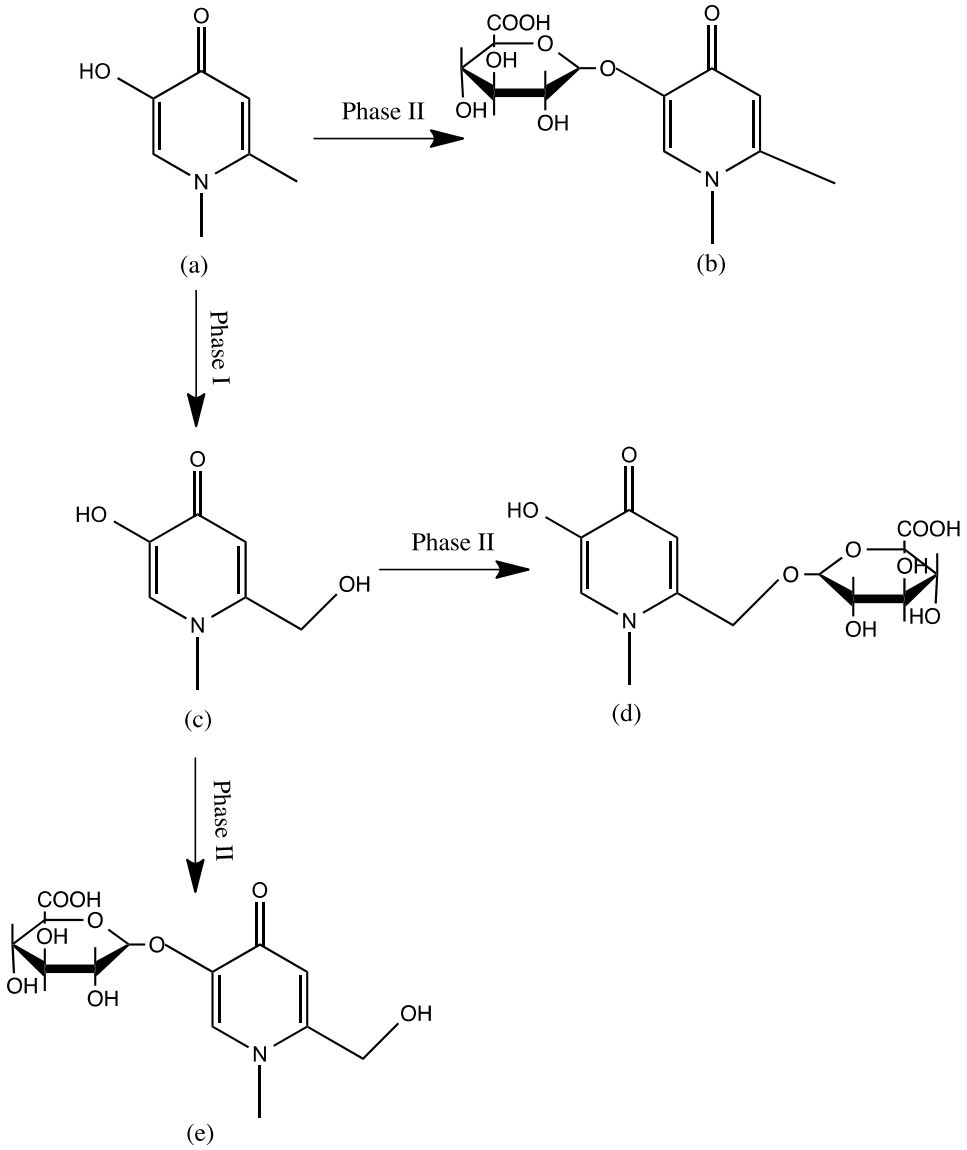

Scheme VI-II-3 Metabolic pathways of CP69

(a) CP69;
(b) 3-O-glucuronide conjugate of CP69;
(c) CP69-6-hydroxymethyl metabolite;
(d) Glucuronide of 6-hydroxymethyl conjugate of CP69;
(e) 3-O-glucuronide conjugate of CP69-6-hydroxymethyl metabolite

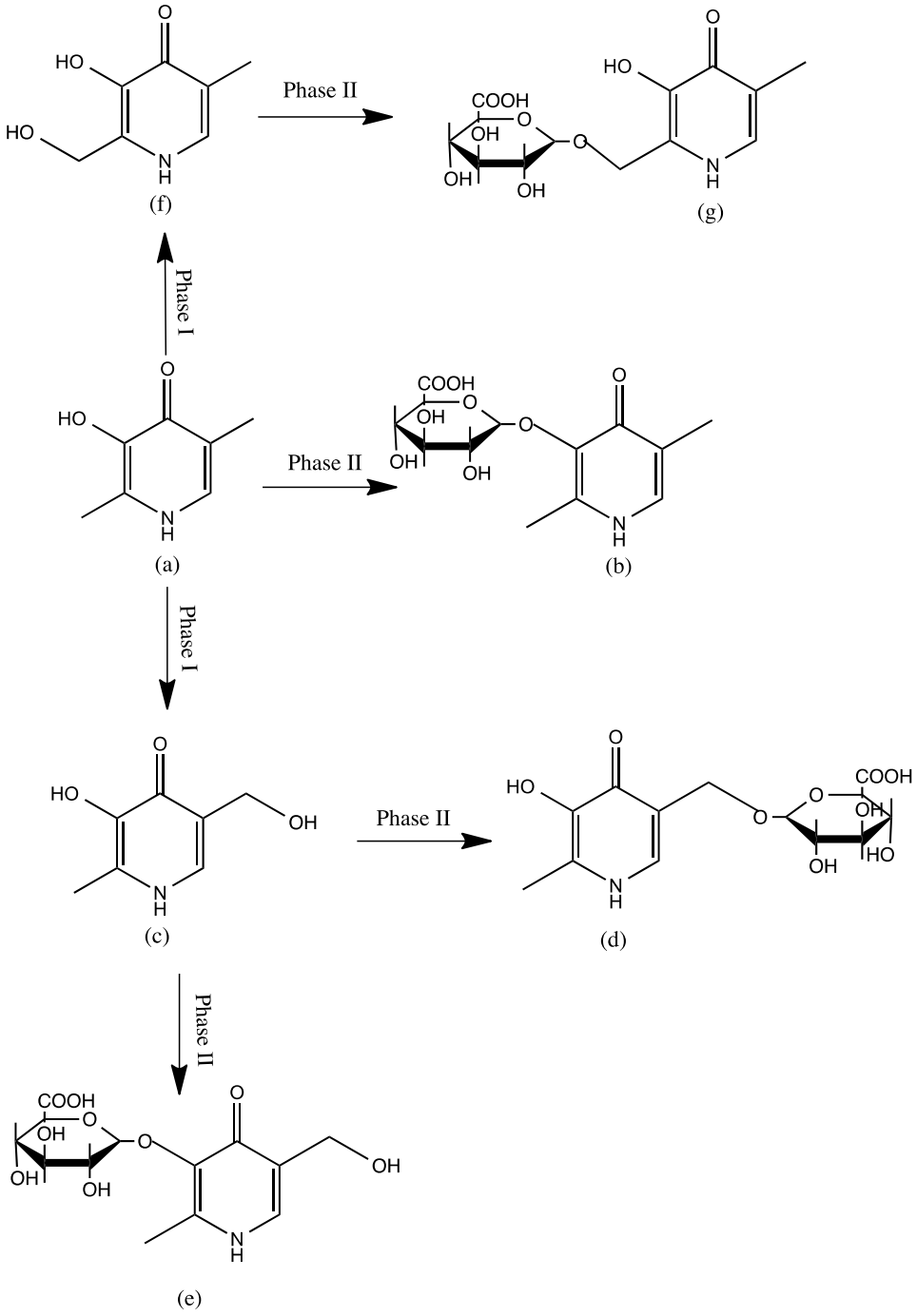

Scheme VI-II-4 Metabolic pathways of CP616

(a) CP616;
(b) 3-O-glucuronide conjugate of CP616;
(c) CP616-5-hydroxymethyl metabolite;
(d) Glucuronide of 5-hydroxymethyl conjugate of CP616;
(e) 3-O-glucuronide conjugate of CP616-5-hydroxymethyl metabolite;
(f) CP616-2-hydroxymethyl metabolite;
(g) Glucuronide of 2-hydroxymethyl conjugate of CP616

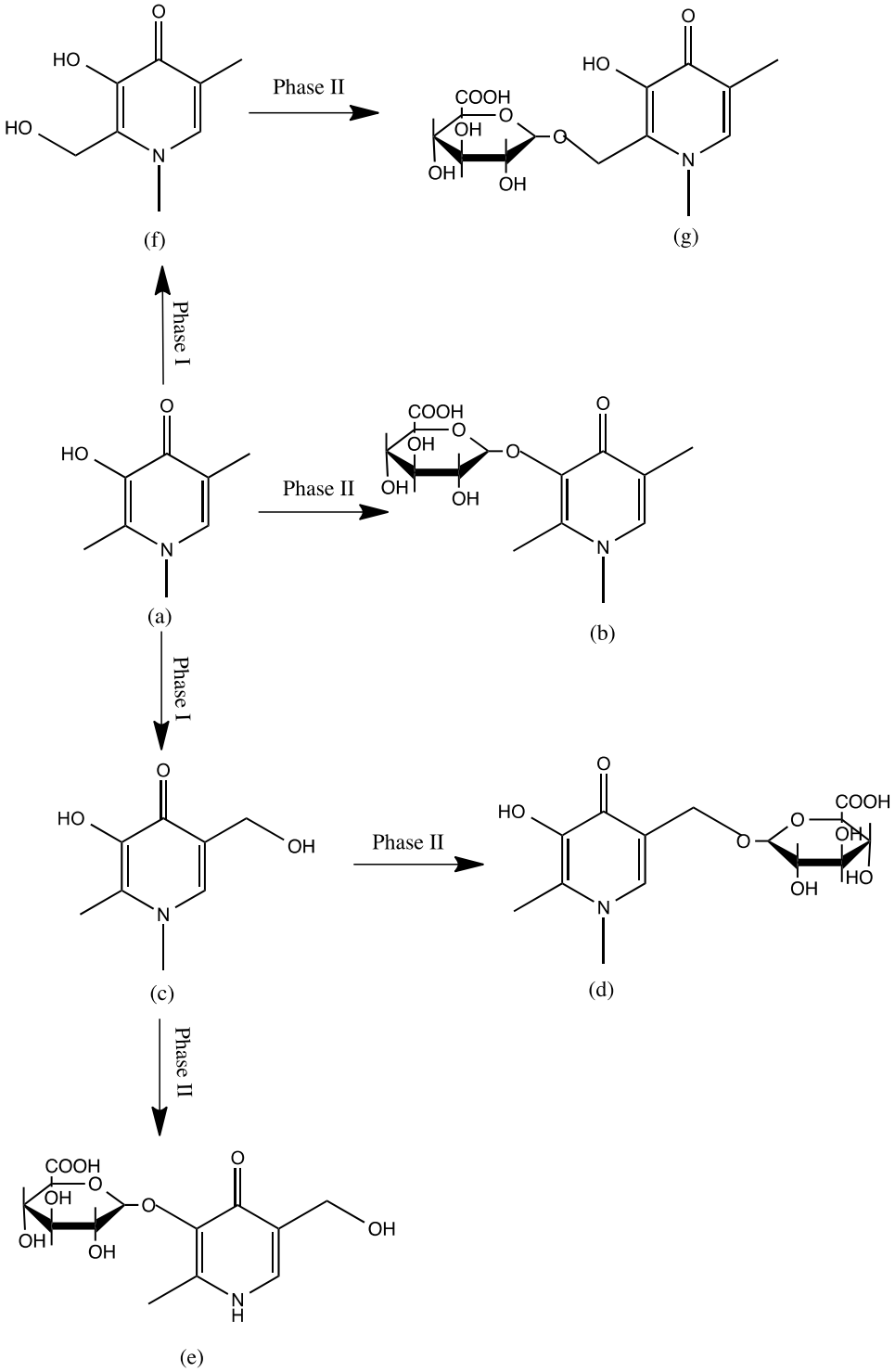

Scheme VI-II-5 Metabolic pathways of CP617

(a) CP617;
(b) 3-O-glucuronide conjugate of CP617;
(c) CP617-5-hydroxymethyl metabolite;
(d) Glucuronide of 5-hydroxymethyl conjugate of CP617;
(e) 3-O-glucuronide conjugate of CP617-5-hydroxymethyl metabolite;
(f) CP617-2-hydroxymethyl metabolite;
(g) Glucuronide of 2-hydroxymethyl conjugate of CP617

VI-III Metabolic conversion of pegylated hydroxypyridinones

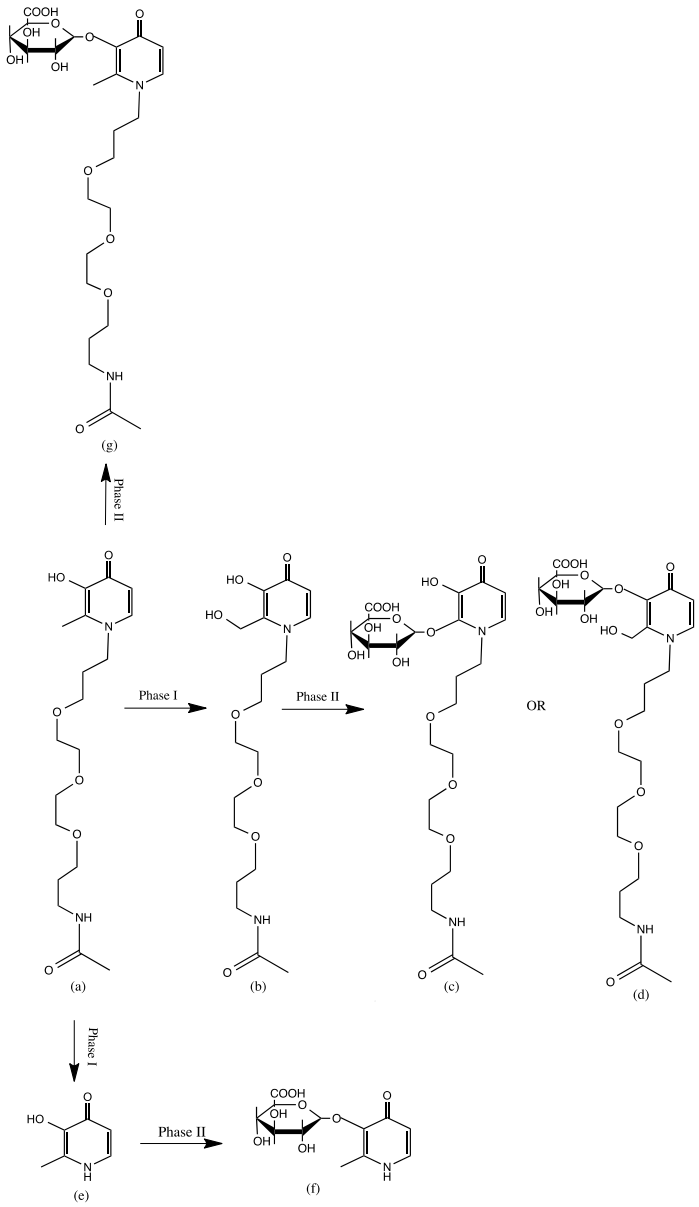

Scheme VIII-1 Metabolic pathways of C21

(a) C21;
(b) C21-2-hydroxymethyl metabolite;
(c) Glucuronide of 2-hydroxymethyl conjugate of C21;
(d) 3-O-Glucuronide conjugate of C21-2-hydroxymethyl metabolite;
(e) N-dealkylated metabolite of C21;
(f) 3-O-glucuronide conjugate of N-dealkylated metabolite of C21
(g) 3-O-Glucuronide conjugate of C21

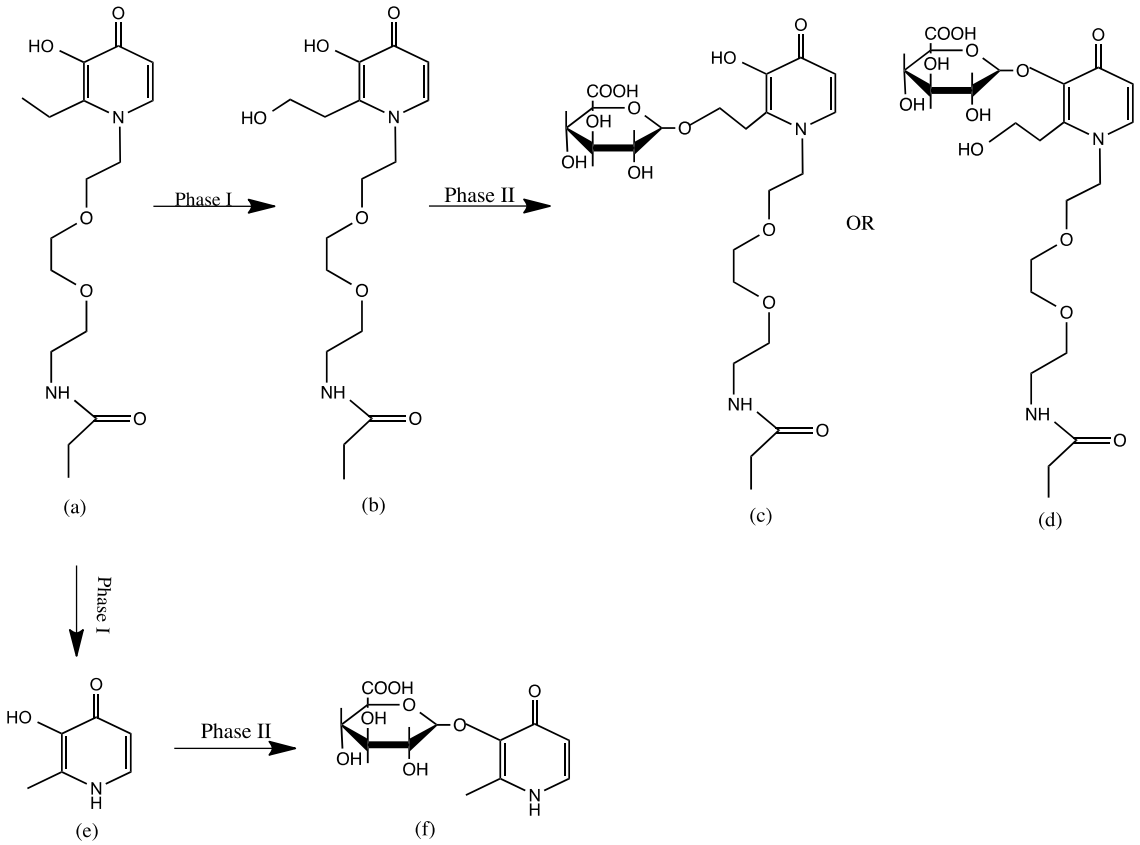

Scheme VIII-2 Metabolic pathways of 6d

(a) 6d;
(b) -2-hydroxymethyl metabolite;
(c) Glucuronide of 2-hydroxymethyl conjugate of C11;
(d) 3-O-Glucuronide conjugate of C11-2-hydroxymethyl metabolite;
(e) N-dealkylated metabolite of C11;
(f) 3-O-glucuronide conjugate of N-dealkylated metabolite of C11

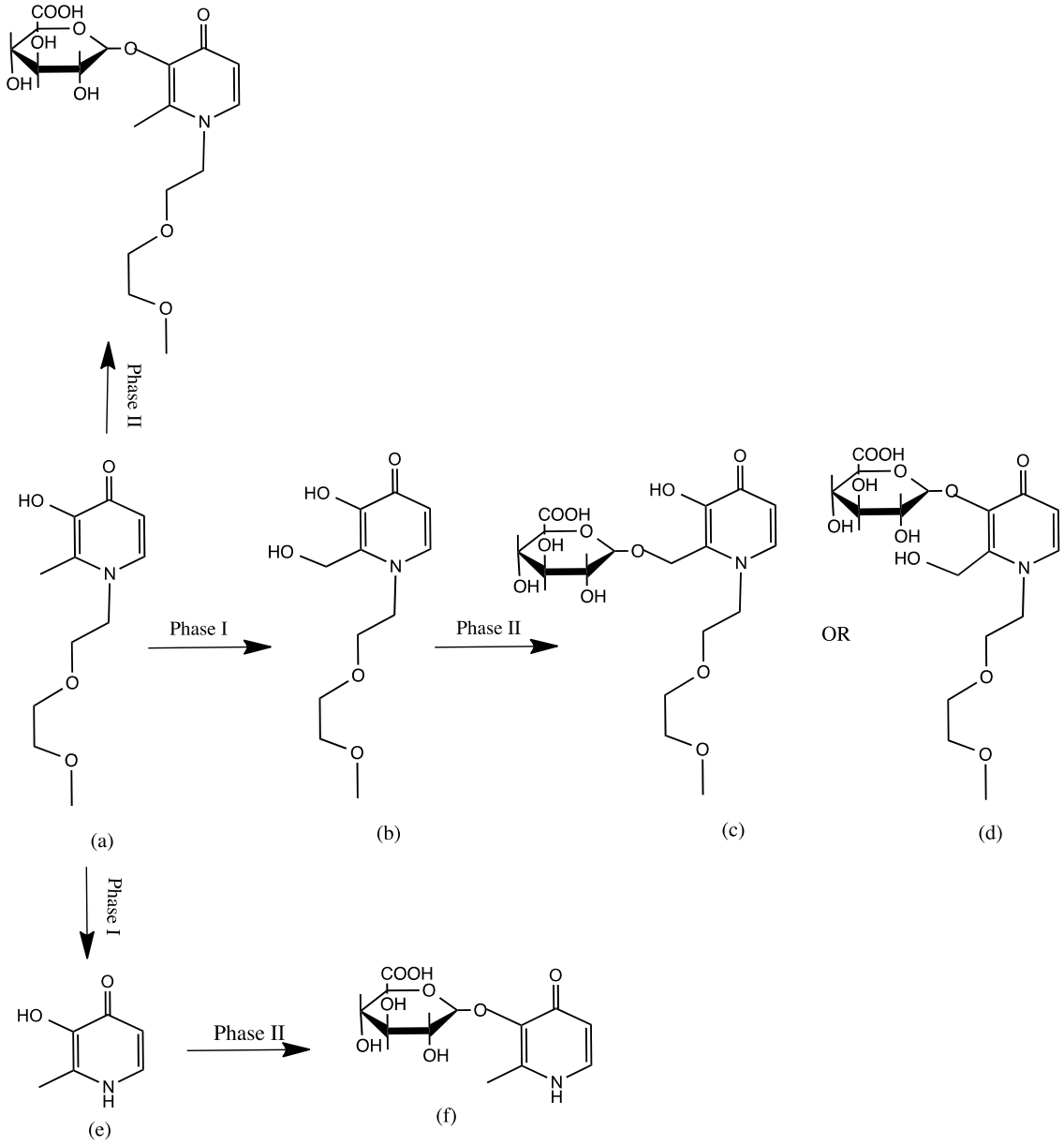

Scheme VIII-3 Metabolic pathways of C31

(a) C31;
(b) C31-2-hydroxymethyl metabolite;
(c) Glucuronide of 2-hydroxymethyl conjugate of C31;
(d) 3-O-Glucuronide conjugate of C31-2-hydroxymethyl metabolite;
(e) N-dealkylated metabolite of C31;
(f) 3-O-glucuronide conjugate of N-dealkylated metabolite of C31
(g) 3-O-Glucuronide conjugate of K31

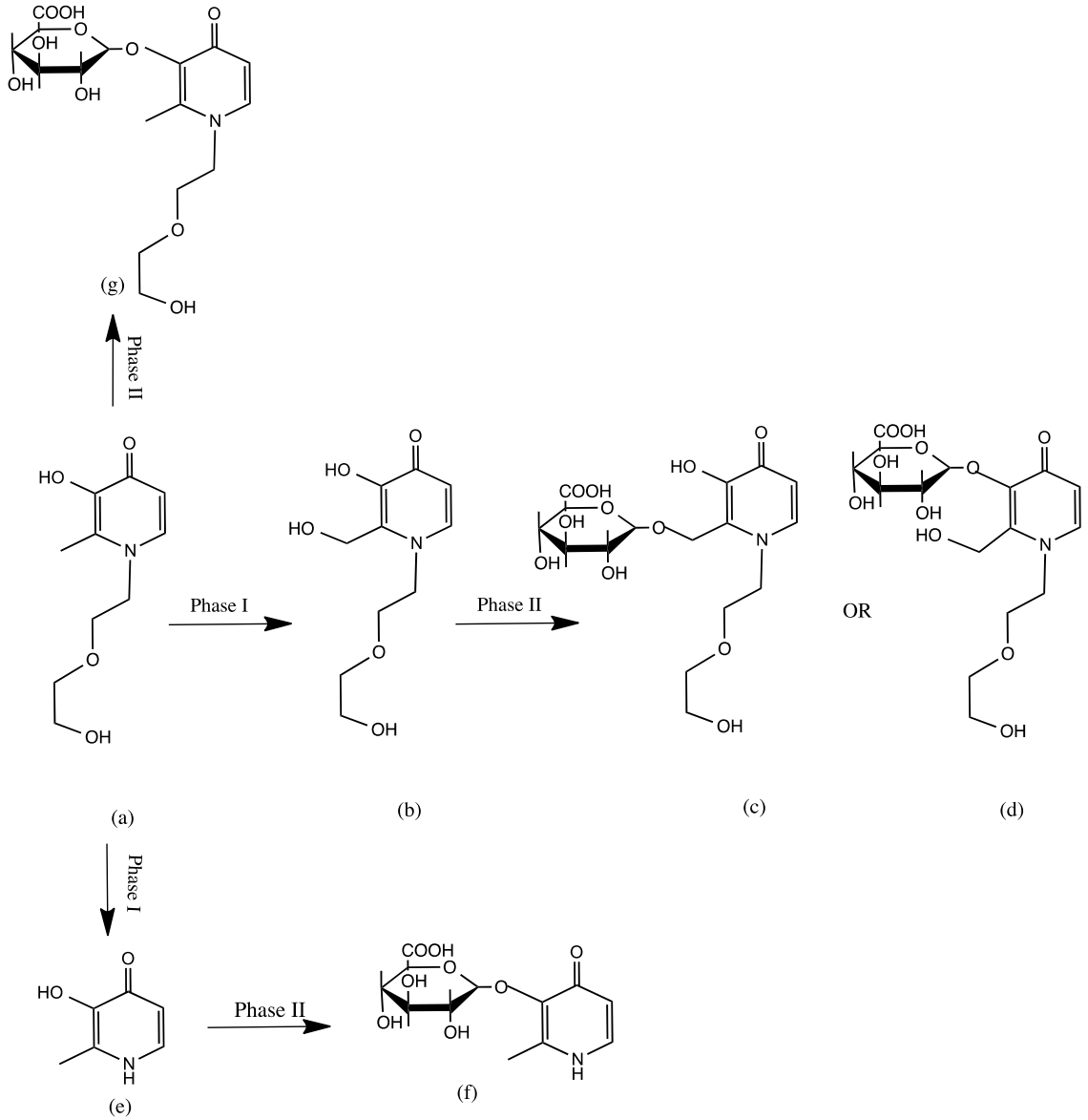

Scheme VIII-4 Metabolic pathways of K31

(a) K31;
(b) K31-2-hydroxymethyl metabolite;
(c) Glucuronide of 2-hydroxymethyl conjugate of K31;
(d) 3-O-Glucuronide conjugate of K31-2-hydroxymethyl metabolite;
(e) N-dealkylated metabolite of K31;
(f) 3-O-glucuronide conjugate of N-dealkylated metabolite of K31
(g) 3-O-Glucuronide conjugate of K31

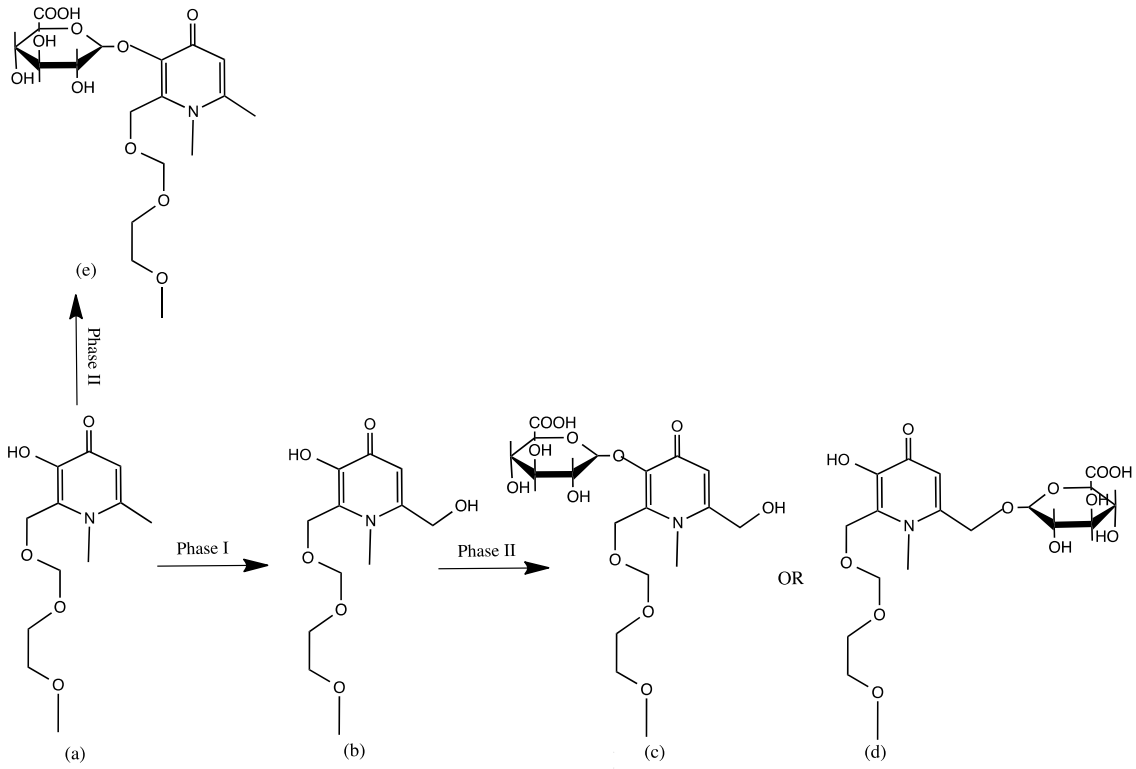

Scheme VIII-5 Metabolic pathways of K8

(a) K8;
(b) K8-6-hydroxymethyl metabolite;
(c) 3-O-Glucuronide conjugate of K8-6-hydroxymethyl metabolite;
(d) Glucuronide of 6-hydroxymethyl conjugate of K8;
(e) 3-O-Glucuronide conjugate of K8

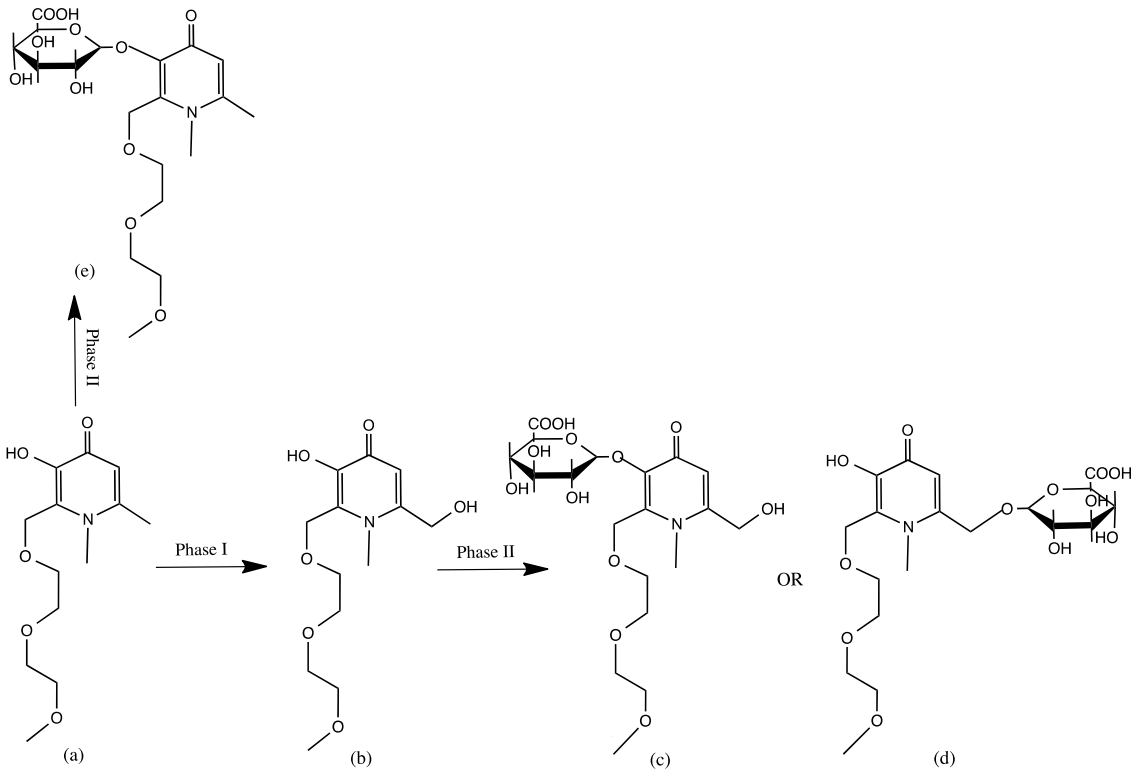

Scheme VIII-6 Metabolic pathways of K5

(a) K5;
(b) K5-6-hydroxymethyl metabolite;
(c) 3-O-Glucuronide conjugate of K5-6-hydroxymethyl metabolite;
(d) Glucuronide of 6-hydroxymethyl conjugate of K5;
(e) 3-O-Glucuronide conjugate of K5

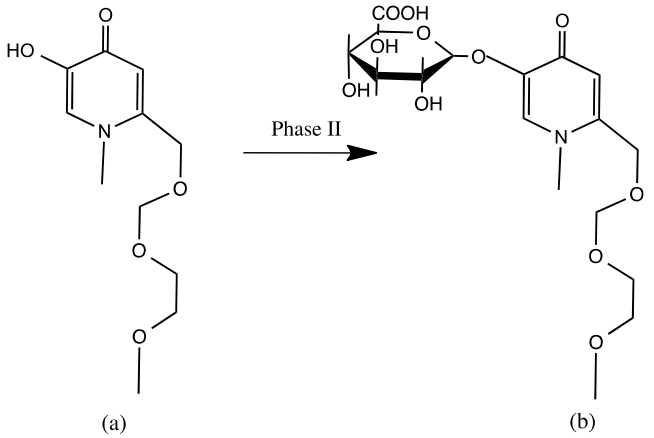

Scheme VIII-7 Metabolic pathways of K7

(a) K7
(b) 3-O-Glucuronide conjugate of K7

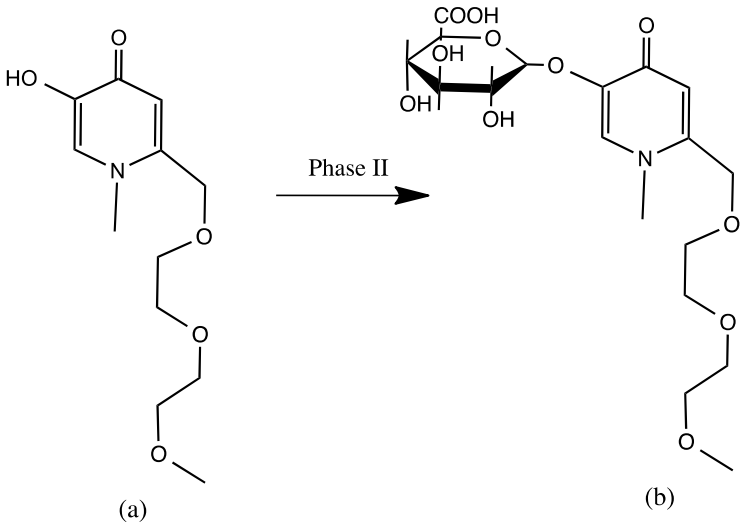

Scheme VIII-8 Metabolic pathways of K6

(a) K6
(b) 3-O-Glucuronide conjugate of K6

Appendix VII

Table VII-1: Iron mobilisation efficacy study group 1 (11 male SD rats).

CN128	B.W.	% Iron mobilisation	% Efficacy	% Recovery
75	230	5.6	2.0	65.3
150	236	7.6	3.9	85.7
300	239	24.4	20.8	49.7
600	241	35.0	31.3	46.3
1200	243	46.0	42.3	66.5
CP20	B.W.	% Iron mobilisation	% Efficacy	% Recovery
75	244	1.9	-0.6	59.0
150	244	2.0	-0.4	80.7
300	251	5.0	2.8	57.6
600	253	10.5	8.1	64.5
1200	255	29.5	27.1	71.7
Water	B.W.	% Iron mobilisation	% Efficacy	% Recovery
	256	3.6	NA	55.2

Table VII-2: Iron mobilisation efficacy study group 2 (11 female SD rats)

CN128	B.W.	% Iron mobilisation	% Efficacy	% Recovery
75	229	4.6	0.8	80.6
150	227	13.7	9.9	95.1
300	222	14.1	10.3	87.8
600	221	35.5	31.7	97.4
1200	219	50.9	47.1	90.6
CP20	B.W.	% Iron mobilisation	% Efficacy	% Recovery
75	217	2.4	0.0	70.2
150	216	2.5	0.1	66.1
300	215	7.9	6.3	78.3
600	214	20.6	18.2	57.9
1200	213	33.2	30.8	59.5
Water	B.W.	% Iron mobilisation	% Efficacy	% Recovery
	209	3.8	NA	65.5

Table VII-3: Iron mobilisation efficacy study group 3 (11 male SD rats)

CN128	B.W.	% Iron mobilisation	% Efficacy	% Recovery
75	254	6.1	4.5	71.1
150	262	10.6	9	73.6
300	268	22.7	21.1	44.4
600	268	56.6	54.9	82.6
1200	284	65.1	63.4	92.6
CP20	B.W.	% Iron mobilisation	% Efficacy	% Recovery
75	289	0.9	-1.5	57.8
150	292	2.2	-0.2	59.6
300	300	5.7	2.4	85.6
600	302	20.8	18.4	60.5
1200	308	35.5	33.0	58.6
Water	B.W.	% Iron mobilisation	% Efficacy	% Recovery
	309	1.7	NA	82.6

Table VII-4: Iron mobilisation efficacy study group 4 (11 female SD rats)

CN128	B.W.	% Iron mobilisation	% Efficacy	% Recovery
75	225	7.0	4.4	77.7
150	224	9.7	7.1	91.9
300	224	17.0	14.4	97.2
600	218	27.0	24.4	91.0
1200	214	55.5	52.9	84.5
CP20	B.W.	% Iron mobilisation	% Efficacy	% Recovery
75	214	1.1	-1.3	58.4
150	213	2.7	0.3	68.0
300	212	6.0	2.7	82.6
600	211	24.7	22.3	71.6
1200	210	28.3	25.9	60.5
Water	B.W.	% Iron mobilisation	% Efficacy	% Recovery
	208	2.6	NA	79.7

Table VII-5: Iron mobilisation efficacy study group 5 (11 male SD rats)

CN128	B.W.	% Iron mobilisation	% Efficacy	% Recovery
75	250	7.7	3.9	80.0
150	270	11.9	8.2	91.5
300	272	27.7	24.0	97.8
600	273	29.1	25.4	92.1
1200	274	36.5	32.8	83.1
CP20	B.W.	% Iron mobilisation	% Efficacy	% Recovery
75	279	1.6	-0.8	30.7
150	279	3.0	0.6	65.5
300	281	9.9	8.4	50.2
600	282	20.6	18.2	57.9
1200	289	33.2	30.8	59.5
Water	B.W.	% Iron mobilisation	% Efficacy	% Recovery
	289	3.8	NA	79.9

Table VII-6: Iron mobilisation efficacy study group 6 (11 female SD rats)

CN128	B.W.	% Iron mobilisation	% Efficacy	% Recovery
75	309	3.0	1.2	68.8
150	293	11.3	9.5	46.6
300	292	28.2	26.4	49.6
600	289	40.1	38.3	52.5
1200	286	54.1	52.3	50.0
CP20	B.W.	% Iron mobilisation	% Efficacy	% Recovery
75	284	1.7	-0.1	65.7
150	277	4.1	2.3	48.9
300	277	5.8	4.6	59.5
600	269	25.2	23.4	48.8
1200	268	31.7	29.9	52.0
Water	B.W.	% Iron mobilisation	% Efficacy	% Recovery
	254	1.8	NA	66.2

Table VII-7: Iron mobilisation efficacy study group 7 (11 male SD rats)

CN128	B.W.	% Iron mobilisation	% Efficacy	% Recovery
75	285	7.6	5.1	75.5
150	290	21.0	18.5	58.4
300	299	25.5	23.1	88.0
600	304	41.3	38.9	58.8
1200	307	49.0	46.6	63.1
CP20	B.W.	% Iron mobilisation	% Efficacy	% Recovery
75	311	3.2	0.7	76.1
150	317	3.6	1.1	70.0
300	323	4.2	1.7	72.3
600	327	32.3	29.9	65.9
1200	344	36.9	34.5	97.8
Water	B.W.	% Iron mobilisation	% Efficacy	% Recovery
	345	2.6	NA	72.6

Table VII-8: Iron mobilisation efficacy study Group 8 (11 female SD rats)

CN128	B.W.	% Iron mobilisation	% Efficacy	% Recovery
75	306	8.7	5.2	66.2
150	305	8.9	5.5	55.9
300	305	20.8	17.3	71.4
600	291	27.1	23.6	59.4
1200	288	51.7	48.2	56.7
CP20	B.W.	% Iron mobilisation	% Efficacy	% Recovery
75	281	2.5	-1.0	73.7
150	280	5.9	2.4	64.9
300	271	13.1	9.6	74.5
600	269	20.2	16.7	81.3
1200	260	21.4	17.6	73.0
Water	B.W.	% Iron mobilisation	% Efficacy	% Recovery
	240	3.5	NA	64.1

Table VII-9: Iron mobilisation efficacy study group 9 (11 male SD rats)

CN128	B.W.	% Iron mobilisation	% Efficacy	% Recovery
75	227	7.3	5.5	81.2
150	236	9.6	7.8	58.9
300	246	16.9	15.1	43.8
600	248	46.6	44.8	48.0
1200	252	61.3	59.5	47.8
CP20	B.W.	% Iron mobilisation	% Efficacy	% Recovery
75	270	1.5	-0.3	65.5
150	279	2.7	0.9	67.4
300	289	5.0	3.2	68.7
600	290	27.4	25.6	53.8
1200	291	36.0	34.2	61.8
Water	B.W.	% Iron mobilisation	% Efficacy	% Recovery
	295	1.8	NA	59.5

Table VII-10: Iron mobilisation efficacy study group 10 (11 female SD rats)

CN128	B.W.	% Iron mobilisation	% Efficacy	% Recovery
75	270	6.0	3.3	64.1
150	269	10.1	7.5	57.5
300	269	12.8	10.1	76.4
600	267	28.8	26.1	66.2
1200	264	42.1	39.4	92.8
CP20	B.W.	% Iron mobilisation	% Efficacy	% Recovery
75	263	0.9	-1.8	82.4
150	262	1.2	-1.5	96.9
300	262	4.5	1.9	96.9
600	262	10.5	7.8	83.3
1200	261	31.0	28.3	65.4
Water	B.W.	% Iron mobilisation	% Efficacy	% Recovery
	260	2.7	NA	68.3

Table VII-11: Dose response study of CN128 (N=10)

Chelator	Dose (µmol/kg)	Dose (mg/kg)	Iron Mobilisation (%)	Efficacy (%)	Recovery (%)	No.
CN128	75	22	6.4 ± 1.7	3.6 ± 1.7	73.1 ± 6.7	10
CP20	75	10	1.8 ± 0.7	−0.7 ± 0.8	64.0 ± 14.2	10
CN128	150	44	11.4 ± 3.6	8.7 ± 3.9	71.5 ± 18.2	10
CP20	150	21	3.0 ± 1.3	0.6 ± 1.2	68.8 ± 12.7	10
CN128	300	89	21.0 ± 5.3	18.3 ± 5.7	70.6 ± 22.0	10
CP20	300	42	6.7 ± 2.7	4.4 ± 2.8	72.6 ± 14.2	10
CN128	600	177	36.7 ± 9.2	33.9±10.2	69.4 ± 19.6	10
CP20	600	83	21.3 ± 6.5	18.9 ± 7.0	64.6 ± 11.3	10
CN128	1200	354	51.2 ± 8.1	48.5 ± 9.1	72.8 ± 17.9	10
CP20	1200	167	31.7 ± 4.3	29.2 ± 5.0	66.0 ± 12.8	10

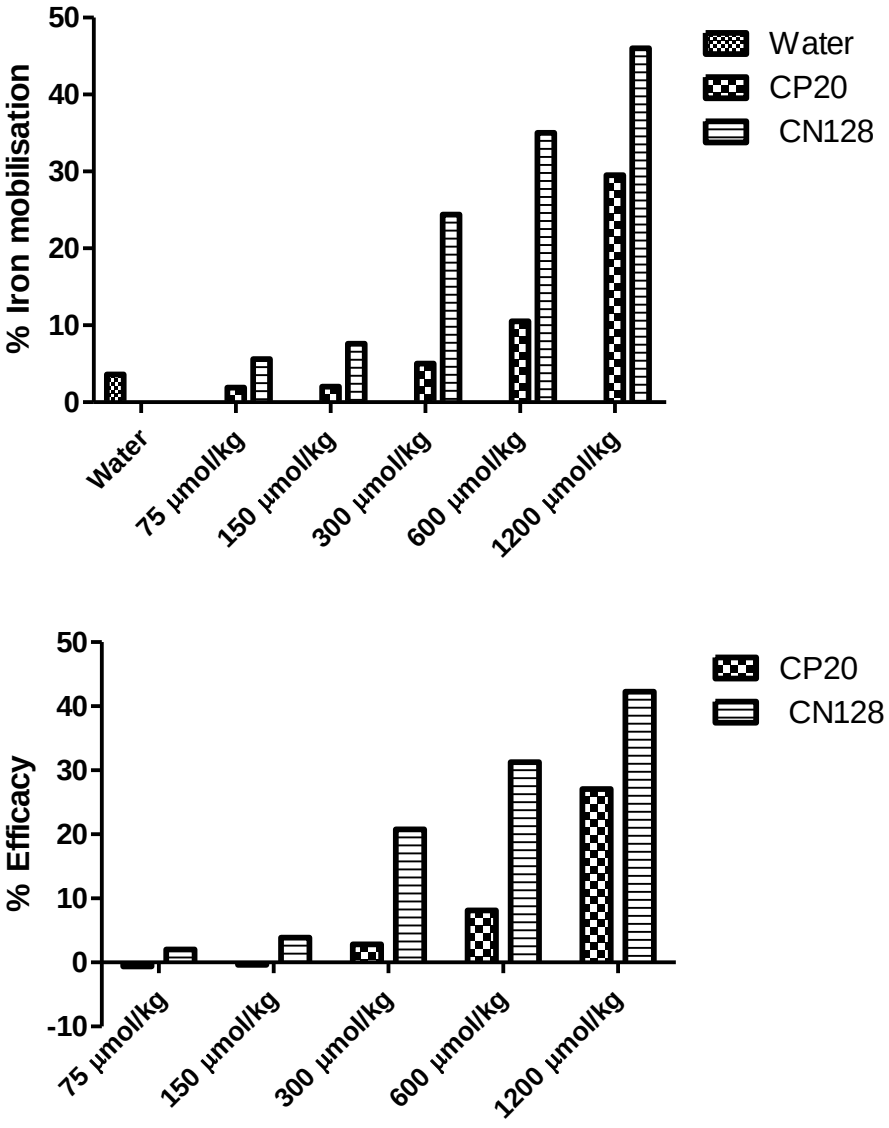

Figure VII-1: Iron mobilisation and efficacy of CN128 (Group 1)

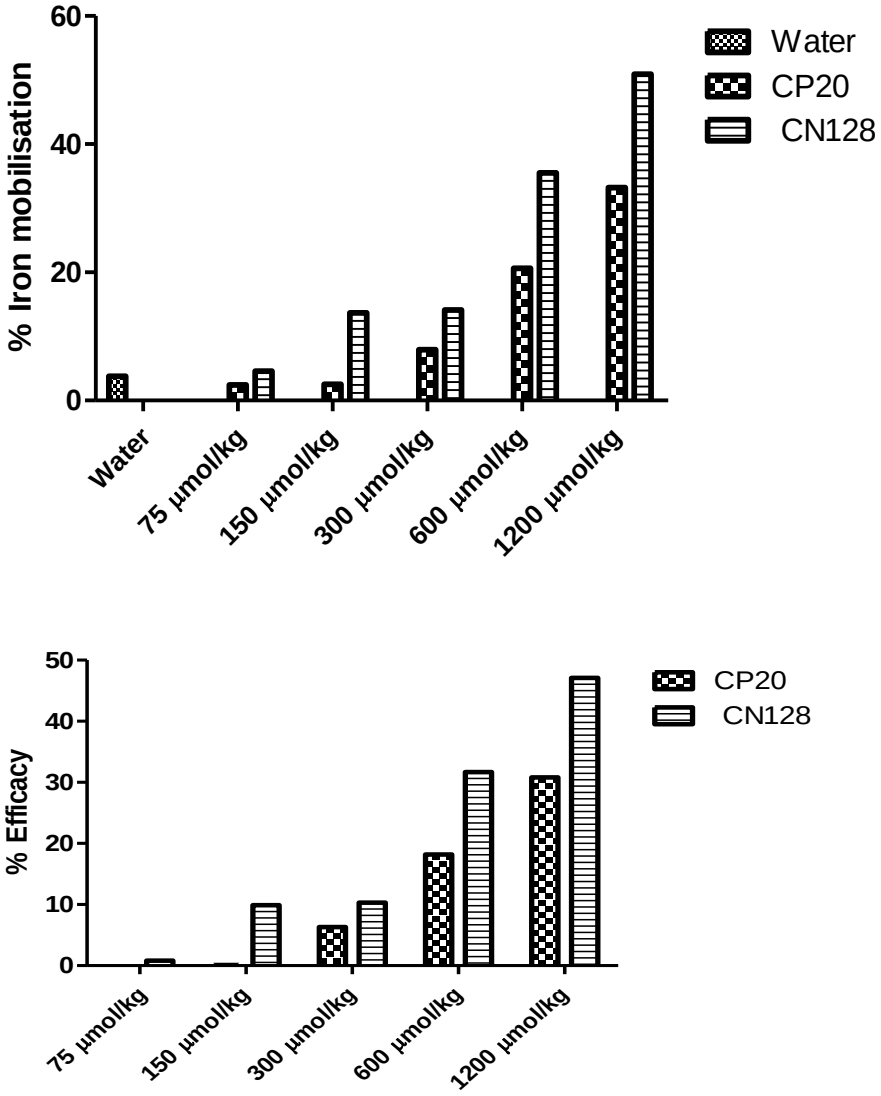

Figure VII-2: Iron mobilisation and efficacy of CN128 (Group 2)

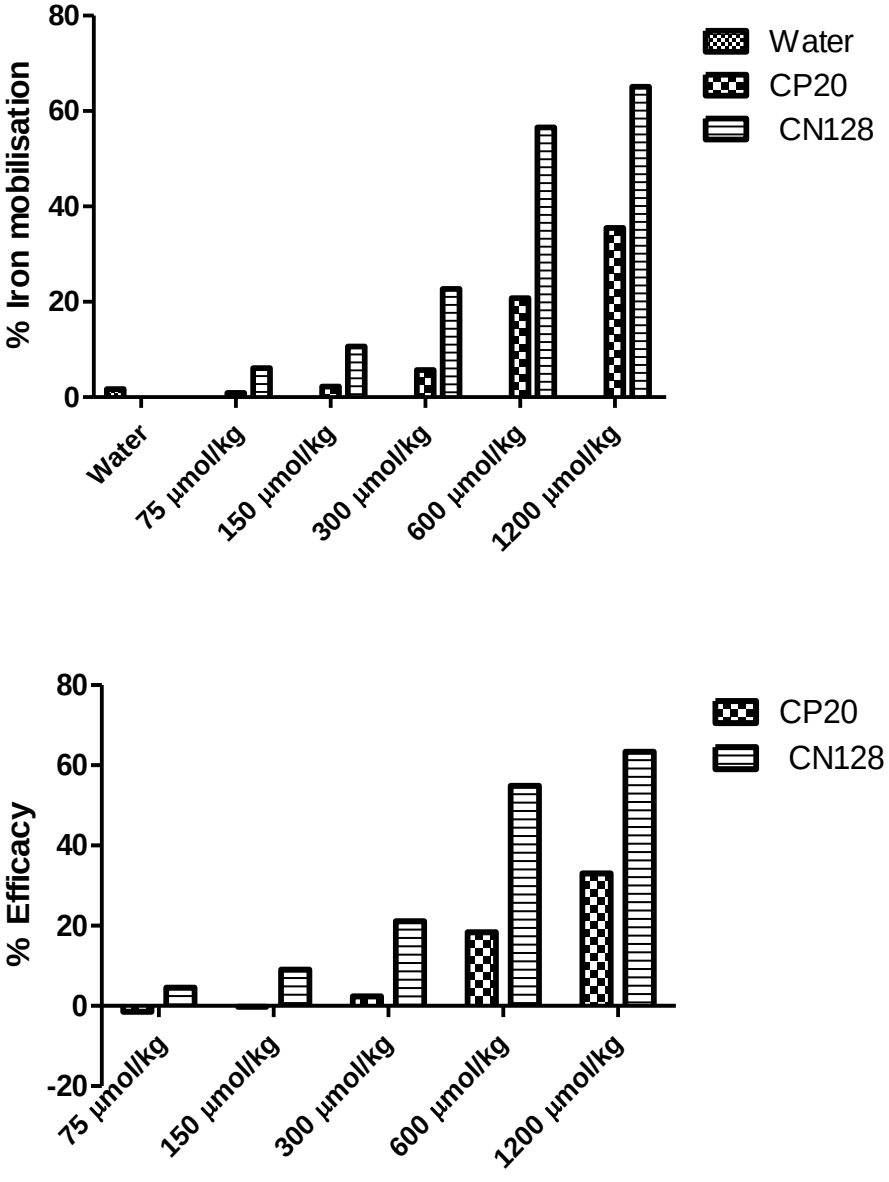

Figure VII-3: Iron mobilisation and efficacy of CN128 (Group 3)

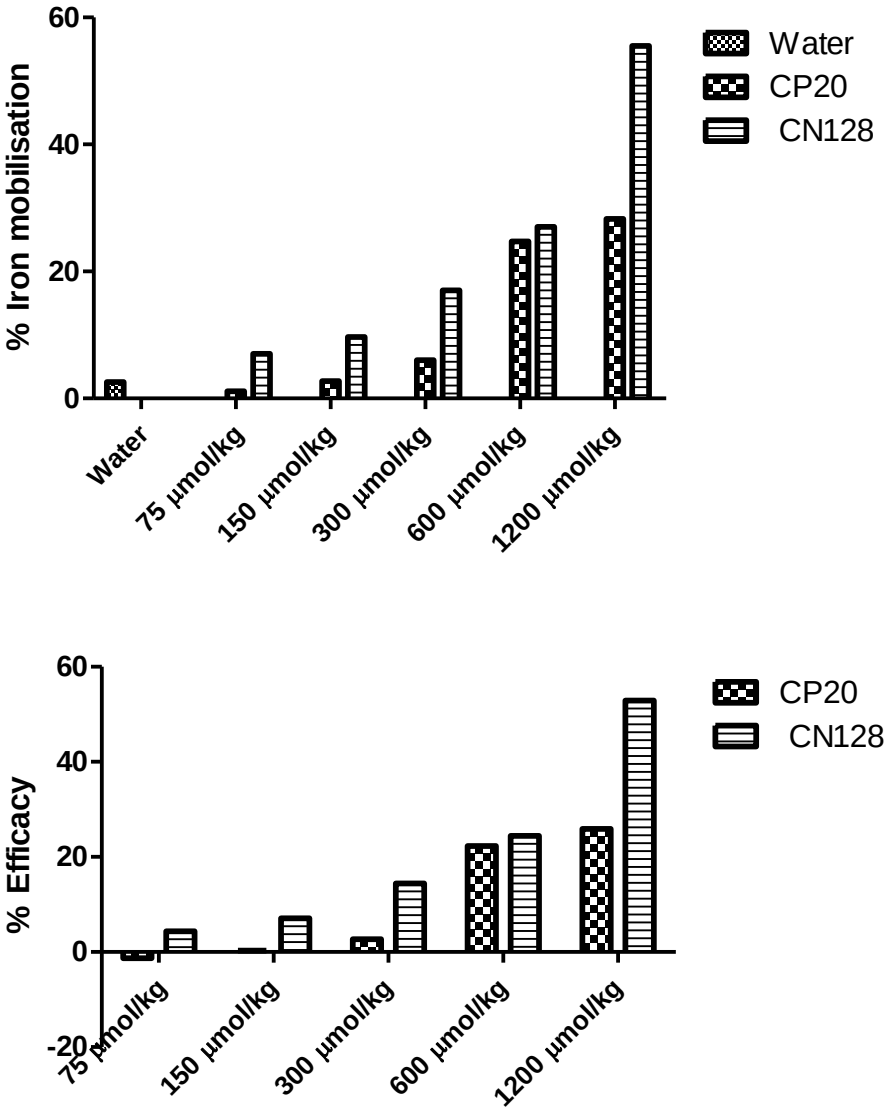

Figure VII-4: Iron mobilisation and efficacy of CN128 (Group 4)

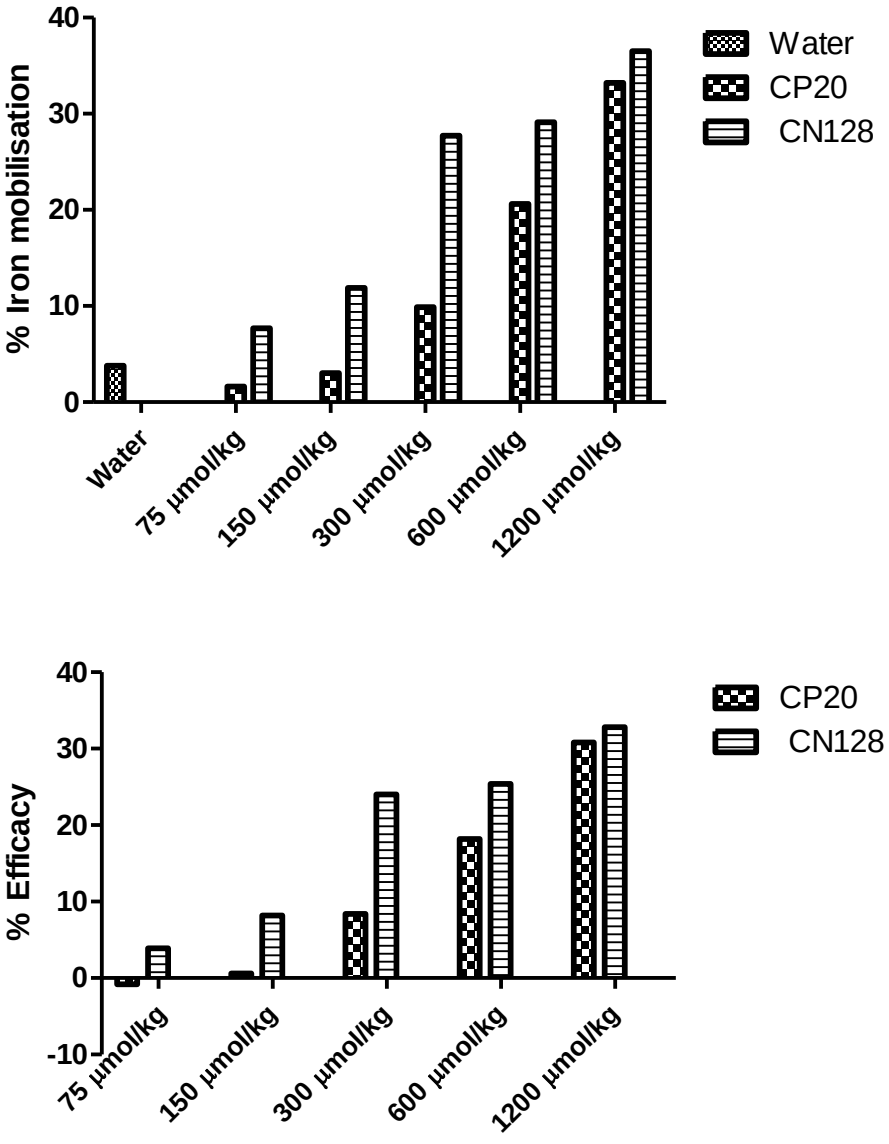

Figure VII-5: Iron mobilisation and efficacy of CN128 (Group 5)

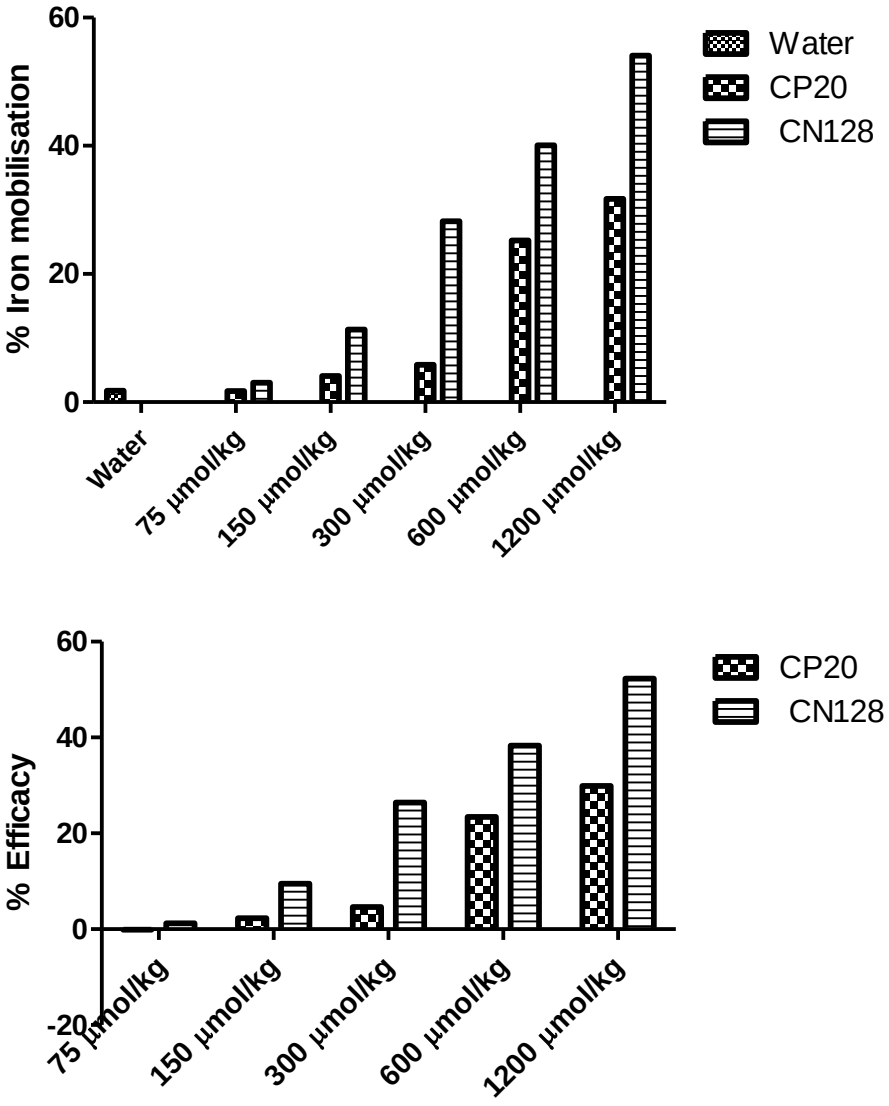

Figure VII-6: Iron mobilisation and efficacy of CN128 (Group 6)

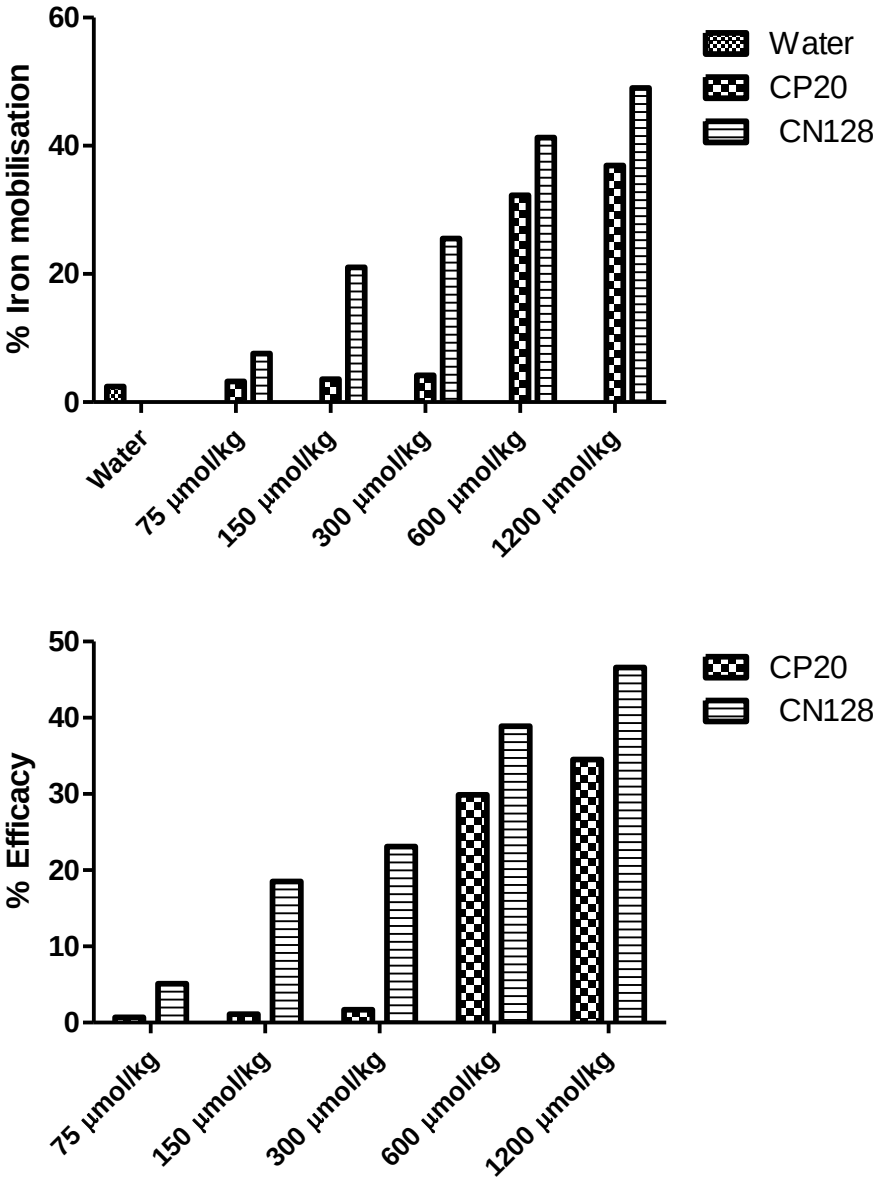

Figure VII-7: Iron mobilisation and efficacy of CN128 (Group 7)

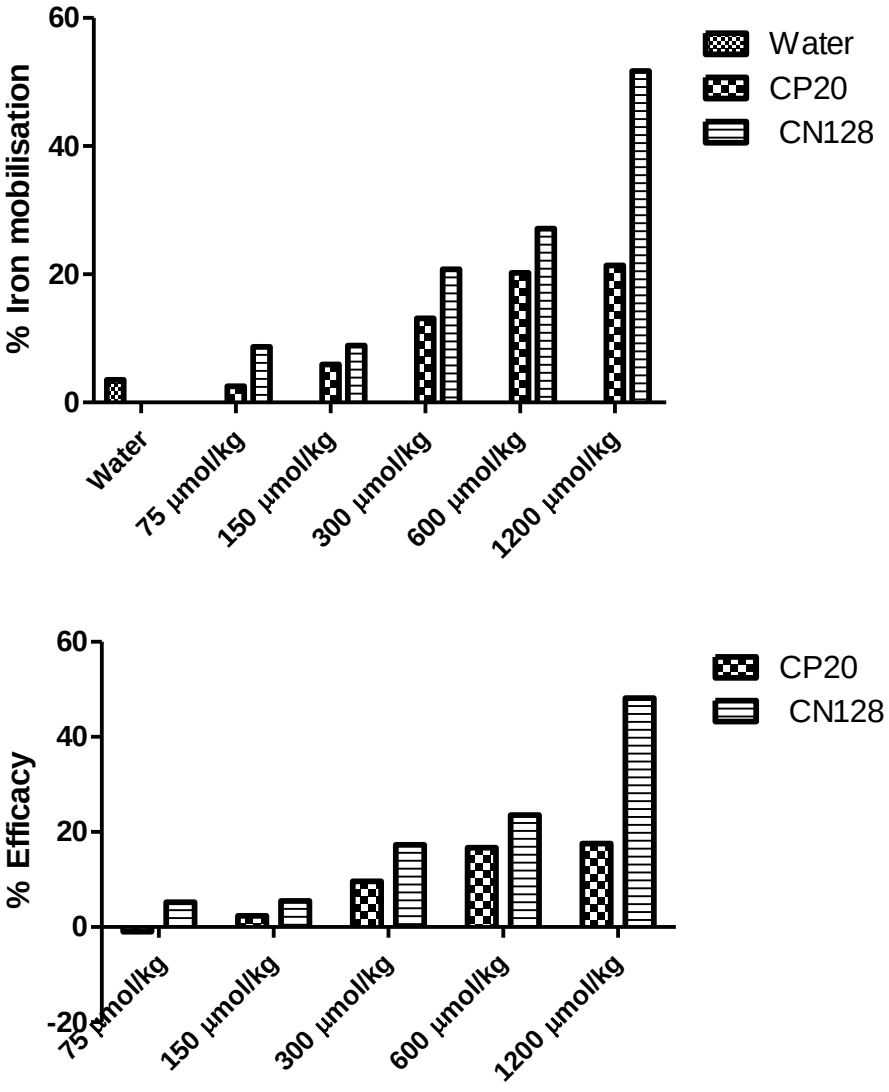

Figure VII-8: Iron mobilisation and efficacy of CN128 (Group 8)

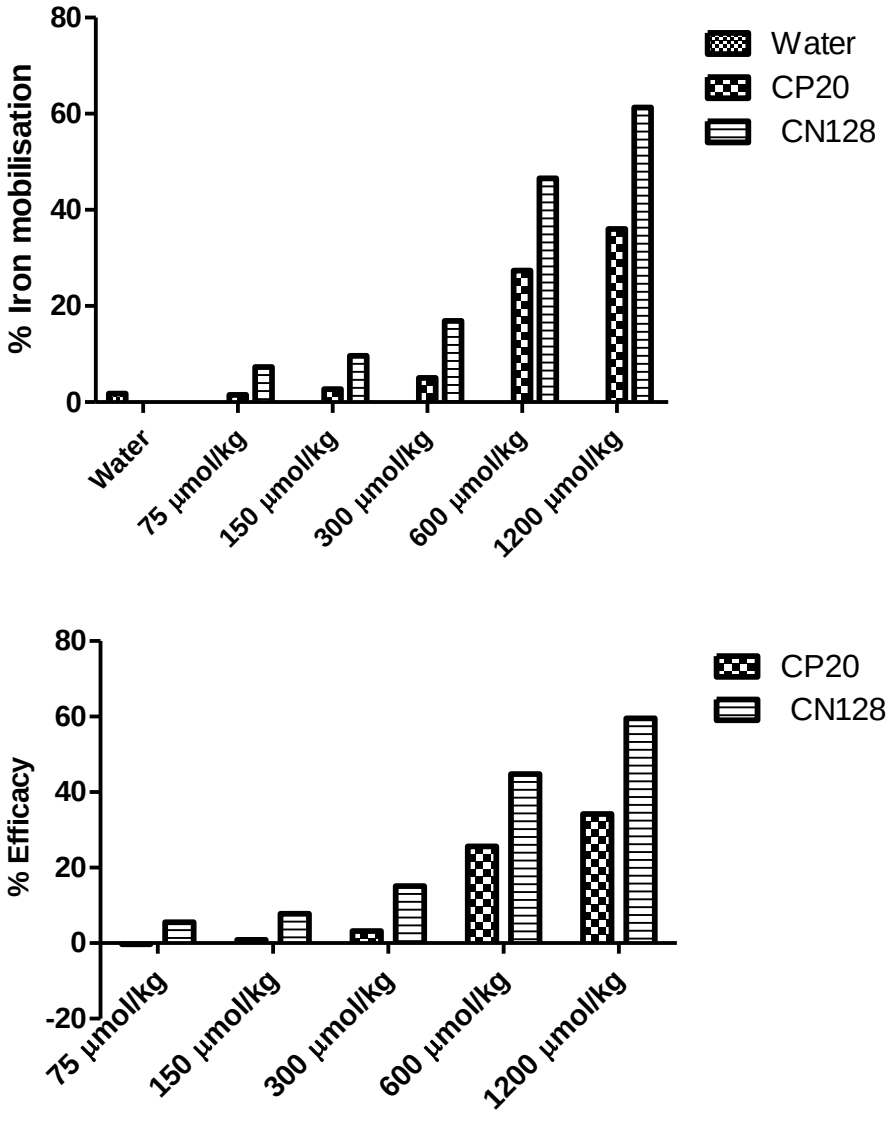

Figure VII-9: Iron mobilisation and efficacy of CN128 (Group 9)

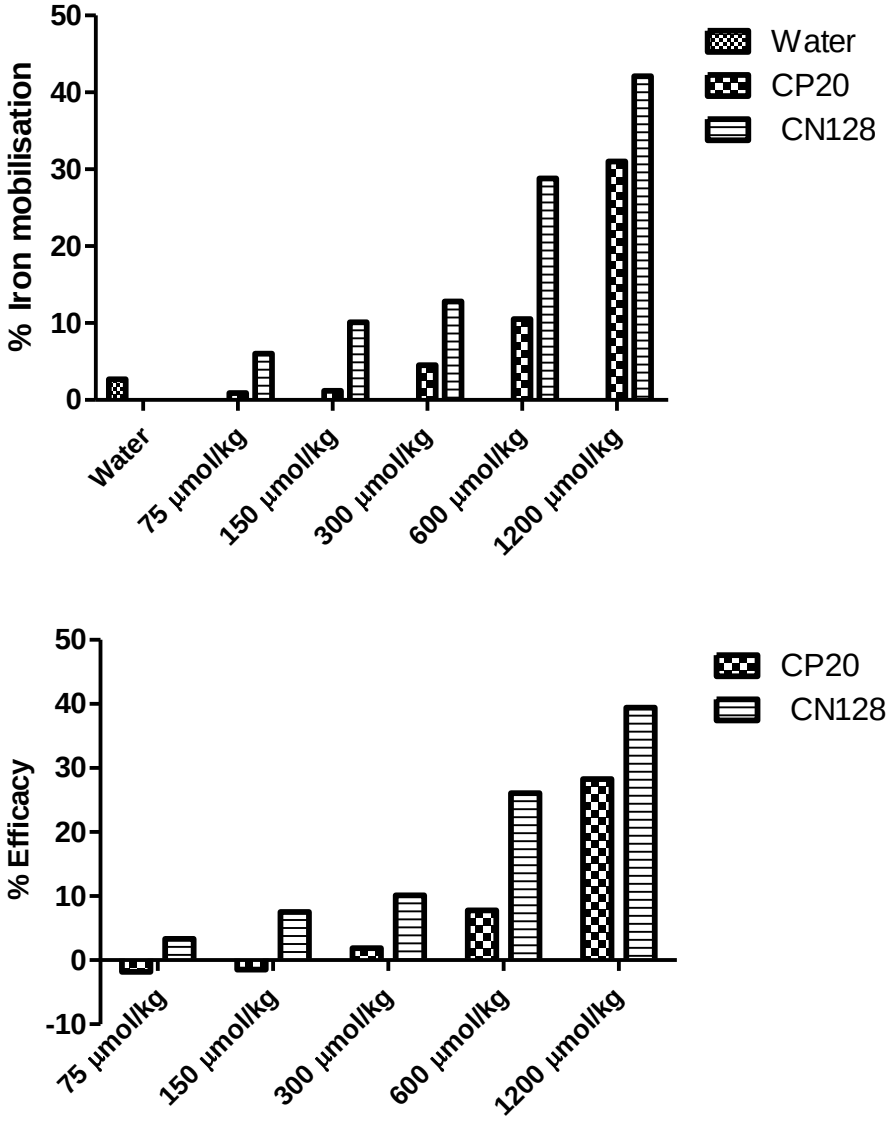

Figure VII-10: Iron mobilisation and efficacy of CN128 (Group 10)

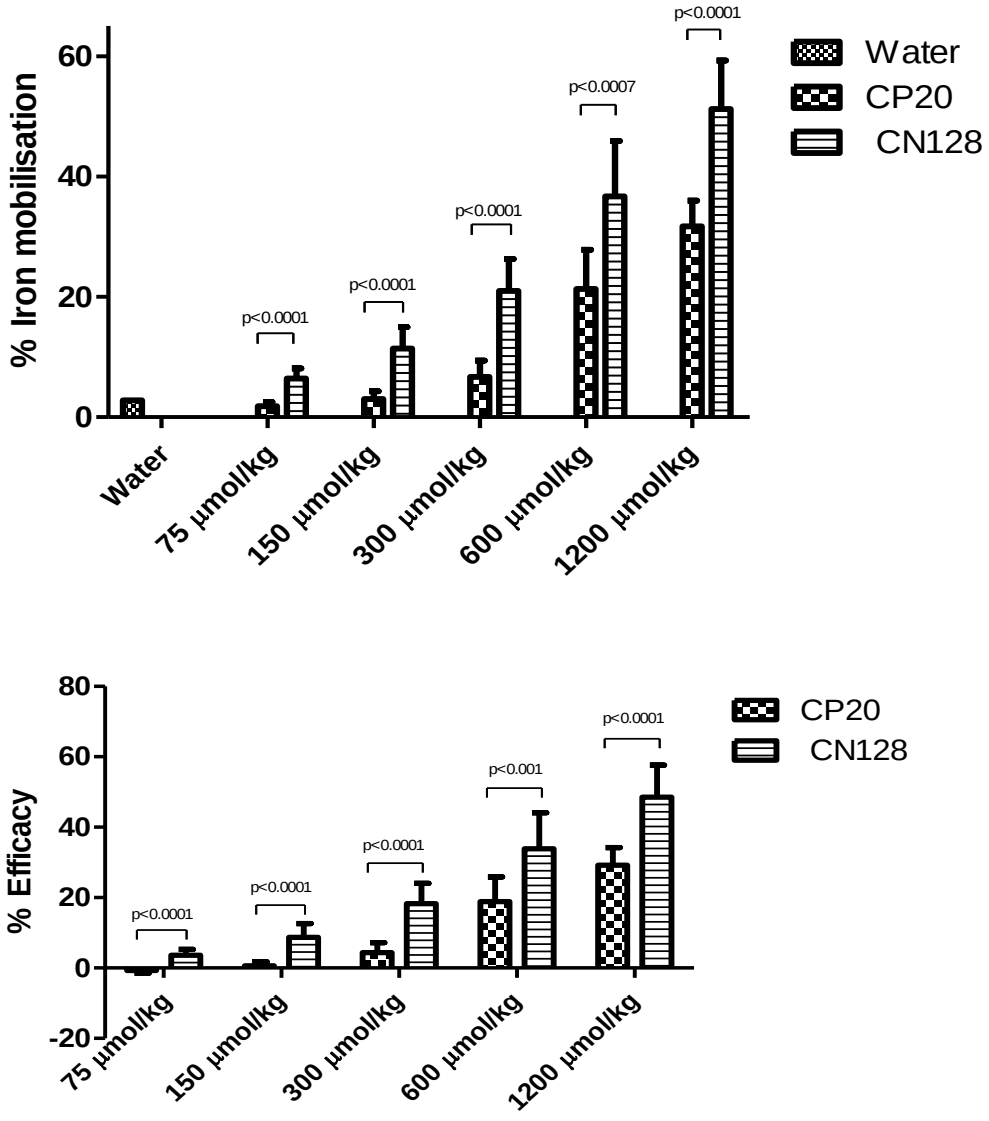

Figure VII-11: Iron mobilisation and efficacy of CN128 (N=10)